

Space Weather Alert Network at Two Lagrangian Points

AE3200 Design Synthesis Exercise Final Report

Group 6

Simon van Diepen	4442229	Olivier Moriaux	4478290
Nathan Griffioen	4275772	Simon van Overeem	4442423
Ferran van Kan	4477278	Nikhil Wessendorp	4432290
Krijn de Kievit	4441052	Tim de Wilde	4449916
Christopher de Koning	4456831	Nick Wildemans	4433971

Supervisor	Dr. ir. E.N. Doornbos	Tutors	D. Dolkens, MSc
Date of Delivery	July 3, 2018		L. Laguarda Sanchez, MSc



[This page was left blank intentionally]

CONTENTS

Nomenclature	v
Executive Summary	vi
1 Introduction	1
2 Market Analysis	2
2.1 Space Weather Impact	2
2.2 Stakeholder Analysis	2
2.3 Competitors	4
2.4 Current Market	4
2.5 Future Market	4
2.6 Return on Investment	6
3 Trade-Off Revision	7
3.1 Solar Electric Propulsion	7
3.2 Solar Sail - Chemical Propulsion Hybrid Solution	7
3.3 Final Trade-Off	8
4 Functional Diagrams	10
4.1 Functional Flow Diagram	10
4.2 Functional Breakdown Structure	11
5 Sustainable Development Strategy	12
5.1 Criteria	12
5.2 Weight Allocation	13
5.3 Assessment	13
5.4 Analysis of Phases	15
5.5 Requirements	16
6 Payload	17
6.1 Monitoring Objectives	17
6.2 Instrument Description	18
6.3 Instrument Protection	26
6.4 Technical Risk Assessment	27
6.5 Reliability, Availability, Maintainability, and Safety Characteristics	27
6.6 Compliance Matrix	28
6.7 Conclusion and Recommendations	32
7 Telemetry, Tracking and Command Characteristics	33
7.1 Data rate	33
7.2 Link budget	33
7.3 TT&C Architecture	36
7.4 Data Handling	37
7.5 Risk Analysis	37
7.6 Reliability, Availability, Maintainability, and Safety Characteristics	38
7.7 Requirement Compliance	38
7.8 Conclusion and Recommendations	39
8 Astrodynamic Characteristics	40
8.1 Method	40
8.2 Launch	41
8.3 L5	44
8.4 L1	48
8.5 Launch Date Sensitivity	50
8.6 Verification and Validation	50
8.7 Risk Analysis	51
8.8 Requirement Compliance	52
8.9 Conclusion and Recommendations	53
9 Main Propulsion System	54
9.1 Thruster Selection	54
9.2 Propellant Tanks	55
9.3 Presurant Tank	57
9.4 Feed System Design	58
9.5 Leakage	60
9.6 Pressure Drop and Mass Estimation	60
9.7 Propulsion Sensitivity	63
9.8 Risk Analysis	64
9.9 Reliability, Availability, Maintainability, and Safety Characteristics	64
9.10 Requirement Compliance	65
9.11 Conclusion and Recommendations	66
10 Thermal Characteristics	67
10.1 Thermal Requirements	67
10.2 Thermal Environment Model	68
10.3 ANSYS® Model	73

10.4	Sensitivity Analysis	76
10.5	Verification and Validation	77
10.6	Risk Analysis	79
10.7	Reliability, Availability, Maintainability, and Safety Characteristics	79
10.8	Requirement Compliance	79
10.9	Conclusion and Recommendations	80
11	Power Characteristics	81
11.1	Mission Phase Power Required	81
11.2	Mission Phase Power Generation	82
11.3	Electrical Layout	85
11.4	Sensitivity Analysis	85
11.5	Risk Analysis	86
11.6	Reliability, Availability, Maintainability, and Safety Characteristics	86
11.7	Requirement Compliance	87
11.8	Conclusion and Recommendations	87
12	Attitude Determination and Control Characteristics	88
12.1	Mission Modes and Corresponding Requirements	88
12.2	External and Internal Disturbances	90
12.3	Attitude Control Actuator Sizing	93
12.4	Wheel and Thruster Selection	95
12.5	Attitude Determination Sensor Selection	97
12.6	Sensitivity Analysis	99
12.7	System Overview	99
12.8	Verification and Validation	99
12.9	Risk Analysis	100
12.10	Reliability, Availability, Maintainability, and Safety Characteristics	100
12.11	Requirement Compliance	101
12.12	Conclusion and Recommendations	102
13	Structural Characteristics	103
13.1	Loads	103
13.2	Material Characteristics	104
13.3	Primary Structure Design	109
13.4	Secondary Structure Design	112
13.5	Tertiary Structure Design	118
13.6	Centre of gravity and moment of inertia	121
13.7	Verification and Validation	121
13.8	Reliability, Availability, Maintainability, and Safety Characteristics	122
13.9	Requirement Compliance	123
13.10	Conclusion and Recommendations	123
14	Interfaces	125
14.1	N2-Chart	125
14.2	Hardware Block Diagram	125
14.3	Software Block Diagram	126
14.4	Communication Flow Diagram	126
15	Mass and Cost Budget	128
16	Post-DSE Activities	130
16.1	Project Design and Development Logic	130
16.2	Manufacturing, Assembly and Integration Plan	132
16.3	Operations and Logistics Concept Description	133
16.4	Project Gantt Chart	135
17	Conclusion	136
	Bibliography	138
A	Work Division	141

Nomenclature

List of Abbreviations

ACE	Advanced Composition Explorer
ADCS	Attitude Determination and Control System
AU	Astronomical Unit
C&DH	Command and Data Handling
CME	Coronal Mass Ejection
DSE	Design Synthesis Exercise
EPS	Electric Power System
GEO	Geostationary Earth Orbit
GMAT	General Mission Analysis Tool
L1	Lagrange Point 1
L5	Lagrange Point 5
MMH	Monomethyl Hydrazine
NASA	National Aeronautics and Space Administration
NTO	Nitrogen Tetroxide (N ₂ O ₄)
OB1	Observation Beacon 1, heading to L1
OB2	Observation Beacon 2, heading to L5
RTG	Radioisotope Thermoelectric Generator
SEZ	Solar Exclusion Zone
SNR	Signal to noise ratio
TEC	Thermal Expansion Coefficient
TNT	2,4,6-Trinitrotoluene
TT&C	Telemetry, Tracking & Control
UTC	Coordinated Universal Time

List of Symbols

α	Angular acceleration	[rads ⁻²]
α_t	Thermal Expansion Coefficient	[$\mu\text{m}^\circ\text{C}^{-1}\text{m}^{-1}$]
Δp	Pressure Drop	[Pa]
ΔV	Velocity Increment	[ms ⁻¹]
ΔV_{ins}	Orbit Insertion Velocity Increment	[ms ⁻¹]
δ	Deflection	[m]
\dot{m}	Mass Flow	[kgs ⁻¹]
\dot{m}_0	Pressurant Gas Mass Flow	[kgs ⁻¹]
η_{BAT}	Battery Discharge Efficiency	[-]
η_{cell}	Cell Efficiency	[-]
η_d	Day time efficiency	[-]
γ	Specific Heat Ratio	[-]
ν	True Anomaly	[rad]
Ω	Right Ascension of the Ascending Node	[rad]
ω	Argument of Perigee	[rad]
ρ	Density	[kgm ⁻³]
ρ_p	Propellant Density	[kgm ⁻³]
σ_y	Yield Stress	[Pa]
DOD	Depth of Discharge	[-]
θ	Escape Burn Angle	[rad]
θ	Incidence Angle	[rad]
A	Area	[m ²]
A	Solar Panel Area	[m ²]
a	Semi-major Axis	[m]
A_{ss}	Solar Sail Area	[m ²]
b	Thickness	[m]
C_{clamp}	Clamping Coefficient	[-]
C_{sp}	Specific Cost	[USDm ⁻³]
D	Pipe Diameter	[m]
E	Young's Modulus	[Pa]
e	Eccentricity	[-]

e	Pipe Roughness	[m]
E_{bat}	Energy Required by Battery	[J]
F	Force	[N]
f	Pipe Friction Factor	[-]
F_T	Thrust	[N]
G	Gravitational Constant	[m ³ kg ⁻¹ s ⁻²]
g_0	Gravitational Acceleration at Sea Level	[ms ⁻²]
I	Mass moment of inertia	[kgm ²]
i	Inclination	[rad]
I_{sp}	Specific Impulse	[s]
k	Thermal Conductivity	[Wm ⁻¹ K ⁻¹]
L	Length	[m]
L	Pipe Length	[m]
L_D	Total Degradation	[-]
M	Internal Moment	[Nm]
m	Mass	[kg]
m_0	Pressurant Gas Mass	[kg]
M_e	Mass of the Earth	[kg]
m_f	Spacecraft mass after burn	[kg]
m_p	Propellant Mass	[kg]
M_s	Solar Mass	[kg]
m_{fuel}	Fuel Mass	[kg]
m_{sc}	Spacecraft Mass	[kg]
P_0	Pressurant Tank Pressure	[Pa]
P_p	Propellant Tank Pressure	[Pa]
P_s	Solar radiation pressure	[Pa]
P_{bat}	Power Required by Battery	[W]
P_{req}	Power Required	[W]
Q	First Moment of Area	[m ³]
R	Specific Gas Constant	[Jkg ⁻¹ K ⁻¹]
R	Sun-Earth distance	[m]
r	Sun-Satellite distance	[m]
Re	Reynolds Number	[-]
S	Bending Stiffness	[Nm ⁻¹]
S	Solar Irradiance	[Wm ⁻²]
T	Torque	[Nm]
t	Time	[s]
T_0	Pressurant Tank Temperature	[K]
t_b	Burn Time	[s]
t_{dist}	Discharge Time	[s]
V	Shear Force	[N]
V_p	Propellant Tank Volume	[m ³]
v_p	Propellant Flow Velocity	[ms ⁻¹]
v_{sc}	Satellite velocity	[ms ⁻¹]
V_{Xt}	Velocity in X-Direction after Insertion Burn	[ms ⁻¹]
V_{Yt}	Velocity in Y-Direction after Insertion Burn	[ms ⁻¹]
V_{Zt}	Velocity in Z-Direction after Insertion Burn	[ms ⁻¹]
X	Distance in X-Direction	[m]
Y	Distance in Y-Direction	[m]
y_{max}	Maximum Distance from Neutral Axis	[m]
Z	Atomic number	
Z	Distance in Z-Direction	[m]

EXECUTIVE SUMMARY

On a daily basis, the Sun experiences solar weather events, such as coronal mass ejections (CMEs) and solar flares. Varying in size, they are characterised by violent outbursts of matter and energy from the Sun's surface. In the rare case of a CME of significant size hitting Earth, it could have immense consequences for the electrical power grid, especially at auroral latitudes. CMEs cause large disturbances to the Earth's geomagnetic field, which result in an increased energy flux. In turn, this would induce large power surges in power lines, electrical wiring, and pipelines. If a system is not protected from such surges, it could short-circuit and be damaged or destroyed. Adverse space weather effects are not only limited to Earth-based electronics but also satellites, which are even more exposed to space weather than Earth-based electronics due to trapped particles. Without an early warning of an incoming CME, the damage of an extreme CME would be catastrophic, causing up to \$10 trillion in damage just from damaged infrastructure.¹

The purpose of this report is to present the preliminary design of a Space Weather Alert Network (SWAN) consisting of two satellites, called Observation Beacon 1 (OB1) and Observation Beacon 2 (OB2). By having continuous communication with Earth, early warnings can be given and excessive damage may be averted. Previously, a project plan, baseline design report and midterm design report have been written about the investigation and the trade-offs necessary for certain design decisions, the results of which are used in this report. [1-3]

OB1 and OB2 will venture to the Sun-Earth system's Lagrangian Point 1 (L1) and Lagrangian Point 5 (L5). These Lagrangian points are of interest since they allow spacecraft to remain stationary in them relative to the Sun and Earth, with only very little fuel consumption. This makes L1 and L5 ideal for continuous monitoring from a single position. In Figure 1 the exact location of all Lagrange points are given, but the main focus will lie on L1 and L5. Due to its location between the Sun and the Earth, L1 is ideal for in-situ measurements of incoming CMEs. Since warnings sent from L1 might not always be early enough, an additional satellite can be positioned in L5 to enable remote sensing of the Sun and the heliosphere between the Sun and Earth. This satellite can monitor activity on the surface of the Sun, and send a warning when increased solar activity is observed. In addition, due to the counter-clockwise rotation of Sun from the perspective of Figure 1, an L5 satellite will observe one side of the Sun before that side faces the Earth. Lastly, L5 also boasts a clear view of the heliospheric plane between the Sun and Earth, allowing for remote tracking of CME propagation².

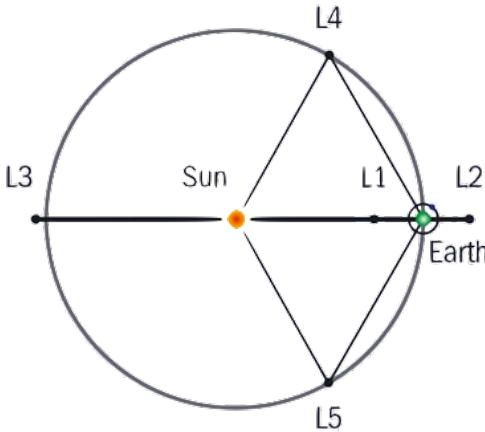


Figure 1: The Positions of the Lagrange Points Relative to the Earth and Sun²

The general idea about the mission together with the need for two satellites at the L1 and L5 points is clear, therefore this report will primarily focus on the design of every subsystem. The two spacecraft have two different transfer trajectories towards respectively L1 and L5, also both satellites have a different set of payload instruments, L1 mainly consists of in-situ measurement instruments and L5 mainly consists of remote sensing instruments. Therefore the two satellites have very distinct properties and thus every subsystem will be sized accordingly for both OB1 and OB2.

The main subsystems which will be designed in this report are the Payload, Attitude Determination & Control Subsystem (ADCS), Telemetry, Tracking & Command (TT&C), Control & Data Handling (C&DH), Propulsion, Electronic Power

¹<http://www.dailymail.co.uk/sciencetech/article-5128079/Doomsday-solar-storm-devastate-Earth-moment.html>

²http://www.labspaces.net/blog/895/The_Lagrange_points____Nature___s_parking_spots

System (EPS), Thermal Control and Structures. For each of these subsystems a preliminary sizing has been performed in which the main characteristics are designed and determined, furthermore, CAD models have been made to give a visual representation of the design. The main characteristics of each subsystem for OB1 are shown in Table 1. For OB2 a different set of spacecraft characteristics have been developed which are shown in Table 2.

Research has already been done on the payload in the midterm report, however their main characteristic requirements are given in this report together with the influence they have on the other subsystems. [3] In this report the decision has been made to make a distinction in payload instruments on OB1 and OB2, this was for cost budget reasons and additional instruments which were necessary to get the required data for a warning system. This indirectly means that every other subsystem has to be designed twice as well, due to the different power, mass, stability and thermal characteristics of both spacecraft.

The Attitude Determination & Control Subsystem has been sized according to the stability and pointing accuracy requirements of the payload instruments together with the requirement arising from the TT&C subsystem such that the antenna should always point towards the Earth. From these requirements, Star trackers, Sun sensors and gyroscopes have been placed on the satellite to determine the attitude of the spacecraft. Furthermore, reaction wheels together with thrusters should make the spacecraft able to control the attitude around three axes at all times. The purpose of the reaction wheels is to make sure that the stability requirements of the payload and antenna are met and momentum is stored, the main function of the thrusters is then to dump momentum.

The Telemetry, Tracking & Command department should be able to cope with the data generated by the different payload instruments. Therefore the data rate of both satellites which has to be sent to Earth has been determined and a link budget has been set up. Moreover, the TT&C subsystem should be designed such that there is a redundant antenna system to ensure direct communication to Earth at all times.

The Control & Data Handling department has determined the ground stations which could be used to ensure the connection with the satellite. Therefore NASA's Deep Space Network and ESA's ESTRACK has been chosen because these stations give an assurance that communication with the satellites OB1 and OB2 is always possible. Lastly, to limit the data rate of both spacecraft a compression type and compression ratio has been chosen and analysed such that the data can be compressed.

The propulsion system has been sized for the transfer orbit towards L1 and L5, which has been simulated in GMAT. For both spacecraft, the propulsion trade-off has been analysed and the main conclusion from this trade-off was that chemical propulsion will be the main propellant type throughout the entire mission lifetime. For the chemical propulsion type, the propellant type and mass have been determined together with the pressurant type and mass. Lastly, the propellant tanks have been sized and chosen from already available propellant tanks.

The Electrical Power Subsystem has been sized to generate the required power for all the instruments and the rest of the subsystems. Specific characteristics such as the mass and capacity of this subsystem have been determined. Furthermore, an electrical block diagram has been generated to give an overview of the electrical wiring throughout the satellite. During the lifetime of the satellites the main electrical power source is chosen to be solar cells, but during burns and transfers batteries will also be used.

The thermal environment of the spacecraft has been analysed throughout the entire spacecraft lifetime. This means that the temperature of the spacecraft is modelled from the launch pad until the end-of-life manoeuvre. Important for the thermal subsystem is the orientation with respect to the Earth and Sun because the main thermal control mechanism used is passive control by different coatings and/or foils around the spacecraft. These coatings and/or foils have been chosen in such a way that the steady state temperature of both spacecraft falls between the operational requirements set by the instruments and subsystems. Furthermore, an ANSYS® model has been made to model the temperatures inside the satellite for different critical subsystems or instruments of the spacecraft.

Lastly, the structures department has sized the spacecraft structure on which all instruments and subsystems are mounted. Vibration and stress analysis has been performed on the satellite and subsystems outside the bus of the satellite such as the solar panels and the booms on which the magnetometer is attached. Furthermore, CAD models of the subsystems and the entire spacecraft have been made to provide a visual representation of the spacecraft. FEM analysis of these CAD models has been performed to look at the stress and deflections of the bus of the satellite.

Table 1: L1 Spacecraft Characteristics

L1 Spacecraft Design		
General Properties	Mass	Dry mass: 226.6kg
		Propellant mass: 31.2kg
		Wet mass: 257.7kg
	Dimensions	0.821 m x 0.821 m x 1.56 m
	Cost	€317.8 million
	ΔV	180.9 ms ⁻¹
	MMOI around x, y, z	57.82 kgm ² , 83.09 kgm ² , and 39.95 kgm ²
Payload	In-situ	Magnetometer
		Faraday Cup
		SEP Monitor
	Remote Sensing	Coronagraph
		X-ray Sensor
ADCS	Sensors	1 TERMA T2 Star trackers
		7 S3 Sun Sensors
		2 LN-200S Northrop Grumman IMUs
	Actuators	16 MR-111C 4N Thrusters
		4 Surrey 10SP-M Reaction wheels
TT&C	Antenna	Diameter: 0.2m
		Type: Horn antenna
	Coding	BPSK Reed Solomon (255,223)
		Viterbi R=0.5 SNR = 2.7 dB
	Data rate	30 kbps
Backup antenna	Low-gain helical	
C&DH	Ground Station	NASA's Deep Space Network ESA's ESTRACK
	On-board processor	RAD750
	Compression Ratio	1
Propulsion	Thruster	AMBR Aerojet Rocketdyne
		Thrust: 623N, I_{sp} : 333s
	Propellants	NTO: 14.4 kg
		MMH: 12.0 kg
	Pressurant	Helium: 50L
Tanks	NTO: 13.6L 80197-1 Northrop Grumman	
	MMH: 14.5L 80342-1 Northrop Grumman	
	He: 50L PVG-50 MT Aerospace	
EPS	Solar Arrays	Type: Extendable Triple-Junction GaAs ultraflex
		Area: 1.4 m ²
		Power: 463.6 W
	Batteries	Type: Li-Ion
		Mass: 0.23 kg Capacity: 28.7 Wh
Thermal	Operational Temperature	Minimum: 19°C
		Maximum: 24°C
	Passive insulation	Front: Hughson white paint Z-202 + 1000 ESH UV
		Back and right: Electroplated gold
		Left: Blue Copper foil tape sanded Top and bottom: Kannigen - Nickel alloy
Structures	Ti-6Al-4V central stiffening cylinder	
	Ti-6Al-4V rectangular frame carrying the main loads	
	Nomex honeycomb core with CF face sheets on outer side of the frame	
	Most payload is contained within the central cylinder	

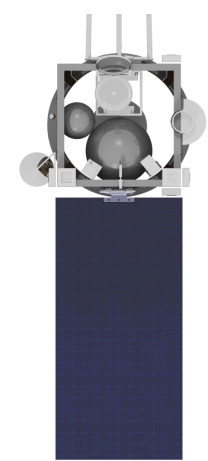


Table 2: L5 Spacecraft Characteristics

L5 Spacecraft Design			
General Properties	Mass	Dry mass: 447.8kg	
		Propellant mass: 826.6kg	
		Wet mass: 1274.4kg	
	Dimensions	1.297 m x 1.297 m x 2.398 m	
	Cost	€342.8 million	
	ΔV	2707.5 ms ⁻¹	
	MMOI around x, y, z	513.09 kgm ² , 743.81 kgm ² , and 422.22 kgm ²	
Payload	In-situ	Magnetometer	
	Remote Sensing	Magnetograph	
		EUV Imager	
		Coronagraph	
		X-ray Sensor	
		Heliospheric Imager	
ADCS	Sensors	2 TERMA T2 Star trackers	
		7 S3 Sun Sensors	
	Actuators	2 LN-200S Northrop Grumman IMUs	
		16 MR-111C 4N Thrusters 4 Honeywell HR 0610 Reaction wheels	
TT&C	Antenna	Diameter: 1.44m Type: Deployable parabolic antenna	
	Coding	BPSK Reed Solomon (255,223) Viterbi R=0.5 SNR = 2.7 dB	
		Data rate	77 kbps
	Backup antenna	Low-gain helical	
C&DH	Ground Station	NASA's Deep Space Network ESA's ESTRACK	
	On-board processor	RAD750	
	Compression Ratio	9.6	
Propulsion	Thruster	AMBR Aerojet Rocketdyne Thrust: 623N, I_{sp} : 333s	
		Propellants	NTO: 381.5 kg MMH: 319.0 kg
	Pressurant		Helium: 140L
	Tanks	NTO: 393L PTP-393 MT Aerospace MMH: 288L PTP-288 MT Aerospace He: 2x 70L PVG-70 MT Aerospace	
Solar Arrays		Type: Extendable Triple-Junction GaAs ultraflex Area: 1.7 m ² Power: 556.2 W	
		Batteries	Type: Ni-H2 Mass: 6.32 kg Capacity: 379.0 Wh
Thermal	Operational Temperature		Minimum: 18°C Maximum: 23°C
			Passive insulation
	Structures	Ti-6Al-4V central stiffening cylinder	
		Ti-6Al-4V rectangular frame carrying the main loads	
Nomex honeycomb core with CF face sheets on outer sides in frame			
Most payload is contained within the central cylinder			



1

INTRODUCTION

This Final report marks the fourth and final milestone of the Design Synthesis Exercise (DSE) of designing a satellite system at Lagrangian points L1 and L5 to monitor space weather phenomena from the Sun. This mission is called project SWAN: Space Weather Alert Network. The goal of this satellite system is to provide an early warning system for solar weather phenomena that may be hazardous to Earth's technological infrastructure. Before this report, three other reports, namely a project plan, baseline report, and midterm report were written. [1–3]

This report specifies the detailed design of the subsystems of the satellites. In particular, astrodynamics, payload, Telemetry, Tracking & Command (TT&C) system, propulsion system, Attitude Determination and Control System (ADCS), thermal control system, power system and the structure will be discussed.

First of all a market analysis is performed in Chapter 2. In addition to the propulsion system trade-off performed in the midterm report, this report contains a more detailed analysis on the propulsion trade-off in Chapter 3. This is followed by the updated functional diagrams of the system in Chapter 4. Consequently, a sustainable development strategy is developed in Chapter 5 as this is an important factor in the design. After that, the design of the mission will be discussed starting with the payload that will be used to monitor space weather at the two Lagrangian points in Chapter 6. The payload will gather data, which will need to be sent to Earth. The design of a communication system will therefore be discussed in Chapter 7. In order to be able to execute the mission, it is necessary to perform a detailed astrodynamics design of the mission in order to be able to travel to the L1 and L5 points, which will be discussed in Chapter 8. This astrodynamics analysis is followed by the design of the main propulsion system for both spacecraft in Chapter 9. When the exact trajectory to both Lagrangian points is known, it is possible to perform a detailed analysis on the thermal and power characteristics of the spacecraft in order to regulate the temperature of both spacecraft and to make sure that the spacecraft are able to generate sufficient power for the subsystems. This will be discussed in Chapter 10 and Chapter 11 respectively. A number of requirements arise from the design of the payload, TT&C system, propulsion system and power system regarding pointing of the spacecraft. For this reason, the ADCS system will be designed in Chapter 12. Finally, after designing each subsystem of the spacecraft, these subsystems need to be fitted into a structure that is able to cope with the loads the spacecraft will experience during the mission. The structural design will be discussed in Chapter 13. Subsequently, after designing the spacecraft subsystems, the interfaces between each of the subsystems will be discussed in Chapter 14, followed by the budgets of the main system parameters in Chapter 15. The report finalises with the activities that need to be performed after the DSE in Chapter 16 and the conclusion and recommendations.

In this report, both spacecraft will have a specific reference name. The spacecraft to L1 will be referenced as Observation Beacon 1 (OB1) while the spacecraft to L5 will be referenced as Observation Beacon 2 (OB2).

An important final note is that this project assumes that the mission takes place in an "ideal universe". Currently, NOAA is committed to space weather missions to L1, starting with DSCOVR, so that ESA can spend its resources towards an L5 mission. However, in the ideal universe project SWAN is a product of all different space agencies around the world that work together as one. Thus, there are no political issues regarding cooperation between the National Aeronautics and Space Administration (NASA), the European Space Agency (ESA), the National Oceanic and Atmospheric Administration (NOAA), etc.



2

MARKET ANALYSIS

For every project to become reality a market analysis should be performed to determine if the investment made is actually worth it. In this chapter, the incentive for investment in this project is analysed. Due to the project aiming towards a warning system, for which the data will be publicly available, the direct return on investment (ROI) will be very minimal. Since no single company, taking into account this fact in combination with the large investment needed, will set aside the full budget needed for this project, it is assumed that the project is funded by a governmental organisation such as ESA or NASA.

2.1. SPACE WEATHER IMPACT

The damage to Earth if a large coronal mass ejection were to hit Earth directly would be very significant. Researchers from the Harvard-Smithsonian Centre for Astrophysics estimate that the damages to the global economy could reach \$10 trillion if such an event occurred in the coming decade and that recovery would take several years. This could rise to \$20 trillion in damages accounting for the technological advancements made in coming years¹. Moreover, it is estimated that the damage to just the US economy could be \$40 billion per day². Thus, although no direct return on investment is obtained, massive damages to almost every company and government on the planet can be prevented by a system providing early warnings of coronal mass ejections. One could say that the potential market value of this system could become the same as the value damages it would prevent, meaning it would be worth 10 trillion. Even if the extreme solar weather is not observed in the mission lifetime, a great deal of scientific data about solar weather can be obtained, adding value to the scientific community. One might argue that the chance of occurrence of such a massive event is very low, but it turns out that is much higher than expected. Riley [4] states that the chance of a Carrington event occurring in the coming decade is a surprisingly high 12%.

Even when such an event does not occur, ESA estimated that the annual damages of space weather at the current time are approximately €200 mln [5], of which 30-40% would be borne by the European Union. The severity of significant space weather events directly tied to the main incentive to invest in this project. Having a space weather system in place would allow, for instance, for satellites to be turned to face away from the sun, and power stations to be stopped temporarily, which would greatly reduce the economic impact of such a storm hitting Earth.

2.2. STAKEHOLDER ANALYSIS

To start any market analysis, it is important to determine the stakeholders of the project. The project does have multiple stakeholders who may influence or be affected by the success and results of the mission. The stakeholders can be divided into primary and secondary stakeholders. Primary stakeholders are those that will directly use the data for either space weather prediction or model development and validation. The DSE board is included since they define the outline of the project. Secondary stakeholders are those that will not directly use the data, but could be interested in the data when a solar storm is detected.

Primary Stakeholders

- Space Agencies (e.g. NASA, ESA, Roscosmos).
- Space weather warning services (e.g. NOAA).
- Scientists involved in solar weather and magnetohydrodynamics who want to test their models with the mission data.
- DSE board.

¹<http://www.dailymail.co.uk/sciencetech/article-5128079/Doomsday-solar-storm-devastate-Earth-moment.html>

²<https://www.extremetech.com/extreme/243255-massive-solar-storm-cost-us-economy-40-billion-per-day>

Secondary Stakeholders

- The general public
 - Emergency response services
 - Power providers
 - Electrical grid maintenance companies
 - Data handling companies
 - The military
 - Insurance companies
 - Geological companies such as off-shore and pipeline maintenance companies.
 - Companies and organisations providing satellite services such as
 - Communication services
 - Broadcasting services
 - Military satellite services
 - Navigational data services
 - Earth weather forecast services
 - Earth observation services
 - Scientific data services
 - Educational services
 - Manned spaceflight services
 - Space tourism services
- and many more
- Aurora watching tourism providers
 - (European) Governments
 - Non-Governmental Organisations (NGO's) such as environmental, health and human rights organisations
 - International institutions such as the United Nations (UN)
 - Airlines
 - Space weather enthusiasts

The stakeholders are also shown in the stakeholder map in figure Figure 2.1.

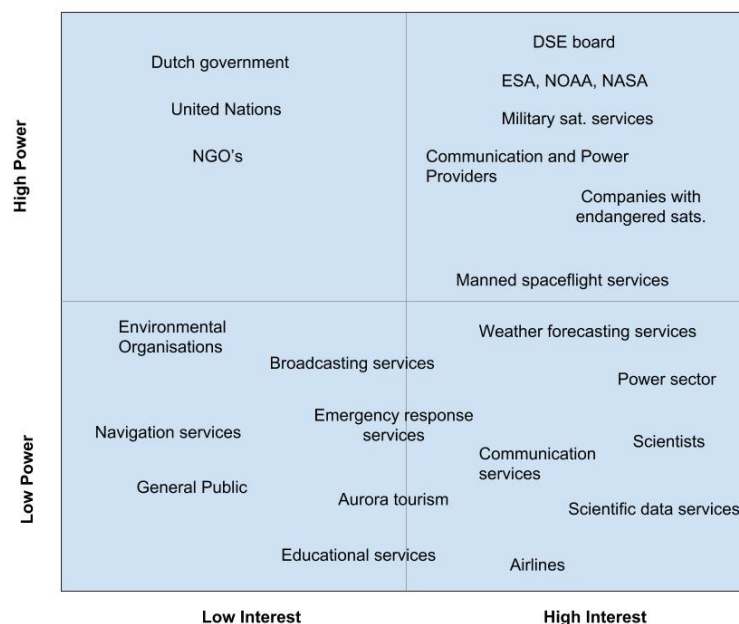


Figure 2.1: Stakeholder Map for the SWAN Mission

Stakeholders like the Dutch government have relatively high power but will likely have a relatively low interest in the project. On the other end of the spectrum, scientists have a relatively limited influence on the mission but have a large interest as measurements of the solar environment could lead to new discoveries about the nature of space weather.

There is also a large degree of scientific interest in the mission as the data collected by these spacecraft could be used for improving the understanding of solar weather and magnetohydrodynamics. Moreover, recent research into improving space weather detection algorithms making use of artificial intelligence requires a lot of data for validation and improvement of these forecasting models.³ On top of this, the mission could also serve as a platform to improve the detection of approaching Near-Earth Objects (NEO's). Due to background light from the sun, it can be difficult to observe NEO's from Earth that are approaching at a path that lies close to the direction of the sun (as viewed from Earth).[6] A scanning

³<https://bit.ly/2L25F1I>

instrument at a Lagrange point looking back to Earth could make use of the shade of the spacecraft and more reliably detect these NEOs. However, as the expected margin in the cost budget for such additions is quite low, this should only be incorporated if additional funding for this is provided by an organisation actively involved in the detection of NEOs.

Lastly, data handling companies are also an important party in this project. These companies can perform value increasing operations on the publicly available raw data which they can sell to other institutions. This way, they can build a market of their own where they charge customers a certain amount in exchange for processed and interpreted data. An example of this could be an aurora tourism operator paying a certain data handling company to provide them with analysed data about when auroras will occur since the tourism operator itself does not have the means to analyse the raw data.

2.3. COMPETITORS

Before the current mission, numerous spacecraft were launched with the purpose of performing scientific measurements on the sun and observing solar behaviour. Most of these missions were launched in the 1990's, the main examples being ACE, SOHO and the STEREO spacecraft. These spacecraft are still operational but are far beyond their design life (more than 20 years). This means that their technology is outdated and the chance of them failing is relatively high. The most recent mission was the DSCOVR launched in 2015, but this too has origins that can be traced back to the 1990's, when Al Gore conceived the mission as an Earth observation mission. Although the project was adapted to a solar and Earth observation mission in 2012, the design of the spacecraft is still not optimal for solar observation as Earth observation also had to be designed for.

Moreover, all these missions went only to the Sun-Earth L1 point, with the exception of the STEREO spacecraft, which went into Earth-trailing orbits. Adding an observation from the Sun-Earth L5 point would significantly improve the monitoring and warning capabilities as the side-view of the L5 spacecraft could provide far superior data on the progression of a coronal mass ejection through space as compared to data from the L1 point. A two-spacecraft mission to both the L1 and L5 points would provide the benefits of both, with the additional benefit that both spacecraft could be perfectly matched as to obtain maximum combined useful output, one spacecraft providing data that the other lacks or adding a measurement point in space which could aid the accuracy of the warning and result in better data for model validation.

Due to the assumption during this project that the mission is operated in a perfect world where there is an overarching governmental organisation which performs this mission, similar project from organisations such as ESA and NASA/NOAA are not considered to be competitors. In reality, ESA is planning to perform a similar mission. [6]

2.4. CURRENT MARKET

Raw space weather prediction data from government-funded projects is generally publicly available through space weather prediction centres (data providers). However, users of space weather predictions require processing of this raw data and application of the information to their specific needs. These users generally require the following information to be extracted from the raw data: where and when a disruptive event will occur, how long it will last, what the likelihood of occurrence is, and what the resulting damage would be.

In a survey conducted in 2001 as part of a consortium of European companies (led by Alcatel space), organisations and agencies from various market sectors influenced by space weather were questioned about their willingness to pay for data processing services. From this, it was concluded that the companies prefer to employ specialist services as opposed to a general service.[7] This behaviour is also what is observed in the market, where users who are aware of the benefits of space weather predictions employ specialists to make sense of the data. A representation of this market structure is shown in Figure 2.2.[8]

From this diagram, it can also be noted that the scientific community can impose data requirements in the form of more accurate data allowing for proper scientific analysis. However, this will impose more stringent constraints on certain spacecraft instruments. Although this might make the mission sub-optimal for space weather alert purposes, not adding these features could make some stakeholders (e.g. the board of directors of ESA and the scientists) consider the mission as a waste of money. It is therefore very important to find a good balance between the alert function and the scientific function in this project. Failing to do so could result in the project being cancelled due to budget allocation to another project that has more direct application. In order to more thoroughly analyse the nature of the market, a SWOT analysis was performed. The results of this analysis are shown in Table 2.1.

2.5. FUTURE MARKET

Since the current budget of €800 mln is relatively low, future investors and governments might be more inclined to invest in the project. After the end of life of the first satellites, new satellites of the same, or a very similar design could be deployed. This means that the costs of those spacecraft would be significantly lower than the first iteration. The only

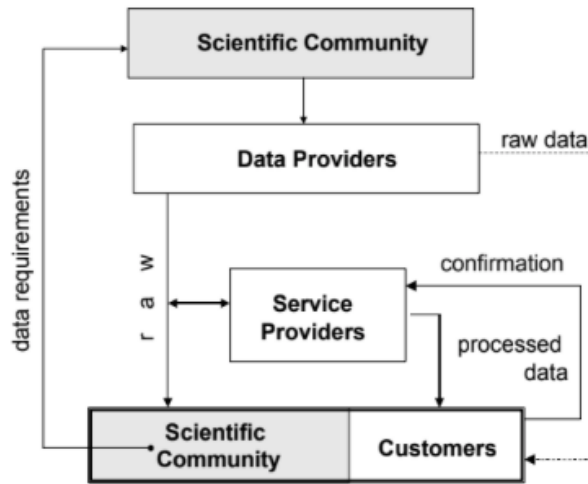


Figure 2.2: Current space weather market structure[8]

Table 2.1: SWOT of space weather prediction market

Strengths	<ul style="list-style-type: none"> Increasing importance of space weather as dependent market sectors grow. Market not yet saturated Lack of significant competition
Weaknesses	<ul style="list-style-type: none"> Limited awareness of problem [8] Limited user awareness of space weather prediction benefits [8] Consumers (planet population) do not pay for the service even though they use it. Dependency on government funding policies to space projects
Opportunities	<ul style="list-style-type: none"> Need for replacement of current ageing L1 missions Current monitoring systems at L1 are not optimised for space weather purposes Improved warning data from space weather monitoring system at L5 Can use the mission to commercialise improved space weather prediction models Numerous opportunities for providing value-added services to the raw prediction data [5]
Threats	<ul style="list-style-type: none"> Competition from currently ongoing missions (SOHO, STEREO) Project cancelling (such as with DSCOVR) Possible funding cut Limited attention, prioritising projects with a short-term importance.

constant costs would be the equipment and launch costs. However, additional development costs would be minimal. Of course, operational costs would continue with the same rate as for the first family of spacecraft.

As mentioned before, performing value-adding practices on the raw data of the satellites is very important. However, as shown in a study performed by ESA, not many companies are currently present that actually perform these actions.[5] It is estimated that these services are worth approximately €4-5 mln annually. This value will only increase as the world becomes increasingly dependent on electrical systems.

Moreover, in the same study, it is shown that the awareness in certain sectors about the benefits of this data to their sector is very limited. This mainly involves the geological, insurance, military and tourism sectors. Once these sectors are made aware of these benefits, a lot of possible capital can be made available for companies providing these benefits. Governmental Agencies could provide education about the problem of space weather, while commercial companies can provide value-added data.

3

TRADE-OFF REVISION

This chapter will describe a revision of the trade-offs done in the midterm phase of the DSE as described in the midterm report.[3] This was mainly done because hybrid options were not considered and some realisations after the performance of this trade-off changed its outcome. The options that are considered again are solar electric propulsion, the MMH-nitrogen tetroxide propellant combination as well as the combination of chemical propulsion and a solar sail. The propulsion system that comes out best in this trade-off is the one that will be chosen for the final design.

3.1. SOLAR ELECTRIC PROPULSION

The use of solar electric propulsion was reconsidered as a main propulsion system option. Currently, the only solar observing spacecraft situated in a Lagrange point that is still within its mission span is the DSCOVR spacecraft [9]. Other space weather observing spacecraft are already operative for a longer period than the planned mission, what results in the risk of the spacecraft becoming inoperative in the near future. For this reason, the requirement was set that the space weather alert system shall be operative before 2025, which is at twice the lifetime of the DSCOVR mission. In the midterm report [3], an analysis was performed on the post DSE operations, what resulted in a launch date in July or August 2023. Furthermore, it was determined that the use of solar electric propulsion to L1 and L5 have a time of flight of 1.15 years and 3.00 years respectively.[3] Due to the fact that both spacecraft consist of different payload as explained in Chapter 6, it is necessary to have both spacecraft operational before 2025 in order to meet the earlier stated requirement. For this reason, the use of solar electric propulsion would be unacceptable for a mission to L5. According to the midterm report [3], two identical spacecraft in terms of subsystems such as EPS, ADCS and propulsion system are in favour compared to two non-identical spacecraft. Therefore, it was decided to eliminate solar electric propulsion from both the L1 and L5 propulsion trade-off matrices.

3.2. SOLAR SAIL - CHEMICAL PROPULSION HYBRID SOLUTION

Another possibility that was not considered in the initial trade-off as described in the midterm report[3], is using a combination of a solar sail and chemical propulsion. In this option, the main chemical propulsion system would be used to travel to L1 or an equilibrium point a bit closer to the sun. After arriving, the solar sail would be deployed. This would allow the spacecraft to stay in the artificial equilibrium point, resulting in a greater warning time. Moreover, the solar sail could be used for station keeping. For L5 this option is not considered, as there is no benefit to a small solar sail as moving closer to the sun is not an advantage, while using a solar sail as a main propulsion system was discarded immediately due to the cost as explained in the midterm report.[3]

To calculate the effect of the solar sail on the warning time properly, a more thorough look needs to be taken to the definition of the L1 point. In the L1 point, the gravitational force of the Earth, Sun and the centrifugal force are all in balance. This can be denoted mathematically as

$$\frac{GM_s m_{sc}}{(r-R)^2} - \frac{GM_e m_{sc}}{R^2} - \frac{m_{sc} v_{sc}}{(r-R)^2} = 0 \quad (3.1)$$

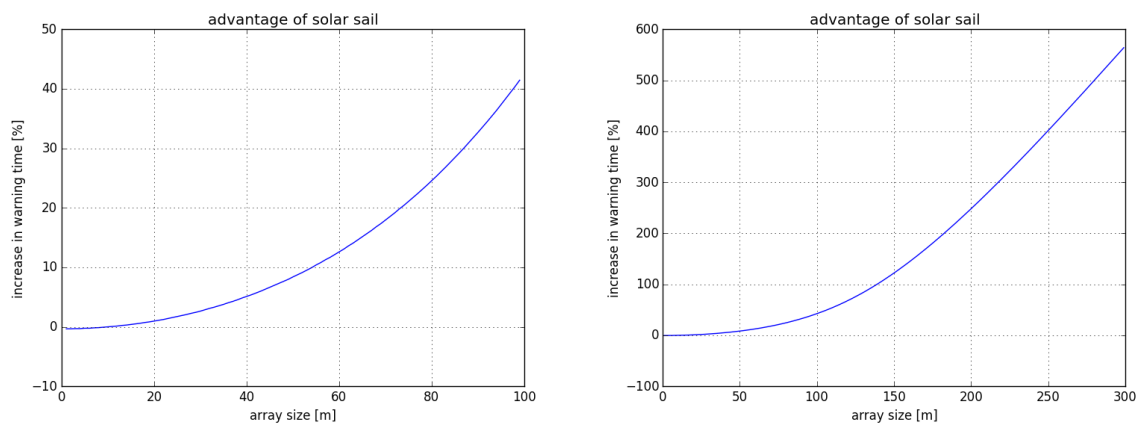
where G is the gravitation constant, equal to $6.674 \cdot 10^{-11} \text{ m}^3 \text{ kg}^{-1} \text{ s}^{-2}$. M_s and M_e are the respective masses of the Sun and the Earth, r is equal to 1 AU and R is the distance between the spacecraft and the Earth in m. v_{sc} is the orbital velocity of the spacecraft in ms^{-1} . Adding the force generated by the solar sail $F_{ss} = P_s A_{ss}$, the equation becomes

$$\frac{GM_s m_{sc}}{(r-R)^2} - \frac{GM_e m_{sc}}{R^2} - \frac{m_{sc} v_{sc}}{(r-R)^2} - P_s A_{ss} = 0 \quad (3.2)$$

where P_s is the solar radiation pressure at the position of the satellite, which can be calculated from the Einstein relation for photon momentum, $p = \frac{E}{c}$. The solar pressure is inversely proportional to the distance between the spacecraft and the Sun. A_{ss} is the area of the solar sail. After rearranging, the following equation is satisfied at the artificial equilibrium point.

$$\frac{r^3}{(r-R)^3} - \frac{M_e}{M_s} \frac{r^3}{R^2(r-R)} - \frac{P_s A_{ss} r^3}{GM_s m_{sc} (r-R)} - 1 = 0 \quad (3.3)$$

From this equation, it can be deduced that for a higher solar sail area will move the artificial equilibrium point towards the sun. Figure 3.1a shows the percentage increase of the distance from the Earth of this point compared to L1 (and thus a similar increase in warning time). Note that the x-axis shows the sail side length of a solar sail. It can be seen that, with a spacecraft total mass at L1 of 427 kg, for the largest actually tested solar sail of 38 x 38 m[10], an increase in warning time of 5% can be obtained. An 85 x 85 m solar sail, which is the biggest proposed conceptual mission[11], results in an increased warning time of about 28%. For the fastest CMEs travelling at 3000 kms⁻¹, this only results in an increase of 1-2 minutes in warning time. This is way too little to have a significant effect on reducing the damages as preliminary warnings will have been sent to Earth already by means of detection from the optical instruments, and everyone will be on full alert. This model is verified by comparing figures as presented by Heiligers[10] for artificial equilibrium points for the 45 kg Sunjammer mission to the output of the program, which only results in a difference of 5%. This difference mainly occurs due to the fact that an ideal solar sail is assumed in this case, while in reality impurities will, of course, decrease the efficiency of the solar sail. Figure 3.1b shows the advantages of a larger solar sail. It can be seen that for a solar sail larger than 150x150 m the use becomes increasingly more advantageous. This size is far beyond what is currently proposed.



(a) Warning time increase for a specific solar sail area. It is assumed that the spacecraft has a total mass of 400 kg, which is an initial estimate of the spacecraft mass based on statistical data.

(b) Warning time increase for a solar sail area up to 300 x 300. This shows that it becomes beneficial to use a solar sail from approximately 150 x 150 m.

Figure 3.1: Advantages of a solar sail.

The easy conclusion that can be drawn is that the spacecraft is just too heavy for it to be effective to use a solar sail and thus it will not be included in the trade-off. Using a solar sail as the main propulsion system is still considered as it is more sustainable.

Hydrazine as a monopropellant was not considered as a feasible option as the specific impulse of this option is much lower (around 220[12]). This would result in an even higher propellant mass and since, as will be explained later, the launcher is already quite approaching its capacity limits, this option would cost too much mass.

3.3. FINAL TRADE-OFF

In the previous section, an explanation was given about why these certain configurations were not included in the trade-off. However, amongst the configurations that were included in the trade-off initially, some changes to the values assigned to the criteria have been changed as well. In the midterm report[3], this initial trade-off is presented. In this trade-off, it turned out that the use of hydrogen peroxide and RP-1 as propellants was the optimal choice for the spacecraft. However, after re-evaluation, this trade-off will have to be redone. It was concluded that the number for the technical feasibility of this propellant combination was overestimated. This is the case because there is currently no commercial propulsion system available that uses these propellants. This means that a new propulsion system would have to be designed and tested specifically for this mission, of which it is doubtful if it would be completed before 2023 within budget. In the project team's own variation of Akin's 39th law of spacecraft design¹, the following is true:

"The three keys to keeping a new spacecraft affordable and on schedule:

1. *No new propulsion systems.*
2. *No new propulsion systems.*
3. *Whatever you do, don't develop any new propulsion systems."*

¹https://spacecraft.ssl.umd.edu/akins_laws.html

Since the technology readiness level of this system is 8, but the development of a propulsion system would cost a lot of money and a lot of time, the score for technical feasibility of the hydrogen peroxide - the RP-1 engine is lowered to 7. Other changes to the trade-off matrix include:

- Changes in the weight, for which an explanation is given below.
- The score of the closer-to-the-sun factor of the chemical propellant options was increased to 7.66, as a feasibly solar sail will only increase the warning time by 28%.

For the L1 trade-off, warning time and technical feasibility received the largest weights amongst the criteria. The warning time is highly important considering it marks the quality of the mission as a warning system. Technical feasibility was put on the same level of importance as the group defined it to be: the ability to complete the mission (both in design and development) with the resources, time and experience available, given the project complexity. As there is a high need for replacement of the current space weather warning systems, the importance of feasibility to complete the mission should be stressed.

For this specific mission, sustainability was allocated a higher weight than mass and cost, as the team is willing to allow a slightly higher cost and mass if it means being more sustainable. Furthermore, cost as a criterion was deemed more important than the mass. This was done because while the cost requirement is quite difficult to comply with for the mission, the launcher has a much higher mass capability than is needed for the mission (making the mass requirement more easy to comply with). Reliability was given a larger weight than the mass considering it would be a big problem if the mission fails, as this would mean a few more years would pass before the current systems can be replaced. However, considering the planned risk mitigation measures are expected to allow for a good reliability to be achieved, reliability was given a lower weight than the cost.

The transfer time was given a rather low weight considering the ranges of values for the different options are all well within the requirement for this criteria. Lastly, volume was given the lowest weight, as the launcher capability is significantly larger than what is needed (even more so than the mass capability). For the L5 trade-off, transfer time, warning time and reliability are not included as criteria. This is because each of the options was allocated the same score for these criteria. The remaining criteria (mass, cost, volume, technical feasibility and sustainability) were scaled accordingly such that the proportion between the weights remained the same as was the case for the L1 trade-off. The result from the trade-off for the missions to L1 and L5 can be observed in Table 3.1 and Table 3.2 respectively. It can be concluded that NTO with MMH would be the optimal option for both spacecraft.

Table 3.1: Propulsion Trade-off for L1. **Red** = Poor, **Orange** = Marginal, **Yellow** = Sufficient, **Green** = Good, **Blue** = Excellent.

Parameter	Mass	Cost	Volume	Technological Feasibility	Transfer Time	Warning Time	Sustainability	Reliability	Final Score
Weight	10	14	4	19	6	19	16	12	
95% Hydrogen Peroxide + RP-1	8.20 <small>Green</small>	9.10 <small>Green</small>	4.38 <small>Orange</small>	8.0 <small>Yellow</small>	10.0 <small>Blue</small>	7.66 <small>Yellow</small>	7.17 <small>Yellow</small>	10.0 <small>Blue</small>	8.19
Solar Sailing	6.63 <small>Green</small>	1.42 <small>Red</small>	10.0 <small>Blue</small>	7.00 <small>Yellow</small>	8.75 <small>Green</small>	10.0 <small>Blue</small>	10.0 <small>Blue</small>	10.0 <small>Blue</small>	7.82
NTO + MMH	10.0 <small>Blue</small>	10.0 <small>Blue</small>	4.86 <small>Orange</small>	10.0 <small>Blue</small>	10.0 <small>Blue</small>	7.66 <small>Yellow</small>	4.17 <small>Orange</small>	10.0 <small>Blue</small>	8.42

Table 3.2: Propulsion Trade-off for L5. **Red** = Poor, **Orange** = Marginal, **Yellow** = Sufficient, **Green** = Good, **Blue** = Excellent.

Name	Mass	Cost	Volume	Technical Feasibility	Sustainability	Final Score
Weight	16	22	6	25	25	
95% Hydrogen Peroxide + RP-1	7.71 <small>Yellow</small>	9.25 <small>Green</small>	8.5 <small>Green</small>	8.0 <small>Yellow</small>	10.0 <small>Blue</small>	8.77
NTO + MMH	10.0 <small>Blue</small>	10.0 <small>Blue</small>	10.0 <small>Blue</small>	10.0 <small>Blue</small>	5.62 <small>Yellow</small>	8.89

4

FUNCTIONAL DIAGRAMS

In this chapter the functional flow diagram and the functional breakdown structure will be provided. With the aid of these tools the operations of the entire mission can be described.

4.1. FUNCTIONAL FLOW DIAGRAM

The functional flow diagram shows the operation and logistics of the whole mission, from design to manufacturing to actual operation of the spacecraft. It is shown in Figure 4.1-4.8. The operational life of the mission can easily be divided into four main mission phases. These are:

- 1. Pre-launch activities:** This phase consists of the design and construction of the satellite, as well as the qualification. After the satellite is built, it of course also needs to be transported to the launch site. This puts constraints on the design of the spacecraft. However, since the spacecraft is relatively small, transportation will not pose a big problem. Testing is an important part of this phase as well. This is normally the phase where the most delays occur.
- 2. Getting into mission position:** This phase includes the launch, as well as the transfer to the Lagrange points. Both spacecraft will be launched on board the same Falcon 9 Block 5 into a GTO orbit. After an inclination change and perigee raise, OB2 will separate from the second stage of the launcher, and perform its escape trajectory burn at perigee. OB1 will stay connected to the launcher and will be boosted to GEO. The launcher will then insert it into the L1 manifold after which it will separate. Both OB1 and OB2 will perform injection burns, after which they can start their mission. This will be explained in more detail in Chapter 8.
- 3. Mission:** After insertion into the specific orbits, both spacecraft will perform their in-situ mission. OB1 will mainly do in-situ measurements, while OB2 will mainly do remote sensing. This phase of the mission will last 5 years.
- 4. End-of-Life:** The final phase of the mission is the end-of-life phase. It will move the spacecraft into an orbit that cannot be harmful for any future missions.

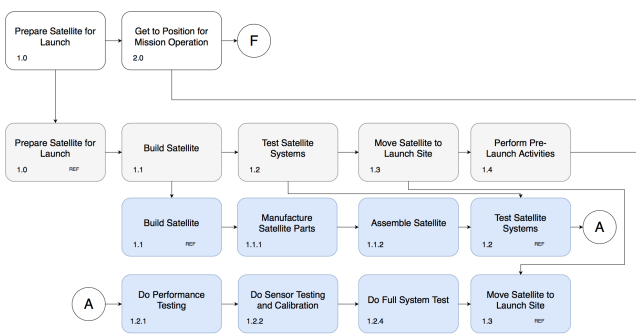


Figure 4.1: Functional Flow Diagram part 1

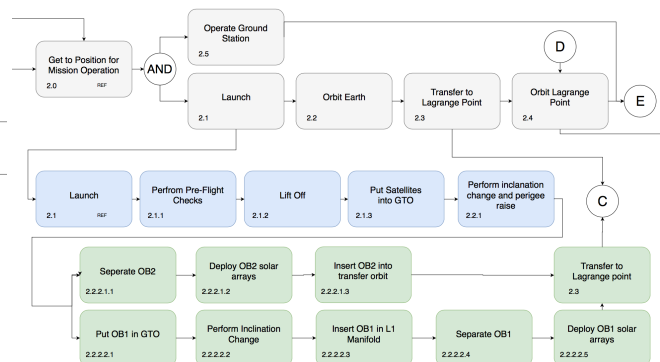


Figure 4.2: Functional Flow Diagram part 2

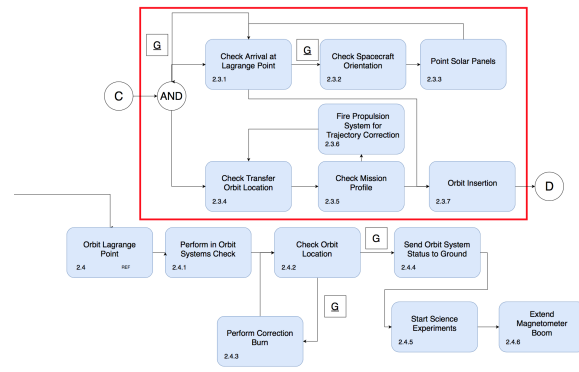


Figure 4.3: Functional Flow Diagram part 3

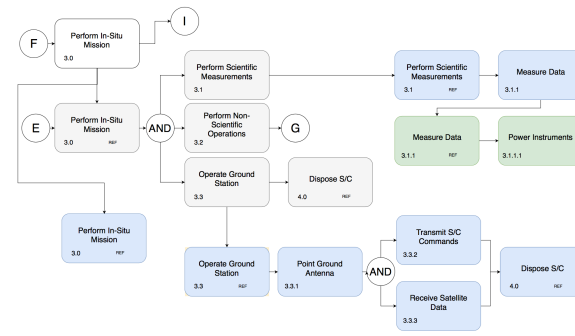


Figure 4.4: Functional Flow Diagram part 4

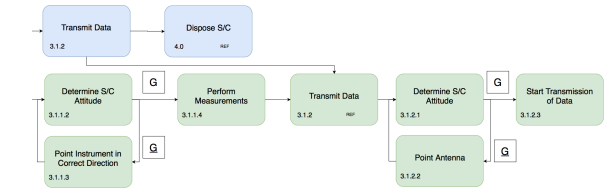


Figure 4.5: Functional Flow Diagram part 5

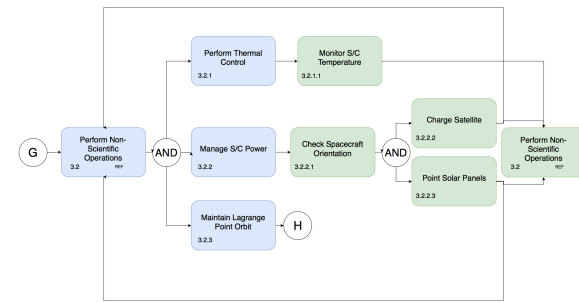


Figure 4.6: Functional Flow Diagram part 6

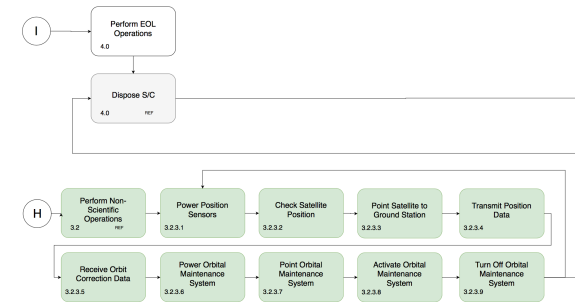


Figure 4.7: Functional Flow Diagram part 7



Figure 4.8: Functional Flow Diagram part 8

4.2. FUNCTIONAL BREAKDOWN STRUCTURE

The functional breakdown structure shows the same as the functional flow diagram, but then not as a sequential but as an "AND" tree. This is shown in Figure 4.9.

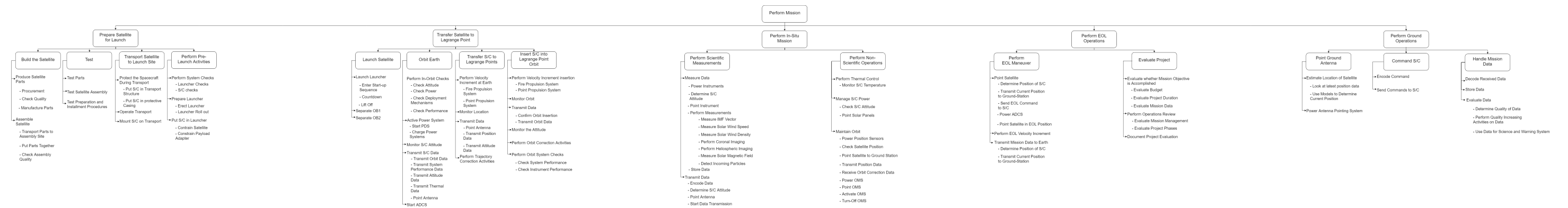


Figure 4.9: Functional Breakdown Structure

5

SUSTAINABLE DEVELOPMENT STRATEGY

For the SWAN project, it is important to incorporate environmental, economic and societal objectives into the project, which will be discussed in Section 5.1. The sustainable development strategy discussed in this chapter will not only touch on how the aforementioned objectives will be integrated into the final product, but also the phases of the design. This will be assessed in Section 5.3 and Section 5.4, respectively. Finally, Section 5.5 will state some additional requirements that follow from this sustainability analysis.

5.1. CRITERIA

To assess the sustainability of both the design process and the product itself a tool for analysing sustainable performance will be described. This tool will integrate the core aspects of sustainability, they are: social, economic and environmental. The various criteria are derived from Basiago [13] and Khan et al. [14]. The key criteria that make up these pillars are defined below.

5.1.1. SOCIAL

The first pillar of sustainability is societal values. The social aspects of sustainability that are relevant to the SWAN mission include the following:

1. Equity
2. Safety
3. Human health
4. Social-political acceptance
5. Impact on existing infrastructure

Criterion 1 aims to reduce the risk of social marginalisation. For the SWAN mission, this applies to the availability of the data obtained. Criterion 2 regards safety, this is crucial throughout all phases of the mission, from development to production to operation and to disposal. Criterion 3 exists to preserve human health by for instance improving working conditions. Criterion 4 is important as social-political factors can adversely affect the mission, this risk becomes more prevalent as the project's impact is of global proportion. Criterion 5 assesses the project's impact on pre-existing infrastructure.

5.1.2. ECONOMICAL

The second pillar of sustainability is made up of economic values, the relevant criteria include:

6. Reduce costs of similar endeavours in the future
7. Economic growth
8. Scientific development

The economic criteria are elaborated upon in the market analysis in Chapter 2. Criterion 6 is of interest as it aims to reduce the cost of a future mission to L1, L5 or for solar weather observations. Criterion 7 pertains to economic growth and describes how investing in this project will "trickle down". Criterion 8 regards the scientific objectives of the mission which are also described in the top level requirements; the mission design itself will also contribute to the scientific community.

5.1.3. ENVIRONMENTAL

The final pillar of sustainability regards the environmental impacts of the project; the main criteria to fulfil are:

9. Resource allocation
10. Effect on climate change
11. Impact on atmosphere
12. Eco-system preservation
13. Disposal

Criterion 9 is about the depletion of resources; one of the goals of sustainable development is to minimise the number of resources used. Criterion 10 aims to describe the project's effect on climate change, this is a topic is key in modern society and should be considered throughout all stages of development. Building on criterion 10, criterion 11 considers the effect on the atmosphere, something that is particularly relevant for launchers and the propellants used for them. Next, criterion 12 regards the preservation of eco-systems, this stipulates that the impact on biological communities should be minimised. In the context of the SWAN project, this should be considered when selecting locations for ground stations. Finally, criterion 13 regards the disposal, this is particularly relevant to satellites used in during the mission. For this criteria the ESA CleanSat¹ and EcoDesign² initiatives shall be adhered to.

5.2. WEIGHT ALLOCATION

For each of the criteria mentioned in Section 5.1 a weight must be allocated. The weights are on the scale: 3.3, 6.6 and 9.9. Determining the weight associated with a criteria is assessed on the basis of how driving the criterion is for the design and the risk associated with neglecting this criterion.

Beginning with equity, a weight of 3.3 is given to it in spite of its importance, as this criterion is not driving the design. Safety on the other hand imposes stringent requirements on the production phase of the mission and as such receives a weight of 9.9. Human health is of utmost importance, however, the phases of the project where human health is at risk are minimal, thus it is given a weight of 6.6. The final social criterion is social-political acceptance, it is important to take it into account, however, in most instances it is not driving the design. The criterion for the impact on existing infrastructure is provided with a weight of 6.6 as it is a key criteria for sustainability in general. Having to reduce the impact on existing infrastructure can drive the design to some extent.

The economical criterion aimed at reducing the costs of future endeavours is allocated a weight of 9.9. The reason for this is that this criterion, in part, also extends the longevity of the mission as subsequent mission can be design based on preexisting knowledge and experience. Next, economic growth has a weight of 3.3 as it is not the core aim of mission, however, at the very least the mission must be economically viable. The criteria targeted at scientific development is provided with weight of 9.9 for similar reasons as reducing the cost of future endeavours.

For the environmental criteria many of the criteria are allocated a weight of 9.9, they include: resource allocation, effect on climate change, impact on atmosphere and disposal. Reason for these these high weights is because the environmental impact must be limited and EOL procedures are clearly prescribed by ESA's CleanSat¹ and EcoDesign² guidelines. The impact on the eco-system is given a lower weight as due to the nature of the mission the risk of this criterion not being met is lower than for the aforementioned criteria.

5.3. ASSESSMENT

In the previous sections, several criteria of sustainability have been briefly addressed including the weights associated with those criteria. These aspects will be incorporated into one tool to assess the sustainability of different aspects of the design. For the trade-off in Chapter 3 a separate criterion called sustainability will be used to analyse the design options on sustainability. This criterion then covers all the aspects given in Section 5.1. To get to a good basis for sustainability every aspect is weighted, using the weights of Section 5.2 for the trade-off and the score of each aspect will be shown. From this trade-off table in Table 5.1 the final sustainability score can be provided.

¹http://www.esa.int/Our_Activities/Space_Engineering_Technology/Clean_Space/CleanSat_new_satellite_technologies_for_cleaner_low_orbits

²https://www.esa.int/Our_Activities/Space_Engineering_Technology/Clean_Space/ecoDesign

Table 5.1: Sustainability trade-off criteria, total weights sum up to 100 %

Aspect	Weight [%]	Poor (0.2)	Marginal (0.4)	Sufficient (0.6)	Good (0.8)	Excellent (1.0)
Equity	3.3	Data available only for highest bidder	Data available only when paid for	Data available for every cooperating company/government	Data available for every company/government	Data available for everyone
Safety	9.9	No safety standards are adhered to	-	All safety standards are met	-	All standards are met and additional safety measures and contingencies are taken
Human health	6.6	Human health is not considered within the working environment and broader communities	Either work environment or external communities are negatively affected	Health conditions for employees and communities are sufficient	Active measures are taken to mitigate potential health hazards	Efforts are made to improve human health
Social-political acceptance	3.3	Locally accepted	-	Nationally accepted	-	Globally accepted
Impact on existing infrastructure	6.6	Negative effect on existing infrastructure	Negatively effect on existing infrastructure are compensated for	Limited effects on existing infrastructure	No effects on existing infrastructure	Effects on existing infrastructure are beneficial
Reduce costs of similar endeavours in the future	9.9	No resources available after design mission and experience within the project is not preserved	No re-usability of design resources	Within own institution the resources can be re-used	Reduce development costs for future missions and infrastructure can be reused within own company	Reduce development costs for future missions by making the design process free to the public and infrastructure can be reused
Economic growth	3.3	The project is not economically viable	The project is not economically profitable	The return of investment is zero	The project is profitable	The economic growth trickles down to society at large
Scientific development	9.9	The methodology of the mission, product and end result are conventional and based on pre-existing knowledge	-	The product combines both pre-existing technologies and new innovations	-	The design methodology and product are innovative
Resource allocation	9.9	High dependency on hazardous materials and resources	Utilisation of hazardous materials	Minimal resource depletion and minimal hazardous materials used	Minimal resource depletion and minimal hazardous materials, waste is recycled	Minimal resource depletion and minimal utilisation of hazardous materials, recycled materials are used and waste is recycled
Effect on climate change	9.9	Unchecked greenhouse gas emission	Check greenhouse gas emission	Minimum greenhouse gasses are emitted	CO ₂ neutral	No greenhouse gasses are emitted

Impact on atmosphere	9.9	Hazardous materials are used	-	Ozone depletion is mitigated	-	Materials that are hazardous for the atmosphere are not used within the Earth's atmosphere
Eco-system preservation	6.6	Operations are damaging to the eco-system	-	Minimal disruptions to eco-systems	-	No disruptions to eco-systems
Disposal	9.9	Lot of debris during disposal	Marginal debris left behind at disposal	Limited debris left behind at disposal	No debris left behind at disposal	No debris left behind at disposal and satellite is recycled

5.4. ANALYSIS OF PHASES

In this section, the sustainable development strategy is applied to the phases of the project and mission. For each of these phases, the most relevant criteria from Table 5.1 will be touched on and in doing so provide a means of assessing the sustainability of these phases. This will also help spawn requirements pertaining to sustainability.

CONCEPT EXPLORATION

During the concept exploration, already a lot of information should be analysed about the sustainability of the concept. All the three pillars; social, economic and environment, should partly be analysed in the concept exploration. The social-political acceptance should be analysed since the designer wants to know if the concept will be accepted by the public. Next to that, the main economic driver for the concept exploration is the economic growth since it is important to know at an early stage if the concept is economically viable or not. Lastly, the resource allocation is important to analyse already at the concept exploration, since it determines what the resources are for the mission and if these have a possible negative impact on the environment.

PRELIMINARY DESIGN

The preliminary design phase is a continuation of the conceptual design phase. During this part of the design, many of the elements that make up the sustainability of the design will be further elaborated upon. The sustainability strategy is of significant importance in this phase since it will impose requirements on the project. For the societal elements, it is important to assess some of the geopolitical complexities that may impact the design. The economic elements are important as requirements SYS-GEN-04 declares that the cost of the mission shall not exceed 800 MEuro. The market analysis is also key in this phase to understand what the economic landscape is for the project. The scientific objectives are also addressed in this phase. In addition to the resource allocation and effects on climate, it is also key to start making efforts for disposal. During this phase, some options for the end of life shall be explored.

DETAILED DESIGN

In the detailed design phase, more emphasis will be made to quantify the impact of the latter stages of the project in terms of sustainability. Furthermore, the design must meet the requirements for sustainability that were devised in the preliminary design phase. It should also be noted that during this phase efforts should be made to organise the work completed in such a way that it is readily reproducible with the goal of making future missions more easy to develop.

PRODUCTION

During the production phase, many of the environmental criteria become relevant. Resource allocation becomes important as a core ideal of sustainable development entails that minimal resources shall be depleted. This can mean that where possible recycled materials are used and waste is recycled. Hazardous materials should not be used and much (if not all) of the production process should occur on-site (or close to) to avoid unnecessary transportation of parts and materials. Limiting transportation can also help reduce costs whilst also reducing one's dependency on infrastructure, thus yielding benefits in both the societal and economic domains.

LAUNCH

An important phase of the mission, albeit brief, is the launch. An important consideration to make during this phase is the type of propellant used as this could adversely affect the atmosphere. Not only is it possible for hazardous materials to be expended, these materials will be expelled at high altitudes increasing their damage potential. Furthermore, at this stage of the mission, one should consider the re-usability of infrastructure for subsequent missions; this pertains to the launcher itself and other systems required for launch.

TRANSFER

For the transfer phase of the mission, it is important to utilise low-energy transfers that will require less propellant to be carried on the spacecraft. This is phase is also an opportunity to prove the feasibility of new innovative technologies; for instance solar sails, thus allowing the project to contribute to scientific development.

MISSION UTILISATION

The phase of mission utilisation is the longest phase of the mission. An obvious consideration for this phase is the type of EPS system used on the spacecraft; solar cells are a good alternative to expendable fuels. It is also important to ensure that the utilisation of ground station does not encroach upon ecological communities. Furthermore, the infrastructure needed for the operation of the mission should be designed with future utilisation in mind. The data obtained from the mission and used for the space weather warning system should aim to be distributed such that it does not marginalise any groups.

END OF LIFE

The end of life disposal is an important part of the mission as it aims to preserve orbits for future use. The CleanSat¹ and EcoDesign² initiatives from ESA are used as guidelines for this phase; it is crucial to remove the spacecraft from the L1 and L5 orbits once they have expired. Alternatively, one can consider the option of returning the spacecraft to Earth for possible re-use of materials.

5.5. REQUIREMENTS

From Section 5.1, Section 5.3 and Section 5.4 requirements for the mission can be made. These requirements are shown in Table 5.2. Note, that requirements SYS-GEN-04 and SYS-EOL-01 are derived from the top level system requirements. Regardless, these requirements are relevant for the sustainable development strategy.

Table 5.2: Sustainability Requirements

Code	Description	Verification Method
SYS-SUS-01	Space weather data shall be available to public	Inspection
SYS-SUS-02	Safety guidelines shall be adhered to at all times	Inspection
SYS-SUS-03	Risks to human health shall be omitted during all phases of the mission	Inspection
SYS-GEN-04	The total cost of the project shall not exceed 800 MEuro	Inspection
SYS-SUS-04	Usage of environmentally hazardous materials shall be minimised	Inspection
SYS-SUS-05	The emission of green house gases during all phases of the mission shall be minimised	Analysis
SYS-EOL-01	The spacecraft shall be capable of performing an end of life manoeuvre	Analysis

6

PAYLOAD

The payload of the SWAN mission is customised to fulfil the goal of monitoring space weather and providing early and accurate warnings of dangerous geomagnetic storms. For this, a complement of eight instruments (four in addition to the instruments described in the midterm report [3]) will feature as part of the SWAN mission. These instruments are needed to predict, detect, analyse and track the propagation of solar weather phenomena such as CMEs. The aim of this chapter is to present a combination of instruments that are capable of providing the aforementioned services.

6.1. MONITORING OBJECTIVES

The SWAN mission is first-and-foremost a space weather observation mission, the mission combines data from two Lagrangian points (L1 and L5) to provide accurate and early warning of the most threatening solar weather phenomena. For this mission to succeed one must identify the most hazardous threats from solar weather and establish thresholds upon which to base a warning system.

6.1.1. SPACE WEATHER

The SWAN mission shall integrate a set of instruments that enable one to observe and predict the solar weather. Observations of key parameters of the solar wind and bulk plasma will be made. These include velocity, density and temperature. The supersonic plasma that composes much of the solar wind is ever-present in interplanetary space; some statistics of the key parameters and elements that make up the plasma bulk are provided by Moldwin [15] and can be seen in Table 6.1.

Table 6.1: Average properties of the solar wind and IMF at 1 AU [15]

Property	Value	Unit
Particle density	5	cm^{-3}
Temperature	1.0	MK
Velocity	400	kms^{-1}
Composition	90% H^+ , 8% He^{2+} and trace amounts of heavier particles	[-]
IMF strength	10	nT

The solar wind is intrinsically anisotropic in terms of heat flow and chemical composition. This arises from the fact that the mechanisms that govern the origin and acceleration of the solar wind are complex. Fluctuations in particle density and composition can (in part) be attributed to coronal mass ejections (CMEs). CMEs are events that cause large masses of energetic matter to be ejected into space. The magnetic field, velocity, density and temperature of the bulk plasma that defines the CME are key characteristics that describe its interaction with the Earth. The ejecta of the CME is often referred to as solar energetic particles (SEP). These consist primarily electron, protons, alpha particles and heavier elements ($Z > 4$). The energy ranges of the particles are dependent on the mass and velocity of the particle and range from a few keV to hundreds of MeV. During periods of solar minimum, galactic cosmic rays (GCRs) are more prevalent. These particles can achieve upwards of 90% of the speed of light although they are significantly lighter than most SEPs. The movement of the particles that make up the bulk plasma is sporadic due to the presence of Alfvén waves in frozen magnetic fields¹. The waves are the result of forces acting on the magnetic field lines due to its interaction with energetic particles. As a result, these particles oscillate with these Alfvén waves [16]. Moreover, the interplanetary magnetic field (IMF) interacts with the magnetic field of the Earth which in turn affects the plasma environment in the upper atmosphere at auroral latitudes.

These are but a few of the many solar weather phenomena that are present in the interplanetary medium. Yet they are amongst the most threatening to the Earth. For this reason, the instruments integrated into the SWAN mission will aim to monitor the aforementioned phenomena and estimate the effects of solar weather on Earth in real-time. In regard to CMEs, the fastest CMEs recorded by WIND were 1,940km/s [17]. As such the fastest moving CMEs after forming can reach the Earth within 21 hours. Furthermore, from L1 a minimum warning time of 12 minutes can be achieved in the case of fast moving CMEs. In order to give accurate warnings about the solar weather one must define thresholds for the various phenomena, these thresholds will also determine the precision of the instrumentation.

¹<https://svs.gsfc.nasa.gov/4560>

6.1.2. THRESHOLDS

Although all instruments monitor the sun and environment for space weather, the in-situ measurements at L1 provide the final concrete warning if an action has to be taken on Earth, however, certain thresholds have to be identified to base this decision on and this depends on the type and energy of the particles detected. This is based on the NOAA scales for space weather².

Intense solar radiation storms are often accompanied by high energy particle flux that can pose a serious danger to astronauts and passengers on high flying aircraft. Satellites may experience loss of data, single event upsets, loss of control of star trackers and spacecraft, increase in noise levels and permanent damage to solar panels, which can be minimised if a warning is available². This occurs when >10 MeV proton and ion flux levels exceed 10^4 particle flux units (pfu) and when >2 MeV electron flux levels exceed 10^3 pfu, which is categorised as an S4 level storm, occurring less than 3 times per solar cycle. Note that pfu = particles·cm⁻²s⁻¹sr⁻¹.

CMEs also cause severe geomagnetic storms on Earth, which are the cause of power grid malfunctions and blackouts, transformer damage, pipeline currents in excess of hundreds of amps and disruption in high-frequency communication for several days.² This is due to the Sun's magnetic field carried by the CME, which interacts with the Earth's magnetosphere, which in turn causes the Earth's magnetic field to be compressed and re-connect allowing plasma to enter. Severe CMEs with magnetic field strengths from 60 nT to a few hundred nT have adverse effects, especially if the interplanetary magnetic field polarisation is southward. Thus the threshold for detecting a CME will be set at 60 nT (averaged over 3 hours) for the weakest CMEs, which is identified as a major magnetic storm according to the AA scale³[18, 19].

Effects of CMEs also include radio blackouts and on-ground communication failures up to a few hours, characterised by an increase in X-ray flux from the CME. Severe radio blackouts occur at the X10 level² when X-ray flux exceeds 10^{-3} Wm⁻¹, or in extreme cases when it exceeds $2 \cdot 10^{-3}$ Wm⁻¹ (X20 level), happening less than once every solar cycle.

All warnings for severe solar weather will be signalled when the L1 satellite measures characteristics that exceed thresholds above and summarised in Table 6.2. Note that these are the warnings issued for "severe" or "extreme" geomagnetic storms, a full scale of thresholds can be found on the NOAA website².

Table 6.2: Thresholds for severe geomagnetic storms as described by NOAA²

Parameter	Threshold
Electron flux >2.0 MeV	10^3 pfu
Proton flux and ion flux >10 MeV	10^4 pfu
IMF strength	60 nT
X-ray flux	10^{-3} Wm ⁻¹

6.2. INSTRUMENT DESCRIPTION

In addition to monitoring space weather for events that may exceed the thresholds described in Section 6.1.2, the instruments must observe solar activity with the aim of predicting the formation CMEs and improving models that forecast space weather. Much of the data provided by the instruments on the SWAN mission will provide data that will aid in validating models and better the quality of the prediction giving increased warning time. In order to provide the required validation data, the precision of the instruments must exceed that required by the thresholds.

This section provides an overview of all the instruments that are integrated into the SWAN mission. Descriptions and justifications of each instrument are provided in addition to its specifications and function as part of the monitoring system.

6.2.1. GENERAL CONFIGURATION

The instruments necessary for the SWAN mission will be distributed between the two satellites, this distribution was employed as a means to reduce the cost of the mission. Distributing the instruments was done by assessing each instrument and determining at which location (L1 or L5) it would operate most optimally. At L1, the in-situ instruments have the highest priority, as they will measure the severity of the CME propagating towards Earth. These instruments will provide the concrete warning whether or not action has to be taken on Earth to protect infrastructure. Therefore, the magnetometer, X-ray sensor, Faraday cup and SEP monitor have the highest priority. Contrary to this, the L5 measurements prioritise remote sensing, as they will view the Sun from the advancing side, where activity in this region already affects and might affect Earth when this side rotates facing Earth, thereby gaining an increased warning time if activity predicts a catastrophic CME. The L5 point furthermore has an optimal vantage point for viewing the CME's propagation through interstellar space towards Earth, and so the coronagraph, magnetograph, heliospheric imager and the EUV imager have

²https://www.swpc.noaa.gov/sites/default/files/images/NOAA_scales.pdf

³<https://www.ngdc.noaa.gov/stp/geomag/aastar.html>

the highest priority here. For accurate utilisation of the coronagraph two are required as together they provide 3D images of CMEs, as such a coronagraph is also equipped to the L1 satellite. Furthermore, in an effort to improve the availability of validation data and because the budget allowed for it, both an x-ray sensor and magnetometer are equipped on the L5 satellite. The final distribution of instruments can be seen in Table 6.3. Furthermore, how the instruments are integrated into the spacecraft and subsequently interface with the other subsystems can be seen in the hardware/software diagrams in Chapter 14.

Table 6.3: Instrument distribution amongst the L1 and L5 satellites

Instrument	L1	L5
Magnetograph		x
EUV imager		x
Coronagraph	x	x
Heliospheric imager		x
X-ray sensor	x	x
SEP monitor	x	
Faraday cup	x	
Magnetometer	x	x

6.2.2. MAGNETOGRAPH

Firstly, to predict the CME, the surface of the Sun has to be studied for instabilities in the Corona and complex magnetic topologies, which is the source of space weather [20]. A magnetograph is a remote sensing instrument that measures the shift in the polarisation of sunlight, which is directly coupled to the magnetic field strength on the corona, allowing for the visualisation of the disturbances and re-connections of the coronal magnetic field and thus providing an indication that a CME might occur. A vector magnetograph will be used that is able to determine the orientation and magnitude of the field. In addition to the requirements described in the midterm report [3], some detail will be provided on the assessments of the required spectral absorption line and polarisation modes for magnetic field measurements.

SPECTRAL LINE SENSITIVITY

The magnetograph is capable of measuring the magnetic fields of the Sun by observing the Zeeman splitting and linear polarisation of certain spectral lines. One must consider that the sensitivity of certain spectral lines to the presence of magnetic field vary, some lines are insensitive to magnetic fields and instead exhibit transition due to mass motions of large temperature gradients. As such for the purpose of magnetic field measurements, one would ideally utilise a spectral line that is highly sensitive to the presence of magnetic field and insensitive to velocity and temperature. However, all spectral lines are sensitive to velocity and temperature to a certain degree, thus one must carefully select a spectral line to operate with.

Since the SWAN magnetograph will be capable of measuring the magnetic field vector on the surface of the sun it must measure the Stokes- Q, U and V polarisation parameters. These parameters are necessary to describe the magnetic field vector: Q is the intensity difference between horizontal and vertical linearly polarised parameters, U is the intensity difference between linearly polarised components of $\pm 45^\circ$ and V is the intensity difference between right and left-handed circular polarisation parameters. Note that the Stokes I parameter is omitted as it is not required for the determination of the magnetic field strength [21].

To measure the polarisation due to the Zeeman splitting a spectral line must be chosen that is sensitive to this polarisation. Tests from Solana et al. [22] performed with Stokes V noted that the weak and strong magnetic field regimes yielded a response that was proportional to $g_{\text{eff}}\lambda^2$. Where g_{eff} which is a g-factor (Landé) that describes the magnetic moment of a single electron and is specific to a spectral line; λ^2 is the wavelength of the spectral line [23]. Also from Solana et al. [22] a table can be obtained that presents a set of visible and infrared lines that are used in magnetograph imaging, the data collected in this table was received from missions that operate spectrographs and polarimeters, such as SOHO and SDO. From this data, a preference can be made for infrared wavelengths, as they are larger, and the Fe I spectral line as it has a larger effective Landé factor.

In addition to being sensitive to magnetic fields, one must also consider a spectral line that is insensitive to other parameters. For this, we can once more refer to the results from Solana et al. [22]. In their report, they analysed the responses of spectral lines to velocity, temperature and magnetic field strength. They did so by examining so-called response functions that express the atmospheric perturbations to the Stokes profiles, as defined in Collados et al. [24]. The response function from Solana et al. [22] are:

$$R'_{v,\text{LOS}} = e^{-1/2} \frac{A_0^* \lambda_0}{A_1^* c} \quad (6.1)$$

Equation (6.1) is the response function for the Stokes I to the line of sight (LOS) velocity perturbation. One can see that there is a dependency on the wavelength, λ_0 , yet Solana et al. [22] reported that there is a greater dependence on the shape ratio $\frac{A_0^*}{A_1^*}$ (* denotes the Stokes I shape ratio). This shape ratio is defined as the spectral line depth over the line width. This area ratio is greatest for Fe I with a wavelength of 630.25 nm, thus this spectral line is most sensitive to velocity.

$$R'_{T,LOS} = \frac{\partial A_2}{\partial T} \propto \frac{\partial B_\lambda [T(\tau_\lambda = 1)]}{\partial T} \quad (6.2)$$

Similarly, Equation (6.2) shows the response function of the Stokes I parameter to perturbations in the temperature. Here A_2 is the continuum intensity; noteworthy is that Solana et al. [22] found that this response function is proportional to B_λ , which is the Planck function. The derivative of the Planck function with respect to the temperature decreases with λ_0 , thus Fe I 630.25 nm will be most sensitive.

$$R'_{B,LOS} = e^{-1/2} \frac{A_0^V}{A_1^V} g_{\text{eff}} \lambda^2 \quad (6.3)$$

Finally, Equation (6.3) is the response function of the Stokes V parameter to perturbation in the magnetic field strength. As expected the $g_{\text{eff}} \lambda^2$ is prominent in this equation due to its dependence on the Zeeman effect. Also, the shape ratio $\frac{A_0^V}{A_1^V}$ (V denotes the Stokes V shape ratio) is present in this function. Larger wavelengths are more sensitive to perturbations of the magnetic field, such is the case with the Fe I 1564.8 nm spectral line. It should be noted that Solana et al. [22] made a distinction between the weak and strong field regimes, for the strong regime larger wavelengths are preferred, yet for the weak regime, both long and short waves are applicable. Regardless, from the response functions provided by Solana et al. [22] one can conclude that the Fe I 1564.8 nm spectral line is most optimal as it is sensitive to magnetic field perturbations and relatively insensitive to velocity and temperature perturbations.

Since the magnetograph is equipped with an etalon it is capable of measuring different narrow band wavelengths, this enables the instrument to measure the magnetic field strength at different wavelengths that may be more sensitive to other parameters. This allows one to improve the precision of the instrument as data obtained at smaller (noisier) wavelengths can be used to remove noise from the larger wavelength data. It is recommended that research is conducted into the feasibility of this type of data handling for the magnetograph.

CROSSTALK

Since vector magnetographs must measure the polarisation of the Stokes-Q, U and V parameters there is the risk of crosstalk. As described by Spirock [22], crosstalk is defined as the contamination of the Stokes-Q and/or U images by Stokes V images. If crosstalk is present in the solar magnetograph then the Stokes-Q and U images will exhibit features of longitudinal magnetic fields that are present in the Stokes V images. The contamination is witnessed in the Stokes-Q and U images since the longitudinal magnetic fields are much stronger than the transverse magnetic fields. In Spirock [22] a method for determining which features are cross talk is suggested, it requires one to examine the correlation between the Stokes-V & Q and Stokes-V & U, which in the case of crosstalk will contain a degree of overlap. An example of crosstalk can be seen in Figure 6.1, in this image contours, indicate areas where the magnetic field strength exceeds 20 G in the Stokes-V parameter image, these contours are then plotted in the Stokes-Q image to highlight features present due to crosstalk. It should be noted that the amount of crosstalk in this image is exceptionally high, in the order of 42%; typical values are in the order of 5% [22].

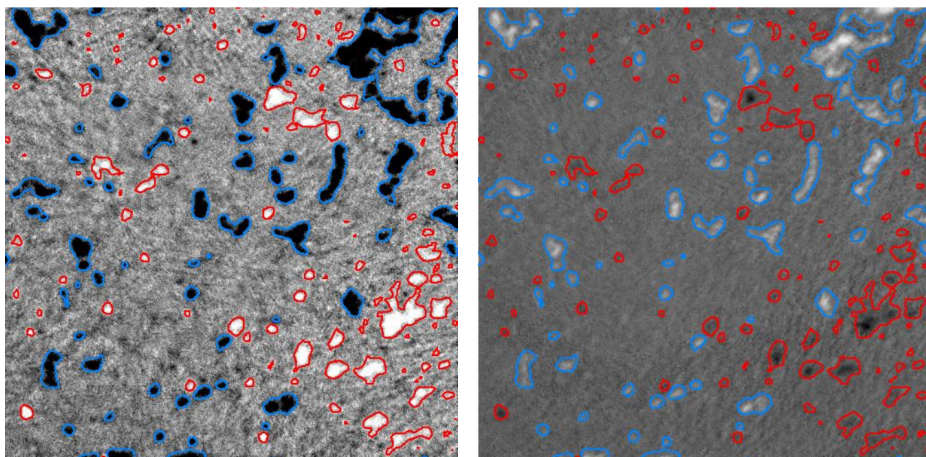


Figure 6.1: An example of cross talk: Stokes-V parameter (longitudinal magnetogram) left and Stokes-Q parameter (transverse magnetogram) right [22]

The SWAN magnetograph shall be corrected for crosstalk to minimise the effects of Stokes-V contamination in the Stokes-Q and U images. This is done by applying a linear best fit to the Stokes-V & Q and Stokes-V & U scatter plots, resulting in the average amount of crosstalk present which is then removed from the Stokes-Q and U image. However, due to the nature of the line best fit method, not all the effects of crosstalk is removed.

SPECIFICATIONS

In Table 6.4 the specifications of the SWAN magnetograph are provided. Most of these specifications are derived from the requirements for the magnetograph described in the midterm report [3]. Some amendments to those requirements include the dynamic range of the system which is $\pm 4,096$ nT. This range based on the range necessary to reliably measure sunspot regions. A study from Norton et al. [25] using data from SDO, concluded that active regions on the surface of the sun exhibit peak magnetic field strengths up to 4,000 G. These active regions are typically associated with sunspots which display temporal fluctuations in magnetic field strength. Norton et al. [25] reported that active region can fluctuate up to 94 G/yr, this imposes a pixel depth requirement that is large enough to measure these fluctuations. For the SWAN magnetograph bit depth is 12-bits this results in a resolution of 2 nT which is sufficient to measure the fluctuations in magnetic field strength.

Table 6.4: Magnetograph specifications

Parameter	Value	Unit
Resolution	1	arcseconds
FoV	31.1	arcminutes
Cadence	1	minutes
CCD screen resolution	2014x2048	-
Spectral line	Fe I	-
Wave length	156.5	Å
Bits/pixel	12	-
Dynamic range	$\pm 4,096$	nT
Dimensions	30x40x120	cm ³

6.2.3. EUV IMAGER

The magnetograph provides the earliest data on the possible formation of CME's by examining the magnetic field of the sun. The EUV imager, on the other hand, can image the corona, normally not possible in the visible spectrum as the photosphere's brightness obscures the corona. This allows for the visualisation of the intricate magnetic structures that are responsible for the violent eruptions when a CME occurs as the plasma trapped in the field lines radiate in the EUV spectrum. The EUV imager, in tandem with the magnetograph, will provide data on the formation of solar weather phenomena on the surface of the sun. Although the addition of the EUV imager to the SWAN mission might not improve the warning time of the monitoring system, the instrument will provide data that will improve the accuracy of warnings and validation models for space weather forecasting. The inclusion of the EUV imager on OB2 arises from the fact that the western hemisphere of the Sun is more relevant for remote sensing.

SPECIFICATIONS

The specification of the EUV imager are listed in Table 6.5. To properly view these structures, the instrument will image the sun at a wavelength of 17.1 nm (Fe-IX emission band) as this is near the soft X-ray region, where additional structures are visible and as this band is most common as well. with an angular resolution of at most 3 arcseconds [26]. Therefore, with a resolution of 1024 pixels, it will have a field of view of 50 arcminutes, which is sufficient to view the corona where these anomalies occur. With a cadence of 1 minute (sufficient for viewing CME eruptions[26]) and 7 bits/pixel, the data rate becomes 125 kbps. From reference missions [27], its cost is 15 mln Euros, has a volume of 26x12x12 cm³ and also operates near room temperature like the X-ray sensor, consuming 12W and weighing 10kg[26, 28, 29]. With the magnetograph, this instrument can provide a more detailed and qualitative analysis of these structures, allowing for better models and predictions to be made.

6.2.4. CORONAGRAPH

Furthermore, to detect the CME in its initial phase, the outer corona needs to be imaged, as this is the first region it will pass through. For this, a coronagraph will be used, which captures sunlight that has been Thomson-scattered off of free electrons in the K-corona plasma while blocking out the direct sunlight (much brighter, which would otherwise obscure the CME) with an occulter and eliminating the resultant diffraction patterns with a series of correction lenses [30], thus the CME's structure and size can be seen. It does this by superimposing 4 exposures of 4 seconds and then

Table 6.5: EUV Imager specifications

Parameter	Value	Unit
Resolution [26]	3	arcsecond
FoV	50	arcminute
Cadence [26]	1	minutes
Bits/pixel	7	-
Spectral band	17.1	nm
Dynamic range	128	-

subtracting the background noise. These images are then used to determine the size, velocity and impact time on Earth, and are often also used as initial conditions for models to predict its impact time and severity on Earth. The inclusion of the coronagraph on both OB1 and OB2 is the result of the coronagraph operating more efficiently at the Lagrangian points than coronagraphs that would operate from LEO [30]. The coronagraphs placed at the L1 and L5 points attain a 240° coverage of the Sun's corona, this enables one to capture a 3D images of phenomena in the Sun's corona, including CME's. This data is important for monitoring the space weather as the coronagraph provides the initial condition to the solar events that influence the solar weather on Earth.

SPECIFICATIONS

For optimal operation of the coronagraph the instrument must meet the requirements described in the midterm report [3]. These requirements translate to instrument specifications that are summarised in Table 6.6.

Table 6.6: Coronagraph specifications

Parameter	Value	Unit
Resolution	53	arcseconds
FoV	15.07	degrees
Cadence	12	minutes
CCD screen resolution	1024x1024	-
Bits/pixel	12	-
Spectral band	400-900	nm
Dimensions	70x30x30	cm ³

6.2.5. HELIOSPHERIC IMAGER

Once a CME is detected by the coronagraph and EUV imager and it has traversed the corona, SWAN will track its propagation through interplanetary space to Earth using a heliospheric imager. The heliospheric imager works on the same principle as a coronagraph, however, the scattered light is about 2 orders of magnitude smaller than the K-corona and other planets. So to capture the CME, careful stray light rejection using baffle system (to limit diffraction) and long exposures of up to 20 minutes are needed. To do this, 30 times 40-second exposures are summed to increase the signal to noise ratio, and post-processing of the data is further needed to subtract the averaged background light, finally revealing the CME. This instrument is used to better predict its impact and for model validation.

The heliospheric imager is integrated into the OB2 satellite because its position at L5 provides it with a unique vantage point that oversees space between the Sun and Earth. This view allows the heliospheric imager to track the CME as it propagates through space. In addition to tracking CME's the heliospheric imager is also capable of capturing the solar wind, this is ideal for predicting the effects of solar weather on Earth. Due to the long exposures necessary for the instrument data from the heliospheric imager will be updated every 20 minutes, thus models that monitor and predict the solar weather will also be updated with this frequency.

SPECIFICATIONS

The specifications for the heliospheric imager are presented in Table 6.7. The specifications for the heliospheric imager are derived from the requirements for the instrument that are explained in the midterm report [3].

6.2.6. X-RAY SENSOR

The in-situ instruments will provide the warning to Earth if a CME can potentially cause damage to Earth's infrastructure. Many spacecraft with a similar mission to SWAN (GOES, SOHO and SDO[27, 31]) also incorporate an X-ray sensor to help gain a better understanding of the dynamics in the corona and get an advanced warning time of catastrophic CMEs. The X-ray sensor simply measures the total flux of X-rays coming from the sun, as it has been found that about 20 min before

Table 6.7: Heliospheric imager specifications

Parameter	Value	Unit
Resolution	3.52	arcminutes
FoV	60	degrees
Cadence	20	minutes
Bits/pixel	16	-
Spectral band	500-700	nm

a CME occurs, there is a spike in X-ray flux between 0.1 - 0.8nm and that there is a correlation between the intensity of this spike and the CME's velocity[32, 33], thus providing a better prediction in combination with the other remote sensing instruments. The x-ray sensor will provide early and accurate warnings for CME's and is equipped to both OB1 and OB2. The reason for this is because OB1 is then capable of detecting CME's that are ejected into the path of the Earth, whereas OB2 can detect CME's ejected from the western hemisphere of the Sun. Note that the measurements made by the x-ray sensor are crucial as high x-ray fluxes can exceed the thresholds prescribed by NOAA (see Section 6.1.2) and thus warrant warnings.

SPECIFICATIONS

Due to the fact that the x-ray is a new inclusion to the SWAN mission since the midterm report the most important specifications of the x-ray sensor shall be mentioned here. A complete list of the specifications can also be seen in Table 6.8. It needs a cadence of maximum 1 minute, as these spikes usually last this long [32, 33]. The instrument itself is small, weighing just 2kg, having a power consumption of 1W and a data generation of 2 kbps [34]. It has dimensions of 10x10x8 cm³, operates near room temperature and costs 7 mln Euros[27, 34]. To properly measure the X-ray flux, it has to view the sun (32 arcminutes at 1AU) plus 5 arcminutes on each side [34], and a margin of 13 arcminutes on each side for pointing accuracy. This yields a total field of view of 68 arcminutes and a pointing accuracy of 13 arcminutes. Lastly, the sensor is also sensitive to incoming electrons, therefore a magnet of strength 0.08 T is placed in front of the aperture, to deflect electrons with energies up to 5 keV.

Table 6.8: X-ray sensor specifications

Parameter	Value	Unit
FoV	68	arcminutes
Spectral band	1-8	Å
Dimensions	10x10x8	cm ³

6.2.7. FARADAY CUP

The next in-situ instrument is the Faraday cup. This system is integrated into the OB1 satellite and will provide data on the key parameters of the solar wind and bulk plasma; the parameters include velocity, density and temperature. These parameters are important for validating models that predict effects of solar weather on Earth. The data from the Faraday cup will provide input values for solar weather models which allow for accurate estimations of the solar wind and solar events.

The Faraday cup consists of a circular sensor plate, that is divided into 3 sectors, and a set of wire mesh grids. In short, the velocity distribution is measured by recording the current that is induced by ions, with a particular energy range, on the sensor plate. Some advantages of the Faraday cup system include it being impervious to contamination due to radiation and photons. Also due to the Faraday cups high angle of acceptance of 60°, it is able to measure large velocities, this is a useful trait since CME's are capable of reaching speeds of 2,000 km/s at L1 [15][16]. Furthermore, the high cadence (3 s) of the system allows for accurate recording of the anisotropies of the solar wind and CME's [35].

OPERATION

As mentioned previously, the Faraday cup consists of a collector plate and a set of wired-mesh grids. Two of these grids make up the modulator and are provided with a high voltage 200 Hz DC-biased square-wave. One of the grids is provided a voltage of V_1 and the other a voltage of V_2 , with $V_1 < E/q < V_2$. Here E is the energy of the particle and q is the energy of one electron. The modulator grids ensure that particles with an energy between 0.2 keV/e to 20 keV/e are able to impinge on the sensor plate; this range is chosen as it encompasses the majority of the particles that make up the bulk plasma [16]. It should be noted that an added advantage of the Faraday cup system is that the modulation voltages V_1 and V_2 are variable thus the key parameters of higher/lower energy particles can also be measured. Another grid is used to deflect photoelectrons due to sunlight away from the sensor plate; this grid is negatively DC-biased. Lastly, before the particles reach the sensor plate, they encounter the suppressor plate. This plate functions to reduce losses due to the

back-scattering of electrons in addition to preventing secondary electrons from escaping the aperture [35]. The particles that make it through the modulator are then detected on the sensor plate. The current induced by these particles is then converted to a digital signal by means of an analogue-to-digital converter [36].

When measuring the velocity distribution there is a dependency on the angle at which the particle hits the detector. Due to the nature of the sensor, it is only capable of measuring the component of the velocity that is normal to the surface of the sensor. This means that if particles are entering the Faraday cup at a large incidence angle then the normal component will be smaller, hence it can be modulated by a lower V_1 and V_2 window. By altering the modulation window the velocity distribution can be obtained [36]. The data that is obtained from each operating window can also be used to estimate the temperature and density of the plasma. The measurements result in a plot that shows the induced current against the incidence angle. Where the modulation window is coupled with the velocity, the temperature can be obtained by assessing the width of the peak in the plot and the density can be ascertained from the total induced current [36].

The fact that the OB1 spacecraft is three-axis stabilised poses a challenge for the Faraday cup as it cannot use rotational motion to scan the solar wind and determine the 3D properties. This issue is solved by using a sensor plate that is divided into three sectors, the 3D distribution is then related to the ratios of the current induces on each of the three sectors. This design is similar to the design for the Triana Faraday cup [35]. Furthermore, since the instrument must continuously be pointed towards the Sun it must endure harsh thermal environments. In an effort to allow the system to operate within these thermal conditions the system feature a reflective heat shield, akin to the Triana Faraday cup [35].

SPECIFICATIONS

The specifications of the Faraday cup system are presented in Table 6.9. The design of the SWAN Faraday cup is based on the design of the Triana Faraday cup system [36]. This system has already been proven in conditions similar to that of the SWAN mission. The system is favoured for its real-time measurements indicated by the cadence (3 s), and its high precision with is being capable of an angular resolution of 3° by 3° . In Table 6.9 the velocity-, density- and temperature range are all capable of measuring the most extreme solar storms and CMEs [15] [16]. The Faraday cup makes up one half of the solar wind monitoring system, the other component is the SEP monitor which will be discussed next.

Table 6.9: Faraday cup specifications

Parameter	Value	Unit
FoV (in ecliptic-plane)	45	$^\circ$
FoV (out of ecliptic-plane)	15	$^\circ$
Acceptance angle	± 60	$^\circ$
Angular resolution	3x3	$^\circ$
Cadence	3.0	s
Energy range	0.2 - 20	keV
Velocity range	200 - 2,000	kms^{-1}
Density range	0.1 - 100.0	$\text{particles}\cdot\text{cm}^{-3}$
Temperature range	<4.0	MK
Dimensions	D15x9	cm^3

6.2.8. SEP MONITOR

The second part of the solar wind monitor focuses on the threats of solar energetic particles (SEP's). As mentioned in Section 6.1.1 SEP's are a potential hazard for Earth infrastructure as high fluxes can cause permanent damage to the instrumentation and onboard computers of satellites. Contrary to what the name suggests, the SEP monitor not only measures solar radiation, in the advent that galactic cosmic rays (GCR's) are more prevalent than SEP's the instrument will measure the flux associated with GCR's. The SWAN SEP monitor will make a distinction between electrons and ions, the latter includes protons, alpha particles and heavier ions ($Z>4$).

SPECIFICATIONS

In Table 6.10 the specifications of the SEP monitor are presented. The SEP monitor instrument consists of two apertures that fulfil the tasks of measuring electrons and ions. The architecture of the SEP monitor is based on ESA's next-generation radiation monitor [37]. The electron detector consists of an aluminium housing that contains a collimator. The opening in the aluminium housing is composed of a circular cone-like shape that decreases in diameter near the collimator. The rate at which cone hollows out determines the energy range of the electrons that are able to reach the collimator. In this case the energy range spans from 0.8 MeV to 7.0 MeV [37]. The system operates in two channels: 0.8 - 2.0 MeV ad 2.0 - 7.0 MeV. These ranges are chosen such that they coincide with the thresholds in Section 6.1.2.

As for the ion detector is a cylindrical aperture made from copper and aluminium, that is divided by degraders and diodes. Ions with sufficient energy can bypass the diodes and be detected. The ion detector has three bins: 10 - 100 MeV, 100 -

200 MeV and >200 MeV. Again these bins coincide with the thresholds in Section 6.1.2 [37]. The data measured by the SEP monitor will be compared with the thresholds and in the case that the fluxes are exceeded a warning will be sent. This concludes the discussion of the instruments that make up the solar wind monitoring system.

Table 6.10: SEP monitor specifications

Parameter	Value	Unit
Electron energy range (dual channel)	0.8 - 2.0	MeV
	2.0 - 7.0	MeV
Ion energy range (triple channel)	10 - 100	MeV
	100 - 200	MeV
	>200	MeV
Dimensions	10x10x10	cm ³

6.2.9. FLUXGATE MAGNETOMETER

The final instrument, the triaxial fluxgate magnetometer of which there are two, are integrated into both OB1 and OB2. The magnetometer is capable of measuring the interplanetary magnetic field (IMF) vector. These measurements are important since the direction and magnitude of the IMF can determine how it will interact with the magnetosphere of the Earth. The instrument itself consists of three orthogonal electromagnets. A sense coil is constructed around each of the electromagnets and is able to measure changes in the magnetic field of the magnet due to the IMF. These changes are coupled with IMF vector.

MAGNETIC CLEANLINESS

A subject regarding the magnetometer not fully elaborated upon in the midterm [3] is magnetic cleanliness. The presence of onboard magnetic fields imposes constraints on the design as the noise generated by stray fields will create noise in the measurements of the magnetometer. While the effect of constant fields can be removed through calibration, time-varying stray fields can cause problems for the system. In an effort to mitigate the effect of time-varying stray fields a so-called "magnetic cleanliness program" will be implemented in the detailed design phase.

Firstly, the magnetometers shall be mounted on a boom. The length of this boom is 6.13 m. This length is a preliminary estimate that is based on an empirical relation between the magnetometer accuracy and boom length of spacecraft that operate two magnetometers. The data for this relation is obtained through OSCAR⁴ Mounting the magnetometer suite on a boom allows the instrument to be positioned away from the spacecraft body and the stray fields that exist there. The magnetometer suite includes two magnetometers, one is mounted at the end of the boom and the other at the half-way point of the boom. Dual magnetometers improve the accuracy of the system since the enable one to discern the magnetic field produced by the spacecraft from the ambient field. This works in the following way: Since the spacecraft-generated magnetic field decreases with distance there is a spatial gradient between the magnetometer sensors. The ambient magnetic field measured by the two magnetometers can be assumed to be equal since its spatial gradient is negligible over the length of the boom. Therefore each magnetometer measures the same ambient magnetic field, yet a different magnetic field produced by the spacecraft; as such these two magnetic fields can be separated allowing for more accurate measurements. In this case, the use of two magnetometers allows for a smaller boom. Another advantage of having dual magnetometers is that it allows for monitoring variations of the spacecraft induced magnetic field. Lastly, having two magnetometers provides redundancy for the measurements, something that has been used in past missions [38].

However, using this method to solve for the stray fields and then remove it from the measurements requires that the stray fields are larger than the noise. In Carter et al. [39] two methods are described that deal utilise dual magnetometers: averaging and gradiometry. Gradiometry involves measuring both the IMF and the stray field with two magnetometers; then one can simply remove the stray fields from the measurements. Whereas averaging simply averages the measurements of both magnetometers. Carter et al. [39] tested these methods for the GOES-R mission and found that gradiometry is more effective than averaging when the stray fields are twice as large as the noise, else averaging provides more accurate results. These conditions will also apply to the SWAN mission, as such both the averaging and gradiometry methods will be available.

Furthermore, Carter et al. [39] go on to say that one can improve the averaging method by modelling the sources of the stray fields, the effect of these fields can then be removed from the data. To do this one requires algorithms that characterise the stray fields caused by other subsystems. Carter et al. [39] also provide three algorithms for the solar arrays, reaction wheels and thrusters, such models will also be used in the SWAN mission. Selection of these algorithms will be conducted in the detailed design phase.

⁴<https://www.wmo-sat.info/oscar/>

As part of the magnetic cleanliness program, it is also necessary to devise a magnetic field budget of all the subsystems on the spacecraft. Doing so will allow one to model the effects of the static stray fields and gain a better indication of the length necessary for the boom. Furthermore, in the case that the magnetic field budget exceeds the limits measurements can be taken to reduce its impact. These include but are not limited to: preventing the coiling of cables as this will induce stray magnetic fields and ensuring that all components that induce magnetic fields are not pointed in the same direction, as this would amplify the effect.

SPECIFICATIONS

The specification of the SWAN magnetometers are shown in Table 6.11. The specifications for the instrument are based on the requirements for the device that are described in the midterm report [3]. This concludes the list of instruments that are integrated into the SWAN mission.

Table 6.11: Magnetometer specifications

Parameter	Value	Unit
Dynamic range	± 204.8	nT
Digital resolution (12-bit)	0.1	nT
Zero level drift	0.5	nTyr ⁻¹
Cadence	0.1	s
Boom length	6.13	m
Dimensions	20x10x5	cm ³

6.3. INSTRUMENT PROTECTION

A challenge for the SWAN mission is that both spacecraft are three-axis stabilised. This means that Sun facing instruments will be continuously exposed to solar radiation. This results in harsh thermal environments that the instruments must operate in. In addition, there is also the likelihood of charged particles interacting with the instruments such as lenses or detector plates. These interactions can cause erroneous measurements and in some cases impact the electronics. Such events are increasingly likely in the case of a CME, as such measures must be taken to protect the instrumentation against these hazards.

For the optical instruments, doors are equipped that can be deployed. This protects the lenses and baffles from charged particles that can interface with them. To prevent this and charged particles from contaminating in-situ measurements magnets can be used. These magnets can prevent electrons from entering the aperture of the instruments. Such magnets are used in the SEP monitor to prevent electrons from contaminating the measurements [37]. In the case of OB1, since it is equipped with a particle detector (SEP monitor), it can anticipate the increase of charged particle fluxes. Electrons are often a precursor for heavier ions, thus if the SEP monitor detects an increase in electron flux the operator can decide to close the door that covers the coronagraph aperture. Such measures prevent the remote sensing instruments from operating, however, in-situ instruments are still capable of measuring during these instances. This shields the instrument from charged radiation. Unfortunately, OB2 is not equipped with a particle detector, as such this preventative measure cannot be undertaken.

Electrons are of particular concern as they can induce deep dielectric (DD) charging [40]. Although DD charging is more a concern for spacecraft in the magnetosphere of the Earth, a CME can also yield large fluxes of electrons and protons.

DEEP DIELECTRIC CHARGING

DD charging occurs when charged particles interact with the spacecraft and induce charges on the internal components. Alternatively, the notion of internal charging applies to the case where charge accumulates on the surface of the spacecraft, these surfaces can subsequently conduct electric fields on components within the spacecraft [41]. When the charge is building up the likelihood of a spontaneous discharge increases. This discharge can be instigated by the penetration of a single charged particle that impacts the dielectric. The triggering mechanism for the discharge can often be attributed to the solar minimum phase where GCR's are more prevalent.

There are various parameters that influence the occurrence of discharge events, these are described by Lai et al. [41]. First, there is the energy of the incoming particle, this along with the thickness of the material and material type determine how what particles can penetrate it. Another crucial parameter is the fluence, that is the amount of flux over a period of time. The fluence and the leakage flux can be likened to the in-going and out-going charge. If the fluence exceeds the leakage flux one will experience a buildup of charge. The leakage flux can be managed by utilising conductive materials. Furthermore, to prevent a discharge from affecting mission-critical components one can use a component layout that can divert large electric surges away from onboard instruments and electronics.

THERMAL

In addition to DD charging, the radiation that affects the spacecraft also creates harsh thermal environments for the instruments. Temperatures can be regulated through the use of heaters and surfaces that radiate heat; this is discussed in more detail in Chapter 10.

6.4. TECHNICAL RISK ASSESSMENT

In Table 6.12 the technical risks pertaining to the payload of the SWAN mission are presented. The table displays the likelihood and impact of each risk, for the risks that pose threats to the mission, methods for mitigating those risks are described.

Table 6.12: Payload Risk Register. Likelihood: HU = highly unlikely, U = unlikely, SL = some likelihood, L = likely, HL = highly likely. Impact: M = marginal, S = some, H = high, C = catastrophic

Risk	Consequence	Likelihood	Impact	Mitigation
One or more instruments fail	Not all data will be available	HU	C	-
Optical instrument is contaminated	Instruments make incorrect measurements	L	H	The payload is protected from contamination (see Section 6.3)
One of the magnetometer decays faster than expected	Instrument data becomes unreliable over time	SL	S	Use the second magnetometer for calibration
Magnetometer fails	Missing measurement data	HU	S	The magnetometer system is fully redundant
Active calibration magnetometer fails	Noise cannot be removed from signal	U	S	Average the measurements of both magnetometers
SEP monitor is highly contaminated	Data becomes unreliable	U	H	Magnets and filters are used to reduce contamination
X-ray sensor is contaminated by electrons	Data becomes unreliable	U	H	Magnets deflect incoming electrons

6.5. RELIABILITY, AVAILABILITY, MAINTAINABILITY, AND SAFETY CHARACTERISTICS

As for every subsystem of the SWAN mission a RAMS (reliability, availability, maintenance and safety) analysis is conducted. In terms of reliability, however, little data is available since all the instruments are specialised, so such early estimates for the reliability will be inaccurate without testing the instruments. To ensure reliability, the instruments will be built in a clean environment under the right conditions to properly function in space, and before launch, they will be tested to ensure everything works within nominal parameters. In case of possible radiation/particle damage, they will have a safe mode to minimise this and prevent failure. Furthermore, instruments such as the magnetometer are placed on a boom to minimise interference from other systems and increase reliability.

Since the instruments are specialised they are often not readily available. For the instruments that can be purchased off the shelf, such as the magnetometer, they must be hardened to endure the space environment and be integrated on other subsystems such as booms. There is the option to utilise the architecture of preexisting instruments from other missions that meet the requirements for the instruments. However, this will likely yield a set of instruments that are over-designed since most space instrumentation is designed for scientific purposes and not solely space weather monitoring.

Maintenance only applies to when the spacecraft is on the ground, during production. Maintenance is considered in the sense that one must be capable of integrating and removing instruments from the spacecraft with relative ease. If instruments fail aboard the spacecraft, nothing can be done to repair them, however, updates in software can be sent via up-link. Moreover, it is also crucial that the necessary safety measures are conducted that ensure that the instruments are not damaged during production or throughout the mission life. No hazardous coatings or materials are used on the instruments, and the optical instruments have doors to protect from radiation or dust in case necessary. Redundancy is not actively applied to all instruments as this would increase the cost beyond the limit. However, the magnetometer,

X-ray sensor and coronagraph instruments are redundant as if one fails, the other can still operate, albeit less accurately or effectively.

6.6. COMPLIANCE MATRIX

The requirement compliance matrix is presented in Table 6.13. It is assumed that a manufacturer will develop the instruments with the specifications mentioned in this chapter, thus fulfilling the requirements in the matrix. Therefore it is not possible to assess the compliance of each requirement, the matrix is still presented as it provides a means to communicate the requirements/specifications of the instruments to a potential manufacturer.

Compliance with these requirements should pose a little issue, this is because many of the instrument specifications are similar to instruments that already exist. Furthermore, the SWAN mission aims to conduct solar weather monitoring, meaning the scientific objective is secondary, to that effect the payload is not required to ground-breaking. Some challenges might arise from the fact that none of the instruments has operated at L5. One concern is the data rate for the optical instruments, if this is too high then compromises will need to be made on the quality of the data; this analysis will be conducted in Section 7.4.

Table 6.13: Orbit Requirement Compliance Matrix

Identifier	Requirement	Met?	Confirmation
Magnetometer			
PL-MTM-01	The interplanetary magnetic field instrument shall be able to measure the interplanetary magnetic field vector in-situ	TBD	-
PL-MTM-02-a	The magnetometer shall be capable of measuring magnetic field within the range ± 204.8 nT	TBD	-
PL-MTM-03-a	The total power usage of the interplanetary magnetic field instrument(s) in one spacecraft shall not exceed 10 W	TBD	-
PL-MTM-04-b	The total mass of the interplanetary magnetic field instrument(s) in one spacecraft shall not exceed 5.0 kg	TBD	-
PL-MTM-05	The volume of the interplanetary magnetic field instrument in one spacecraft shall not exceed $<20>x <10>x <5>cm^3$	TBD	-
PL-MTM-05.1	The volume of the magnetometer electronics in one spacecraft shall not exceed $20 \times 10 \times 5 \text{ cm}^3$	TBD	-
PL-MTM-05.2	The volume of the magnetometer sensor in one spacecraft shall not exceed $4 \times 4 \times 4 \text{ cm}^3$	TBD	-
PL-MTM-06-a	The total cost of the interplanetary magnetic field instrument(s) in one spacecraft shall not exceed 3 MEuros	TBD	-
PL-MTM-07	The magnetometer system shall be fully redundant.	TBD	-
PL-MTM-08	The magnetometer shall be able to make triaxial (vector) measurements.	TBD	-
PL-MTM-09	The interplanetary magnetic field instrument shall be rigidly attached to the satellite	TBD	-
PL-MTM-10	The sensor shall not endure temperature extremes beyond -100 to $+200$ °C.	TBD	-
PL-MTM-11-a	The error of fixture of the magnetometer sensor shall be known within ± 0.5 °	TBD	-
PL-MTM-12.1-a	The magnetometer shall have a digital resolution of 0.1 nT.	TBD	-
PL-MTM-12.2	The onboard electronic shall be capable of digitising the magnetic measurements to a 12-bit resolution.	TBD	-
PL-MTM-13.1-a	The possible variation of the magnetic field of the spacecraft at the position of the sensor due to spacecraft internal magnetic field shall be less than 5 nT.	TBD	-
PL-MTM-13.1-b	The possible variation of the magnetic field of the spacecraft at the position of the sensor due to spacecraft internal magnetic field shall be more than 1 nT.	TBD	-
PL-MTM-13.2	The variation in magnetic field shall occur over a timespan of $<TBD>$ days	TBD	-
PL-MTM-14-a	The total noise level of the magnetometer shall not exceed 0.5 nT.	TBD	-
PL-MTM-15.1	The magnetometer shall have a zero level drift less than 0.5 nT/yr.	TBD	-
PL-MTM-15.2	The electronics of the magnetometer shall not endure temperature extremes beyond -55 to $+75$ °C.	TBD	-

PL-MTM-16	The static magnetic influences of the onboard electronics shall be measured for calibration of the magnetometer.	TBD	-
PL-MTM-17-a	The orientation of the magnetometer sensor shall be known within $\pm 33'$ (arcminutes)	TBD	-
PL-MTM-18	The data rate of the magnetometer shall be 0.72 kbps	TBD	-
PL-MTM-19	The measurement frequency of the magnetometer shall be 10 Hz	TBD	-
Coronagraph			
PL-CRG-01	The coronal imaging instrument shall be able to perform coronal imaging	TBD	-
PL-CRG-02-a	The operating temperature of the coronagraph shall be between 273.15 - 313.15K	TBD	-
PL-CRG-03-a	The non-operational temperature of the coronagraph shall be between 253.15 - 328.15K	TBD	-
PL-CRG-04	The coronal imaging instrument at L1 shall be rigidly attached to the spacecraft	TBD	-
PL-CRG-05	The pointing accuracy of the coronal imaging instrument shall be at least 4.3' (arc-minutes)	TBD	-
PL-CRG-06	The angular resolution (plate scale) of the coronagraph shall be at least 53"/pixel (arc-second/pixel)	TBD	-
PL-CRG-06.1	The coronagraph shall have an in plane FOV of at least 15.07 degrees	TBD	-
PL-CRG-06.2	The coronagraph shall have an out of plane FOV of at least 15.07 degrees	TBD	-
PL-CRG-06.3	The temporal cadence of the coronagraph shall be at most 12 minutes	TBD	-
PL-CRG-06.4	The screen size of the detector shall be 1024x1024 pixels	TBD	-
PL-CRG-07-a	The pointing stability of the coronal imaging instrument for a single exposure shall be at least 26.5" in 4 seconds	TBD	-
PL-CRG-07-b	The pointing stability of the coronal imaging instrument for a single exposure shall be at least 10" in 4 seconds	TBD	-
PL-CRG-08-a	The coronagraph shall have a signal to noise ratio of at least 4	TBD	-
PL-CRG-09	The coronagraph shall image the corona with a wavelength of at most 900nm	TBD	-
PL-CRG-10	The coronagraph shall image the corona with a wavelength of at least 400nm	TBD	-
PL-CRG-11	The total power usage by the coronal imaging instrument(s) in one spacecraft shall not exceed 50 W	TBD	-
PL-CRG-11-a	The total power usage by the coronal imaging instrument(s) in one spacecraft shall not exceed 29.5 W	TBD	-
PL-CRG-12-a	The total mass of the coronal imaging instrument(s) in one spacecraft shall not exceed 10.5 kg	TBD	-
PL-CRG-13	The total cost of the coronal imaging instrument(s) in one spacecraft shall not exceed 15 million Euros	TBD	-
PL-CRG-14	The total volume of the coronal imaging instrument(s) in one spacecraft shall not exceed 0.708 x 0.295 x 0.295 m ³	TBD	-
PL-CRG-15	The data rate of the coronagraph shall not be higher than 23.3 kbits/s	TBD	-
Heliospheric Imager			
PL-HSI-01	The heliospheric imaging instrument shall be able to perform heliospheric imaging	TBD	-
PL-HSI-02	The total power of the heliospheric imaging instrument(s) in one satellite shall not exceed 20 W (including the heater)	TBD	-
PL-HSI-03	The total mass of the heliospheric imaging instrument(s) in one spacecraft shall not exceed 17 kg	TBD	-
PL-HSI-04	The total cost of the heliospheric imaging instrument(s) in one spacecraft shall not exceed 1 million Euros	TBD	-
PL-HSI-05	The total volume of the heliospheric imaging instrument(s) in one spacecraft shall not exceed 0.8 x 0.3 x 0.3 m ³	TBD	-
PL-HSI-06	The temperature of the heliospheric imager be kept at a temperature between 203 K and 243K for operation	TBD	-
PL-HSI-07	The heliospheric imager shall be attached to the spacecraft with an accuracy of 20 arcminutes	TBD	-

PL-HSI-08	The on board post-processing of the heliospheric imaging instrument shall have a capacity of at least 24 bits	TBD	-
PL-HSI-9	The heliospheric imager shall have a resolution of at least 1024 pixels across	TBD	-
PL-HSI-10	The heliospheric imager shall have an angular resolution of at most 3.52 arcminutes	TBD	-
PL-HSI-11	The heliospheric imaging instrument shall continuously be in the process of monitoring the heliosphere	TBD	-
PL-HSI-12	The heliospheric imager shall have an in plane field of view of at least 60 degrees	TBD	-
PL-HSI-13	The out of plane field of view of the heliospheric imaging instrument shall be at least 3 degrees	TBD	-
PL-HSI-14a	The heliospheric imager shall have a pointing stability of at most 7.03 arcminutes per 20 minutes	TBD	-
PL-HSI-15	The heliospheric imager shall have a stray light rejection of under $10^{(-12)}B_0$	TBD	-
PL-HSI-16	The heliospheric imager shall capture scattered light from the plasma of wavelengths between 600-700 nm	TBD	-
PL-HSI-17	The heliospheric imager's CCD shall be kept at a temperature between 193K and 213K for operation	TBD	-
Magnetograph			
PL-MNG-01	The solar magnetic field measuring instrument shall be able to measure the magnetic field at the surface of the Sun	TBD	-
PL-MNG-02	The total power of the solar magnetic field measuring instrument on one spacecraft shall be lower than 25 W	TBD	-
PL-MNG-03	The total mass of the solar magnetic field measuring imaging instrument in one spacecraft shall not exceed 26 kg	TBD	-
PL-MNG-04	The total cost of the solar magnetic field measuring instrument on one spacecraft shall not exceed 15 MEuros	TBD	-
PL-MNG-05	The total volume of the solar magnetic field measuring instrument in one spacecraft shall not exceed $0.3 \times 0.4 \times 1.2 \text{ m}^3$	TBD	-
PL-MNG-06	The temperature of the solar magnetic field measuring instrument shall not become below 283.15 K during operation	TBD	-
PL-MNG-07	The temperature of the solar magnetic field measuring instrument shall not exceed 303.15 K during operation	TBD	-
PL-MNG-08	The solar magnetic field measuring instrument shall be rigidly attached to the spacecraft	TBD	-
PL-MNG-09	The solar magnetic field measuring instrument shall have a signal to noise ratio of higher than 1000	TBD	-
PL-MNG-10	The temporal cadence of the solar magnetic field measuring instrument shall be smaller or equal to 1 minute	TBD	-
PL-MNG-11	The angular resolution of the solar magnetic field measuring instrument shall be smaller or equal to 1" (arcsecond)	TBD	-
PL-MNG-12	The FOV of the solar magnetic field measuring instrument shall be larger or equal than 34.1' (arcminutes)	TBD	-
PL-MNG-13	The temperature of the solar magnetic field measuring instrument shall not become below 233.15 K during non-operation	TBD	-
PL-MNG-14	The temperature of the solar magnetic field measuring instrument shall not exceed 343.15 K during non-operation	TBD	-
PL-MNG-15	Each pixel in the CCD shall have a resolution of 12 bits per pixel	TBD	-
PL-MNG-16	The data rate of the magnetograph shall not be higher than 575.9 kbps	TBD	-
PL-MNG-17	The pointing accuracy shall be at least 0.55 arcminutes.	TBD	-
PL-MNG-18	The dynamic range of the magnetograph shall be ± 4096 Gauss.	TBD	-
X-Ray Sensor (XRS)			
PL-XRS-01	The X-ray sensor shall be able to measure the X-ray flux from the sun	TBD	-
PL-XRS-02	The X-ray sensor shall have a pointing accuracy of 13 arcmin	TBD	-
PL-XRS-03	The X-ray sensor shall have a field of view of 68 arcmin	TBD	-
PL-XRS-04	The X-ray sensor shall be able to measure X-rays with a wavelength between 1 and 8 Angstrom	TBD	-
PL-XRS-05	The orientation of the X-ray sensor shall be known to within 2 arcsec	TBD	-

PL-XRS-06	The X-ray sensor shall be able to deflect incoming electrons of up to 5 keV	TBD	-
PL-XRS-07	The X-ray sensor's mass shall not exceed 2kg	TBD	-
PL-XRS-08	The X-ray sensor's power shall not exceed 1W	TBD	-
PL-XRS-09	The data rate of the X-ray sensor shall not exceed 2 kbps	TBD	-
PL-XRS-10	The X-ray sensor's volume shall not exceed 0.1x0.1x0.08 m ³	TBD	-
PL-XRS-11	The X-ray sensor DHU's volume shall not exceed 0.15x0.08x0.08 m ³	TBD	-
PL-XRS-12	The X-ray sensor's cost shall not exceed 7 mln Euros	TBD	-
PL-XRS-13	The X-ray sensor shall be kept within the temperature range of <TBD>K and <TBD>K	TBD	-
EUV Imager			
PL-EUVI-01	The EUV imager shall be able to image the sun in extreme ultra-violet spectrum	TBD	-
PL-EUVI-02	The EUV imager shall have an angular resolution of 3 arcsec	TBD	-
PL-EUVI-03	The EUV imager shall have a field of view of 50 arcmin	TBD	-
PL-EUVI-04	The EUV imager shall have a resolution of 1024x1024 pixels	TBD	-
PL-EUVI-05	The EUV imager shall be able to image in the spectral band of Fe-IX (171 Angstrom)	TBD	-
PL-EUVI-06	The EUV imager's mass shall not exceed 10kg	TBD	-
PL-EUVI-07	The EUV imager's power shall not exceed 12W	TBD	-
PL-EUVI-08	The data rate of the EUV imager shall not exceed 125 kbps	TBD	-
PL-EUVI-09	The EUV imager's volume shall not exceed 0.26x0.12x0.12 m ³	TBD	-
PL-EUVI-10	The EUV imager DHU's volume shall not exceed 0.15x0.08x0.08 m ³	TBD	-
PL-EUVI-11	The EUV imager shall require a pointing accuracy of 15 arcsec	TBD	-
PL-EUVI-12	The EUV imager's cost shall not exceed 15 mln Euros	TBD	-
PL-EUVI-13	The EUV imager shall be kept within the temperature range of <TBD>K and <TBD>K	TBD	-
Faraday Cup			
PL-FC-01	The Faraday cup of the solar wind monitor system shall measure particles within the range 200 eV/e to 20 keV/e.	TBD	-
PL-FC-02	The Faraday Cup shall be pointed towards the Sun.	TBD	-
PL-FC-03	The field-of-view of the Faraday cup shall be ±45° in the ecliptic-plane and ±15° out of the ecliptic-plane.	TBD	-
PL-FC-04	The acceptance angle of the Faraday cup shall be ±60°.	TBD	-
PL-FC-05	The angular resolution of the Faraday cup shall be 3° by 3°.	TBD	-
PL-FC-06	The cadence of the Faraday cup system shall be 3s.	TBD	-
PL-FC-07	The Faraday cup shall be capable of measuring densities within the range 0.1 to 100 particles/cm ³ .	TBD	-
PL-FC-08	The Faraday cup shall be capable of measuring solar wind velocity up to 2,000 km/s.	TBD	-
PL-FC-09	The Faraday cup shall be capable of measuring particle temperatures upto 4.0 MK.	TBD	-
PL-FC-10	The Faraday cup system shall require 4 W of power.	TBD	-
PL-FC-11	The mass of the Faraday cup system shall not exceed 5 kg.	TBD	-
PL-FC-12	The dimensions of the Faraday cup shall not exceed 15.0 cm diameter and 9.0 cm height.	TBD	-
PL-FC-13	The Faraday cup system shall cost 5M Euros.	TBD	-
PL-FC-14	The Faraday cup sensor shall operate within a temperature range of -20°C to 40°C.	TBD	-
PL-FC-15	The Faraday cup electronics shall operate within a temperature range of -10°C to 30°C.	TBD	-
PL-FC-16	The Faraday cup system shall have a data rate of 0.16 kbps	TBD	-
SEP monitor			
PL-SEP-01	The SEP monitor shall measure the electron flux in two channels	TBD	-
PL-SEP-01.1	The SEP monitor shall measure electron flux between 0.8 and 2.0 MeV.	TBD	-
PL-SEP-01.2	The SEP monitor shall measure electron flux above 2.0 MeV.	TBD	-
PL-SEP-02	The SEP monitor shall measure the proton flux in two channels.	TBD	-
PL-SEP-02.1	The SEP monitor shall measure proton flux between 10.0 MeV and 100.0 MeV.	TBD	-

PL-SEP-02.2	The SEP monitor shall measure the proton flux above 100.0 MeV.	TBD	-
PL-SEP-03	The SEP monitor shall measure the flux of heavy ions ($Z>4$) with energies below 200.0 MeV.	TBD	-
PL-SEP-04	The mass of the SEP monitor system shall not exceed 1.4 kg.	TBD	-
PL-SEP-05	The SEP monitor system shall require 2.5 W of power.	TBD	-
PL-SEP-06	The SEP monitor system shall have a data rate of 0.075kbps.	TBD	-
PL-SEP-07	The SEP monitor system shall cost 10M Euros.	TBD	-
PL-SEP-08	The volume of the SEP monitor shall not exceed 0.1x0.1x0.1 m ³	TBD	-

6.7. CONCLUSION AND RECOMMENDATIONS

As mentioned at the beginning of this chapter, the aim of the SWAN mission is to monitor space weather and provide early and accurate warnings of dangerous geomagnetic storms. This chapter aims to deliver a combination of instruments that are capable of delivering these requirements. In Section 6.2 all the instruments are described. These instruments are chosen such that they are capable observing solar weather events mentioned in Section 6.1.1 from detection to arrival at L1. The system is able to provide warnings if and when certain parameters of the solar wind or CME's exceed the thresholds described in Section 6.1.2. This concludes the discussion on the payload, some recommendations will follow after which the TT&C and data handling of the SWAN mission will be discussed.

During the project a meeting was established with S&T⁵. From this meeting the notion of measuring solar radio bursts (SRB's) with from L1 and L5 discussed. SRB's are of interest since they can impact terrestrial navigation. Mystery still shrouds the governing mechanisms that drive SRB's, however, radio telescopes on Earth are attempting to reveal the radio burst distributions and thus the underlying mechanisms. Since the solar radio emissions travel near the speed of light the advantage of detecting these emissions at L1 or even L5 is yet to be explored. Regardless, according to Giersch et al. [42], solar radio bursts effect and are affected by solar weather, this may make detecting SRBs with the SWAN mission worthwhile.

The inclusion of an electron spectrometer on OB2 is also recommended. It is recommended that this option is assessed for it can improve the protection of the sensitive optical instruments on the L5 spacecraft. It was mentioned that OB1 can close the door of the coronagraph, thus shielding is from charged particles, when a peak in electron flux is detected. OB1 is able to do so since it is equipped with the SEP monitor which incorporates an electron spectrometer. The ability to detect electron flux can be provided with a simple (single bin) electron spectrometer, would allow OB2 to also protect its optical instruments.

The gradiometry method of the magnetometer should be assessed to verify that it is truly capable of measuring large, instantaneous changes of onboard stray fields. If it cannot measure such changes one might impose requirements on the variation of magnetic fields over a period of time or simply apply the averaging method described by Carter et al. [39].

Another notion that should be explored is the possibility of integrating the magnetograph and EUV imager into a single instrument. Such an integration would be possible as both instruments observe a similar spectrum of light and would mean one less instrument required for the SWAN mission. For this system to work one must delve into the optical design requirements for each instrument and assess how one can incorporate them into a single instrument. Unfortunately, the project lacked the optical engineering knowledge to conduct this assessment.

⁵<https://www.stcorp.nl/>

7

TELEMETRY, TRACKING AND COMMAND CHARACTERISTICS

The TT&C system of SWAN will have to accommodate and handle all the telemetry and scientific data from all sub-systems within the spacecraft, while also receiving telemetry from the ground and maintaining control of the spacecraft throughout its mission lifetime. Without this, the spacecraft would not communicate and the mission would fail. This section aims to size the entire TT&C system.

7.1. DATA RATE

To fulfil the purpose of the mission, the scientific data generated from the instruments has to be sent down continuously, and to do this first the data rate has to be found. From Table 7.1, it can be seen that the raw data rates for OB1 and OB2 are 29.66 and 744.32 kbps, respectively, however it was found that the latter is too much for the system to handle, as the SNR would be too low (see Table 7.2). For OB1, since most instruments are not optical instruments and there is plenty of link margin, no compression will be applied. So in order to get the data rate of OB2 down to increase the SNR (since there is more energy per bit), one solution is to crop the image and send only relevant data. For example, the magnetograph produces a square image of the Sun with a field of view of 34.1 arcminutes, while its diameter is only 31.9 arcminutes across. Removing the unnecessary data already results in a 31% reduction in data. Furthermore, it was decided to apply compression to the data. This can either be lossless or lossy. Lossless compression (such as PNG) involves reducing the amount of data without losing any of the information (or quality) by getting rid of redundancy in the data. This however, does not achieve the required decrease in data, and therefore lossy compression was implemented. With lossy compression, one can decrease the data even more, at the expense of an 'acceptable' amount of quality loss. This is hard to define and there are many parameters that measure this. There are furthermore many different algorithms to do this that produce different results. Many spacecraft use and are increasingly using JPEG 2000 (JP2) as it can operate at higher compression ratios (CR) without generating the blocky and blurry artefacts that present themselves with the DCT JPEG-baseline [43] (however it does still produce ring artefacts like JPEG) while also having more efficient, but more complex coding.¹

As every image will behave differently to compression and to adhere to a certain quality standard, sample images of the instruments were tested using a program called Advanced Batch Image Converter. This is a very crude estimation, as sample images obtained have already been compressed lossily (no lossless format is available). Therefore, tests of different compression ratios by the program were compared to an image that was compressed 'losslessly' by the program (even though it is already compressed). If the images are compressed with final compression ratios lower than that shown in Table 7.1, then on initial inspection no difference can be distinguished, even when zooming in by a factor of 30. This can be seen for example with the magnetograph in Figure 7.1. Usually, compression tends to preserve the boundaries (with the exception of ring artefacts) while blurring out homogeneous regions, which is much less in JP2. Therefore, these compression ratios were deemed adequate.

7.2. LINK BUDGET

Once the data rate has been established, a link budget analysis is performed to determine if the required signal to noise ratio is high enough. This will involve a trade off between the power of the transmitter and the size (and hence gain) of the transmitter antenna on the spacecraft. The receiver antennas on Earth will be a combination of 6 x 34m and 1 x 70m antennas from NASA's Deep Space Network (DSN), and 3 x 35m and 6 x 15m antennas from ESA's ESTRACK. The 34/35m antennas will be used for OB2, as L5 is 100 times further away, and the 15m antennas for OB1, ensuring full 24 hour coverage.^{3 4} Furthermore, according to the International Telecommunication Union (ITU) and the available bands from NASA's deep space network, SWAN is limited to 4 frequency bands: S, X, K and K_a band, in order of increasing frequency. The K band is only available for near Earth downlink (under 2 million km) and the K_a band is only available for deep space

¹<http://www.stat.columbia.edu/~jakulin/jpeg/artifacts.htm>

²<https://sdo.gsfc.nasa.gov/data/>

³<https://deepspace.jpl.nasa.gov/about/complexes/>

⁴http://www.esa.int/Our_Activities/Operations/Estrack/Estrack_ground_stations

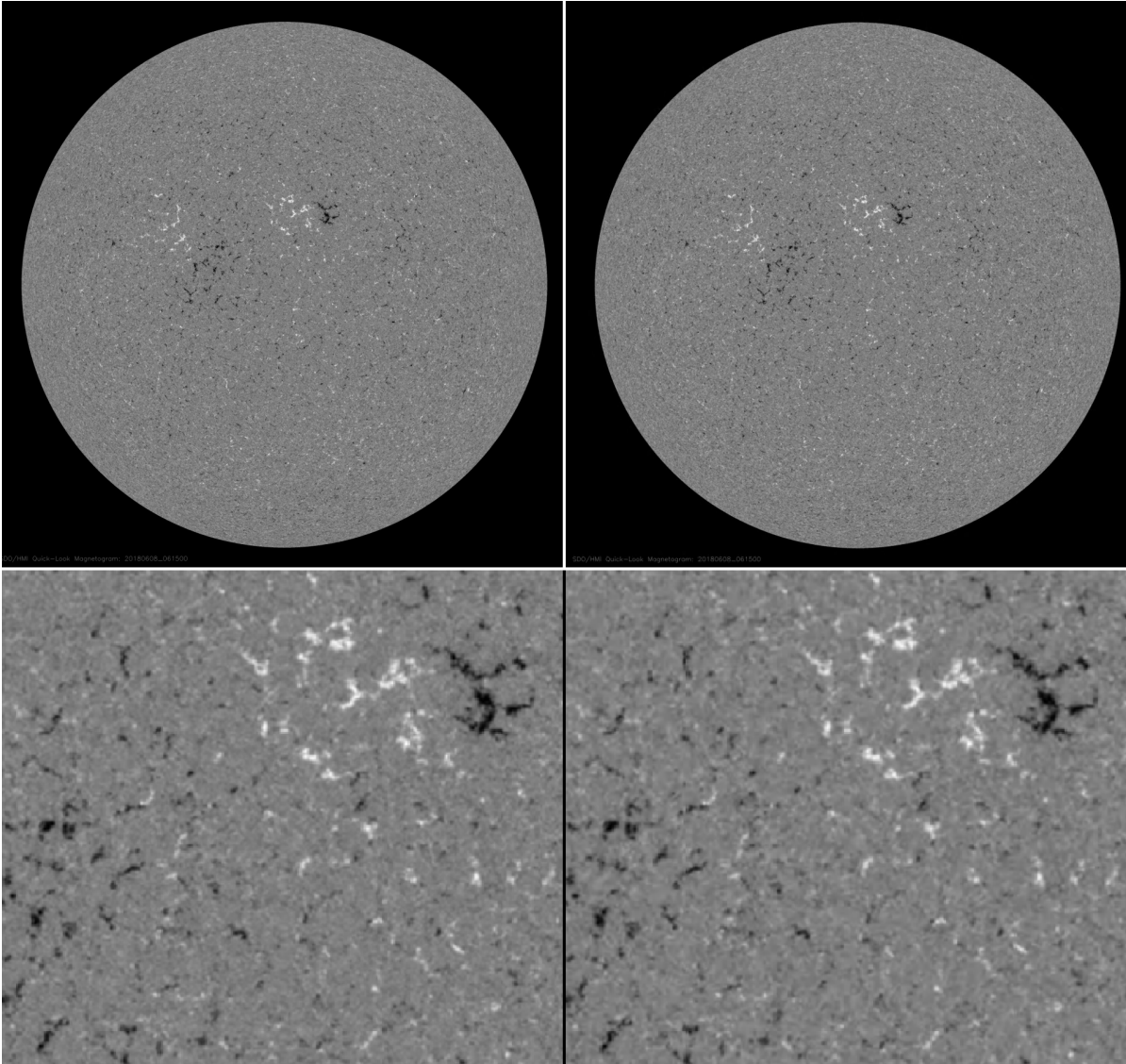


Figure 7.1: Compression of magnetogram. Left: Lossless compression. Right: Lossy compression with a compression ratio of 12^2

missions (greater than 2 million km). [44] Generally, higher frequencies means higher energy, so less power is needed to transmit the data, however one has to pay attention to atmospheric attenuation, which is particularly prominent in high frequencies. For this reason, the X-band was chosen at a frequency of 8.45GHz for both spacecraft, as the K_a band suffers from a 20dB rain attenuation, whereas the X-band only suffers from a 1dB loss. [45] This is assuming the International Telecommunication Union permits the use of this band. The link budget was calculated using the model in SMAD [45] [46] and can be found in Table 7.2, and calculations were checked by hand.

Here, the antenna gain (G) is calculated using Equation (7.1), where D is the diameter and $\eta = 0.6$ [45] is the efficiency typical of a parabolic antenna. This is valid for both horn and parabolic dish antennas, however horn antennas can only achieve a gain up to 25dB, and therefore is suitable only for OB1. There is also a pointing loss (L_{pr}) associated with the antenna arising from pointing inaccuracies, which is given by Equation (7.1) [45], e_t being the pointing accuracy and $\alpha_{\frac{1}{2}} = \frac{21}{\lambda D}$ being the half width beam angle (note that in this case L_{pr} is in dB). Since the pointing accuracy of the instruments are much stricter than $\alpha_{\frac{1}{2}}$, this loss can be neglected, as the loss is only 1dB at 0.5° for the parabolic antenna and 12° for the horn antenna. However the pointing loss of the ground station although small, cannot be ignored and is 0.12dB. The biggest loss to the link budget is the space loss (L_s), resulting from the great distances involved between the spacecraft and Earth. It is calculated using Equation (7.1) [45], where λ is the wavelength and S the distance between the satellite and Earth. Since OB2 is 100 times as far away, its space loss is 10^4 times greater, and thus requires more power and a bigger antenna. Lastly, the system noise is characterised by the system noise temperature, which in the case of SWAN is 135K [45].

$$G = \left(\frac{\pi D}{\lambda}\right)^2 \eta, L_{pr} = -12 \left(\frac{e_t}{\alpha_{1/2}}\right)^2, L_s = \left(\frac{\lambda}{4\pi S}\right)^2 \quad (7.1)$$

Table 7.1: Data Rate of both spacecraft, where CR is the compression ratio. Note that the data is divided by the compression ratio and multiplied with the factors.

Payload:	OB1 (L1)		OB2 (L5)	
	CR	Data Rate [kbps]	CR	Data Rate [kbps]
Magnetometer	1	0.72	1	0.72
Coronagraph	1	24.7	16	24.7
Heliospheric Imager	-	-	2	14
Magnetograph	-	-	12	575.9
X-ray sensor	1	2	-	-
EUV Imager	-	-	8	125
Faraday Cup	1	0.16	1	2
SEP Monitor	1	0.075	-	-
System Performance	1	2	1	2
Raw data rate		29.66		744.32
Compressed data rate		29.66		76.88
	Factor		Factor	
Redundancy	1.01		1.01	
Block Coding	2.29		2.29	
Total Data Rate		68.50		177.58

Table 7.2: Link Budget for OB1 and OB2

Link Budget:	OB1 (L1)		OB2 (L5)	
	-	dB	-	dB
Gains:				
Transmitter power	60	17.78	75	18.75
Transmitter antenna	188.17	22.75	9754.97	39.89
Receiver antenna	$1.06 \cdot 10^6$	60.25	$5.44 \cdot 10^6$	67.35
Losses:				
Transmission [45]	0.9	-0.46	0.9	-0.46
Space loss	$3.54 \cdot 10^{-24}$	-234.51	$3.54 \cdot 10^{-28}$	-274.51
Atmospheric attenuation	0.79	-1	0.79	-1
Pointing loss	0.97	-0.12	0.97	-0.12
Data rate	68,499	48.36	177,584	52.49
System Noise N_0	$1.86 \cdot 10^{-21}$	-207.30	$1.86 \cdot 10^{-21}$	-207.30
E_b	$5.41 \cdot 10^{-19}$	-182.67	$6.95 \cdot 10^{-21}$	-201.58
E_b/N_0	290.33	24.63	3.73	5.72
E_b/N_0 required		2.7		2.7
Margin		21.93		3.02

Adding all the gains and subtracting the losses, the received signal has to meet a certain SNR. This is determined by the bit error rate, modulation type and the block error coding type. The modulation determines how the digital data is encoded and transmitted to Earth. Binary-phase shift keying is a type of modulation that places all of the power into the data, and thus achieves the best power efficiency theoretically possible. This modulation will be used for SWAN as it is relatively simple to implement and used on a lot of spacecraft [45]. Furthermore, when data is sent down, there is a chance that it is misread. When this happens, either the data can be re-sent, or block error coding can be used. One type, forward error correction coding, increases redundancy by adding extra bits to the data to minimise the chance that the whole data is corrupt, since even though there are more bits (and so more chance that a bit is corrupt), the data can still be read even when a bit is corrupt. This means that the data rate increases, but the required SNR decreases, such that it is beneficial. If both a Reed Solomon (255,223) (meaning that for every 255 bits transmitted, 223 bits are useful) and a Viterbi algorithm with a coding rate of $\frac{1}{2}$ (for every 2 bits transmitted, 1 is useful), the data rate increases by a factor of 2.287, but the SNR decreases from 8.5 to 2.7 dB (for a bit error rate of 10^{-4}). [46] Note that there should be a 3dB (factor of 2) margin between the actual SNR and the required SNR.

7.3. TT&C ARCHITECTURE

Once the data rate has been determined, the antenna diameter and the transmitter power can be tuned to meet the required SNR of 2.7dB + 3dB margin, however these parameter influence the SNR differently. If the data rate increases by a factor of x , then in order to still meet the required SNR (which would otherwise decrease by a factor x), the power would have to increase by a factor of x or the antenna diameter by a factor \sqrt{x} . Therefore it is more effective to increase the antenna diameter than the power, and so in combination with the transmitter power shown in Table 7.2, the antennas will be a 0.2m diameter horn antenna for OB1 and a 1.44m diameter parabolic dish antenna for OB2. Note that for uplink, the data rate is around 2 kbps for both spacecraft, as only telemetry has to be communicated, and so this link will also satisfy the required SNR. In addition, both spacecraft will feature 6dB low gain antennas for communication near Earth when the main antennas are not pointed at Earth and when only telemetry has to be sent down. For OB2 this is possible only up to 25 million km, then the parabolic antenna has to be used. Moreover, with the allocated power the link margin for OB1 is 21.93dB, which is more than enough to satisfy the required SNR, however for redundancy if the main antenna fails on OB1 the low gain antenna can take over and still satisfy this. OB2 does not have a secondary redundant antenna as it would require an additional parabolic antenna of same size, which is unfeasible, however for both spacecraft, backup redundant electronics and transmitters will be installed on the main antennas in case there is a failure, increasing the reliability of the TT&C system. Lastly, in case of a temporary blackout, the TT&C system is designed to accommodate double the data rate in order to ensure all data accumulated gets sent back down. For OB1, this is possible as the link margin is sufficient, and for OB2, the 70m diameter ground station antenna from the DSN can be used for a limited amount of time (as there is only one, and other spacecraft also require this antenna).

The type of horn antenna will be a cylindrical horn antenna, with a diameter of 0.2m and an optimal length of 0.376m which minimises reflections and maximum gain.[47] Assuming an aluminium horn antenna, its mass will be 0.835kg. The low gain antenna is simple a helical structure 0.3m in length and 0.1m in diameter, weighing about 0.377kg. The horn antenna on OB1 is placed on the side of the spacecraft, while the low gain antenna is placed on the back such that they both point towards Earth at L1. In the case of OB2, the parabolic antenna consists of a reflector dish and a feed (horn) antenna, mounted on an arm at the focus of the parabola. The antenna has a diameter is 1.44m and a total height of 0.66m. As the launcher can easily accommodate the launcher, the antenna will already be mounted on the side of the spacecraft at an angle of 30° to point towards Earth. The reflector will be made out of a sandwich metal-composite structure reinforced by a stiffening web to deal with launch loads and provide stiffness. Typical areal densities are around 5 kgm⁻², [48], and so the total mass of the antenna, transmitter and structure should not exceed 10kg⁵.

As mentioned above, the antenna on OB2 is to be mounted to the spacecraft at an angle of 30° when it is at L5. However to be able to transmit the 2 kbps telemetry with Earth during transfer as well (where beyond 25 million km the low gain antenna will be too weak, and so the parabolic antenna has to be used), it has to rotate to 50° from the side as the spacecraft itself will always be pointed to the Sun. To do this, one edge of the reflector will be hinged, and 2 actuators of length 0.845m when extended and 0.5m when retracted will hold up the other end. These actuators are located at a distance of 0.9m from the hinge, and will have pinned connections at both ends. Figure 7.2 shows its position when at L5. The 2 actuators are separated by 1.26m. This ensures that disturbances and variations in the orbit and the shift in position of L5 does not affect the link.

To ensure the hinge and actuators withstand launch loads, the forces in the hinge and actuators from axial, lateral and vibrational accelerations combined (from the launcher specifications) were found by taking the equilibrium of forces and moments, assuming that these accelerations act through the centre of gravity. Taking into account that the lateral loads can be both to the sides and in/out of the plane in Figure 7.2, all the load cases were examined and the highest tensile and compressive loads were analysed for yielding and buckling. The highest compressive loads in the actuators occurred with an axial acceleration of 8.5g (plus the 5.1g from vibrations), an in-plane lateral acceleration of 2g (plus 1.6g from vibrations) to the left in Figure 7.2 and an out of plane acceleration of 3g (plus 1.6g), resulting in a total force of 520N in compression. As expected, the buckling case was driving, and was calculated with Equation (7.2), where F is the force in the actuator, E is the E-modulus of the material (71.1 GPa for Al 7075), $K=1$ for pinned connections, and L being the length of the actuator. Rearranging for the moment of inertia I , it was found that the radius needed to be 4mm in order to not buckle. For the design, a radius of 5mm was chosen.

$$F = \frac{\pi^2 EI}{(KL)^2} \quad (7.2)$$

Lastly, radio tracking using the telecommunication system can be used to determine the distance and velocity that the spacecraft is relative to Earth throughout its lifetime, as this method is quite precise up to a few AU. To do this, observations of the spacecraft by two or more ground stations can be done to triangulate its position. This can be done simultaneously (however this is difficult and expensive as 2 ground stations are needed at the same time) or separately by combining multiple sets of measurements over time. Since the spacecraft remain in close proximity to the Lagrangian points and with the telemetry from the spacecraft, its position and orientation can be known relatively easily.

⁵<https://descanso.jpl.nasa.gov/DPSummary/Descanso3--Cassini2.pdf>

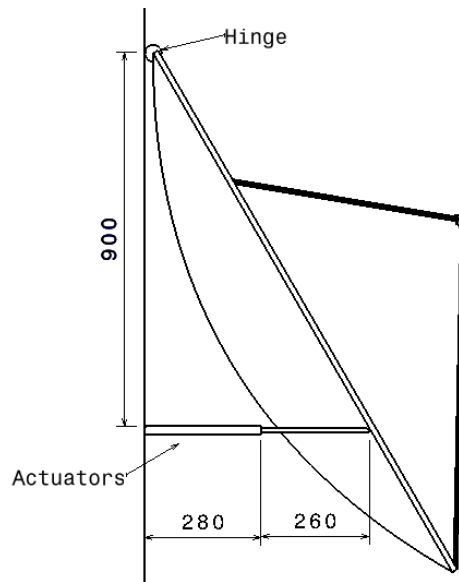


Figure 7.2: OB2 High gain antenna and its mountings

7.4. DATA HANDLING

In order to compress and encode data, handle telemetry from the ground and control the spacecraft mostly autonomously, a data handling system is needed that communicates between all the subsystems. As can be seen in Figure 7.3, the system is centralised, with the processor controlling all functions of the spacecraft. To overcome the problem of a single point failure and make the system redundant, 2 extra backup processors are added. The system then acts in parallel, which increases reliability as opposed to a series system where each sub-system has its own processor: if one sub-system's processor fails, the whole subsystem and hence the mission fails as well. Furthermore, in case of fatal error due to single event upsets for example, backup storage/ROM is also added that is routinely checked and updated, and in case necessary, new software can be sent from Earth. The total storage capacity will be set at 10GB, which is enough to store 2 weeks worth of data. The processor in question will be the radiation hardened, 2.1 MIPS at 200MHz RAD750 processor from BAE Systems Electronics ⁶, that can withstand a total dose of 1Mrad and is latchup immune. This processing power is more than enough, with an estimated MIPS required of 0.27 [45] from reference missions and empirical data. This is a standard processor for space applications, and many missions such as Solar Dynamics Observatory, STEREO and DSCOVR use this or its predecessor. In total, the CPU and motherboard will consume 10W of power and can operate between 218 and 343 K. ⁶. Communication between and within the subsystems can be seen in Chapter 14 with the software block diagram.

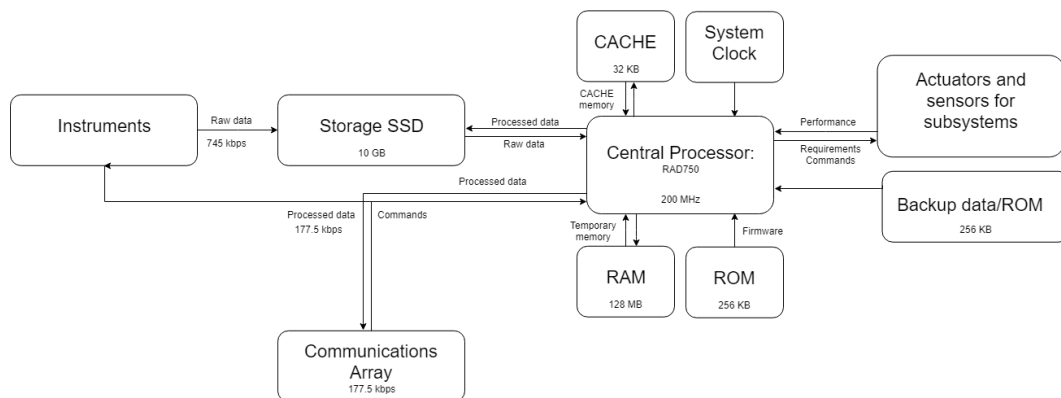


Figure 7.3: Data handling block diagram on board SWAN

7.5. RISK ANALYSIS

As with any system, there are always risks involved, and it is important to know what these risks are. Depending on the likelihood and impact of the risk, they might have to be mitigated to avoid them or decrease their effect. Below are some risks associated with the TT&C system that could occur during SWAN's lifetime. These mitigations will ensure that the risks are minimised or that the impact changes to marginal. The only element that is not redundant is the main parabolic antenna on OB2, as adding an extra antenna is not feasible given the limitations with space on OB2.:

⁶<https://www.baesystems.com/en/download-en/20161103152954/1434555668211.pdf>

Table 7.3: TT&C Risks. Likelihood: HU = highly unlikely, U = unlikely, SL = some likelihood, L = likely, HL = highly likely. Impact: M = marginal, S = some, H = high, C = catastrophic

Risk	Consequence	Likelihood	Impact	Mitigation
Solar weather event disrupts communication	Temporary disruption in communications to ground	HL	S	Data rate can be doubled if necessary to handle accumulated data
Main communication antenna failure	Permanent disruption and mission failure	U	C	Redundancy is added to OB1. For OB2, it is impractical
Antenna mounting failure	Decrease or loss of effectiveness	U	H	Rigorous testing of structure and actuators to withstand harsh conditions and launch loads
Communication antenna pointing is inaccurate	Decrease or loss of effectiveness and SNR	U	H	Actuators are present to control position of antenna to account for any inaccuracies in spacecraft or L5 position. For L1 this can be neglected
Signal to noise ratio is insufficient	Data is corrupt and incomplete	SL	S	A margin of 3dB is added to the required SNR
ITT does not give permission for frequency band use	TT&C system has to be redesigned	SL	M	None. A redesign with new antennas and weights might be needed
Data generation causes overflow in data handling	Data received is incomplete or lagging	SL	S	Processor and storage is designed to cope with loads far beyond that of SWAN
Processor failure due to radiation	Complete spacecraft failure	L	C	Radiation hardened processor (and 2 backups) is used
Fatal data corruption in internal storage or processor	Complete spacecraft failure	L	C	Backup storage and boot sequence is on board to automatically recover
BUS failure	Complete spacecraft failure	U	C	BUS is tested rigorously to ensure it functions properly

7.6. RELIABILITY, AVAILABILITY, MAINTAINABILITY, AND SAFETY CHARACTERISTICS

In order to ensure the spacecraft can still operate when a component fails, redundancy is added to increase reliability, however this often implies extra costs and mass, which may be more difficult than to ensure the system does not fail in the first place. There is limited redundancy for SWAN. If the main horn antenna on OB1 fails, the allocated power ensure that the low gain antenna can take over all the data. However if OB2's main parabolic antenna fails, there is no redundancy due to distance. If so, a second parabolic dish would have to be added, which is not practical due to space limitations, and so this part is mission critical. As with all systems, tests will be done before launch to ensure everything works. In case there is a temporary blackout, the data rate can be doubled (for a limited amount of time for OB2 with the 70m DSN antenna) to send all the accumulated data down and meet the 99% data availability requirement. For on board processing, the systems are radiation hardened so that they can operate in radiation intense environments, and in the event that the primary processor does fail, 2 additional processors are added as the system is centralised. All TT&C components are standard off the shelf products, such as the processor, motherboard, transmitter and antenna. They are readily available (although expensive) and no rare or hazardous material are used or either contained. As with all other subsystems, it is hard to maintain a spacecraft, however with redundancy and possible software or procedural updates such as with compression techniques or control systems, failure of the system can be averted.

7.7. REQUIREMENT COMPLIANCE

Now that the whole TT&C system has been designed, the requirements have to be checked whether they have been met or not. This can be seen in Table 7.4. Note that for the volume, cost and reliability, no concrete values can be found for the components.

Table 7.4: TT&C requirement compliance matrix.

Identifier	Requirement	Met?	Confirmation
General TTC-GEN-01	The TT&C system shall be able to handle a data rate from the instruments of 745 kbps	✓	Table 7.1

TTC-GEN-02a	The TT&C system shall be able to encode the digital measured data to be sent down	✓	Section 7.2
TTC-GEN-02b	The TT&C system shall be able to add redundancy to the data	✓	Section 7.2
TTC-GEN-03	The total mass of the TT&C system of OB2 shall not exceed 15 kg	✓	section 7.3
TTC-GEN-04	The total power used by the TT&C system of either spacecraft shall not exceed 100 W	✓	Table 7.2
TTC-GEN-05	The total volume of the TT&C system shall not exceed <td>m3	TBD	-
TTC-GEN-06	The total cost of the TT&C system shall not exceed <td>euro	TBD	-
TTC-GEN-07	The reliability of the TT&C system shall be higher than 99 % [49]	TBD	-
TTC-GEN-10	At least 99% of all measured data shall be sent down to Earth	✓	Section 7.3
TTC-GEN-11	The signal to noise ratio of the signal transmitted shall be at least 2.7dB	✓	Table 7.2
TTC-GEN-13a	The margin in the link budget shall be at least 3 dB	✓	Table 7.2
OB1			
TTC-ANT-OB2-01	The gain of the main antenna of OB1 shall be at least 1.6dB	✓	Table 7.2
TTC-ANT-OB2-02	The pointing error main antenna of OB1 shall be at most 70 degrees during safe mode operation	✓	Section 7.2
TTC-ANT-OB2-03	The pointing error of the main antenna of OB1 shall be at most 12 degrees during operational mode	✓	Section 7.2
TTC-ANT-OB2-04	The low gain antenna of OB1 shall be used until the spacecraft reaches L1	✓	Section 7.3
TTC-ANT-OB2-05	The main antenna of OB1 shall be deployed when the spacecraft reaches L1	✓	Section 7.3
TTC-ANT-OB2-06	The main antenna of OB1 shall have a maximum diameter of 0.5 m	✓	Table 7.2
TTC-ANT-OB2-07	The processor on OB1 shall be able to withstand the radiation environment at L1	✓	Section 7.4
OB2			
TTC-ANT-OB2-01	The gain of the main antenna of OB2 shall be at least 39.87dB	✓	Table 7.2
TTC-ANT-OB2-02	The pointing error main antenna of OB2 shall be at most 90 arcminutes during safe mode operation	✓	Section 7.2
TTC-ANT-OB2-02a	The pointing error of the main antenna of OB2 shall be at most 30 arcminutes during operational mode	✓	Section 7.2
TTC-ANT-OB2-04a	The main antenna of OB2 shall be deployed when the spacecraft is 25 million km from Earth	✓	Section 7.3
TTC-ANT-OB2-04b	The low gain antenna of OB2 shall be used until the spacecraft is 25 million km from Earth	✓	Section 7.3
TTC-ANT-OB2-05	The main antenna of OB2 shall have a maximum diameter of 2 m	✓	Table 7.2
TTC-ANT-OB2-06	The processor on OB2 shall be able to withstand the radiation environment at L1	✓	Section 7.4

7.8. CONCLUSION AND RECOMMENDATIONS

Without the TT&C system, SWAN would not be able to communicate with Earth and could not perform its mission. Thus, to accommodate the raw data rate of OB1 and OB2 of 30 and 745 kbps respectively, data compression is applied at L5 so that the data rate of OB2 decreases to 77 kbps. Using BPSK with Reed Solomon (255,223) and Viterbi R=0.5, the antenna of OB1 is a 0.2m horn antenna and at OB2 a 1.44m deployable parabolic antenna to satisfy the required SNR of 2.7dB and transmit the data to NASA's Deep Space Network and ESA's ESTRACK. Both spacecraft feature low gain antennas for redundancy or communication near Earth. Furthermore, data handling on board SWAN is done using a redundant centralised processor using the RAD750 radiation hardened processor, which compresses the scientific data, handles telemetry from the ground and between the subsystems and relays commands.

A recommendation for the data handling is to assess the onboard processing of the images of the Stokes parameters that are obtained by the magnetograph. The images shown in Figure 7.1 are not directly obtained from the magnetograph; processing is required. It is preferred to conduct this processing onboard as it would otherwise require transmission of the three Stokes parameter images, thus raising the required data rate. The computational power requirements for this processing is still to be assessed. This assessment is important as it will determine whether this type of data handling is feasible. Furthermore, due to the processing of the magnetograms and the subsequent compression applied to these images, one must analyse the data loss due to the compression. As a precaution, the bits per pixel have been increased from 8 to 12. This will reduce the margin of error since each pixel has a resolution of 2 nT.

8

ASTRODYNAMIC CHARACTERISTICS

This chapter will present the launch sequence and transfer characteristics for both OB1 to L1 and OB2 to L5, from launch to end of life.

8.1. METHOD

To be able to analyse the astrodynamic characteristics of the mission, a programme is needed that can calculate the propagation of the spacecraft over time. This programme is explained in Section 8.1.1. The coordinate systems used within this project and the rest of the chapter are explained in Section 8.1.2.

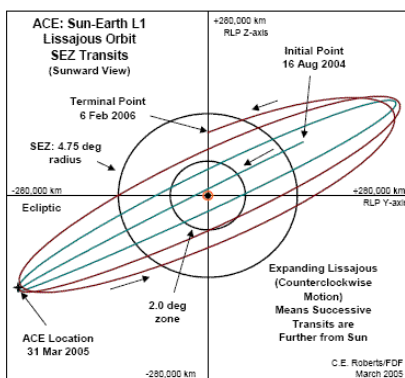
8.1.1. GENERAL MISSION ANALYSIS TOOL

The astrodynamic characteristics of both spacecraft and the launch sequence are determined using the General Mission Analysis Tool (GMAT) developed by NASA.¹ GMAT is an open-source spacecraft trajectory and mission design software. From the launch onwards, every aspect of the mission can be programmed in GMAT, including engine burns and gravity perturbations.

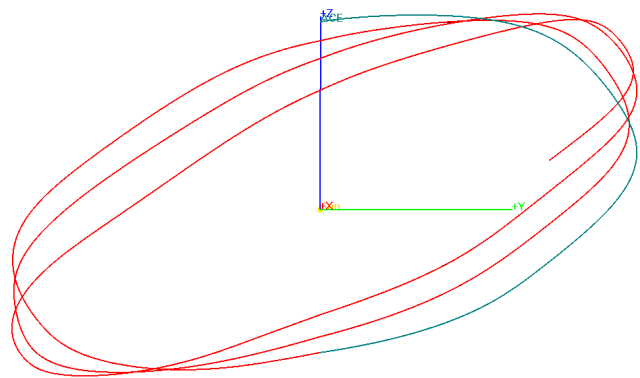
PROGRAMME VERIFICATION AND VALIDATION

NASA has already performed all necessary verification and validation procedures for GMAT. These have been documented in S. Hughes et al. (2013).[50] They have performed system tests, component tests, bug fixing, performance improvements, documentation improvements, and maintenance preparations. By running these tests over the course of multiple months, they are confident the programme performs as it should.[50]

An additional verification that is also provided is example programmes to be run in GMAT. One of these programmes simulates ACE's trajectory around L1.¹ The result can be seen in Figure 8.1b. When comparing to the actual trajectory flown by ACE in Figure 8.1a. The results yielded are similar expanding Lissajous-trajectories, and therefore GMAT is considered to be validated.



(a) ACE's Actual Trajectory²



(b) ACE's Trajectory From GMAT

Figure 8.1: Validation of GMAT using ACE's Trajectory

8.1.2. COORDINATE SYSTEMS

A number of coordinate systems have been used in the modelling of the trajectories. In this section, an explanation of each coordinate system is given. All used coordinate systems are right-handed.

¹<https://software.nasa.gov/software/GSC-17177-1>

²<http://www.srl.caltech.edu/ACE/images/lissajous.gif>

EARTH-EQUATORIAL FRAME

This frame is fixed to the centre of Earth. The X-axis points in the direction of the vernal equinox. This is the direction of the Sun as seen from Earth at the moment that night and day are exactly equal in length in the spring season. This direction slightly moves over time due to the precession of Earth's rotational axis, which is the reason the conditions of the year 2000 are used.[51, 52] The Z-axis points along the rotational axis of the Earth in the direction of the North pole. The Y-axis completes the right-handed coordinate system, and thus crosses the equator. The XY-plane is therefore the same as the equatorial plane of Earth. Note that this frame does not rotate along with Earth.

EARTH-ECLIPTIC FRAME

This frame is also fixed to the centre of Earth. The X-axis again points in the direction of the vernal equinox in 2000, similar to the Earth-Equatorial Frame. The Y-axis points in the direction of the summer solstice of the northern hemisphere. This is the direction of the Sun as seen from Earth at the moment that the Sun is exactly in zenith on the Tropic of Cancer. As this direction also slightly moves over time due to the Earth's precession, again the conditions of the year 2000 are used.[51, 52] The Z-axis completes the right-handed coordinate system. The XY-plane of this frame is the ecliptic plane in which the Sun lies, and is at an angle of 23.45° with the equatorial plane. Note that this frame does not rotate along with Earth.

SUN-ECLIPTIC FRAME

The Sun-Ecliptic Frame has the exact same axis directions as the Earth-Ecliptic Frame. The only difference is the centre of this frame is in the centre of the Sun instead of in the centre of Earth. This frame can also be seen as a Sun-fixed frame, as in this frame the motion of the planets is near-circular.

SUN-COROTATING FRAME

This frame is also centred at the Sun like the Sun-ecliptic frame. The X-axis in this frame will always point to Earth, which causes the frame to rotate along with Earth around the Sun. This also means the X-axis lies in the ecliptic plane, which is the XY-plane of the Earth-Ecliptic Frame. The Z-axis coincides with the Z-axis from the Sun-Ecliptic frame. The Y-axis completes the right-handed system, and will also lie in the ecliptic plane.

L1-COROTATING FRAME

The L1-Corotating frame behaves similarly to the Sun-Corotating frame. It is centred at the Sun-Earth Lagrange point 1. The X-axis points will always point towards Earth. The Z-axis is parallel and in the same direction as the Z-axis of the Sun-Corotating frame. The Y-axis once again completes the right-handed system, and will lie in the ecliptic plane.

L5-COROTATING FRAME

The L5-Corotating frame is centred at the Sun-Earth Lagrange point 5. The frame again behaves similarly to the Sun-Corotating frame, as it always has its X-axis pointed at Earth. The Z-axis again is parallel and in the same direction as the Z-axis of the Sun-Corotating frame. The Y-axis completes the right-handed system, which causes it to lie in the ecliptic plane.

8.2. LAUNCH

In this section, the launch sequence is elaborated upon. First, the launch requirements will be revisited in Section 8.2.1. Then, the different launch pad options will be discussed in Section 8.2.2. Subsequently, the launch parameters are shown in Section 8.2.3. Finally, the launch sequence is shown in Section 8.2.4.

8.2.1. LAUNCH REQUIREMENTS

In the Baseline and Midterm reports, a number of requirements for the launch sequence have been set.[2, 3] These requirements are listed below. The arrival epoch requirement from Chapter 3 is also included in this list.

- Both spacecraft shall be launched in a single rocket.[3]
- The launcher shall be a Falcon 9 Block 5 rocket, costing \$62 million.[3]
- OB1 shall insert into the manifold from Geostationary Orbit (GEO) with a -2.3° inclination.[3, 53]
- OB1 shall be directly behind Earth as seen from L1 at the moment of insertion into the manifold.[3, 53]

- OB2 shall depart in the ecliptic plane.[3, 54]
- OB2 shall have a transfer time of less than 1.5 years.[3, 54]
- Both spacecraft are ready for launch in July 2023.[2]
- Both spacecraft shall have inserted into orbit before 2025.

8.2.2. LAUNCH PAD

The spacecraft will launch with the Falcon 9 BLock 5 rocket, which is operated by SpaceX. Therefore, one of the SpaceX launch pads will have to be used:³

- Cape Canaveral Launch Complex 40
- Vandenberg Air Force Base Space Launch Complex 4 East
- Kennedy Space Centre Launch Complex 39A
- SpaceX South Texas Launch Site.

The South Texas launch site is not yet operational,⁴ and its capabilities are not yet known. For Cape Canaveral it is known that launches into parking orbits with an inclination in the range of 28°-58° can be achieved.[55] For the Vandenberg Air Force Base, parking orbits with an inclination of 63°-107° can be achieved.[55] The Kennedy Space Centre is at 28.45° latitude, which is also the lowest inclination it can achieve without inclination change maneuvers.⁵ As the inclination necessary for the spacecraft to L5 is in the ecliptic plane, or 23.45° inclined with respect to the Earth-Equatorial frame, Cape Canaveral is the best site to launch from, as this will require the lowest inclination change.

8.2.3. LAUNCH PARAMETERS

An orbit is defined by 7 parameters: the semi-major axis a , the inclination i , the eccentricity e , the right ascension of the ascending node Ω , the argument of perigee ω , the true anomaly ν , and the epoch t . Ω is defined as the angle between the X-axis of the Earth-Equatorial frame and the point where the orbit crosses the equatorial plane from the southern hemisphere into the northern hemisphere (called the ascending node). ω is defined as the angle between the ascending node and perigee, while ν is the angle between perigee and the actual location of the spacecraft at time t . Ω , ω , and ν are all positive counter-clockwise.

An eighth parameter is required to fully determine and constrain the launch sequence. This is the departure angle of OB2 θ . This angle is defined as counterclockwise positive from the negative Y-axis of the Earth-Ecliptic frame, and represents the angle at which the burn to escape and towards L5 is initiated. At this point, the velocity should be as high as possible to limit the escape burn, which occurs at perigee.

The launcher itself is also analysed. It consists of two stages, where the second stage is restartable multiple times.⁶ It can carry two spacecraft with a separation fairing in between. The specifications of both stages are listed in Table 8.1.

Table 8.1: Falcon 9 Launcher Specifications

Stage	Thrust [kN]	Specific Impulse [s]	Burn Time [s]	Dry Mass [kg]	Fuel Mass [kg]
First	7,607 ⁶	282 ⁷	162 ⁶	22,200[56]	108,651.9
Second	934 ⁶	348 ⁶	397 ⁶	4,000[56]	398,574.5

The fuel mass in Table 8.1 is calculated using Equation (8.1).⁸

$$m_{\text{fuel}} = \dot{m} t_b = \frac{t_b F_T}{I_{sp} g_0} \quad (8.1)$$

In this equation, m_{fuel} is the total fuel mass, \dot{m} is the mass flow, t_b is the burn time, F_T is the thrust, I_{sp} is the specific impulse, and g_0 is the gravitational acceleration at sea-level on Earth. As all these values are known from Table 8.1, the fuel mass can be calculated.

³<http://www.spacex.com/about/capabilities>

⁴<https://www.theguardian.com/us-news/2018/jan/28/spacex-texas-boca-chica-brownsville-border-wall>

⁵<https://www.allmanpc.com/2012/07/optimum-space-station-orbit-inclination-for-space-shuttle-support-missions/>

⁶www.spacex.com/falcon9

⁷<https://web.archive.org/web/20130501002858/http://www.spacex.com/falcon9.php>

⁸<https://www.grc.nasa.gov/www/k-12/airplane/specimp.html>

8.2.4. LAUNCH SEQUENCE

Using the requirements from Section 8.2.1 and the constraints from Section 8.2.2 and Section 8.2.3, the launch sequence can be devised. The chosen launch sequence is listed below.

1. Launch from Cape Canaveral in a 28° inclined 185km parking orbit
2. Once the ecliptic plane is crossed, perform a burn to raise apogee to GEO
3. At apogee, simultaneously change the inclination to the ecliptic plane and raise perigee to 200km
4. Release OB2 on the way back to perigee
5. At perigee, OB2 will burn itself to escape velocity, while the launcher, with OB1 still attached, will continue to apogee
6. At the second reach of apogee, perform a burn to reach a circular GEO
7. Change inclination to -2.3° with respect to the ecliptic, such that the lowest inclination is reached once OB1 and L1 are exactly on opposite sides of Earth
8. At the lowest inclination, perform a burn to insert into the manifold
9. Release OB1 in the manifold

This launch sequence, along with the required ΔV and the fuel mass per stage is shown in Table 8.2. Also shown are the orbit parameters at that stage of launch, and the throttle setting during the burn. The throttle capabilities allow the second stage engine to throttle back to 38.5%. [57] As the structure in Chapter 13 will be designed to withstand 8g of acceleration, the throttle setting is chosen such that 8g is reached exactly at the end of the burn.

Table 8.2: Launch Sequence Parameters

Burn	Launcher mass [kg]	ΔV given [ms^{-1}]	First stage fuel mass [kg]	Second stage fuel mass [kg]	Perigee [km]	Apogee [km]	Inclination [°]	Throttle [%]
Before launch	535116.0	0	398575	108652	0	0	28	N.A.
After first stage burn	136541.4	3777.24	0	108652	0	0	28	100
After first stage jettison	114341.4	0	0	108652	0	0	28	N.A.
After insertion into parking orbit	35248.9	4015.93	0	29559	6556	6556	28	100
After apogee raise	17117.2	2465.16	0	11428	6556	42157	28	100
After perigee raise + inclination change	16485.4	128.36	0	10796	6571	42157	23.45	100
Release OB2	15220.0	0	0	10796	6571	42157	23.45	N.A.
After perigee raise	9870.1	1478.03	0	5446	42157	42157	23.45	82.9
After inclination change	9519.6	123.43	0	5095	42157	42157	21.15	79.9
After manifold insertion	6213.4	1456.00	0	1789	N.A	N.A	N.A	52.1
Release OB1	5789.3	0	0	1789	N.A	N.A	N.A	N.A

It is important to note that the launch sequence in which OB2 is brought to escape by the launcher was also looked into. While it is theoretically possible in the two-body problem to enter a highly elliptical orbit when decelerating from the escape orbit, it was shown using GMAT that these highly elliptical orbits are unstable in the multi-body problem. OB2 will therefore require more propellant to be able to propel itself into escape orbit.

It turns out the launch parameters are all driven by the departure angle of OB2. The relations for the initial values are shown in Equation (8.2) to Equation (8.7). The values of θ , i , Ω , ω , and ν are all in degrees.

$$a = 6556 \text{ km} \quad (8.2)$$

$$e = 1e - 16 \quad (8.3)$$

$$i = 28 \quad (8.4)$$

$$\Omega = \theta - 180 - \frac{180}{\pi} \cos^{-1} \left(\frac{-23.45}{28} \cos \left(\theta \cdot \frac{\pi}{180} \right) \right) \quad (8.5)$$

$$\omega = 90 + \frac{180}{\pi} \cos^{-1} \left(\frac{-23.45}{28} \cos \left(\theta \cdot \frac{\pi}{180} \right) \right) \quad (8.6)$$

$$\nu = -\frac{180}{\pi} \cos^{-1} \left(\frac{-23.45}{28} \cos \left(\theta \cdot \frac{\pi}{180} \right) \right) \quad (8.7)$$

The launch date was chosen to be 29 July 2023 in correspondence with the Post-DSE Gantt chart in Section 16.4. The launch epoch is also dependent on θ , and is expressed in the modified Julian calendar. In this date format, 30155 represents 29 July 2023, 12:00:00.000, while 30156 represents 30 July 2023, 12:00:00.000.[58] This results in Equation (8.8).

$$t = 30155.1215278 + \frac{\theta - 180 - \frac{180}{\pi} \cos^{-1} \left(\frac{-23.45}{28} \cos \left(\theta \cdot \frac{\pi}{180} \right) \right)}{360} \quad (8.8)$$

As all parameters are driven by θ , the final departure parameters can only be determined once the trajectory to L5 has been determined. This is done in Section 8.3, but the resulting launch sequence already is shown in Figure 8.2, Figure 8.4, and Figure 8.3. In these figures, the green line represents the joint trajectory of OB1 and OB2 together with the launcher. The blue line represents the escape trajectory of OB2, while the red line represents the trajectory of OB1 and the launcher after OB2 has separated. In Figure 8.2, the entire launch sequence can be seen in the Earth-Ecliptic frame.

The inclination changes that are performed in steps 3 and 7 can be seen in Figure 8.4. It can be seen that the insertion into the manifold by OB1 indeed occurs at the lowest inclination in the orbit. It can also be seen that the manifold insertion by OB1 is significantly out of the ecliptic plane.

The circular orbits, geo-transfer orbit (GTO) and escape trajectories from above the ecliptic plane are shown in Figure 8.3. The trajectories of the two GTOs do not coincide due to the inclination change that has occurred between them. It is to be noted that the orientation of Earth is shown at the end epoch, and not at the launch epoch.

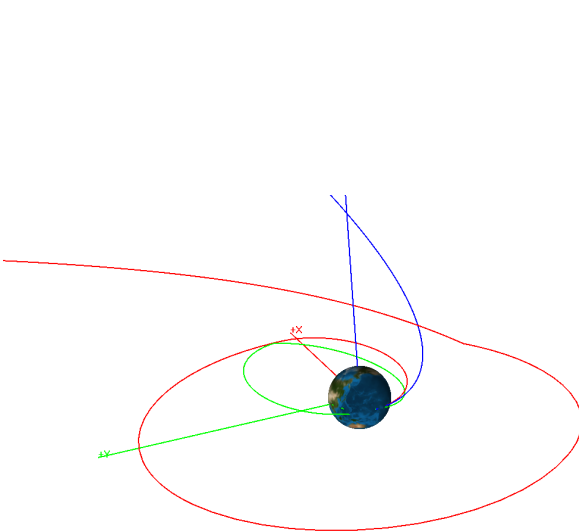


Figure 8.2: Full Launch Sequence in Earth-Ecliptic Frame

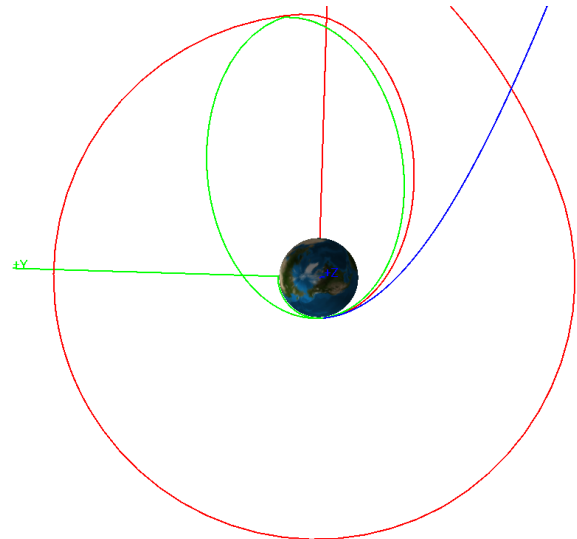


Figure 8.3: Launch Sequence Top View in Earth-Ecliptic Frame

8.3. L5

In this section, the entire astrodynamical life of OB2 after it has separated from the launcher is described. First, the transfer and insertion will be shown in Section 8.3.1. Then, the orbit will be described in Section 8.3.2. The end-of-life manoeuvre will be shown in Section 8.3.3, after which the sensitivity of the orbit will be analysed in Section 8.3.4.

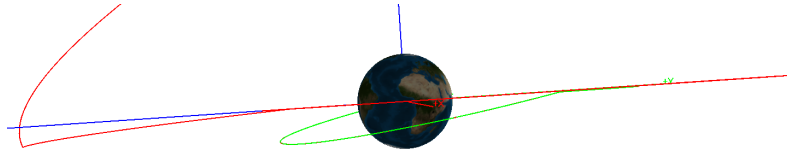


Figure 8.4: Launch Sequence Inclination Changes in Earth-Ecliptic Frame

8.3.1. TRANSFER AND INSERTION

The transfer to L5 is governed by two parameters: the departure angle θ , and the time of flight. The requirement for the transfer time is that OB2 has to arrive less than 1.5 years after departure from Earth. In the circular-restricted three-body problem transfer times of around 420 days are possible.[54] However, to properly model the transfer to L5, the eccentricity of Earth's orbit will be taken into account, along with the influences of Mercury, Venus, Mars, Jupiter, Saturn, and the Moon. Initially, the ΔV applied at Earth to go to the escape orbit was also varied, but it was fixed to 949 ms^{-1} since this yields the best results.

The transfer time and departure angle are determined by the insertion point into the Lagrange point orbit. The insertion point and the insertion velocities were varied until a stable orbit was reached. The insertion location and velocity are shown in Table 8.3, along with the arrival velocity. All values are given in the L5-Corotating Frame.

Table 8.3: Insertion Location and Velocity in the L5-Corotating Frame

Parameter	Arrival Value	Insertion Value
$V_x [\text{ms}^{-1}]$	804.59	-2.200
$V_y [\text{ms}^{-1}]$	-1,488.7	-2.000
$V_z [\text{ms}^{-1}]$	2.8457	0.02375
$X [\text{km}]$	20,896	20,896
$Y [\text{km}]$	819.18	819.18
$Z [\text{km}]$	-1,449.3	-1,449.3

The values in Table 8.3 determine the insertion velocity increment ΔV_{ins} , the departure angle, and the transfer time, and with these values also the launch parameters from Section 8.2.3. These values are shown in Table 8.4.

Table 8.4: Launch and L5 Transfer Parameters

Parameter	Value	Unit
ΔV_{ins}	1691	$[\text{ms}^{-1}]$
Transfer Time	406.788	[days]
θ	282.27	[°]
Ω	2.216	[°]
ω	190.05	[°]
ν	-100.05	[°]
t	29 July 2023	15:03:52
Arrival time	8 September 2024	20:36:03

This insertion burn takes 35m54s to complete, and requires a total impulse of 1.509 MNs, which will be important in Chapter 9. The transfer can be seen in Figure 8.5 in the Sun-Fixed frame, and in Figure 8.6 in the Sun-Corotating frame. The out of plane movement of the transfer is at most 22,000km. The transfer is at it's closest point 1.006AU from the Sun, and at it's furthest point 1.212AU. In Figure 8.6 it can be observed that both the Earth and L5 slightly move. This is the effect of the eccentricity of Earth's orbit.

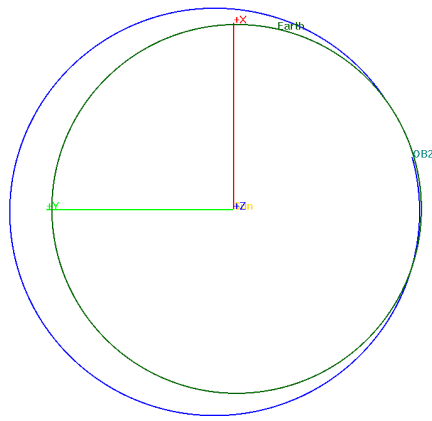


Figure 8.5: Transfer to L5 in the Sun-Fixed frame

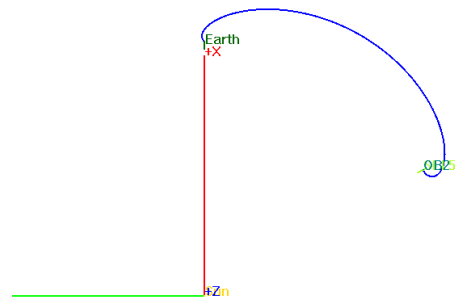


Figure 8.6: Transfer to L5 in the Sun-Corotating frame

8.3.2. ORBIT AROUND L5

Once the spacecraft has inserted into orbit around L5, it will have to stay there for 5 years. As it turns out, if the insertion velocities from Table 8.3 are used, the orbit around L5 is stable, even if perturbations from Mercury, Venus, Mars, Jupiter, Saturn, and the eccentricity of Earth's orbit are taken into account. The orbit over the course of 5 years can be seen in Figure 8.7.

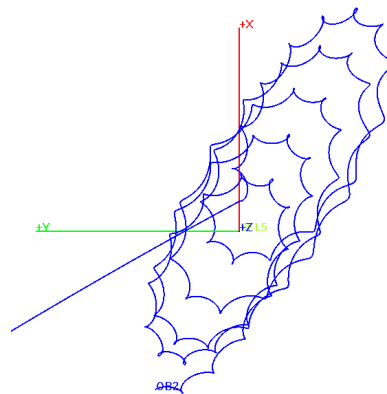


Figure 8.7: Orbit around L5 over 5 Years in the L5-Corotating Frame

Even though orbits around L5 are smooth orbits in literature, it can be observed that this orbit is far from smooth.[54, 59] This can be attributed to the perturbations that were taken into account. The drift that can be observed over time can also be attributed to these perturbations. This drift can also be seen in Figure 8.8, which represents the location of the spacecraft over the course of 5 years. It can be seen that the orbital period is about 1 year. The perturbations cause a higher frequency oscillation in all 3 directions. The maximum and minimum distances which are attained during this orbit are shown in Table 8.5.

Table 8.5: Maximum and Minimum Orbit Distance to L5 in the L5-Corotating Frame

Direction	Maximum Distance [km]	Minimum Distance [km]
X	157,374	-117,784
Y	67,929	-109,144
Z	10,474	-10,480

8.3.3. END OF LIFE MANOEUVRE

Once the 5 years are over, OB2 will have to leave L5, according to ESA's CleanSpace initiative.⁹ To accomplish this, a burn will be performed that will push OB2 out of L5. This manoeuvre can be seen in Figure 8.9 over the course of 15 years. As can be seen, OB2 very slowly drifts towards Earth. This manoeuvre requires a burn of 32 ms^{-1} . This burn has been propagated for over 100 years, and it never gets within 550,000 km from Earth or L5.

⁹https://www.esa.int/Our_Activities/Space_Engineering_Technology/Clean_Space

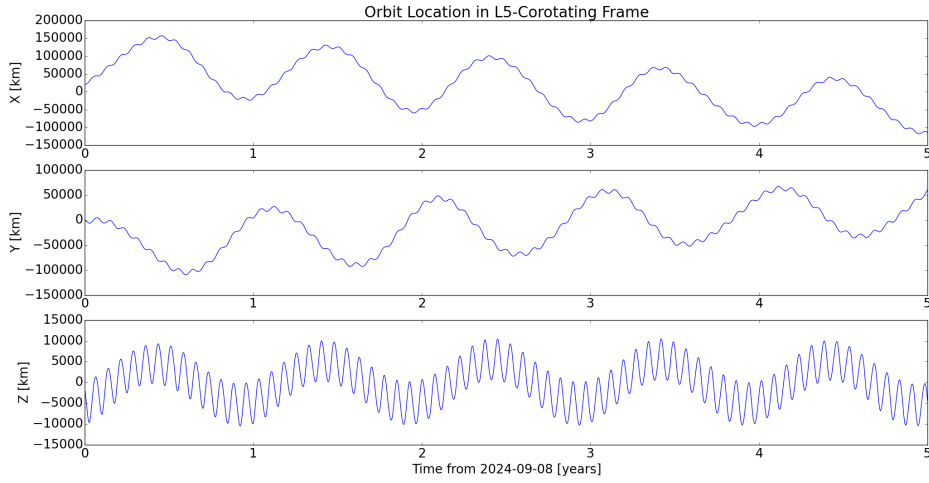


Figure 8.8: Location of Orbit around L5 over Time in L5-Corotating Frame

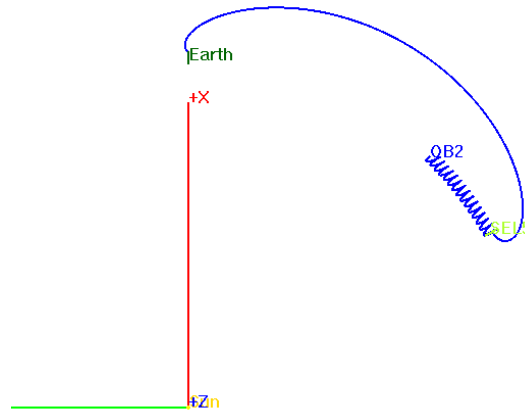


Figure 8.9: End of Life Manoeuvre for OB2 in Sun-Corotating Frame

8.3.4. ORBIT SENSITIVITY ANALYSIS

To test the sensitivity of the orbit around L5, the GMAT model has been run with an insertion velocity error of 5% in X, Y, and Z-direction in the L5-Corotating frame. These cases were tested with the maximum and minimum distances in X, Y, and Z as seen in Table 8.5. The result can be seen in Table 8.6. As can be observed, even in the worst case scenario, the distance to L5 is at most 176,393 km. This means the drift due to a velocity error is not strong enough to push OB2 into an unstable orbit. Therefore no correction burns will be necessary when an insertion velocity error of 5% is made.

Table 8.6: Insertion Velocity Error Analysis in the L5-Corotating Frame

Case	min(X) [km]	max(X) [km]	min(Y) [km]	max(Y) [km]	min(Z) [km]	max(Z) [km]
Nominal	-117,784	157,374	-109,144	67,929	-10,480	10,474
1.05V _{X_i}	-78,847	160,540	-110,383	50,549	-10,480	10,474
0.95V _{X_i}	-156,716	154,219	-107,910	85,315	-10,480	10,474
1.05V _{Y_i}	-137,465	153,732	-107,164	76,542	-10,480	10,475
0.95V _{Y_i}	-98,103	161,019	-111,125	59,317	-10,479	10,474
1.05V _{Z_i}	-117,785	157,374	-109,144	67,929	-10,482	10,477
0.95V _{Z_i}	-117,784	157,374	-109,144	67,928	-10,476	10,471
0.95V _{X_i} , 1.05V _{Y_i} , 1.05V _{Z_i}	-176,393	150,584	-105,932	93,933	-10,483	10,478

The sensitivity of the timing of the burn used to escape from Earth was also analysed. To achieve this, the burn was simulated to start 1 second late. It was shown that if the insertion speeds are changed slightly, OB2 will still enter a stable orbit around L5, albeit a larger and shifted one compared to the nominal orbit in Figure 8.7. The new parameters are shown in Table 8.7.

Table 8.7: Escape Burn Delay Sensitivity. Velocities in $[\text{ms}^{-1}]$, Positions in $[\text{km}]$ in the L5-Corotating Frame

Case	V_{X_I}	V_{Y_I}	V_{Z_I}	min(X)	max(X)	min(Y)	max(Y)	min(Z)	max(Z)
Nominal	-2.20	-2.00	0.02375	-117,784	157,374	-109,144	67,929	-10,480	10,474
1s delayed	-4.00	7.00	0.02375	-108,458	266,959	-181,083	78,483	-10,394	10,386

8.4. L1

In this section, the lifetime of OB1 in terms of its astrodynamics characteristics after it has separated from the launcher are described. The launcher will separate from OB1 right after it has inserted into the manifold that will transfer it to L1. First, the transfer and insertion manoeuvre will be described in Section 8.4.1. Then, the orbit around L1 will be described in Section 8.4.2. The End of Life manoeuvre will be shown in Section 8.4.3, after which the sensitivity of the orbit is analysed in Section 8.4.4.

8.4.1. TRANSFER AND INSERTION

For the transfer to L1 a manifold is used, which is a low ΔV path through space.[53] According to literature, the transfer should take 122.9 days and require an insertion burn of $1,456 \text{ m}^{-1}$. [53] It is also known that the insertion point into the manifold lies exactly at the opposite location of Earth as L1 is. Using this information, the out-of-plane burn angle for the launcher and the insertion burn magnitude into orbit can be determined. The burn direction to insert into orbit is fixed to the velocity direction to limit the amount of variables. The variables defining the transfer and insertion are shown in Table 8.8.

Table 8.8: L1 Transfer Parameters

Variable	Value	Unit
Launcher burn angle	42.649	$[\text{^\circ}]$
Transfer time	122.9	$[\text{days}]$
ΔV_{ins}	-62.4	$[\text{ms}^{-1}]$
Arrival time	1 December 2023 00:39:40	

With these values, the transfer can be determined. The entire transfer is shown in Figure 8.10 in the XY-plane, in Figure 8.11 in the XZ-plane, and in Figure 8.12 in the YZ-plane, all in the L1-Corotating frame. When comparing this transfer to the transfers obtained in [53], it can be seen that these almost exactly match. The amplitude of the motion in Y-direction is 600,000 km, and the amplitude in Z-direction is 90,000 km.

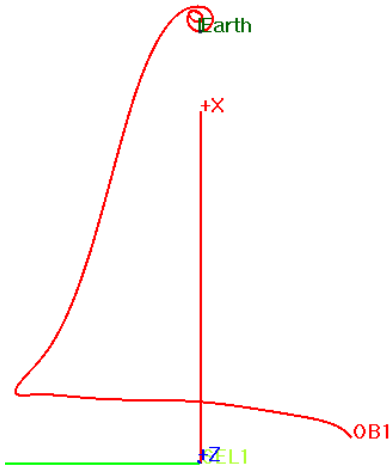


Figure 8.10: Transfer to L1 in the XY-Plane of L1-Corotating Frame



Figure 8.11: Transfer to L1 in the XZ-Plane of L1-Corotating Frame

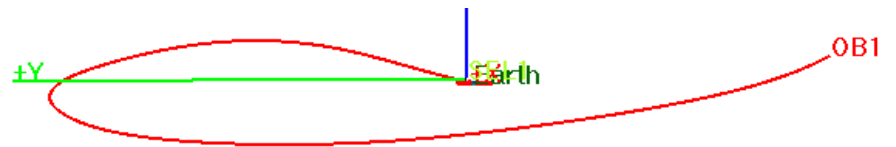


Figure 8.12: Transfer to L1 in the YZ-Plane of L1-Corotating Frame

8.4.2. ORBIT AROUND L1

The orbit around L1 is unstable. It was chosen that a correction burn will be done every time OB1 has 0 velocity in Y-direction and negative velocity in X-direction in the L1-Corotating frame. These burns are shown in Table 8.9. It is important to note that both spacecraft will have to operate simultaneously for 5 years. This means the 5 years for OB1 will only start once OB2 has arrived (8 September 2024), and OB1 will thus orbit L1 for almost 6 years.

Table 8.9: Correction Burns for L1

Date	Time [UTC]	ΔV [ms^{-1}]	Date	Time [UTC]	ΔV [ms^{-1}]
22 May 2024	07:39:59	-3.52	29 April 2027	21:54:21	11.45
16 November 2024	09:44:24	-7.34	29 October 2027	05:23:48	2.2
9 May 2025	10:34:11	7.8	20 April 2028	05:31:26	9.48
5 November 2025	13:25:19	24.3	18 October 2028	21:38:09	3.45
3 May 2026	00:20:35	11.2	11 April 2029	06:11:34	7.1
1 November 2026	12:26:38	29.65			

This means that 117.5 ms^{-1} of ΔV will have to be taken on board for orbit maintenance. The orbit is shown in Figure 8.13 in the XY-plane, and Figure 8.15 in the XZ-plane, both in the L1-Corotating frame. The orbit in the YZ-plane is also shown in Figure 8.14, combined with the Solar Exclusion Zone (SEZ). The SEZ was preliminarily determined to be a circle of 93,500 km around the Sun, in which the solar radiation creates higher noise.[3] As can be seen, the spacecraft passes through the lower end of the SEZ 4 times during it's lifetime. ACE has performed similar manoeuvres multiple times during it's lifetime, and has never lost any data.¹⁰ It is therefore expected that this will not cause any problems. However, a detailed analysis of the signal-to-noise ratio at different angles with respect to the Sun has to be performed to determine the actual size of the SEZ. Next to this, the start of the end-of-life de-orbiting manoeuvre can be seen in all three figures. The parameters of the orbit are given in Table 8.10.

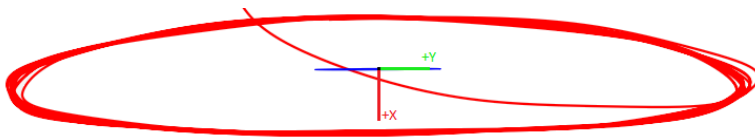


Figure 8.13: Orbit around L1 in the XY-plane in the L1-Corotating Frame

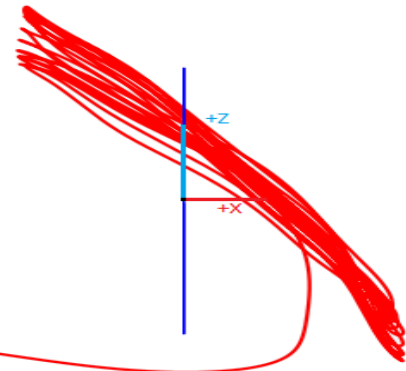


Figure 8.15: Orbit around L1 in the XZ-plane in the L1-Corotating Frame

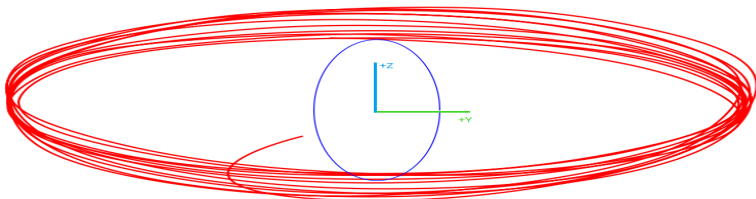


Figure 8.14: Orbit around L1 in the YZ-plane in the L1-Corotating Frame

Table 8.10: Maximum and Minimum Orbit Distance to L1 in the L1-Corotating Frame

Direction	Maximum Distance [km]	Minimum Distance [km]
X	198,906	-150,940
Y	562,139	-548,834
Z	137,099	-112,220

8.4.3. END OF LIFE MANOEUVRE

End of Life in L1 is relatively easy, as the point is unstable. Both shooting OB1 towards Earth and towards a heliocentric orbit were analysed. It was shown using GMAT that impacting the spacecraft on Earth would result in a near vertical descent at 11 kms^{-1} . This would result in the spacecraft clearing the entire atmosphere in 10 seconds, which is not enough to ensure it would burn up. The kinetic energy of OB1 when impacting Earth is equal to 6.2 tonnes of TNT. This will do serious damage, should it hit in a city, which is the reason it was decided to shoot OB1 towards a heliocentric orbit. This is shown in Figure 8.16. This orbit has been propagated for over 100 years. In this time frame, the closest pass to L1 is at 3,365,921 km. Since this is about 6 times the maximum orbit distance, this is considered a safe distance.

8.4.4. ORBIT SENSITIVITY ANALYSIS

To test the sensitivity of the orbit around L1, a 5% error in the insertion orbit ΔV was given as input to the GMAT model. It was found that the orbit of OB1 is highly sensitive to these changes. To minimise the impact of such an insertion error,

¹⁰http://www.srl.caltech.edu/ACE/ace_mission.html

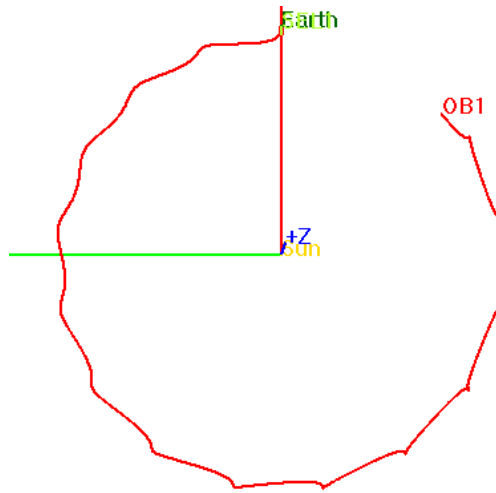


Figure 8.16: End of Life Manoeuvre for L1 in the Sun-Corotating Frame

a correction burn has to be applied 1 hour after the start of the insertion. The correction burn that has to be applied is 100.2% of the magnitude of the error, where it's direction is parallel to the insertion burn in the corrective direction.

However, this correction burn is not enough to fully stabilise the orbit. All other correction burns stated in Table 8.9 will also change. It was found that the shift in these burns is limited to $\pm 1 \text{ ms}^{-1}$.

The insertion burn is not the only burn that is sensitive. All correction burns show similar behaviour, and have similar effects on all consecutive burns. This means that most likely more orbit manoeuvres will have to be performed than initially stated. For the detailed design, it is recommended that the option of multiple burns per orbit for orbit stability is analysed.

The timing of the launcher burn into the manifold is also analysed. The burn was delayed by 1 second, which meant the insertion burn had to be increased by 4 ms^{-1} . The other burns also changed similarly to the incorrect orbit insertion velocity.

8.5. LAUNCH DATE SENSITIVITY

Since the launch window is very small, additional launch times have to be investigated. It was found that if the launch is scheduled 7 August or later, the orbit at L5 will increase in amplitude beyond the limits set by the requirements in Table 8.13. Therefore all dates from 29 July until 6 August were analysed. The results for L5 are shown in Table 8.11. It is to be noted that no transfer can be performed on 2 August, because the transfer will be given an out of plane gravity assist by the Moon. The transfer to L1 is also slightly affected by a new launch date, causing similar movements as described in Section 8.4.4.

Table 8.11: Launch Windows

Date	Time	θ [deg]	Transfer Time (L5) [days]	ΔV_{ins} (L5) [kms^{-1}]
29 July 2023	15:03:52	282.268	406.788	1.691
30 July 2023	15:04:31	283.140	406.337	1.680
31 July 2023	15:05:28	284.413	404.979	1.631
1 August 2023	15:06:29	285.770	404.141	1.607
2 August 2023	—:—	—.—	—.—	—.—
3 August 2023	15:05:48	284.677	404.723	1.641
4 August 2023	15:05:49	284.891	368.652	1.647
5 August 2023	15:07:27	287.041	403.456	1.605
6 August 2023	15:08:04	287.858	402.951	1.594

8.6. VERIFICATION AND VALIDATION

In Figure 8.17 the comparison of the calculated transfer orbit to the transfer orbit as seen in literature can be found.[54] It can be seen that the calculated transfer in Figure 8.17b matches the transfer from literature in Figure 8.17a very well. The transfer times also match within 5%, as the transfer in literature was predicted to take 420 days.[54] The slight discrepancy

is to be expected, as literature assumes a circular restricted three body problem, meaning the eccentricity of Earth's orbit and the disturbances of other planets are excluded.[54] It is therefore concluded the results match very well, and the programme that calculates the transfer to L5 is verified.

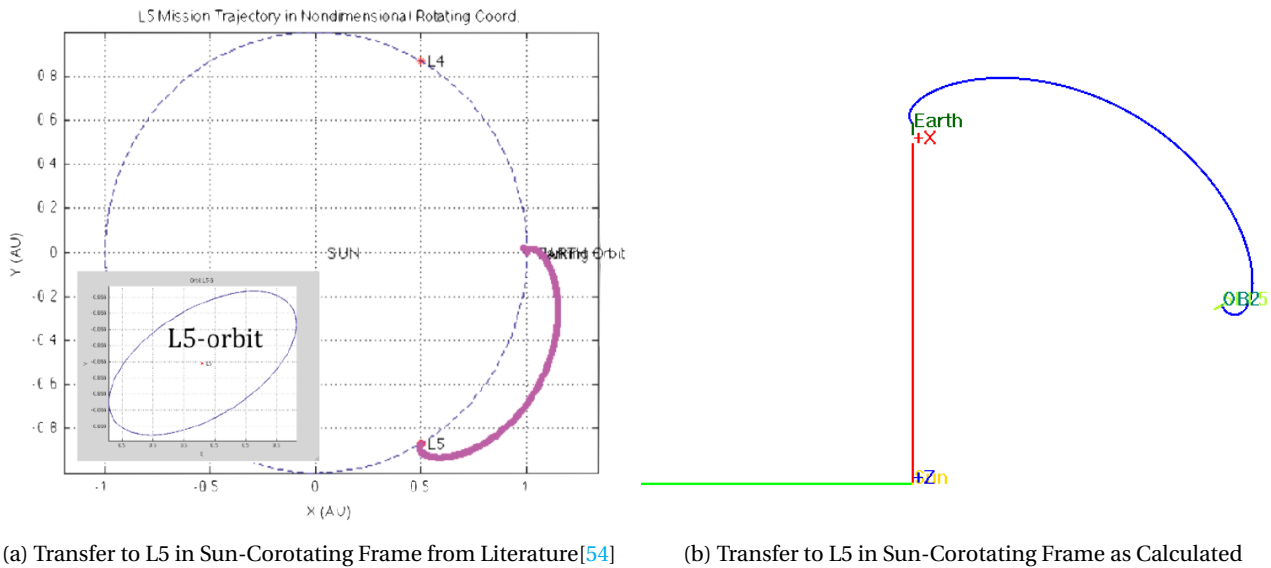


Figure 8.17: L5 Transfer Comparison

The transfer to L1 can be seen in Figure 8.18 where it is compared to literature.[53] As can be seen, the shape of the calculated transfer in Figure 8.18b perfectly matches the shape of the predicted transfer from literature in Figure 8.18a. The predicted transfer time and ΔV from literature were 122.9 days and $1,456 \text{ ms}^{-1}$ respectively, which match perfectly to the calculated values.[53] The programme calculating the transfer to L1 is therefore considered verified.

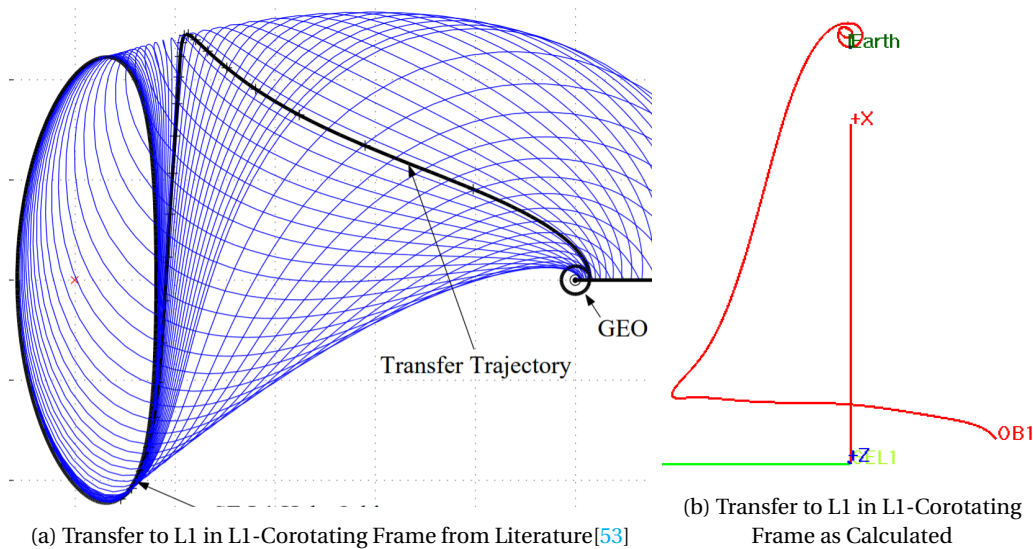


Figure 8.18: L1 Transfer Comparison

The orbit around L1 can be seen in Figure 8.19 where it is compared to the orbit from SOHO.¹¹ It can be seen that the calculated halo orbit in Figure 8.19b follows the same pattern as SOHO in Figure 8.19a as it oscillates around the Z-axis. The orbit in the XY-plane in Figure 8.19c also resembles SOHO's orbit very well. As the calculated orbit resembles the mission pattern of an active mission, the results given by the model for L1 are considered validated.

8.7. RISK ANALYSIS

In Table 8.12 all the risks associated to the astrodynamics are listed.

¹¹https://soho.nascom.nasa.gov/about/images/halo_orbit.gif

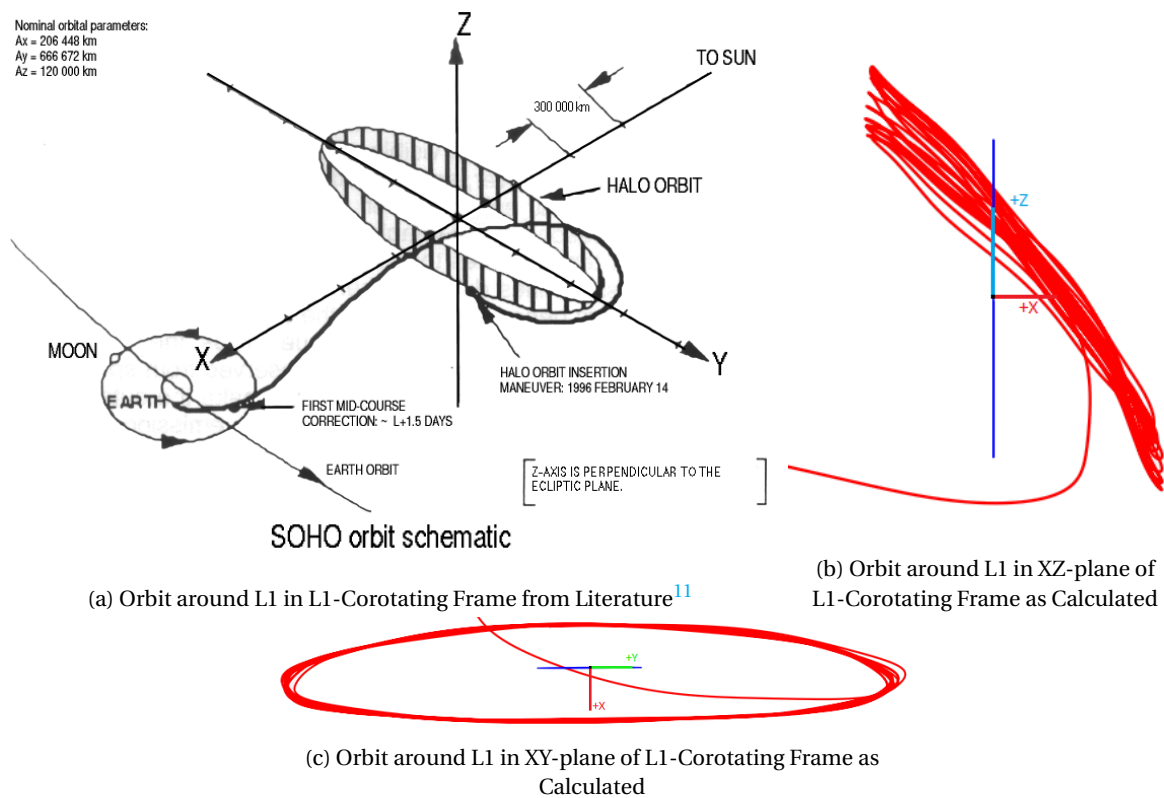


Figure 8.19: L1 Orbit Comparison

Table 8.12: Astrodynamics Risk Register. Likelihood: HU = highly unlikely, U = unlikely, SL = some likelihood, L = likely, HL = highly likely. Impact: M = marginal, S = some, H = high, C = catastrophic

Risk	Consequence	Likelihood	Impact	Mitigation
End Of Life measurement failure	Spacecraft continues to occupy space in valuable orbit	U	H	Add redundancy in propulsion system, take additional fuel
Launcher failure	Loss of both spacecraft	U	C	Choose reliable launcher
Collision with space debris	Loss of spacecraft	U	C	Spend as little time as possible in Earth orbit, add strengthening parts to structure
Wrong orbit insertion	Unable to intersect with Lagrange orbit	HU	C	Take fuel for correction burns
Orbit maintenance failure	OB1 is lost within 6 months, OB2 cannot perform End of Life burn	U	C	Add redundancy in propulsion system
Orbital miscalculation	Unable to intersect with Lagrange orbit, or unable to orbit	U	C	Perform proper Verification and Validation

8.8. REQUIREMENT COMPLIANCE

In Table 8.13 all requirements for the astrodynamics are shown, and is determined whether they have been met.

Table 8.13: Orbit Requirement Compliance Matrix

Identifier	Requirement	Met?	Confirmation
General			
SYS-GEN-04	The total launch costs shall not exceed 90 M euros	✓	Section 8.2.1
L1 orbit			
ORB-L1-01	The transfer to L1 shall take at most 75 m/s of velocity increment	✓	Table 8.8
ORB-L1-02	The transfer to L1 shall take at most 150 days	✓	Table 8.8
ORB-L1-03	The orbit at L1 shall have a semi major axis lower than 600,000 km	✓	Table 8.10
ORB-L1-04a	The orbit at L1 shall be a halo orbit	✓	Figure 8.15
ORB-L1-05a	The orbit at L1 shall not move within the inner 90% of the Solar Exclusion Zone	✓	Figure 8.14
L5 orbit			
ORB-L5-01	The transfer to L5 shall take at most 430 days	✓	Table 8.4
ORB-L5-02	The transfer to L5 shall take at most 2700 m/s of velocity increment	✓	Section 8.3.1
ORB-L5-03	The orbit at L5 shall have a semi major axis lower than 179000 km	✓	Table 8.5
ORB-L5-05	The orbit at L5 shall have an inclination with respect to the ecliptic plane of 0 degrees	✓	Figure 8.8
ORB-L5-06	The orbit insertion at L5 shall not take more than 3.5 MNs of total impulse	✓	Section 8.3.1
ORB-L5-07	The total burn time during insertion shall be lower than 1.5 hr	✓	Section 8.3.1
Launcher			
ORB-LAU-01	The launcher shall be able to give the spacecraft going to L1 a velocity increment of 14500 m/s	✓	Table 8.2
ORB-LAU-02	The launcher shall insert the spacecraft going to L1 into the manifold orbit heading to L1 from GEO	✓	Figure 8.2
ORB-LAU-04	The launcher shall be able to give the spacecraft going to L5 a velocity increment of 10300 m/s	✓	Table 8.2
ORB-LAU-05	The launcher shall insert the spacecraft going to L5 into a GTO orbit	✓	Figure 8.2
ORB-LAU-06	The launcher shall insert the spacecraft going to L5 in an orbit with an inclination of 0 degrees with respect to the ecliptic	✓	Figure 8.4

8.9. CONCLUSION AND RECOMMENDATIONS

The most important parameters for the transfers are summarized in Table 8.14.

Table 8.14: Summary of Important Values

Parameter	OB1	OB2
Launch time	29 July 2023 15:03:52	
Arrival time	1 December 2023 00:39:40	8 September 2024 20:36:03
$\Delta V_{\text{transfer}} [\text{ms}^{-1}]$	62.4	2640
$\Delta V_{\text{orbit maintenance}} [\text{ms}^{-1}]$	117.5	0
$\Delta V_{\text{EOL}} [\text{ms}^{-1}]$	1	32

The following recommendations are made for future research:

- An analysis of the possibility of multiple correction burns per orbit for L1 is advised, as this might decrease the sensitivity and total propellant needed.
- An analysis of whether a second burn during the transfer to L5 might decrease the amount of ΔV required for insertion is advised.
- It is advised to analyse the ΔV requirements for different launch dates for L1 in more detail.
- An analysis of the size of the SEZ due to the Signal to Noise ratio requirements is advised.

Due to these recommendations, it is almost certain that the orbits defined in this chapter are suboptimal. However, they do demonstrate that the mission is feasible.

9

MAIN PROPULSION SYSTEM

In Chapter 3 it was shown that the propulsion system that should be used for this mission is a hydrazine-NTO liquid bipropellant propulsion system. This section describes the design of the main propulsion system. All numbers presented in the explanations are for OB2 going to L5. At the end of the section, the results for OB1 are also presented. The propellant mass can be determined using the ideal rocket equation (Equation (9.1)) and the velocity increments presented in Chapter 8, assuming the dry mass after each burn includes the propellant mass needed for subsequent burns [12].

$$m_p = m_f \left(e^{\frac{\Delta V}{g_0 I_{sp}}} - 1 \right) \quad (9.1)$$

where m_p is the required propellant mass. m_f is the final mass of the satellite after the burn. ΔV is the required velocity increment, g_0 is the gravitational acceleration at the surface of Earth and I_{sp} is the specific impulse. This analysis results in the values presented in Table 9.1. Note that this analysis assumes a spacecraft dry mass of 390 kg for OB1 and 450 for OB2.

Table 9.1: Propellant masses for OB1 and OB2 for different burns.

Burn	propellant mass	
	OB1	OB2
Escape	-	275.1
Insertion	8.1	326.8
Orbit Maintenance	14.8	3.6
EOL	0.1	3.5

9.1. THRUSTER SELECTION

Several manufacturers have commercially available engines that run on these propellants. These include Ariane Group¹, Aerojet Rocketdyne², Northrop Grumman³ and MOOG⁴. Table 9.2 shows different performance parameters for different engines of these manufacturers. The selection is first done for the spacecraft going to L5, as the ΔV requirements are a lot more stringent for this spacecraft than for the spacecraft going to L1. A similar trade-off is done for the L1 spacecraft propulsion system, but this has a lot fewer requirements on the engine than the L5 mission.

A required burn time to insert the spacecraft into an orbit around L5 can be determined by taking into account that the total impulse required for this is approximately 1.28 MNs. This figure divided by the nominal engine thrust will provide the required burn time. If this burn time is higher than the burn time the engine is qualified for, the engine will be discarded immediately. The amount of cycles that the engines are qualified for is left out as it is much higher (>70) than the required 2-3 restarts of the main propulsion system of the SWAN satellites. The engine size is left out as well since the size ranges (60 - 70 cm length and 25-40 cm diameter) do not differ by a lot and are not so big that they could pose a problem when fitting the spacecraft in the launcher.

From the calculation of this maximum burn time, it can immediately be concluded that the TR-308, S200, R-1E and R-42DM are not suitable for the mission, as either their required burn time is longer than the longest qualified burn time, or they do not meet the requirement of the insertion burn time not being longer than 1.5 hr (ORB-L5-07). A selection can be made out of the remaining thrusters. This will be done in the way general trade-offs are done in this report. The criteria are the engine required burn time, the total mass of the propulsion system using a certain type of engine (including fuel and tank mass), the system approximate cost and the total volume of the system. The burn time is given a weight of 25%, as the orbit around L5 becomes more unstable as the burn time becomes longer and thus a burn time as short as possible is wanted. Mass is given a weight of 30% for the reason that the launcher capabilities are stretched to the limit and the

¹<http://www.space-propulsion.com/spacecraft-propulsion/apogee-motors/>

²<https://www.rocket.com/propulsion-systems/bipropellant-rockets>

³<http://www.northropgrumman.com/Capabilities/PropulsionProductsandServices/Pages/BipropellantEnginesAndThrusters.aspx>

⁴<http://www.moog.com/products/thrusters.html>

Table 9.2: Commercial main thruster performance parameters.

Engine	Manufacturer	Thrust [N]	ISP [s]	Maximum Burn Time [s]	Mass [kg]
LEROS 1b[60]	MOOG	635	317	2,520	4.5
LEROS 1c[60]	MOOG	458	324	5,800	4.3
LEROS 2b[60]	MOOG	407	318	4,000	5
TR-308[61]	Northrop Grumman	471.5	322	3,000	4.76
S400-12[62]	Ariane Group	420	318	3,960	3.6
S400-15[62]	Ariane Group	425	321	6,660	4.3
S200[62]	Ariane Group	216	270	11,400	1.9
R-1E[63]	Aerojet Rocketdyne	111	280	Unlimited	2
R-4D[63]	Aerojet Rocketdyne	490	307	12,000	4.31
HiPAT[63]	Aerojet Rocketdyne	445	322	3,600	5.44
R42[63]	Aerojet Rocketdyne	890	303	3,940	4.53
R-42DM[63]	Aerojet Rocketdyne	890	327	1,000	7.3
AMBR[63]	Aerojet Rocketdyne	623	333	2700	5.4

spacecraft should be as light as possible. Cost is given the same weight since the budget is very tight, and all the systems should be designed as cheap as possible. Volume is given a weight of 15%. It is lower than mass and cost since it is not close to the launcher capabilities. However, a large volume also means a large area and moment of inertia, which would result in a larger mass of the thermal control and ACS systems. The best score receives a 10 and the other scores are scaled with respect to this. This results in the trade-off matrix shown below.

Table 9.3: Main thruster trade-off for L5. **Red** = Poor, **Orange** = Marginal, **Yellow** = Sufficient, **Green** = Good, **Blue** = Excellent.

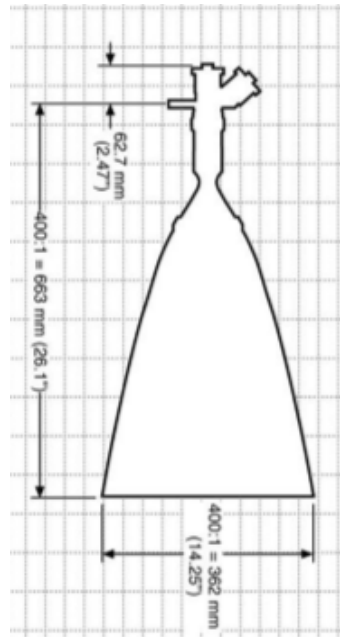
Name	Burn Time	Mass	Volume	Costs	Final Score
Weight	25	30	15	30	
LEROS 1b	8.09 <small>Green</small>	9.40 <small>Green</small>	9.40 <small>Green</small>	9.73 <small>Blue</small>	9.17
LEROS 1c	5.54 <small>Orange</small>	9.58 <small>Blue</small>	9.66 <small>Blue</small>	9.85 <small>Blue</small>	8.66
LEROS 2b	5.55 <small>Orange</small>	9.46 <small>Green</small>	7.94 <small>Green</small>	8.97 <small>Green</small>	8.11
S400-12	5.69 <small>Orange</small>	9.46 <small>Green</small>	7.94 <small>Green</small>	8.97 <small>Green</small>	8.14
S400-15	5.22 <small>Orange</small>	9.47 <small>Green</small>	9.55 <small>Blue</small>	9.80 <small>Blue</small>	8.51
R-4D	5.93 <small>Orange</small>	8.96 <small>Green</small>	9.03 <small>Green</small>	9.55 <small>Blue</small>	8.39
HiPAT	5.97 <small>Orange</small>	9.61 <small>Blue</small>	8.06 <small>Green</small>	9.04 <small>Green</small>	8.29
R42	10 <small>Blue</small>	8.81 <small>Green</small>	8.88 <small>Green</small>	9.48 <small>Green</small>	9.32
AMBR	7.96 <small>Green</small>	10 <small>Blue</small>	10 <small>Blue</small>	10 <small>Blue</small>	9.49

As can be concluded from the trade-off, the best engine for the mission would be the AMBR engine by Aerojet Rocketdyne. It can also be directly concluded that the trade-off will not be very sensitive to the assigned weights, as the AMBR rocket engine scores 10 in all but one of the categories. In Figure 9.1a the physical engine is shown, while Figure 9.1b shows the dimensions of this engine.[63]

For a minimum spacecraft weight at EOL, this engine would accelerate the spacecraft with an estimated dry mass of 400 kg with about 1.6 ms^{-1} , which would be the biggest load on the spacecraft after the launch.

9.2. PROPELLANT TANKS

The same design philosophy that applies to the thrusters also applies to the tanks. There are plenty of commercial suppliers of tanks. This will greatly reduce the cost of tank development and qualification, although it might be needed to select a non-optimal tank for this mission. However, since the cost budget is very tight while the mass budget is not, it is decided that the tanks can be sub-optimal for the benefit of a lower cost. Again, the requirements on the L5 spacecraft are much more stringent and therefore the analysis for this spacecraft is performed first. The required volume for the oxidizer and fuel tank are 287 and 383 L respectively. This accounts for an ullage volume of 5%.[64]



(a) Physical appearance of the AMBR rocket engine.

(b) Dimensions of the AMBR rocket engine.

Figure 9.1: AMBR rocket engine by Aerojet Rocketdyne.[63]

First, the configuration of the tanks should be decided upon. Since the tanks are relatively large and have a large mass moment of inertia, one could decide to take four tanks, two oxidizers and two fuel, instead of just 2. This will weight more and take up more volume, but the moment of inertia about each of the spacecraft axes is potentially lower. Because larger tanks would reduce the complexity and cost of the system, mainly in terms of the integration into the spacecraft, an initial configuration with two tanks is chosen. This will have a huge impact on the ACS design and thus this choice will have to be reassessed if it turns out to be unfeasible. For the L1 mission, this is much less of a problem, as the tanks will be much smaller and thus can easily be integrated when using only two tanks.

Secondly, there are two different types of tanks that can be chosen. The first is a diaphragm tank, in which a flexible diaphragm is inserted in the tank, below which the propellant is kept. The diaphragm can then be squeezed into the thruster by pressurant gas around the diaphragm. The other option is a tank using propellant management devices (PMDs). These are devices that guide the propellants into the feed system, while the pressurant gas is kept in the tank. In this case, no physical separation between the pressurant gas and the propellant is present. A diaphragm tank is shown in Figure 9.2a and a PMD tank is shown in Figure 9.2b.

From suppliers such as Ariane Group⁶, Northrop Grumman⁷ and MT Aerospace⁸, it is found that most spacecraft tanks are PMD tanks, definitely for the sizes required for the L5 mission. This is why for the L5 mission a PMD tank is chosen. Another advantage of this tank is that the full volume of the tank (taking a bit of margin for expansion of the propellants) can be used for propellant storage. In diaphragm tanks, a large part of the tank is used to store the pressurising gas. Moreover, since these tanks are not designed for high pressures, the required volume of pressurant gas will be much larger in this case than if a separate, very high-pressure tank and a pressure regulator were used.

Table 9.4 shows all the tanks that can be used for the mission manufactured by the aforementioned suppliers. It shows bipropellant tanks for the main propulsion system, hydrazine monopropellant tanks for possible use in the ACS and high-pressure Helium/Nitrogen tanks, which can be used for propellant tank pressurisation.

Looking at this table, it becomes clear that the PTP-393 of MT Aerospace is the best option for the fuel tank. For the oxidizer tank, two options are possible, being the 282L OST 25/0 or the PTP-288. However, because of its lower mass and volume, it is beneficial to choose the PTP-288 tank of MT Aerospace. The maximum expected operating pressure (MEOP) of both of these tanks is equal to 20 bar. This is compatible with the thruster, which has a required inlet pressure of 12.1-22.4 bar[63].

⁵http://www.phoenixpumps.com/goulds-water-technology-diaphragm-bladder-tanks_8_1171_1077.html#.Wx5kkYVOJaQ and <http://www.pmdtechnology.com/>

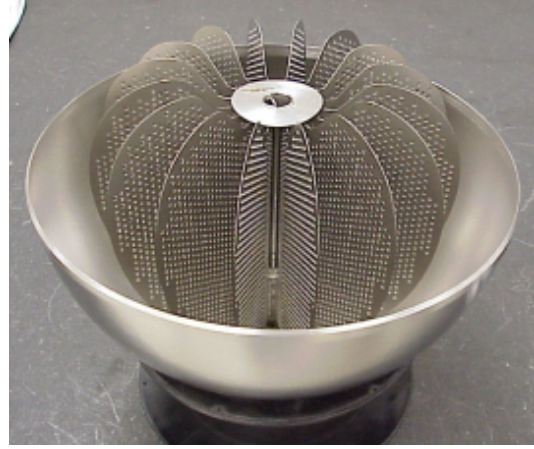
⁶<http://www.space-propulsion.com/spacecraft-propulsion/bipropellant-tanks/index.html>

⁷<http://www.northropgrumman.com/Capabilities/PropellantTanks/Pages/default.aspx>

⁸<https://www.mt-aerospace.de/tanks-products.html>



(a) Cut-out of a diaphragm tank.



(b) Propellant Management Devices in a tank.

Figure 9.2: Different possible tank types⁵

9.3. PRESURANT TANK

Sutton and Biblarz[64] state that the pressurant gas that should be used for this propellant combination is helium, as nitrogen gas will dissolve in the NTO. Moreover, if nitrogen gas were to be used, about 2.5 times as much mass of pressurant gas would be needed. They give an equation to make an initial estimate of the minimum pressurant gas mass needed for the mission.

$$m_0 = \frac{p_p V_p}{RT_0} \left(\frac{\gamma}{1 - \frac{p_p}{p_0}} \right) \quad (9.2)$$

In Equation (9.2) m_0 is the pressurant gas mass in kg, p_p is the propellant tank pressure in Pa, normally taken to be the lowest inlet pressure of the thruster excluding pressure losses in the feed system[45]. V_p is the volume of the propellant tank in m^3 , R is the specific gas constant for the pressurant gas in $Jkg^{-1}K^{-1}$ and T_0 is the minimum temperature of the propellant tank in K, γ is the ratio of specific heats of the pressurant gas and p_0 is the pressure of the pressurant gas tank.

Since the only high-pressure tanks that have been found have a design pressure of 310 bar, this value will be used for p_0 . The propellant pressure is set to 12.1 bar, the volume is equal to the combined volume of both of the propellant tanks and the temperature is the lowest temperature allowed for these tanks, equalling zero °C. γ and R are gas constants and are equal to 1.66 and 2080 $Jkg^{-1}K^{-1}$ for helium.

From this analysis, it is determined that a helium gas mass of 2.95 kg is needed. From NIST, the density of helium at this pressure and a temperature of 0°C is equal to 47.198 kgm^{-3} . This results in a required tank volume of 62.5 L. However, this volume is needed when no pressure losses occur in the feed system from the tank to the thruster. However, due to leaking, as explained in Section 9.5, the biggest tank is not big enough and thus multiple tanks are needed. This second tank can then also be used for pressurising the ACS system. Pressure drop calculation needs to show what volume tank is needed to allow for a higher pressure in the pressurant tank.

The pressurant mass flow can be determined by taking the derivative of Equation (9.2). It can be assumed that the gas properties stay the same and the pressurant tank pressure and temperature do not change over this infinitesimal timestep. This results in

$$\dot{m}_0 = \frac{p_p \frac{dV_p}{dt}}{RT_0} \left(\frac{\gamma}{1 - \frac{p_p}{p_0}} \right) \quad (9.3)$$

here, $\frac{dV_p}{dt}$ is equal to the volume flow rate of the main thruster. The mass flow rate of the engine is equal to 204 gs^{-1} and the OF is equal to 1.1.[63] This results in a fuel mass flow of 97.1 gs^{-1} and an oxidiser mass flow of 106.9 gs^{-1} . Taking a density of MMH to be equal to 875 kgm^{-3} and that of NTO equal to 1440 kgm^{-3} [65], the total volume flow rate of the

Table 9.4: Possible tanks for the SWAN mission.

Bipropellant Tanks

Name	Manufacturer	Type	Total Propellant Volume [L]	Mass [kg]	Diameter [mm]	Length [mm]	MEOP [bar]
80342-1 ^a	Northrop Grumman	Diaphragm	14.5	2.7	327	327	36.2
80184-1 ^a	Northrop Grumman	Diaphragm	13.6	1.6	322	322	40.33
80197-1 ^a	Northrop Grumman	Diaphragm	13.6	1.3	240	240	33.09
80321-1 ^a	Northrop Grumman	Diaphragm	13.6	1.65	347	347	30
180L biprop tank ^b	Ariane Group	PMD	180	21	623	907	21
198L COG control ^b	Ariane Group	PMD	198	17.5	754	651.5	17.5
235L OST 21/0 ^b	Ariane Group	PMD	235	17.5	756	756	16
282L OST 25/0 ^b	Ariane Group	PMD	282	21	753	643.5	22
PTP-124 ^c	MT Aerospace	PMD	124	9.8	605	695	24
PTP-166 ^c	MT Aerospace	PMD	166	10.8	602	856	20
PTP-267 ^c	MT Aerospace	PMD	267	13.5	604	1171	20
PTP-288 ^c	MT Aerospace	PMD	288	14.5	604	1259	20
PTP-393 ^c	MT Aerospace	PMD	393	17	604	1630	20
PTP-406 ^c	MT Aerospace	PMD	406	17.1	602.7	1693	20
PTP-517 ^c	MT Aerospace	PMD	517	26.1	691	1709	20

Monopropellant Tanks

104 - 177 L hydrazine tank ^b	Ariane Group	PMD	82.4	6.4	856	856	24.6
176L hydrazine tank ^b	Ariane Group	PMD	176.5	13.5	600	896	24.6
PTD-177 ^c	MT Aerospace	Diaphragm	135	15.5	654	827	24
PTD-222 ^c	MT Aerospace	Diaphragm	180.2	17.3	607	1027	24.5
331 L Hydrazine tank ^b	Ariane Group	PMD	331	22.7	753	953.5	19.5

Pressurant Tanks

PVG 40-75 ^c	MT Aerospace	-	40-75	8.5-14.4	432	728	310
PVG 50 ^c	MT Aerospace	-	50	9.5	432	673	310
PVG-65 ^c	MT Aerospace	-	65	12	432	788	310

^a <http://www.northropgrumman.com/Capabilities/PropellantTanks/Pages/default.aspx>^b <http://www.space-propulsion.com/spacecraft-propulsion/bipropellant-tanks/index.html>^c <https://www.mt-aerospace.de/tanks-products.html>

propellant flowing from both tanks is equal to $1.85 \cdot 10^{-4} \text{ m}^3 \text{ s}^{-1}$. Filling this in into Equation (9.3), a required pressurant mass flow of 0.817 gs^{-1} . This can be used as a requirement for the valve selection at a later stage.

9.4. FEED SYSTEM DESIGN

To get the propellants from the tanks to the engines, a feed system is necessary. The feed system consists of tubes, hoses and valves to regulate the flow of propellants within the spacecraft. It is common practice to design a redundant system, in which no single point of failure does not exist. [45, 66] In some cases, such as with the check valves, double redundancy (serial and parallel) is even employed. This design philosophy will also be employed in the current design.

The feed system is normally made out of either titanium or stainless steel. Titanium is more expensive but more corrosion resistant, while stainless steel is readily available but a bit less resistant.[45] The main components of the feed system are the tubing, of which most of the feed system consists. There are both rigid pieces of pipe, as well as bellow sections where the line is flexible. Furthermore, different types of valves are used to control the propellant flow. Pressure regulators are used for decreasing the pressure from the pressurant tanks to the propellant tanks and pressure and temperature sensors can be used to monitor the state of the system at different positions.

Because of its lower cost and more ready availability, stainless steel is chosen as the material for the feed system. This is also recommended by Huzel and Huang[67]. This does mean that the interface between the tank and the feed system cannot be welded. Therefore, an o-ring, bonded seal or crush ring should be used to seal this interface. Metal crush rings are preferable as they are compatible with strong oxidisers, while rubber o-rings or bonded seals are not.

Tubing size is determined by a combination of factors such as available space, allowable pressure drop and of course the mass and cost of the system. Minimal bends and bellow section should be used in the feed system as they greatly increase the pressure drop compared to a straight smooth pipe. This analysis will be described later in this section.

Different types of valves are used in the feed system as well. Normally these are:

- **Control Valves:** The control valves are normally taken to be needle or latch valves, as they can be made very compact.[67] They are used for a lot of cycles to allow propellant to flow to the thrusters. The unpowered position of the valve is also important, as it will determine its state when power is lost. This can either be open or closed depending on the function of the valve. These valves can have a lot of functions such as fill or drain valve, bleed valve, main valve, an emergency valve.
- **Pyrotechnic Valves:** Pyrotechnic valves can normally only be fired once or twice. They are mainly used for safety reasons, for instance, to permanently close off a certain section of the feed system. They too can be in a normally open or closed position.
- **Check Valves:** Check valves only allow flow in one direction. They do not rely on active control but use a mechanical system to operate passively.
- **Pressure Relief Valves:** Pressure relief valves are also passively controlled. Spring force is used to keep the valve closed until the pressure in the tank exceeds a predefined value.
- **Burst Discs:** Burst discs are simple metal discs that break at a predefined pressure. These also are for one-time use.
- **Venturis:** A venturi is basically a supersonic nozzle and can be used in the main line for mass flow control as well as reducing the effects of water hammer.
- **Filters:** A filter is normally placed directly downstream of the fill valve and the tank to keep particles from entering the tank and the thruster.

Moreover, pressure and temperature sensors can be used to monitor the state of the system.

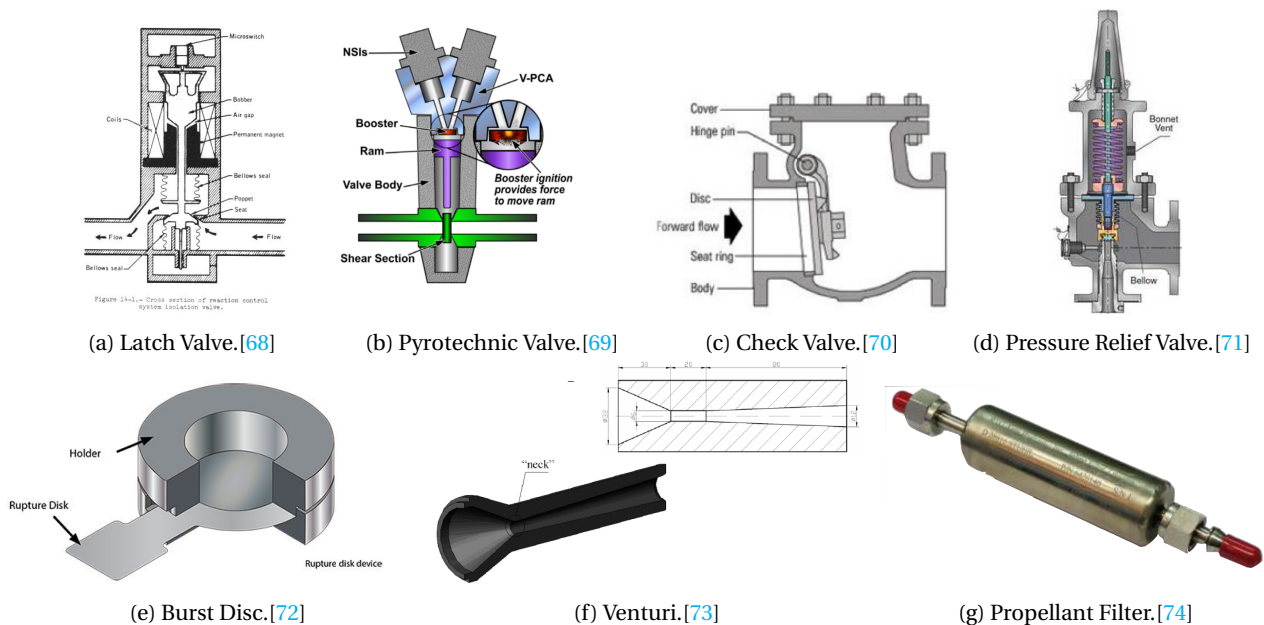


Figure 9.3: Different feed system components.

A simplified configuration of the feed system is shown in Figure 9.4. The pressurant feed system is used to lower the pressure from the pressurant tank to the allowable pressure in the propellant tanks and to isolate the pressurant tank from the fumes that are coming from the propellant tanks. Two propellant feed systems are used, one for the main thruster running from the fuel and oxidiser tanks and one from the ACS fuel tank containing hydrazine.

Figure 9.5 shows the full layout of the feed system. The main fuel feed system is depicted in green and the main oxidizer feed system in red. Their layouts are similar. It can be seen that almost all systems are redundant, apart from the venturi and filters, as they do not contain any moving parts. The tank can be filled through the same line that will be used to pressurise the tank. For safety, multiple pyrotechnic valves have been placed in the system, either to prevent tank premature tank filling or to cut off the main thruster. All sections that can be closed off also contain a drain valve, which means that this section can be emptied at all times, the most important being the drain valve on the bottom of the tank. Burst discs, pressure relief valves and gas drain valves have been placed on top of the tank to allow for depressurisation in case of over-pressurisation. The propellant fill valves are not redundant as they can still be replaced while on the ground.

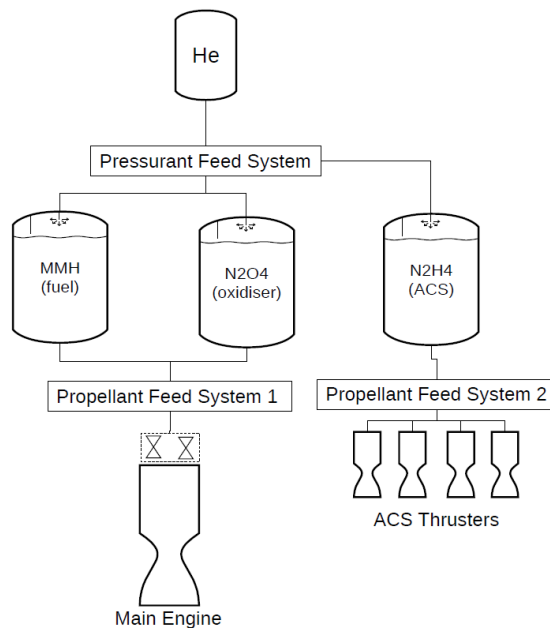


Figure 9.4: Simplified layout of the propellant feed system.

Filters are added directly after the tank and after the fill valve to keep as many particulates from being injected into the tank and the main thruster.

The pressurant feed system is shown in orange. As it is directly connected to the propellant feed systems, it is of vital importance to keep vapours of the propellants from migrating to the pressurant tank, as fumes from the oxidizer and fuel could mix and combust spontaneously, resulting in mission failure. At this connection, burst discs are added to allow pressurisation of the tanks only after the latch valves upstream have opened. A system of four check valves is used to prevent fuel and oxidizer vapours from flowing to the propellant system. Pressure regulators are used for decreasing the pressure from the 310 bar present in the helium tank, to the required 12.1 bar in the propellant tanks. Redundant normally closed pyrotechnic valves are again used to only allow pressurant flow when needed and not before. Normally open pyrotechnic valves are inserted to prevent pressurant flow indefinitely in case of an emergency. The same safety measures as placed on the propellant tanks have also been implemented on the pressurant tank. The propellant tanks will only be pressurised once the spacecraft has reached the position of their first burn to reduce the time the system is exposed to high pressures.

The same architecture can be used for the ACS system, although only the fuel feed system is used since it makes use of a monopropellant fuel. The thrusters have been divided into groups of four, where a full group can be cut-off as well as the individual thrusters. This almost fully mitigates the risk of one thruster continuously firing if a valve breaks down.

9.5. LEAKAGE

An estimation of the leakage over the mission lifetime can be made by component specifications of feed system parts. These are presented in Table 9.5. Multiplying all the numbers in the table, the total leakage flow rate amounts to $1.97 \cdot 10^{-4}$ sccs^{-1} . From the orbit determination, the approximate duration of the mission from the first firing of the main engine is taken to be equal to 6.25 years for L5. This means that the total volume of helium that will leak away from the system is 38.8 L. Taking a 15% margin[75], this results to an additional helium volume of 44.7 L. This means no one tank fits all the pressurant gas and multiple tanks are needed.

9.6. PRESSURE DROP AND MASS ESTIMATION

If the thruster is to be pressurised to at least 12.1 bar, the tanks should be pressurised to a higher value, as there will be pressure losses over the feed system leading up to it.

From simple addition of the values given in Table 9.6, it can be found that the total pressure drop over the valves between the tank and the thruster is equal to 3402 mbar. However, there will also be a pressure drop over straight pipe. The

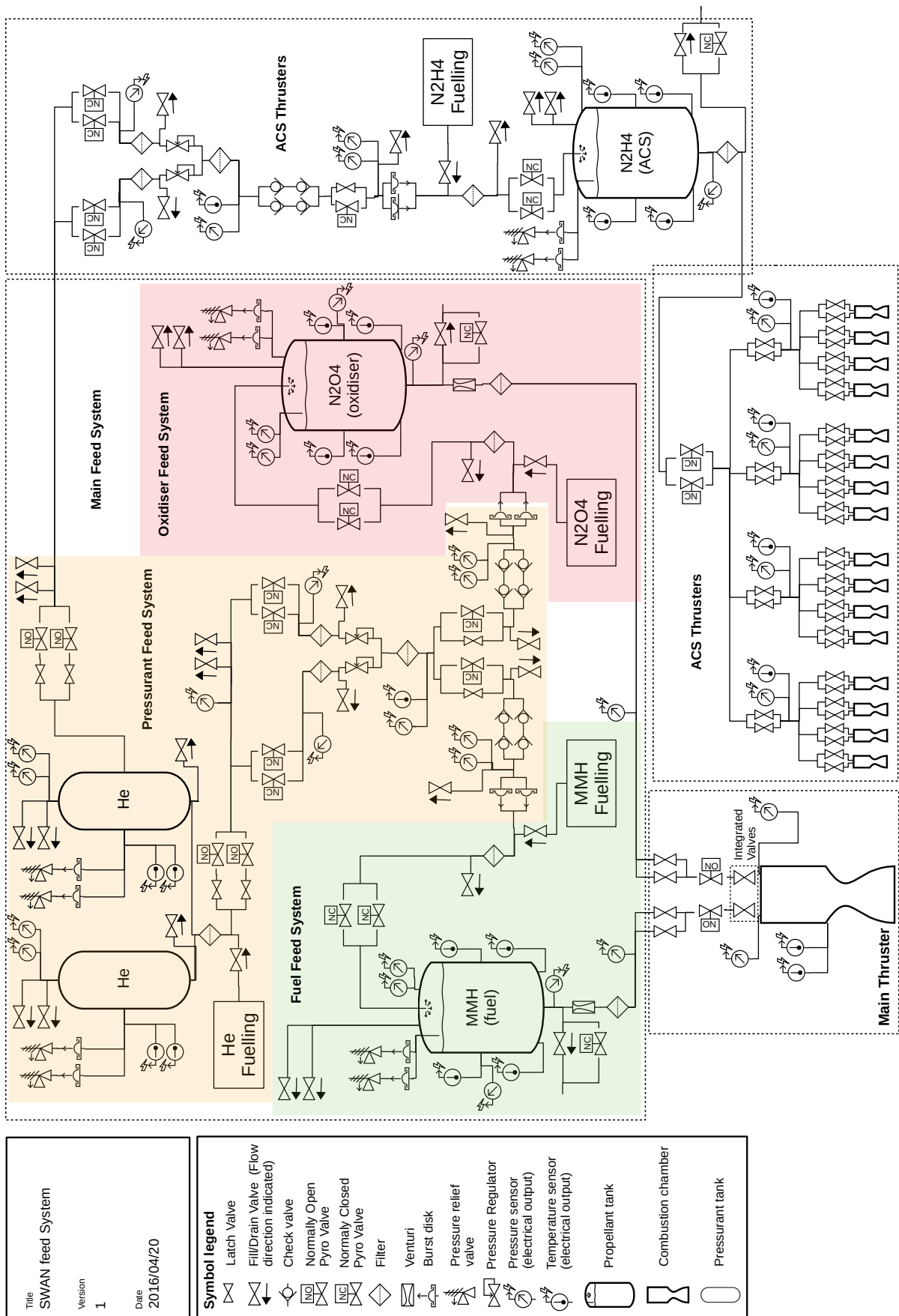


Figure 9.5: Complete layout of the propellant feed system.

Table 9.5: Feed System leakage rates.

Valve Type	External Leakage Rate [scc/s]	Internal Leakage Rate [scc/s]	Number External	Number Internal
Fill/Drain Valve[76]	$1 \cdot 10^{-6}$	$1 \cdot 10^{-6}$	32	32
Pyrotechnic Valve[77]	$1 \cdot 10^{-6}$	$1 \cdot 10^{-6}$	28	3
Latch Valve[77]	$1 \cdot 10^{-6}$	$1.38 \cdot 10^{-3}$	31	0
Main Thruster Valve [77]	$1 \cdot 10^{-6}$	$5 \cdot 10^{-4}$	6	0
Propellant Filter[74]	0	0	12	0
Pressure Regulator[74]	$1 \cdot 10^{-6}$	$1.39 \cdot 10^{-4}$	4	0
Check Valve[78]	$1 \cdot 10^{-6}$	NA	12	0
Pressure Relief Valve[79]	$1 \cdot 10^{-6}$	$1 \cdot 10^{-3}$	0	0
Burst Disc[80]	$1 \cdot 10^{-9}$	NA	16	0
Pressure Sensor[81]	$1 \cdot 10^{-6}$	NA	37	0
Temperature Sensor	0	NA	24	0

Table 9.6: Valve pressure drop and mass

Valve Type	Pressure Drop [mbar]	Mass [g]
Fill/Drain Valve[76]	NA	113
Pyrotechnic Valve[77]	1100	160
Latch Valve[77]	NA	340
Main Thruster Valve [77]	1100	900
Propellant Filter[74]	102	110
Pressure Regulator[74]	NA	1720
Check Valve[78]	NA	20
Pressure Relief Valve[79]	NA	340
Burst Disc[80]	NA	200
Pressure Sensor[81]	NA	75
Temperature Sensor	NA	75

pressure drop over a straight section of pipe can be calculated using the following relation:

$$\Delta p = f \frac{L}{D} \frac{1}{2} \rho_p v_p^2 \quad (9.4)$$

where f is the Moody or Blasius friction factor [82]. One can see that the pressure drop is related to the length to diameter ratio of the pipe, as well as the dynamic pressure of the fluid in the pipe. The friction factor f is not constant and depends on the parameters of the pipe itself, but also of the fluid. However, this constant is known relatively accurately from experimental data. The value of this friction factor is normally shown in so-called Moody diagrams, of which an example is shown in Figure 9.6.

Some empirical relations have also been established for the Moody friction factor. Different relations are valid for different flow regimes. Note that the Reynolds number is calculated using the diameter of the pipe, such that the relation becomes $Re = \frac{\rho v D}{\mu}$ [82].

- Fully developed incompressible laminar flow ($Re < 2320$):

$$f = \frac{1}{Re} \quad (9.5)$$

- Fully developed incompressible turbulent flow:

$$- 2320 < Re < 2 \cdot 10^4$$

$$f = 0.316 \left(\frac{1}{Re} \right)^{0.25} \quad (9.6)$$

$$- 2 \cdot 10^4 < Re < 10^6$$

$$f = 0.184 \left(\frac{1}{Re} \right)^{0.2} \quad (9.7)$$

⁹https://en.wikipedia.org/wiki/Moody_chart

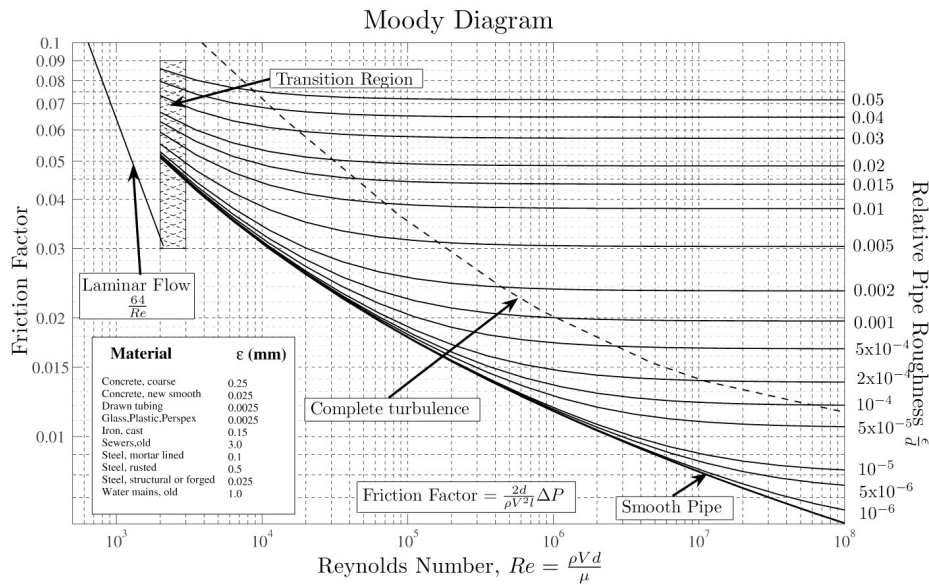


Figure 9.6: Moody diagram showing the friction factor for pipe flow⁹

$$- 3 \cdot 10^3 < Re < 10^7$$

$$0.0032 + 0.221 \left(\frac{1}{Re} \right)^{0.237} \quad (9.8)$$

For non-smooth pipes, the friction factor is not related to the Reynolds number. Instead, it can be calculated using a relation by Nikuradse [82] shown in Equation 9.9.

$$f = 8 \left(2.457 \cdot \ln \left(3.707 \cdot \frac{1}{e/D} \right) \right)^{-2} \quad (9.9)$$

Here, e/D is a measure for the pipe smoothness. Typical values for e are given in Table 9.7 [82].

Table 9.7: Roughness values for different pipe materials.[82]

Material	Roughness value [mm]
Stainless Steel	0.015
Titanium	0.05

If one assumes that the pipe is not entirely smooth, and made out of stainless steel, taking a pipe with an internal diameter of 4 mm, the friction factor becomes equal to 0.0279. This value can also be read off from the graph presented in Figure 9.6. Calculating the velocity from the continuity equation, these become 8.83 and 5.91 ms^{-1} for the fuel and oxidiser respectively. Filling these values in into Equation (9.4), and assuming a conservative pipe length of approximately 2 m (also accounting for the bends in the pipe which increase the pressure drop), the total pressure drop due to piping becomes 4.76 and 3.51 bar for the fuel and oxidiser.

Adding this to the pressure drop over the valves, the fuel tank needs to be pressurised to the maximum operating pressure of 20 bar and the oxidiser tank needs to be pressurised to 19 bar. Filling these values in into equation Equation (9.2) and taking into account the losses of gas due to leakage, the total helium volume amounts to 134 L. This means that 2 helium tanks of 70 L each can be used. From MT Aerospace[83], the mass of these tanks is estimated to be 13.6 kg each. From Table 9.6, the total mass of all the valves is estimated to be 43.6 kg. From the initial configuration of the spacecraft, the total pipe length is estimated to be 10 m. Taking a pipe of 6x1 mm, and a density of stainless steel of 8000 kgm^{-3} ¹⁰, the total mass of the piping becomes 5 kg. Thus, the total mass of the feed system is 48.6 kg. Due to this, the pressurant mass flow will also increase to 1.12 gs^{-1} .

9.7. PROPULSION SENSITIVITY

The sensitivity of the propulsion system can be analysed by looking at the influence of differences in the velocity increments and the spacecraft dry mass on the propellant mass required in each spacecraft. Table 9.8 shows the percentile difference in the propulsion system mass for a difference of 1% in a certain parameter.

¹⁰https://www.engineeringtoolbox.com/metal-alloys-densities-d_50.html

Table 9.8: Sensitivity of propellant mass on changes in different spacecraft parameters.

Changed Parameter	% Change in Propellant Mass	
	OB1	OB2
Dry Mass	5	5
ΔV Escape	-	2.6
ΔV Insertion	1.8	4.8
ΔV Orbit Maintenance	3.4	0.07
ΔV EOL	0.03	0.07
Total ΔV	5.1	7.6

It must also be noted that if the fuel volume of OB1 increases by more than 0.1 L, a bigger tank might have to be selected. This would lead to an entirely new search for tanks. Furthermore, it can be concluded that OB2 is much more sensitive to changes in ΔV than OB1, this is due to the fact that the burn times of OB2 are longer than OB1. This is something to pay attention to and keep in mind in future stages of the design.

9.8. RISK ANALYSIS

Below all the risks associated with the propulsion system are listed.

Table 9.9: Propulsion Risk Register. Likelihood: HU = highly unlikely, U = unlikely, SL = some likelihood, L = likely, HL = highly likely. Impact: M = marginal, S = some, H = high, C = catastrophic

Risk	Consequence	Likelihood	Impact	Mitigation
Explosive Tank Failure	Propellant spilling, damage to spacecraft structure, non-functional main thruster	HU	C	Design safety factors, pressure relief feed system
Tank over-pressurisation	Possible tank failure, higher combustion pressure	L	S	Pressure relief feed system, redundant pressure regulators, pressure range for thruster
Tank leakage	Propellant spillage, possible combustion of fumes, empty tank before EOL	U	H	Careful inspection and testing before launch
Big Feed system leakage	Propellant spillage, possible combustion of fumes, empty tank before EOL	U	H	Testing before launch. Component redundancy
Piping failure	Propellant spillage, non-functional main thruster	HU	C	Very high design safety factors, testing
Valve failure	Blockage of/unwanted propellant flow	HU	H	Component redundancy
Sensor failure	Unknown system performance	SL	M	Component redundancy
Main thruster failure	No large burns possible	SL	H	Testing, usage of RCS thrusters
Fuel and oxidizer fumes coming into contact	Explosion of feed system	HU	C	Redundant check valves

9.9. RELIABILITY, AVAILABILITY, MAINTAINABILITY, AND SAFETY CHARACTERISTICS

An analysis was conducted into the reliability, availability, maintainability and safety of the propulsion system. The system for which this needs extra attention is the feed system. This is the case because it has a lot of possible failure modes and a lot of interconnecting components that all have to fit together while working with very toxic and dangerous propellants.

For this exact reason, all valves that guide propellant to the thruster are redundant. This lowers the chance of failure significantly. Moreover, as explained as well, for safety reasons check valves, burst discs and pyrotechnic valves have been placed at specific points to either keep the propellants from mixing, to prevent premature operation or to shut off the system entirely in case of an emergency. Moreover, a fill drain valve is placed between every section of the valves to prevent the possibility of propellant being trapped between two valves. Multiple passive safety measures are taken and have been included on the tank as well. For example, every tank has two burst discs and pressure relief valves, which prevent the tank from over-pressurising. Furthermore, the tanks do not directly burst at their MEOP. Manufacturers always take into account a relatively large safety factor in the design of the tank. In particular, the burst pressures for the current tanks are 1.5 times larger than the MEOP of the tank. Thus, only in the very rare case that both burst discs or pressure relief valves fail, in addition to a loss of control over the tank valve actuation and rapid pressure build up to over 1.5 times the design pressure, will the tanks burst.

If mixing of propellant through leaks are to be prevented, one could also include for example separation sheets. This will need to be looked into at a later stage of the design. It was decided that the main thruster would not have a spare as it would add too much mass and especially complexity to the system. It is also not deemed necessary as the thruster is fired shortly after launch and not after multiple years of flying through space.

On purpose, the propulsion system was designed only with commercial off-the-shelf (COTS) parts. These parts are readily available and save a lot of costs in developments. Moreover, a lot of experience has been gained in these parts, which increases their reliability. Thus, a slightly non-optimal system is chosen over developing an entirely new one.

9.10. REQUIREMENT COMPLIANCE

Table 9.10 shows the requirement compliance of the propulsion system.

Table 9.10: Propulsion requirement compliance matrix

Identifier	Requirement	Met?	Confirmation
General			
PROP-GEN-05	The reliability of the propulsion system shall be at least 98 %	TBD	-
PROP-GEN-07	The propulsion system shall be restartable	✓	Table 9.2
PROP-GEN-11	The state of the orbit maintenance system shall be changeable	✓	Table 9.2
OB1			
PROP-L1-01	The transfer to L1 shall take at most 30 kg of propellant	✓	Table 9.1
PROP-L1-02	The main engine shall be reignitable at least 2 times	✓	Table 9.2
PROP-L1-03	The orbit maintenance system shall provide at least 117.5 m/s of velocity increment for station keeping	✓	Table 9.2
PROP-L1-04	The propulsion system pointing accuracy shall be 3.44 arcminutes	TBD	-
PROP-L1-05	The total mass of the propulsion system excluding tanks shall not exceed 60 kg	✓	Table 9.11
PROP-L1-06	The total power of the propulsion system shall not exceed 18.2 W	TBD	-
PROP-L1-07	The pressure losses in the feed system shall not be more than 21 bar	✓	Section 9.6
PROP-L1-08	The thrust of the spacecraft main engine shall be at least 400N	✓	Table 9.2
OB2			
PROP-L5-01	The transfer to L5 shall take at most 748 kg of propellant	✓	Table 9.1
PROP-L5-02	The thrust of the spacecraft main engine shall be at least 400N	✓	Table 9.1
PROP-L5-03	The main engine shall be reignitable at least 4 times	✓	Table 9.1
PROP-L5-04	The pressure losses in the feed system shall not be more than 7.9 bar	✓	Section 9.6
PROP-L5-05	The orbit maintenance system shall provide at least 117.5 m/s of velocity increment for station keeping	✓	Table 9.1
PROP-L5-06	The propulsion system pointing accuracy shall be 2.00 arcminutes	TBD	-
PROP-L5-07	The total mass of the propulsion system excluding tanks shall not exceed 80 kg	✓	Table 9.11
PROP-L5-08	The total power of the propulsion system shall not exceed 20.1 W	TBD	-

It can be seen that several of the requirements cannot be checked yet. The pointing accuracy cannot be checked as no selection of thrust vector control actuators has been made. This immediately also means that the power usage of the propulsion system cannot be checked. The mass was initially severely underestimated.

9.11. CONCLUSION AND RECOMMENDATIONS

The same analysis as shown throughout this chapter can be performed for OB1. Table 9.11 highlights the results from this analysis and summarises the findings for OB2. The main thruster for OB1 is chosen to be the same as the one for OB2 because it results in the lowest propellant mass. Moreover, small correction burns can be performed by the ACS system and thus a lower thrust engine for the small burns is not necessary.

Table 9.11: Main parameters of the propulsion system.

Parameter	OB1	OB2
Oxidiser Tank	80197-1	PTP-288
Fuel Tank	80342-1	PTP-393
Pressurant Tank	PVG-50	PVG-70 (2x)
Total Tank Mass [kg]	13.5	58.7
Total Tank Volume [L]	75.5	821
Thruster	AMBR	AMBR
Total Mass [kg]	67.5	112.7

As optimisation of the orbit is performed, it could happen that different tanks have to be selected because it turns out more or less fuel is needed. Moreover, a more accurate estimate of the feed system mass and power usage needs to be made by properly modelling the feed system in CAD software. The pressure drop over the feed system can also be determined more accurately by using, for example, specialised CFD software. The amount of pressurant gas needed was now calculated using analytical equations. This analysis can also be performed more thoroughly after more investigation into the subject. Of course, after the detailed design is finished, the whole system should be tested to verify the calculations and check if it is performing according to specifications. Moreover, integration of the feed system into the spacecraft should be performed. Lastly, proper thrust vector control actuators should be selected and the software for the operation should be written.

10

THERMAL CHARACTERISTICS

Each instrument and subsystem within the spacecraft will generate heat and has a required environment in which it can operate. To comply with this and to ensure safe operation for each of the instruments and subsystems the thermal characteristics need to be determined. Therefore the following question throughout this section can be asked: which thermal environment needs to be generated for all the different instruments and subsystems and how can this be achieved and controlled throughout the entire mission lifetime?

First, all the thermal requirements which are imposed on the thermal control are analysed for each payload instrument and subsystem in Section 10.1. Next two models were made as described in Section 10.2 and Section 10.3. The first model determines the incoming heat flux from the Sun, Earth albedo and Earth infrared radiation throughout the whole mission lifetime (from launch to end-of-life). From these incoming heat fluxes and using the assumption that the satellite can be approximated as one box with the same thermal properties, an overall temperature of the satellite can be calculated. In a second stage, an ANSYS® model will be used to examine the local heat flux and temperatures inside the satellite.

10.1. THERMAL REQUIREMENTS

For every instrument and subsystem, the thermal requirements during the operation were found and are listed in Table 10.1 and Table 10.2. The thermal requirement of the different instruments is coming from Chapter 6. The most driving requirements result in a temperature region in which all subsystems and instruments can operate at 15 °C 30 °C.

Table 10.1: Thermal requirements of different payload instruments

Payload	Min [°C]	Max [°C]
Magnetometer sensor	-100	200
Magnetometer electronics	-55	75
Coronagraph	0	40
Heliospheric imager	-20	30
Magnetograph	-40	70
Faraday cup	-20	40
Faraday cup electronics	-10	30
Most driving requirements:	0	30

Table 10.2: Thermal requirements of different subsystems

Subsystems	Min [°C]	Max [°C]
Communication subsystem [84]	-5	65
Transmitter [84]	10	60
Transponder [85]	0	50
Antenna [45]	-100	100
Antenna dish [85]	-80	60
Antenna elements[85]	-100	150
Power subsystem [84]	0	60
Batteries [45]	10	30
Solar Array [45]	-150	100
Attitude control system [84]	0	60
Attitude control wheel [45]	-10	40
Attitude control electronics[85]	0	40
Earth sensor [85]	-5	50
Propulsion subsystem [84]	5	50
Hydrazine propulsion electronics [85]	5	45
Hydrazine propellant [45]	15	40
General electronics [86]	-10	45
Power regulating unit [85]	0	40
Remote interface unit [85]	-5	60
Structure [85]	-100	100
Most driving requirements	15	30

Besides the thermal requirements imposed on the spacecraft, the power dissipations of each instrument should also be known to fully model the spacecraft thermal control. The SOHO mission was found to have a total dissipated power of 30 W and had a total power usage of 1236W. [87] By scaling the dissipated power according to the ratio of the power usage of the SOHO mission and our mission, values for an internal power dissipation of 10.30 W and 12.31 W were found for OB1 and OB2 respectively. Although this gives a rough indication of the internal heat generation inside the spacecraft, a more accurate estimation could be made by analysing heat dissipation from instruments and spacecraft electronics. However, heat dissipation values of instruments could not be found for most instruments, and the values that were found were negligibly small [88, 89]. Furthermore, heat generation from spacecraft electronics cannot be determined at this

design stage as this requires an estimation of wire resistances of the circuits which in turn depends on aspects like wire length and diameter which have not yet been established. Once more information is known about such properties and the instruments in a detailed design phase, a more accurate estimation of the internal heat generation can be made.

10.2. THERMAL ENVIRONMENT MODEL

In Python™ a model was constructed which incorporates the position of the spacecraft and the earth from GMAT. Using this position data, the distance from the spacecraft to the earth and the sun can be calculated together with effects such as the earth blocking direct sunlight to the spacecraft. The mission was split into four phases corresponding to four different thermal environments to which each spacecraft is exposed. These phases are:

- Phase I: From the start of the launch until fairing separation
- Phase II: From fairing separation until 185 km altitude
- Phase III: From 185 km altitude until spacecraft detachment from the launcher
- Phase IV: From detachment of launcher until end-of-life

During each phase the influence of the three main radiation sources will be analysed; namely direct sunlight, Earth albedo and Earth infrared radiation. Direct sunlight was calculated using Equation (10.1) in which P_{sun} is the power emitted by the sun and d is the distance between the sun and the object. [12]

$$J_s = \frac{P_{sun}}{4\pi d^2} \quad (10.1)$$

It is assumed that the spacecraft receives no solar heat flux if the spacecraft is directly behind the earth from the point of view of the sun. This is modelled in Python™ by performing a geometrical check. The angle between the sun-earth and sun-spacecraft vectors shown in Figure 10.1 is first calculated using the dot product and then used to decompose the spacecraft-Sun vector into a component perpendicular to the Earth-Sun vector and one parallel to it. Two criteria have to be fulfilled for the spacecraft to be in the shadow cone of the earth: the perpendicular component should be smaller than the radius of the Earth and the parallel component should be longer than the Earth-Sun vector. These checks are performed to determine if the satellite receives solar flux at a particular time instant during the mission. Note that a cylindrical shadow cone was assumed for the Earth instead of the umbra-penumbra configuration that occurs in reality since no information could be found about solar intensities inside the penumbra.



Figure 10.1: Spacecraft in shadow of the earth

The second important contribution of radiation is Earth albedo (sunlight reflected from the earth) which can be calculated using Equation (10.2). [12] Although the value of the albedo coefficient a varies locally on the Earth's surface, an average albedo coefficient of 0.4 was assumed over the whole earth. [90, 91] Besides the albedo coefficient the heat flux from albedo is also dependent on the distance from the earth. Since the source of the albedo radiation is strictly speaking at 30 km altitude above the Earth's surface (near the top of the atmosphere where it is reflected), this was chosen as a reference point for computing distances used in Equation (10.2). [90] Lastly, the albedo flux is dependent on the Solar Zenith Angle ϕ (SZA), the angle between the spacecraft and the line connecting the earth and the sun. If the SZA exceeds 90 degrees there is no albedo radiation incident on the spacecraft. [90] This is modelled in Python™ by checking if the distance between the spacecraft and the sun is larger than the earth and the sun.

$$J_a = aJ_s F_a \cos(\phi)$$

$$F_a = \left(\frac{R_e + 30}{d} \right)^2 \quad (10.2)$$

The last form of radiation that the spacecraft is exposed to throughout the mission is the Earth infrared radiation. This can be calculated using Equation (10.3), which is dependent on the distance from the earth and the effective radiating temperature of the earth. [12]

$$J_{ir} = \sigma T_{ir}^4 F_{ir}$$

$$F_{ir} = \left(\frac{R_e}{d} \right)^2 \quad (10.3)$$

The Earth's effective radiating temperature was computed by constructing a heat balance of the Earth using the assumed albedo coefficient as shown in Equation (10.4). [91] As can be seen in Equation (10.4) both the albedo and Earth infrared radiation depends on the distance from the spacecraft to the earth. Beyond a GEO orbit, the distance from the earth is so large that the effects can be considered negligible. [90]

$$J_s \pi R_e^2 (1 - a) = 4\pi R_e^2 \sigma T_{ir}^4 \quad (10.4)$$

The intensities computed for each of the phenomena (sunlight, infrared radiation and albedo radiation) can then be converted to incident power on spacecraft surfaces using Equation (10.5).

$$Q_{\text{sunlight}} = \alpha J_s A_s$$

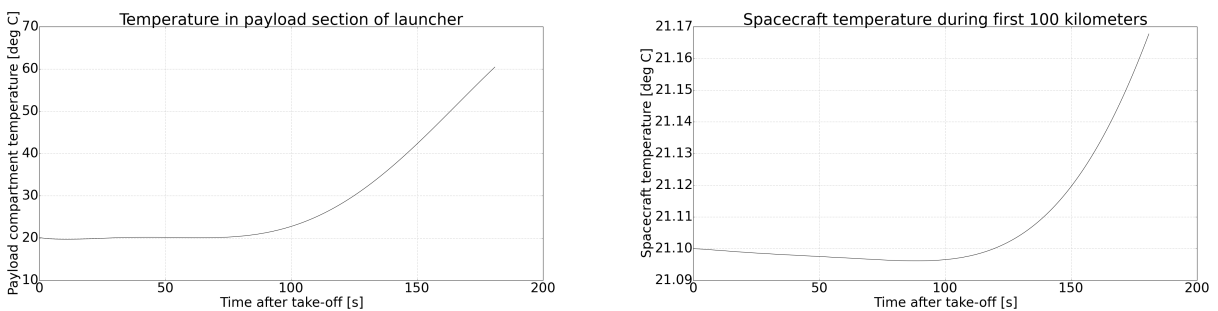
$$Q_{\text{albedo}} = \alpha J_a A_a$$

$$Q_{\text{infrared}} = \epsilon J_{ir} A_{ir} \quad (10.5)$$

In Equation (10.5), α and ϵ represent the absorptivity and emissivity of the different faces of the spacecraft respectively. The absorptivity and emissivity will depend on the foils and coatings used at the faces of the spacecraft. The selection procedure of the coatings will be explained following the description of the different mission phases, and the calculations performed to describe the thermal environment in each of these phases.

PHASE I

The first phase of the mission describes the time from the start of the launch until fairing separation, when both spacecraft are inside the fairing of the launcher. As both spacecraft are protected from Sun and Earth radiation, the only temperature changes the spacecraft will encounter is due to the ambient temperature the spacecraft is exposed to inside the fairing. The temperature profile inside the fairing of the Falcon 9 is given in the manufacturing manual, [57] which was reproduced using a 6th order polynomial as shown in Figure 10.2a.



(a) Falcon 9 payload section temperature profile during launch

(b) Spacecraft temperature during launch

Figure 10.2: Temperature profiles of payload section and spacecraft in phase I

The main assumption made in this phase is that the spacecraft is exposed to the ambient fairing temperature on all sides. This means the effect of the launcher adaptor attached to the bottom face of the spacecraft is neglected. Secondly, it is assumed that the temperature of the spacecraft will only change due to the radiation of energy between the spacecraft

surface and the thermal environment in the fairing (convection is neglected). Furthermore, it is assumed that there is no internal heat generation within the spacecraft during this phase. Lastly, OB2 will be placed inside an inner fairing above OB1, but both spacecraft can be assumed to experience the same thermal environment throughout the launch due to the vent holes present on the inner fairing.

With these assumptions in mind, a thermal balance was set up as shown in Equation (10.6). From the Falcon 9 launch manual the temperature on the launch pad and emissivity of the fairing could be determined to be 21.1 °C and 0.9 respectively. [57] As a first estimate the specific heat of the spacecraft was found to be 600 J·kg⁻¹·K⁻¹. [92] Using the energy balance in Equation (10.6) the temperature variation of the spacecraft could be determined over the launch phase, which is shown in Figure Figure 10.2b. It could be concluded that the spacecraft heats up by about 0.07 °C, which is negligible.

$$\frac{d}{dt}(c_p m_{s/c} T_{s/c}) = Q_{net} = Q_{abs} - Q_{em} = A_{tot} \epsilon_{ir} \sigma (T_f^4 - T_{s/c}^4) \quad (10.6)$$

PHASE II

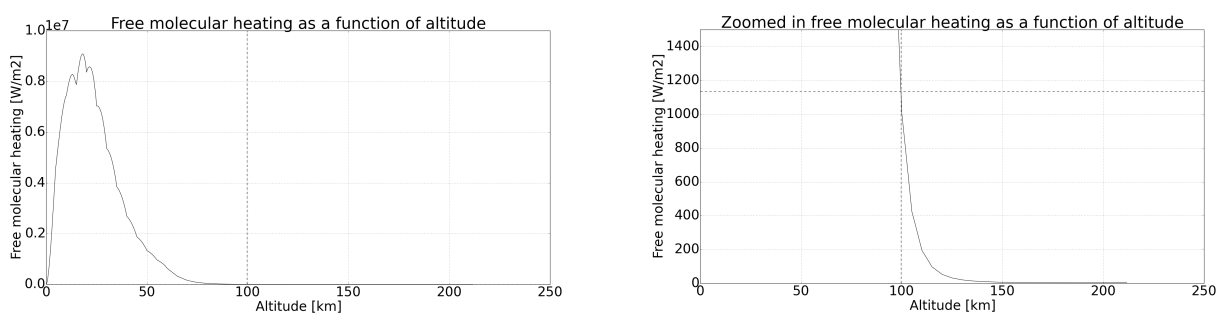
To analyse the second phase, it was first necessary to determine at which altitude the fairing would be deployed (marking the start of this phase). From the launch manual of the Falcon 9, it is stated that the fairing should be removed when the free molecular heating reaches levels below 1135 W·m⁻². [57] The free molecular heating could be determined using Equation (10.7). [90] In this equation there are still three unknowns, namely the accommodation coefficient, the density of the atmosphere and the velocity of the launcher. Generally, the accommodation coefficient is a value between 0.6 and 0.8, but to be conservative a value of 1.0 was selected. [90]

$$J_{fmh} = \alpha \frac{1}{2} \rho V^3 \quad (10.7)$$

Up to a 25-kilometre altitude the density was determined using the International Standard Atmosphere (ISA) model, and from 25 until 185-kilometre altitude the Mean COSPAR International Reference Atmosphere (CIRA) model was used. [93] From these two models the density could be computed at every 5 kilometres. Values between these altitude points were determined through linear interpolation.

To determine the velocity at lower altitudes, a velocity flight profile of the Falcon launcher is needed since GMAT position data (which could be used to compute velocity values) is only available from altitudes starting at 185 kilometres. This data is relatively difficult to find considering SpaceX will not share this kind of information. Therefore optical character recognition from videos of the Falcon 9 launch for the CRS-9 mission was used to obtain the required velocity at different time instances and altitudes.¹

Using these values, the free molecular heating can be calculated and the fairing disposal altitude can be determined. In Figure 10.3a the free molecular heating is shown as a function of altitude. When zoomed in (see Figure 10.3b) the fairing disposal altitude can clearly be seen to be 100 kilometres.



(a) Free molecular heating as a function of altitude for Falcon 9 (b) Zoomed in Free molecular heating around 1135 W·m⁻²

Figure 10.3: Free molecular heating for different altitudes

With the free molecular heating and the fairing separation altitude known, it is still necessary to make some assumptions before one can calculate the temperature variation of OB2 during this phase. First of all, it is assumed that the free molecular heating acts on the front face, the left face is constantly in direct sunlight and the right face is in perfect incident angle for albedo and infrared radiation of the earth. This is the most limiting case in which the spacecraft encounters the most incoming radiation. Again an energy balance can be constructed for this phase, which is shown in Equation (10.8). With this energy balance, it is possible to determine the temperature of the spacecraft, which can be seen in Figure 10.4a.

¹<https://forum.nasaspaceflight.com/index.php?topic=40983.0>

$$\frac{d}{dt}(c_p m_{s/c} T_{s/c}) = Q_{\text{albedo}} + Q_{\text{infrared}} + Q_{\text{sunlight}} + Q_{\text{fmh}} + \sum P_{\text{diss}} - Q_{\text{emitted}} \quad (10.8)$$

OB1 is still in the inner fairing of the launcher and will thus not experience any sunlight or earth radiation. Therefore a different approach for OB1 is developed. Since the launcher is in space with a surrounding temperature of 4 K², it is assumed that space affects the temperature inside the inner fairing through radiation (still no convection and conduction are assumed). Then, the temperature inside the inner fairing affects the spacecraft temperature in the same way as during phase I. The temperature change of OB1 during phase II is shown in Figure 10.4b.

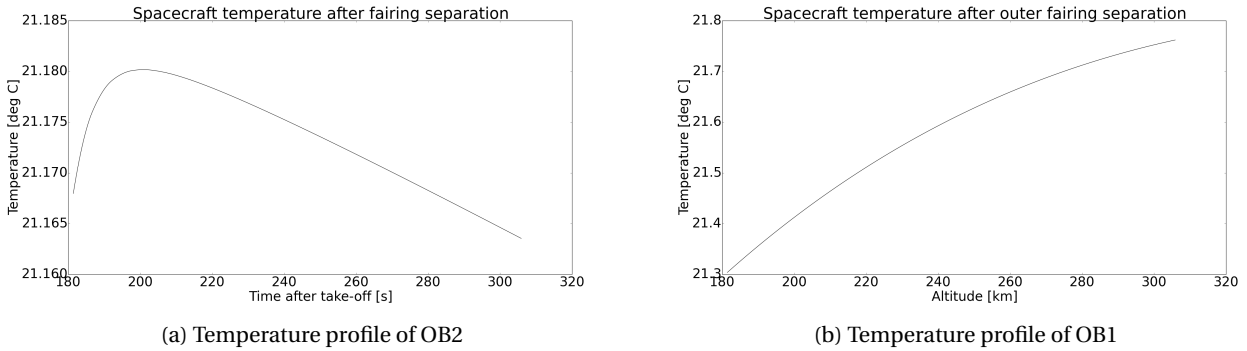


Figure 10.4: Temperature profile of spacecraft during phase II

As can be seen in Figure 10.4a, OB2 first heats up following fairing separation (likely due to an influence of free molecular heating that is still rather high). This increase in temperature quickly levels off and transitions into a decreasing temperature, mostly since the spacecraft are now radiating heat towards space and the influence of free molecular heating decreases rapidly with altitude. Note that the temperature change over this phase is relatively insignificant considering the maximum experienced change is about 0.15 ° C. OB1 heats up by about 0.4 ° C during this phase. This is because although the temperature inside the inner fairing will drop, it will not decrease to a value far below the spacecraft temperature in the small time period that makes up phase 2.

PHASE III

During the third phase, the spacecraft is not free to point wherever it wants as it is still attached to the launcher. One of the assumptions made during this phase is that the bottom face will not see any sunlight or Earth radiation as the spacecraft is fixed to the launcher on this face. The same is true for the top and bottom faces of the spacecraft since the trajectory is almost always in the ecliptic plane. It is also assumed that the launcher is rigidly attached to the launcher such that the orientation of the launcher coincides with that of the spacecraft. As this analysis starts at 185 km and GMAT data is also available beyond this altitude, the trajectory of the launcher, and thus the orientation of the spacecraft is determined from the difference between two data points in GMAT.

With this orientation, the angles between the earth and the spacecraft and the sun and the spacecraft can be found. This is done by first finding the position vector (the vector between two data points) and subsequently applying transformation matrices, to arrive at the vector normal to the right face and the vector normal to the left face (which are simply the position vector rotated clockwise by 90° and 270° respectively). From these three vectors, the influence of the solar flux can be estimated for each surface of the spacecraft. Using a set of geometrical conditions, the surfaces experiencing solar radiation and albedo could be determined, together with the view factors based on the spacecraft orientation. The view factor is then multiplied with the solar intensity together with the area to determine the incident power on the surface.

For OB2 this phase occurs from the outer fairing separation until launcher detachment. The temperature of the spacecraft was calculated using the energy balance shown in Equation (10.9) and temperature variations during this phase are shown in Figure 10.5a.

$$\frac{d}{dt}(c_p m_{s/c} T_{s/c}) = Q_{\text{albedo}} + Q_{\text{infrared}} + Q_{\text{sunlight}} + \sum P_{\text{diss}} - Q_{\text{emitted}} \quad (10.9)$$

For OB1, the sequence of this phase is slightly different. Initially, the spacecraft is surrounded by the inner fairing, and upon detachment of OB2 from the launcher, this fairing is released. While OB1 resides in the inner fairing the thermal environment will be assumed to be the same as for phase II (no direct sunlight and/or earth radiation). The temperature inside the inner fairing will be lowered by radiation to the space environment, and from the inner fairing temperature, the spacecraft temperature can be determined. From the point that OB2 is detached and the inner fairing is released,

²<https://sciencing.com/temperatures-outer-space-around-earth-20254.html>

the same calculation procedure will be used for OB1 as was used for the third phase of the OB2 (calculation of the angles of OB1 with respect to the Sun and Earth such that the radiation on each side of the spacecraft can be calculated). The results of this analysis for phase three of the launch are shown in Figure 10.5b.

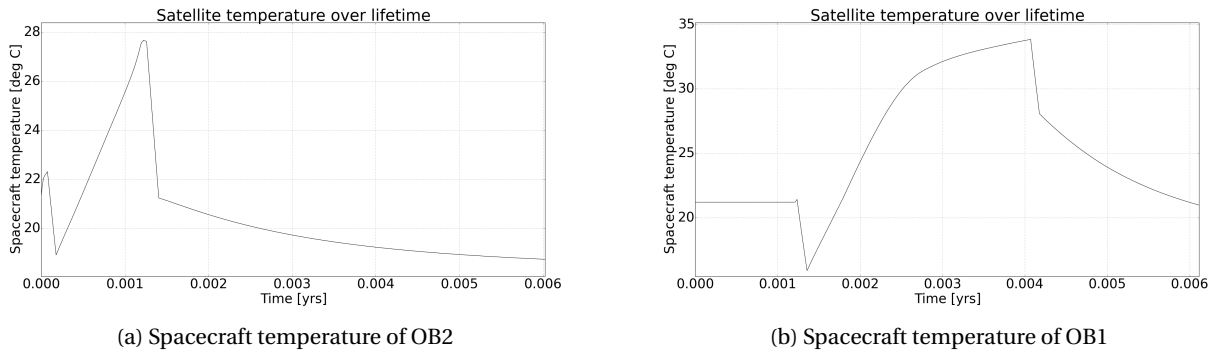


Figure 10.5: Spacecraft temperature in phase III

When one looks closely to the graphs in Figure 10.5 some steep descending parts are visible, which are partly attributed to the change of phase occurring around the 0.0012-year mark before OB2 detaches and 0.0041 years before OB1 detaches. This phase change drastically alters the heat fluxes around the spacecraft at these times, which would not be observed in reality.

PHASE IV

Phase IV is by far the longest phase of the spacecraft mission. This phase starts after launcher detachment and ends at end-of-life. It is assumed that throughout this phase the front face and the solar panels of the spacecraft are constantly pointed towards the Sun. It is also assumed that the spacecraft is in the ecliptic plane, such that the top and the bottom face of the spacecraft will not experience solar or Earth radiation. Similar to phase III, a sequence of geometrical conditions could be used to determine whether the spacecraft is located to the left or right of the Earth, and behind or in front of the Earth. Together with computed view factors, this information can be used to determine the incident power on each surface from the different radiation sources.

From the energy balance in Equation (10.9), the temperature of the spacecraft for OB1 and OB2 can then be calculated. The results of OB2 can be found in Figure 10.6a and the results for OB1 are given in Figure 10.6b. The dashed line in both figures indicates the end-of-life manoeuvre, after which the temperature will increase and decrease more drastically. However, the end of life phase is no longer a concern for the thermal control subsystem, as the temperature variations will simply repeat as the spacecraft remains in orbit. From the point the spacecraft performs the end of life burn, it is no longer important that the spacecraft meet the thermal requirements.

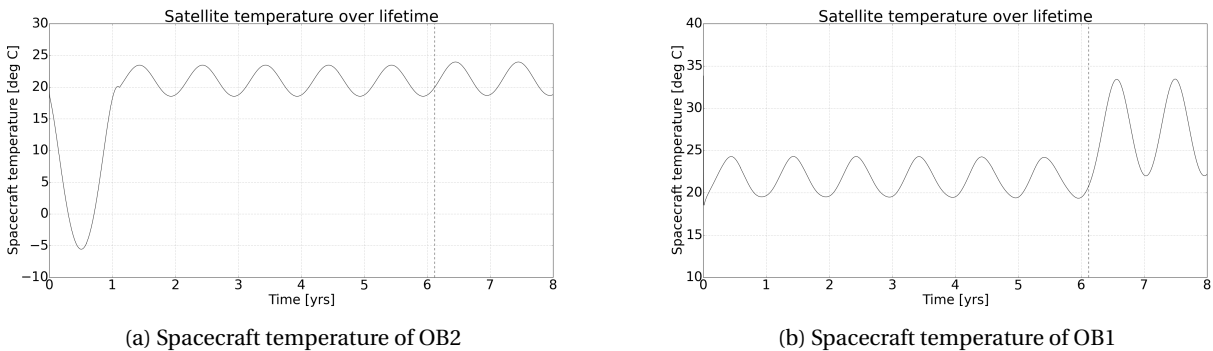


Figure 10.6: Spacecraft temperature in phase IV

As can be observed in figure Figure 10.6b, OB2 will reach a minimum temperature during the transfer period of -5°C, which is far below the lower limit of the operational temperature requirement. However, as this occurs during transfer in which the critical instruments are not yet operational, it is allowed to have these low temperatures over this time period. It is however recommended to look into this further in the detailed design. OB1 will experience temperatures between 15°C and 30°C, which are well within the temperature requirements.

MATERIAL SELECTION

For each of the previously explained calculations to determine the temperature of the satellites, emissivity and absorptivity values were used for the different surfaces according to the coatings selected for the surfaces. The selection of coatings for the surfaces was an iterative process, in which different coatings/foils were chosen until the computed steady state temperature of the spacecraft during stayed between the required interval temperatures during phase IV. As the coating choice was also dependent on the orbit trajectory and dimensions of the spacecraft, these aspects had to first be finalised before coatings for the thermal control could be chosen.

For both spacecraft, it is known that both albedo and infrared radiation will mostly radiate to the left side of the spacecraft. It is also known that the orientation of the spacecraft is such that the front face of the spacecraft will always point towards the sun. Using this information together with the iterative procedure, the appropriate coatings and foils for each side could be determined. The selected coatings are shown in Table 10.3 and Table 10.4 for L5 and L1 respectively.

Table 10.3: Different coatings/materials for each side of OB2

Side	Coating/material	Absorbptivity	Emissivity
Front	Sherwin Williams F8W2030 with Polasol V6V241 [94]	0.36	0.87
Back	Electroplated gold [94]	0.23	0.03
Right	Electroplated gold [94]	0.23	0.03
Left	Y9360- 3M Aluminized Mylar tape [94]	0.19	0.03
Bottom	Electroplated gold [94]	0.23	0.03
Top	Electroplated gold [94]	0.23	0.03

To ensure a passive thermal control system for OB2, the front face (which is always viewing the sun) will use white paint with a relatively high absorptivity and emissivity. For all the other faces the main objective was to limit the emissivity of the rest of the spacecraft, therefore electroplated gold was chosen. Lastly, for the left panel, which was most sensitive to Earth radiation, a slightly smaller absorptivity than electroplated gold was chosen, to limit temperature variations close to the Earth.

To apply the coatings or materials on the surface different techniques will be used. Paints and coatings will be sprayed upon the outer most layer of the spacecraft panel and left to dry. Foils will be wound around the desired panel. These coatings or materials should sustain until end-of-life of the mission, but can degrade over time. This gives a decrease or increase in absorptivity and emissivity. Only this effect will not be much more than 0.03. [95, 96]

Table 10.4: Different coatings for each side of OB1

Side	Coating	Absorbptivity	Emissivity
Front	Hughson white paint Z-202 + 1000 ESH UV [94]	0.40	0.87
Back	Electroplated gold [94]	0.23	0.03
Right	Electroplated gold [94]	0.23	0.03
Left	Copper foil tape sanded [94]	0.26	0.04
Bottom	Kannigen - Nickel alloy [94]	0.45	0.08
Top	Kannigen - Nickel alloy [94]	0.45	0.08

For OB1, the coatings indicated in Table 10.4 will be used. For similar reasons as OB2, the front of the spacecraft is almost always in direct view of sunlight. To extract enough heat from the sun, white paint was used for the front face. For the left side, which receives the most radiation from Earth, a Copper foil was used to increase the temperature during transfer. For the back and right side, the main objective was to limit the emissivity of the material, to limit heat radiation from the spacecraft. The combination of electroplated gold for the back and right side and a Nickel alloy for the top and bottom side resulted in a temperature in the range of 20°C.

10.3. ANSYS® MODEL

Having analysed and quantified the thermal environment of both satellites over the mission's lifetime, the next step in the thermal analysis can be made. A transient thermal analysis can be performed on the main components of the spacecraft to calculate local temperature distributions and their variations throughout the mission. Using such a numerical model, it can be determined whether temperature requirements of critical components can be met with only passive thermal control (based on local placement within the spacecraft) or whether active control is required. In this section, the methodology behind this model will be described and the results presented and analysed.

10.3.1. METHODOLOGY

The localised thermal analysis was performed through a transient thermal analysis on ANSYS Workbench. The analysis was performed for the OB1 satellite over the time region from the point of detachment from the launcher till the start of the End Of Life procedure (phase IV). As the phases of flight preceding, this time region were shown to have a minimal effect on the temperature of the spacecraft these phases were not analysed further using this method.

The first step in the analysis involved specifying the relevant geometry. For this particular case, CAD models of the spacecraft panels, the inner cylindrical structure, the propellant and pressurant tanks and the coronagraph were used as geometry for the model. The components included in the models were the ones with the most stringent thermal requirements. The model was limited to these components and instruments in order to limit the required number of mesh elements (the license is limited to 256k mesh nodes) and to simplify the meshing process itself. For similar reasons, the geometry of the instruments was also simplified to basic cylindrical/cuboidal shapes.

The next step in the analysis consisted of specifying the modes of heat transfer that occur between the different spacecraft components. Over the analysed time period, both spacecraft receive a time varying solar flux on the sun-pointing panel and on the sun-pointing face on the coronagraph. All outer faces of the spacecraft panels were considered to radiate energy towards space. Additionally, surface to surface energy transfer between the inner components of the spacecraft through radiation was also considered. Lastly, the internal heat generation of the spacecraft itself was also accounted for (10.3 and 12.31 Watt for L1 and L5 respectively, as explained in Section 10.1). Since no knowledge exists about the actual distribution of this heat over the spacecraft the power from this heat source was assumed to be distributed equally amongst all inner surfaces within the spacecraft.

In order to calculate the amount of energy radiated from surface to surface inside the spacecraft, ANSYS computes the view factors between user specified surfaces. The program then analyses the radiation and conduction occurring for all bodies considered in the model, using the thermal properties attributed to each body. The thermal properties used in the model are specified in table Table 10.5. Note that in the case of the Nomex spacecraft panels, the volume averaged thermal properties were computed and used according to the proportion of carbon fibre and honeycomb structure that made up the panels.

Table 10.5: Material properties used in ANSYS®

Material	Aluminium	Nomex panels	Titanium	Nitrogen Tetroxide	Hydrazine	Helium
Specific heat [Jkg ⁻¹ K ⁻¹]	910 [97]	1196.2 [97]	526.3 [97]	4690 [98]	1122.5[99]	5190 ^a
Thermal conductivity [Wm ⁻¹ K ⁻¹]	134 [97]	0.645 [97]	6.7 [97]	0.131 [98]	0.314[99]	0.142 ^b
Density [kgm ⁻³]	2810 [97]	133.4 [97]	4430 [97]	550.4 [98]	1021 [99]	179 ^c
Emissivity [-]	0.05[97]	0.85 [97]	0.68 [97]	-	-	-
Absorptivity [-]	0.125v[97]	0.85 [97]	-	-	-	-

^a https://www.engineeringtoolbox.com/specific-heat-capacity-gases-d_159.html

^b https://www.engineeringtoolbox.com/thermal-conductivity-d_429.html

^c https://www.engineeringtoolbox.com/density-materials-d_1652.html

Since the solar flux varies over time, ANSYS requires values for this property to be specified at each time step. As the energy equation to be solved is non-linear with temperature (due to radiative terms) ANSYS defines sub-steps between these time-steps over which the load is incremented from the value of one time-step to the next. For each of these sub-steps, a series of iterations is performed to reach a converged solution for each sub-step and thus for each time-step. [100] The solar flux load was discretised to values for a specific number of time-steps (to keep computational time manageable). Since ANSYS linearly interpolates between load values specified for time-steps and defines substeps at linear increments of specified load values, the discretisation was done such that the linearly interpolated variation of this property still properly represented the same approximate variation of the original solar flux curve over time. The discretisation of the solar flux for OB1 is shown in Table 10.6.

Table 10.6: Discretisation of heat flux of OB1 and OB2

Time L1 [s]	0.0E0	1.4E7	2.9E7	4.5E7	6.2E7	7.7E7	9.3E7	1.1E8	1.3E8	1.4E8	1.6E8	1.7E8	1.9E8
Heat flux L1 [W/m ²]	533	581	544	581	544	581	544	581	543	580	543	580	542

From a preliminary analysis using a coarse mesh, an approximate model of the spacecraft, and an analysis spanning the complete time of phase IV with discretised load values, it was discovered that beyond times 2.93E+07 and 6.09E+07 for L1 and L5 respectively, the solar flux displayed a repeating cyclical variation that corresponds to the final orbit. Due to this repeating solar flux variation and the limited expected influence of internal heat generation, the temperature also varied

cyclically over these time periods. Therefore, the transient thermal analysis was only performed until these times were reached (with the same load discretisation over time as shown in Table 10.6).

Having defined the geometry and thermal boundary conditions for the model, the final and arguably most important step can next be performed by designing a mesh for the different geometries. Within ANSYS one can choose between various different meshing methods, each with their own advantages and disadvantages. The meshing method and element shape were selected mostly such that a desired mesh quality was achieved with the least number of elements, to minimise the required computational time. Average element sizes were specified as requirement for the mesh generation and were also chosen such that a good quality mesh was still achieved while keeping the number of elements used as low as possible. The quality of the mesh was checked using a mesh metric known as the skewness of the elements, which defines how far from its ideal geometry the element shape is. For each of the meshes, a skewness value lower than 0.5 was aimed for (values below 0.5 indicate a 'good' mesh quality, while values below '0.25' indicate an 'excellent' mesh quality [101]).

Table 10.7: ANSYS® mesh characteristics for OB1

Shape	Mesh method	Element type	Average element size OB1 [cm]	# elements OB1	Skewness OB1
Spacecraft panels	tet patch conforming	tetrahedral	4.5	4282	0.28
Cylindrical structure	multizone hex/prism	hexahedral	4.0	2880	0.03
Pressurant tank	sweep	hexahedral	2.5	3215	0.49
Oxidizer tank	tet patch conforming	tetrahedral	1.52	2041	0.41
Fuel tank	tet patch conforming	tetrahedral	2.07	2071	0.41
Coronagraph	sweep	hexahedral	2.76	660	0.22

10.3.2. MODEL RESULTS

The temperature distribution was calculated over the analysis time for each of the bodies in the model during each of the sub-steps. Maximum, minimum and approximate average temperatures observed by each of the bodies are shown in Table 10.8 for OB1. fig. 10.7 shows the resulting temperature distribution at end of life for the different spacecraft components (the spacecraft panels were not shown to improve visibility of the inner components) for OB1. It also shows the mesh used to approximate the geometry of the model.

Table 10.8: Temperature results of the ANSYS model for components of OB1

Body	Max. temperature [°C]	Min. temperature [°C]	Average temperature [°C]
Spacecraft panel	40	-40	0
Cylinder	30	-35	0
Coronagraph	21.1	7.55	12
Fuel tank	-0.78	-25.5	-17
Oxidizer tank	44	-7.3	20
Pressurant tank	46	-18.4	15

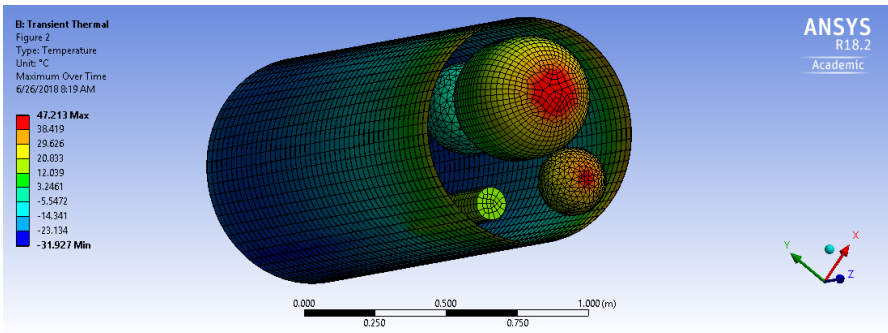


Figure 10.7: OB1 ANSYS temperature results

As can be seen from Table 10.8, the spacecraft panel and cylinder are exposed to temperature ranges well within the capabilities of the materials. The coronagraph also meets its thermal requirements. However, based on the overly cold temperatures of the propellant and pressurant tanks, thermal insulation will be required in order to satisfy the thermal requirements for these components.

Although this analysis gives a good preliminary indication of the expected local temperature ranges for different components, there are several ways in which this analysis can be expanded on in a detailed design phase to yield more significant results. Firstly, if access to a cluster of computer cores could be achieved the available computing power would increase, which would allow the effect of solar panels on the component temperatures to also be modelled. Increased computing power would also make it possible to increase the number of mesh elements (so more instrument and components could be included in the analysis), up till the limit on the number of elements for a student answer's license. Lastly, it would be highly useful to conduct a short term transient analysis to model the effect of an engine burn on the temperatures of the inner spacecraft components (this is most relevant for OB2 considering burn times of the engine on this spacecraft are relatively long compared to that of the engine on OB1).

10.4. SENSITIVITY ANALYSIS

A sensitivity analysis can be performed on various aspects of the thermal control subsystem. The sensitivity of the solar fluxes from the thermal environment model to the various input properties of this model could, for example, be investigated. On top of this, it might also be useful to perform a sensitivity analysis on the results of the numerical model constructed using ANSYS. The influence of a change in the incident solar flux (an input parameter for the numerical model) on the temperatures of different spacecraft components would be interesting to analyse for example. Although the latter study could not be performed due to a lack of time and the excessive time required for each run of the numerical model, it is definitely an interesting aspect to investigate in a subsequent design phase. This is especially the case considering such a sensitivity study would also provide insight into which input variables for the numerical model are driving in determining whether temperature requirements are met or not for certain spacecraft components.

The sensitivity analysis performed on the thermal environment model was used to determine how the change of several parameters influence the final steady state temperature of the spacecraft. The parameters that were analysed included the absorptivity and emissivity of the different spacecraft surfaces since these design parameters could have slightly higher or lower values in reality due to production. Other variables analysed for sensitivity included the albedo coefficient and the effective Earth radiating temperature, as there are different ways to model albedo and Earth infrared radiation. The effect of a slightly different spacecraft specific heat was also determined, as the overall value used in the analysis was taken from a reference mission and this value could be quite different in reality (and in fact is different for different spacecraft components). Lastly, the effect of changing the front face area and the distance to the Sun was also determined. The results of the analysis can be found in Figure 10.8.

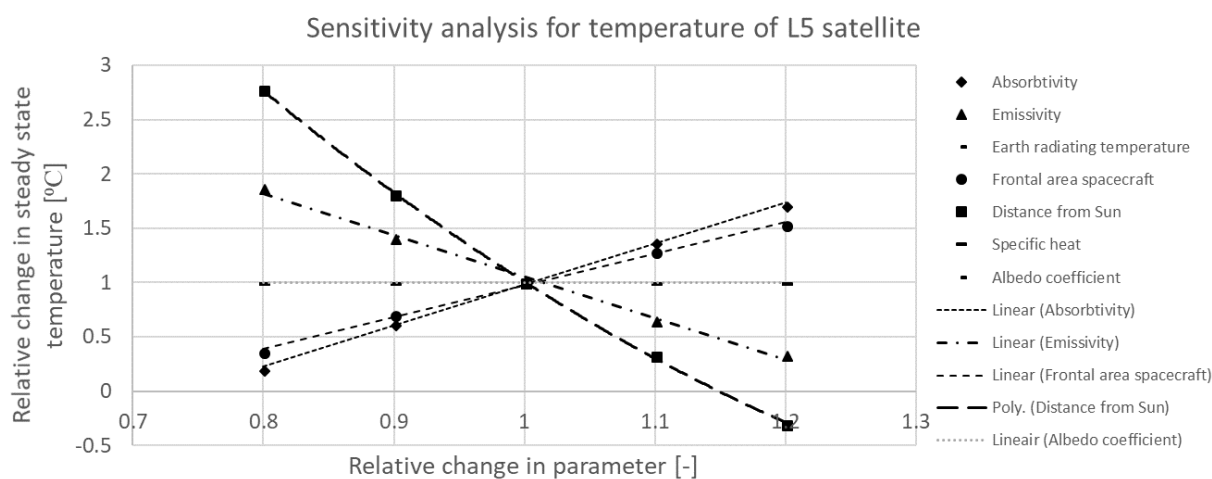


Figure 10.8: Sensitivity analysis for external heat model

From the graphic results of the sensitivity analysis shown in Figure 10.8, it can be noted that almost all parameters have a linear correlation when the parameter is changed. However, for the distance to the Sun, this is not the case since the solar heat flux seen by the spacecraft is a quadratic relation as shown in Equation (10.1). The least sensitive parameter is the frontal area, and the most sensitive parameter is the distance from the sun.

For the sensitivity analysis large changes of the parameters were analysed, but in reality, only small changes due to errors (e.g. production errors) are expected to occur. It could be expected that the emissivity and absorptivity would change slightly, but in case this is for example in the order of 3 %, the steady state temperature change will be in the order of 2°C. Although an error in the distance from the Sun would have the most influence on the steady state temperature, a change of 1 % in the distance to the Sun is highly unlikely to occur as this would correspond to an error in the orbit position of 1,481,019 km, (as reference the halo orbit that is used at L1 is 600,000 km). The same is true for the frontal area, where

a 1 % change in frontal area corresponds to increasing/decreasing the dimensions of the cross section by 16 mm (which is more than the thickness of the structure). Furthermore, the sensitivity of the Earth radiating temperature and Earth albedo coefficient is negligible, because albedo and Earth infrared radiation are only of importance at the beginning of the transfer and not at L1 or L5. Lastly, the sensitivity of the specific heat was also negligibly small, which was not expected. It seems more logical that the specific heat of the spacecraft would be highly influential in determining the final temperature. Therefore this should be investigated in more detail in further analyses.

10.5. VERIFICATION AND VALIDATION

Having constructed thermal models each describing important parameters for the thermal control system, it is important to verify and validate these models to ensure they function properly and produce the right results. The verification and validation steps performed will be described in this section.

10.5.1. VERIFICATION

The first verification method used for the thermal environment model consisted of using two different models to model the geometry in phase III, this was done by the way described in the section and a second method had been established. This was to determine the angles of the Earth and the Sun with respect to the spacecraft position vector. Once these angles were known and if it was known that the spacecraft was before or after the Earth, the contributions of the Sun and Earth to each side of the spacecraft could be computed. For this verification model, the geometry as shown in Figure 10.9 was used.

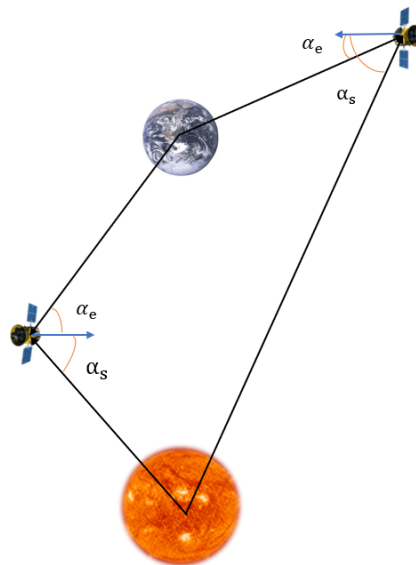


Figure 10.9: Verification geometry for phase III

Moreover, the magnitude of the area exposed to the Earth and the Sun were plotted and analysed together with the position of the spacecraft to observe if the shape and magnitude of these graphs correspond with what is expected. Specifically, the trajectory of the spacecraft and the area of each side (front, back, left and right) exposed to each type of radiation (direct sunlight, albedo and Earth infrared) was plotted. This can be seen in Figure 10.10.

Comparing this to the trajectory of the spacecraft, the parts in which the spacecraft was in the shadow cone of the Earth can be seen (see Figure 10.10a and Figure 10.10d) together with the effect of the solar zenith angle (see Figure 10.10c). Besides this, an occasional immediate drop or increase in exposed area could be noticed (see Figure 10.10a and Figure 10.10f). This is due to a change in phase (and thus thermal environment), specifically from phase III to phase IV. Furthermore, for the albedo radiation first, a peak on the left face is observed, followed by a peak on the right face and then another on the left face (see Figure 10.10c and Figure 10.10e). This corresponds exactly with the spacecraft coming from behind the Earth to behind it and back. Another aspect that can be noted is that the heat flux for the back face is zero during the entirety of phase III (which is shown in Figure 10.10b). This is because the back phase is still attached to the launcher and therefore will not receive any radiation.

For both OB1 and OB2 the shapes and magnitudes have been analysed and some small errors have been extracted. For example, the area of the front face became negative when the spacecraft was positioned before the Earth. Furthermore some steep descending or increasing parts were discovered, this appeared not to be a programming error, but an integration error. This was because the GMAT data did not have a constant step size, but a step size which was very small (in

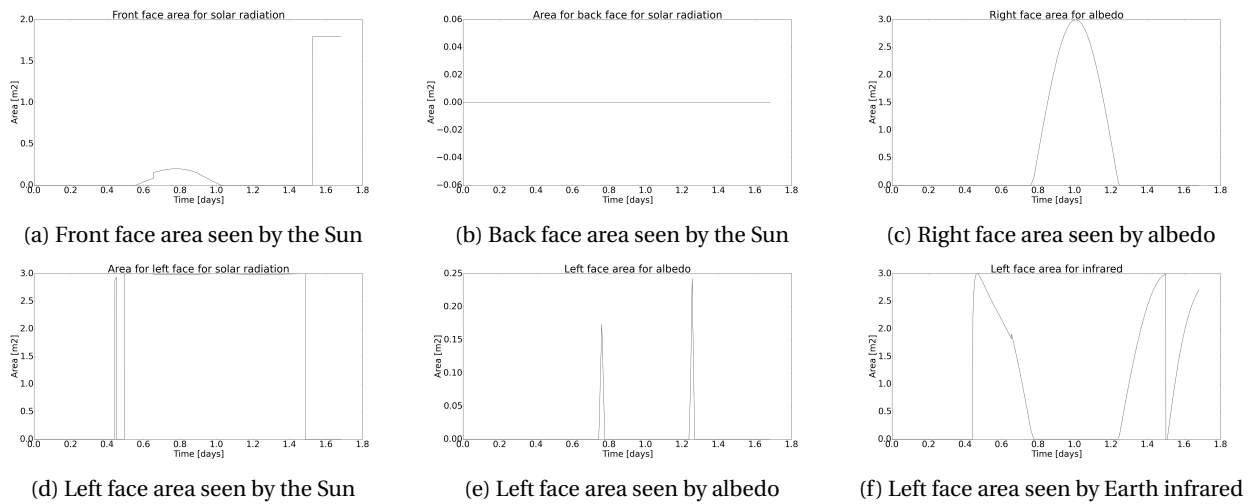


Figure 10.10: Different spacecraft areas on which the Sun and Earth will radiate

the order of seconds) during burn periods. For the rest of the trajectory the step size was in the order of one hour. These changing step sizes cause these steep parts in the graphs.

Lastly, from these graphs, it was discovered that the transition between different phases (mainly phase III and IV) was not smooth. This is because in a single time instance the entire satellite turns from the orientation of the launcher to a state where the front face is pointed towards the sun. This results in a large fluctuation in the receiving sunlight and Earth radiation, this explained the steep parts of the graphs during these transition moments (especially in L1).

The average spacecraft temperature values computed using the thermal environment can also be compared to average temperatures from the ANSYS model for OB1. Although an average temperature was too complex to compute numerically on ANSYS, a qualitative comparison was performed. From the average temperatures observed on ANSYS for OB1, an average temperature offset of approximately 15° could be observed from the temperatures in the thermal environment model. This offset in temperature could be caused by the use of an inaccurate average specific heat value for the spacecraft in the thermal environment model.

10.5.2. VALIDATION

The only aspect of the thermal environment model that was validated was the albedo radiation of the Earth. This was done since there are many different models to analyse the albedo of the Earth. Therefore the results of our model could be compared to the results of a more complex model constructed by ESA. The thermal environment model gave an albedo factor of 0.3, an altitude of 800 kilometres, a solar zenith angle of 0° and an albedo heat flux of 326 Wm^{-2} . The ESA model predicted an albedo level as shown in Figure 10.11, which corresponds to 340 Wm^{-2} . [102]

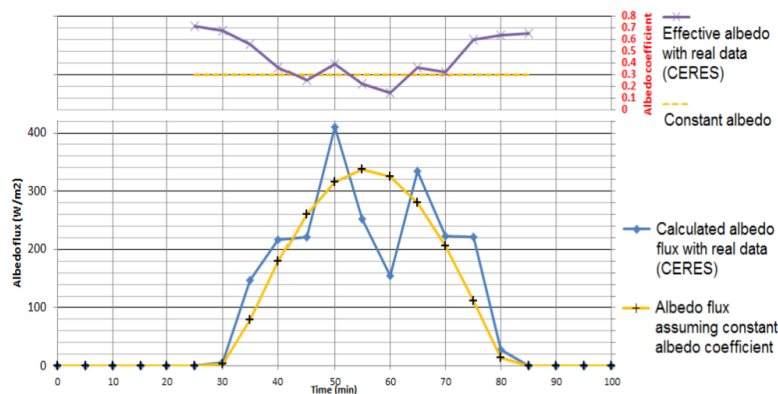


Figure 10.11: Albedo model from ESA [102]

In Figure 10.11 ESA used two models, namely albedo flux values calculated based on a locally varying albedo coefficient with real data and calculations assuming a constant albedo coefficient. As one can see the results from the thermal environment model differ by only 4.3 % from the results of the ESA model with a constant albedo coefficient.

10.6. RISK ANALYSIS

In this section, the risks with regard to the thermal subsystem will be analysed. Risks, their likelihood of occurrence, their impact and mitigation measures to minimise the risks are shown in Table 10.9.

Table 10.9: Thermal Risk Register. Likelihood: HU = highly unlikely, U = unlikely, SL = some likelihood, L = likely, HL = highly likely. Impact: M = marginal, S = some, H = high, C = catastrophic

Risk	Consequence	Likelihood	Impact	Mitigation
Production errors in coatings/foils	Absorbitivity and emissivity change, thus temperature can decrease/increase	L	M	Tests after production of materials
Coating detachment	High absorbitivity of front face, high temperature increase	U	H	Choose coating with a lifetime of at least 6 years
Foil tears apart	High emissivity of spacecraft, temperature will drop significantly	U	H	Careful placement and attachment of foil
Spacecraft will loose orbit control	Distance to the Sun changes, thus temperature of spacecraft will change	SL	M	Redundancy in orbit control maintenance

10.7. RELIABILITY, AVAILABILITY, MAINTAINABILITY, AND SAFETY CHARACTERISTICS

From the risk analysis performed in the previous section, a reliability analysis can be carried out. The reliability for the thermal subsystem is determined mainly from statistical data. It is determined to be 0.995 for a space mission that should function properly for at least six years (five years of mission duration with the additional transfer time). [49] This, of course, depends on whether a passive or active thermal control system is used. An active control system is a more complex subsystem and therefore has a lower associated reliability. Besides the risks mentioned in the risk analysis, there are no further risks for passive control systems. In the statistical data of J. Castet et al. no distinction was made between active and passive thermal control systems. Other studies such as H. Hecht et al. do make this distinction and claim the failure rate of passive control systems is one quarter that of active systems. [49, 103]

It can be concluded that the reliability of the coatings and foils is sufficiently high such that there is no need for measures such as including two layers of foil on top of each other. The safety of the spacecraft can, therefore, be guaranteed without extra measures. Detachment of coatings or foils could be a mission critical event, but in case of small failures, this will have a negligible effect on the spacecraft temperature. Care should thus be taken during production and attachment of the foils and coatings.

Regarding availability, the coatings and foils that are used for the thermal control are standard NASA coatings or foils. [94] These can thus be acquired and used relatively easily. Another important aspect is maintainability, which can be divided into two phases, namely maintainability during the operational lifetime and maintainability during production. The operational lifetime maintainability is not something that needs to be considered as it is firstly very difficult to perform maintenance for the SWAN mission, and secondly not necessary considering a passive control system is used. For maintainability, during the production process, it is important to realise that the foils should be implemented at the very end of the spacecraft assembly process so that everything is still accessible if an instrument or subsystem fails or does not pass tests.

10.8. REQUIREMENT COMPLIANCE

All the requirements for the thermal subsystem are shown in Table 10.10. As can be seen, all the requirements are met, with the reasoning for this shown in the several sections describing this subsystem.

Table 10.10: Thermal Requirement Compliance Matrix

Identifier	Requirement	Met?	Confirmation
TRM-GEN-01	The thermal control system shall be activated no later than 0 seconds after the last stage separates	✓	Section 10.2

TRM-GEN-02	The thermal control system shall be able to determine the temperature with an error of at most 0.1 K	✓	Section 10.2
TRM-GEN-03a	The thermal control system shall keep the temperature in the satellite below 303 K during the payload operational phase	✓	Section 10.2
TRM-GEN-04a	The total mass of the thermal control system of OB1 shall not exceed 17.6 kg	✓	Section 10.2
TRM-GEN-04b	The total mass of the thermal control system of OB2 shall not exceed 20.4 kg	✓	Section 10.2
TRM-GEN-05a	The total power used by the thermal control system of OB1 shall not exceed 81.0 W	✓	Section 10.2
TRM-GEN-05b	The total power used by the thermal control system of OB2 shall not exceed 89.1 W	✓	Section 10.2
TRM-GEN-07	The total cost of the thermal control system shall not exceed €5 mln	TBD	-
TRM-GEN-08	The reliability of the thermal control system shall be higher than 99.5 %	✓	Section 10.7
TRM-GEN-09	The thermal control system shall keep the temperature in the satellite above 288 K during the payload operational phase	✓	Section 10.2

10.9. CONCLUSION AND RECOMMENDATIONS

To conclude this section, the thermal analysis will be evaluated and some final recommendations for a detailed design will be given.

With the thermal requirements given in Section 10.1, the thermal environment could be modelled. From these requirements, it became clear that the average spacecraft temperature should be between 15°C and 30°C, where the instruments limiting these requirements were the heliospheric imager and the coronagraph.

The thermal environment was modelled from launch to end-of-life. From the average spacecraft temperatures computed using this model, it seems that for L1 it is possible to keep the temperature between 15°C and 30°C (also during the transfer) using only passive control through selection of different coatings and foils. The local temperatures of the different spacecraft components were checked using a numerical model constructed on ANSYS®. This model indicated that for OB1 the structural components of the satellite and the coronagraph conform to the thermal requirements. However, thermal insulation layers will need to be included on the pressurant and propellant tanks to ensure these components also satisfy the requirements.

While the thermal environment model indicated OB1 meets the thermal requirements, OB2 had more problems with the temperature requirements set. During the transfer to L5, the temperature was found to drop to -5°C. However, this problem is not particularly significant since the instruments experiencing these temperatures are not operational at these time instances (in non-operating mode the thermal requirements for the instruments are less stringent). Therefore no active thermal control is needed to resolve this issue.

From these conclusions, some recommendations can be made for further research. First of all, in the thermal environment model, a single spacecraft structure was assumed with an average specific heat. This model could be split up, such that different specific heat values for different instruments and subsystems would be used. This would then also allow for a more significant and elaborate verification and validation with the ANSYS® model. Additionally, a similar numerical model could be constructed using ANSYS® for OB2, such that local temperature variations could be computed and verified for this mission as well. Furthermore, the influence of the solar panels on the bus of the spacecraft could be included in future models.

Near the end of the design phase, a mistake was discovered in the value of the internal heat dissipation used. Using a more realistic value equal to the total power of the spacecraft (which is 424.4 W for OB1 and 507.0 W for OB2) temperatures ranging from 70 °C to 120 °C were found using the ANSYS® model and an average temperature around the 80 °C was found using the external heat model. Based on these results, it is likely that new coatings should be selected and radiators should be used to dissipate the heat.

11

POWER CHARACTERISTICS

In order to make the different subsystems of the spacecraft operational, it is necessary to supply power to these subsystems. For this reason, this section will first perform an analysis on the power requirements throughout the mission, after which an electric power system will be designed. An electrical block diagram is also presented to give a visual representation of the power distribution throughout the spacecraft. After designing the full electric power system, a sensitivity analysis will be performed, followed by verification and validation of the design methods used. Furthermore, a Reliability, Availability, Maintainability and Safety analysis will be performed together with a risk analysis. This section concludes with a requirement compliance matrix and a conclusion and recommendation.

11.1. MISSION PHASE POWER REQUIRED

For the analysis of the required power of the spacecraft, the mission has been divided into three separate phases. These phases range from the launch of the rocket up to the end-of-life of the mission. In chronological order, these mission phases are the launcher phase, transfer phase and orbit phase.

11.1.1. LAUNCHER PHASE

The first considered mission phase is the launcher phase. This phase takes from the launch of the spacecraft up to the separation of the spacecraft from the launcher. As has been discussed in Chapter 8, OB2 will first be separated from the launcher approximately 10.5 hours after launch. Subsequently, OB1 will be separated from the launcher 36 hours after launch. In Table 11.1 and Table 11.2, it can be observed that for the launcher phase, power is administered to the spacecraft structure, thermal control, EPS and TT&C. Because the spacecraft is attached to the launcher, the on-board propulsion system does not need to be activated. Furthermore, the payload will only be activated after insertion into orbit around the Lagrange points, thus no power is required for the payload nor data processing. Finally, due to the fact that the spacecraft is attached to the launcher, it is not necessary to perform attitude determination and control.

Table 11.1: Mission Phase Power Required for OB1

Subsystem	Launcher Phase [W]	Transfer Phase [W]	Orbit Phase [W]
Propulsion	-	21.7	21.7
Structures	1.1	1.1	1.1
Thermal Control	81.0	81.0	81.0
Onboard Processing	-	-	57.9
Payload	-	-	44.5
EPS	47.2	47.2	47.2
TT&C	1.0	1.0	75.4
ADCS	-	95.5	95.5

Table 11.2: Mission Phase Power Required for OB2

Subsystem	Launcher Phase [W]	Transfer Phase [W]	Orbit Phase [W]
Propulsion	-	23.9	-
Structures	1.2	1.2	1.2
Thermal Control	89.1	89.1	89.1
Onboard Processing	-	-	63.7
Payload	-	-	85.0
EPS	52.0	52.0	52.0
TT&C	1.0	3.0	87.0
ADCS	-	105.1	105.1

11.1.2. TRANSFER PHASE

The second considered mission phase is the transfer phase. After each spacecraft is separated from the launcher, it will start its transfer to L1 or L5 respectively. The transfer phase covers the the mission from separation from the launcher up to and including the insertion into an orbit around the Lagrange point. For OB1, this phase takes almost 123 days while for OB2, this phase takes almost 407 days. In Table 11.1 and Table 11.2, the required power for each of the subsystems during the transfer phase can be observed. It can be observed that for both OB1 and OB2, the propulsion system and ADCS are activated in order to perform the required burn and attitude control of the spacecraft. Furthermore, it can be observed that the TT&C power for OB2 increases from 1 W to 3 W due to the increased distance from the Earth. The increase in TT&C power for OB1 is negligible and therefore still equal to 1 W.

11.1.3. ORBIT PHASE

The third and last considered mission phase is the orbit phase. In Table 11.1, it can be observed that for OB1 it is still required to power the propulsion system due to the fact that L1 is an unstable point making it a necessity to perform a couple of correction burns. Due to the fact that L5 is a stable point, it is not necessary to perform any correction burns and thus no power is required for the propulsion system during this phase. Furthermore, it can be observed that during the orbit phase, power is required for the payload and onboard processing. The payload (and consequently the onboard processing) will thus only be activated after orbit insertion. Finally it needs to be stressed that for OB1, not all systems will be activated at the same time, which will be elaborated upon in Section 11.2.3.

11.2. MISSION PHASE POWER GENERATION

After dividing the total mission into three mission phases and distinguishing the power required for each mission phase, it is possible to find a suitable power source for each of the mission phases. In this section, an electric power system will be sized for each mission phase.

11.2.1. LAUNCHER PHASE

First of all, the power system for the launcher phase will be chosen. This phase starts with the launch of the two spacecraft. After 37800 s (10.5 hours), OB1 will be separated from the launcher and after 129600 s (36 hours), OB2 will be separated from the launcher. During the launcher phase, the spacecraft is first placed into a fairing. During this phase, the spacecraft will not be exposed to solar irradiance. After separation of the fairing (at a height of 100km), the spacecraft is exposed to sunlight which opens up the possibility to use solar arrays. However, it is not possible to solely use solar panels as the launcher will orbit around the Earth, resulting in the need of a storable energy source. Besides that, the launcher will accelerate with a maximum acceleration of 78.5 ms^{-2} (discussed in Chapter 8). Due to this large acceleration it was decided that it would not be possible to use solar arrays during this phase of the mission. For this reason it is necessary to look for another energy source such as batteries, Radioisotope Thermoelectric Generators (RTGs) or fuel cells. Using Figure 11.1 and due to the fact that it will not be necessary to generate power for large amounts of time (such as 10.5 or 36 hours) after the launch phase, it was decided to use primary batteries that will not be included in the spacecraft but in the launcher. These primary batteries will be discarded together with the launcher after separation of both spacecraft.

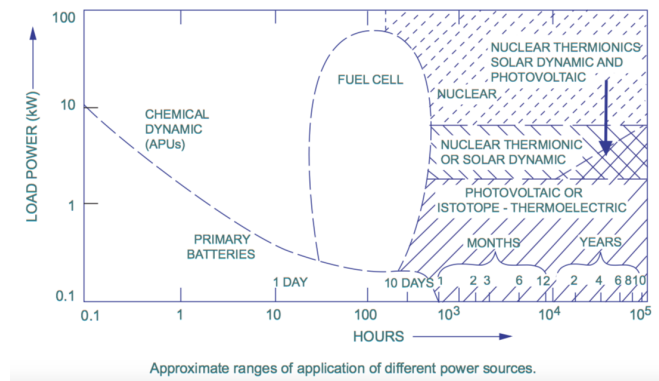


Figure 11.1: Power Source Applicability Chart [104]

It was decided to choose primary batteries with the highest specific power. These batteries are Lithium–thionyl chloride batteries with a specific power of 200 Wh per kg and an energy density of 600 Wh per dm^3 . [12, 105] It is possible to determine the required energy from the battery using Equation (11.1). In this equation, E_{bat} represents the energy required by the battery, P_{bat} represents the power that needs to be generated by the battery, t_{dist} represents the discharge time, DOD is the depth of discharge and η_{BAT} is the battery discharge efficiency. The battery discharge efficiency is equal to the efficiency of the battery multiplied with the efficiency of the discharge electronics and is equal to 90.25 %. [12]

$$E_{\text{bat}} = \frac{P_{\text{bat}} t_{\text{dist}}}{\text{DOD} \eta_{\text{bat}}} \quad (11.1)$$

The power required during the launcher phase for OB1 and OB2 is equal to 130.3 W and 143.3 W respectively. In order to determine the power that needs to be generated by the battery, the daytime efficiency has to be taken into account. The daytime efficiency is equal to the efficiency of the power conditioning and control system multiplied with the efficiency of the power distribution system and is equal to 86.85 %. This results in a required battery power of 150.0 W and 165.0 W for OB1 and OB2 respectively. The discharge time is set equal to the time from launch up to separation of the spacecraft from the launcher plus a safety factor of 10%. Since both batteries are primary batteries, the depth of discharge is equal

to 1. Finally, the discharge efficiency is equal to 76% due to the relatively short discharge time.[106]

This results in an energy of 7.3 kWh and 2.5 kWh for OB1 and OB2 respectively. The total combined battery mass is therefore equal to 49.2 kg and a volume of 16.4 dm³. Finally, it needs to be mentioned that a consultation needs to be done with the launch provider in order to design a safe and reliable battery decoupling system.

11.2.2. TRANSFER PHASE

In this section, the battery sizing for both spacecraft will be performed. Batteries are necessary for this mission due to the fact that it is not possible to point the solar panels towards the Sun for the full mission duration. After the sizing of the batteries has been performed, the solar panel deployment strategy will be explained.

BATTERY SIZING

In Section 11.2.3, it will be determined that for OB1, a solar panel area of 1.4 m² is required and for OB2, a solar panel area of 1.7 m² is required. During the transfer to L1 and L5, it can be concluded from Table 11.1 and Table 11.2 that the power required during transfer to L1 equals 285.0 W and the power required during transfer to L5 equals 315.8 W (including daytime efficiency). Because the power required during the transfer phase is smaller than the power generated during this phase, it is possible to use the solar panels to generate energy. However, this results in the necessity to point the solar panels towards the Sun at all times during the transfer phase.

As was discussed in Chapter 8, the insertion into the transfer orbit to L5 will be performed by OB2 himself and will take 1688 s. A requirement was set that the spacecraft should be able to rotate 180° from stand still to stand still within 2 minutes. Because the angle between the Sun and the solar panel will never be larger than 180°, this will be the maximum time necessary to rotate the spacecraft such that the solar panel is pointed towards the Sun. This results in a discharge time of 1808 s at the beginning of the transfer to L5. Finally, for the insertion into an orbit around L5, the spacecraft will have to change its attitude, perform an insertion burn for a duration of 2154 s and finally change its attitude again in order to face the Sun, resulting in a discharge time of 2394 s. Three types of batteries have been considered to include into the spacecraft. These batteries and some characteristics are shown in Table 11.3. From this table, it can be observed that concerning the energy density and energy efficiency, Li-Ion batteries outperform the other two types. However, due to that fact that the interior of the spacecraft to L5 will experience a temperature of -5 °C for a significant amount of time (see Chapter 10), it was decided to take Ni-H₂ batteries for the spacecraft to L5.

Table 11.3: Secondary Battery Characteristics [45]

Name	Energy Density [Whkg ⁻¹]	Energy Efficiency [%]	Temperature Range [°C]
Ni-Cd	30	72	0 - 40
Ni-H ₂	60	70	-20 - 30
Li-Ion	125	98	10 - 25

It is only necessary to use the batteries at the start of the transfer to L5 and during the insertion into the orbit around L5. Furthermore, after performing an analysis on the power required and the power generated by the solar cells, it turns out that the batteries can be fully recharged during the transfer. For this reason, the batteries will be sized for 2873 s (including a 20% safety margin).

The required energy can be calculated using using Equation (11.1) with a required power of 315.8 W and a discharge time of 2873 s. Due to the fact that the battery only has to discharge a couple of times, the DOD is equal to 1. Finally, the battery discharge efficiency is equal to the battery efficiency (70%) multiplied with the efficiency of the discharge electronics (95%).[12]. This results in a capacity of 398.9 Wh. The specific mass of the Ni-H₂ battery is equal to 60 Wh per kg [12], resulting in a battery mass of 6.32 kg. Finally, the energy density is equal to equal to 60 Wh per dm³ [104], yielding a volume of 6.32 dm³.

For the spacecraft travelling to L1, the burn to insert into the transfer will be provided by the launcher. After this burn, the spacecraft will be separated from the launcher and will be pointed towards the Sun within 2 minutes (according to the earlier stated requirement) in order to generate power using the solar panels. During the insertion into L1 orbit, a 41 s burn will be performed. So, for this insertion burn the spacecraft will first be pointed in the correct position (within 2 minutes), after that the 41 s burn will be performed and finally the spacecraft will be pointed towards the Sun while it has arrived in an orbit around L1. This results in a total discharge time of 281 s. Including a safety margin of 20%, the discharge time is equal to 337 s. It is now possible to use Equation (11.1), to determine the required energy for the batteries of OB1. The power required for the orbit phase to L1 is equal to 247.5 W excluding daytime efficiency and 285 W including daytime efficiency. The DoD is again equal to 1 and the battery discharge efficiency is equal to 93.1%. [12] This results in a capacity of 28.7 Wh. Because the temperature range of the spacecraft to L1 is between 10 and 25 °C (see Chapter 10), Li-Ion batteries can be used. The specific energy and the energy density of Li-Ion batteries are equal to 125 Wh per kg and 250 Wh per dm³ respectively. This results in a battery mass of 0.23 kg and a battery volume of 0.11 dm³.

SOLAR PANEL DEPLOYMENT STRATEGY

In order to prevent the solar panels from experiencing loads that could result into failure, a solar panel deployment strategy has been designed. The solar panels will have to rotate 90° in order to be fully deployed, where the angular velocity of the solar panel will have to increase from 0 rads⁻¹ up to a maximum value at an angle of 45° and then back to 0 rads⁻¹ when the solar panels are fully deployed. In order to ensure that the solar panels are fully deployed when the spacecraft is pointed towards the Sun, it was determined that the solar panels should be able to fully deploy within 30 seconds. This results in a maximum acceleration of the solar panel of 0.6°s⁻² and a maximum angular velocity of 4.5°s⁻¹. After that it is possible to determine the torque required to deploy the solar panels. The required torque can be determined using Equation (11.2). In this equation, T represents the torque, I represents the mass moment of inertia of the solar panels and α is the angular acceleration of the solar panel.

$$T = I \int_0^{30} \alpha(t) dt \quad (11.2)$$

This results in a required torque of 1.3 Nm for OBI's solar panel and 1.0 Nm for OB2's solar panel. Because both the required torque and the required rpm are low, the required power for these type of motors will not exceed 5 W. [107]

11.2.3. ORBIT PHASE

As can be seen in Chapter 8, the orbits of both spacecraft around the Lagrange points are in continuous sunlight. For this reason, solar panels will be used to generate energy for both spacecraft. In order to size the solar panels, it is first necessary to make a decision on the type of solar cells that will be used. Among the solar cells in consideration for the trade-off are a high-efficiency silicon (HES) rigid panel, a HES flexible array, a Triple-Junction (TJ) GaAs rigid panel and a TJ GaAs ultraflex panel, shown in Table 11.4. Their characteristics can be found in Table 11.4.

Table 11.4: Solar Cell Characteristics [12]

Name	Specific power (BOL) [Wkg ⁻¹]	Cell efficiency [-]	Cost [\$kW ⁻¹]	Area per power [m ² kW ⁻¹]	Degradation [%year ⁻¹]
High-efficiency silicon (HES) rigid panel	58.5	0.19	1	4.45	4.0
HES flexible array	114	0.19	1.5	5.12	4.0
Triple junction (TJ) GaAs rigid	70	0.268	1	3.12	1.5
TJ GaAs ultraflex	115	0.268	1.5	3.62	1.5

After analysing these specific characteristics for each of the solar cells, it is possible to generate a trade-off matrix. Each characteristic in the trade off is given a weight, where the higher the weight, the more important a specific design parameter is for the design, meaning the more important the parameter will be for the final solar cell choice. The trade-off table is presented in Table 11.5. It can be observed that the specific power and the area per power have the highest weights, the reason for this being that for the spacecraft, the smallest mass and the smallest required area are considered most important in order to reduce the overall size and mass of the solar panels. After that, degradation is given a score higher than efficiency and cost as it was considered to be favourable to have a low degradation rate due to the mission lifetime of 5 year plus transfer time.

Table 11.5: Solar Cell Trade-off. **Red** = Poor, **Orange** = Marginal, **Yellow** = Sufficient, **Green** = Good, **Blue** = Excellent.

Parameter	Specific Power (BOL)	Efficiency	Cost	Area per Power	Degradation	Final Score
Weight	25	15	15	25	20	100
High-efficiency silicon (HES) rigid panel	5.58 <small>Orange</small>	7.38 <small>Yellow</small>	10.00 <small>Blue</small>	7.31 <small>Yellow</small>	4.38 <small>Red</small>	6.70
HES flexible array	9.92 <small>Blue</small>	7.38 <small>Yellow</small>	7.00 <small>Yellow</small>	6.48 <small>Orange</small>	4.38 <small>Red</small>	7.13
Triple junction (TJ) GaAs rigid	6.48 <small>Orange</small>	10.00 <small>Blue</small>	10.00 <small>Blue</small>	10.00 <small>Blue</small>	10.00 <small>Blue</small>	9.12
TJ GaAs ultraflex	10.00 <small>Blue</small>	10.00 <small>Blue</small>	7.00 <small>Yellow</small>	8.76 <small>Green</small>	10.00 <small>Blue</small>	9.24

From the trade-off table, it can be seen that GaAs cells significantly outperform silicon cells, with the winner being Triple Junction GaAs ultraflex.

After deciding on the type of solar cells, it is possible to determine the size of the solar panels. The size of the solar panels can be computed using Equation (11.3). In this equation, A represents the required area of the solar panel, P_{req} represents the power required by the spacecraft during the orbit phase of the mission. This value includes the daytime efficiency of the spacecraft and is equal to 463.6 W and 556.2 W for OB1 and OB2, respectively. For OB1, this number does not include the propulsion system power. S is the solar irradiance, η_{cell} represents the efficiency of the solar cells and θ is equal to the incidence angle of the sun with respect to the solar panels. This value is assumed to equal 0° , because the spacecraft consists of instruments that continuously have to face the Sun. Finally, L_D represents the degradation factor of the solar panels. Since the mission will only start when OB2 arrives at L5, both spacecraft will have an equal lifetime of 5 years plus the transfer time of the spacecraft to L5. This results in a degradation factor of 0.91 [46], and hence a solar panel area and mass of 1.4 m^2 at 8.87 kg (including structure) for OB1 and 1.7 m^2 at 16.76 kg (including structure) for OB2. Because the required power values have been taken rather conservative, it was decided to not add a safety factor to the solar panel size to take damage of solar panels into account over SWAN's lifetime.

$$A = \frac{P_{req}}{S \cdot \eta_{cell} \cos \theta \cdot L_D} \quad (11.3)$$

As has been discussed in Chapter 8, OB1 will need to perform a number of correction burns for orbit maintenance. The longest burn time is equal to 19 s and besides that, in Section 11.2.2 it was discussed that the spacecraft should be able to change attitude within 2 minutes. During the correction burns, it will not be necessary to activate the payload and data processing as the payload will be pointed away from the Sun. Furthermore, it will not be possible to communicate as the antennas cannot be pointed. This results in the fact that the batteries should be able to deliver a power of 246.6 W, which results in 283.9 W including daytime efficiency for the for a duration of maximum 259 s. Because this only concerns a couple of burns it is not necessary to take battery degradation into account resulting in a Depth of Discharge of 1 with a discharge efficiency of 93.1% as discussed in Section 11.2.2. This results in a required capacity of 21.9 Wh, which is lower than the sized battery capacity of 28.7 Wh. It will thus be possible to perform the correction burns. However, it will be required to recharge the battery within 60 days. In order to determine the power the solar panel has to deliver in order to comply with this requirement, Equation (11.4) can be used. In this equation, P_{SA} represents the power that needs to be delivered by the solar panel to charge the battery, P_{req} represents the power required (equal to 246.6 W), η_n represents the nighttime efficiency (equal to 74.5%) and $t_{recharge}$ represents the time to recharge. This results in a solar array power extra of 1 W. The extra area required for this charging is within the round-off error of the solar panel design, such that it does not change the solar panel area.

Finally, the total mass of the power management can be determined using Equation (11.5). [12] The total mass of the EPS system (solar panels and batteries) for OB1 is equal to 8.87 kg and the total mass of the EPS system for OB2 is equal to 16.76 kg. This results in a power management system mass of 2.93 kg and 5.53 kg for OB1 and OB2 respectively. Finally, the total mass of the power system used for the spacecraft is equal to 11.8 kg for OB1 and 22.3 kg for OB2 (including structure).

$$P_{SA} = \frac{P_{req} t_{dist}}{\eta_n t_{recharge}} \quad (11.4)$$

$$M_{PMD} = 0.33 M_{EPS} \quad (11.5)$$

11.3. ELECTRICAL LAYOUT

Figure 11.2 shows a preliminary layout of the EPS system. Note that the performance of all systems are monitored during the entire mission. It can be observed that the primary batteries are the primary power source during the launcher phase and the solar arrays are the primary power source during the rest of the mission. The power is distributed among the secondary batteries and the rest of the spacecraft using the power regulation system and the power distribution system. The power is delivered to the TT&C system, the propulsion system, the payload, ADCS and C&DH system.

11.4. SENSITIVITY ANALYSIS

The sensitivity analysis for the electric power section can be discussed shortly. In case the solar irradiance is changed by 5%, the size of the solar panels increases or decreases by 0.1 m^2 . Thus an increase in solar irradiance decreases the size of the solar panel while a decrease solar irradiance increases the size of the solar panel. Furthermore, the mass of the solar panel is mainly dependent on the power required during the orbit phase. This value is divided by the specific mass in order to obtain the mass of the solar panel. This results in the fact that in case the required power changes by 5%, the mass changes by 5% as well.

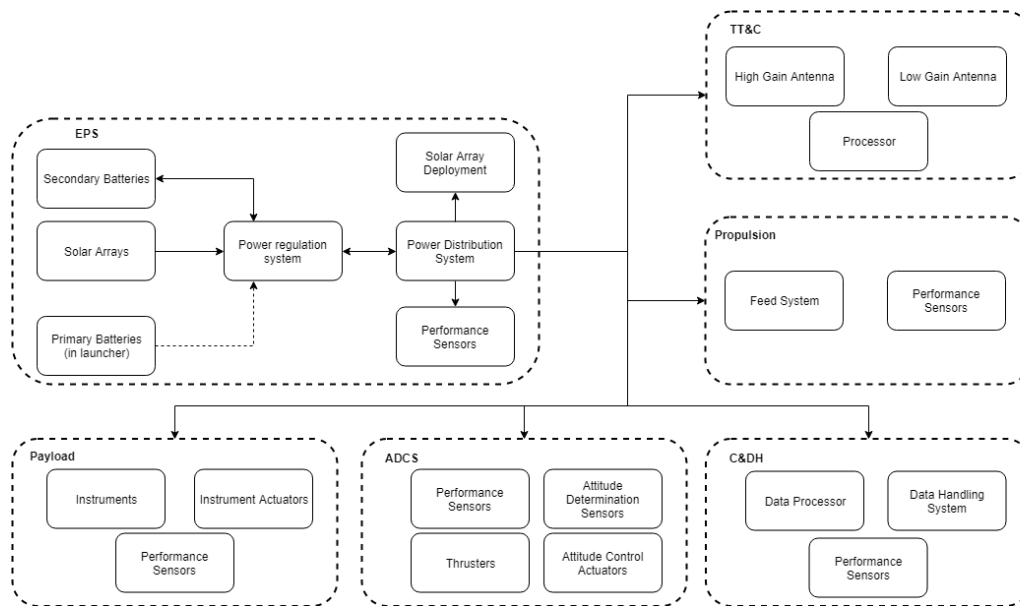


Figure 11.2: Layout of the EPS system.

11.5. RISK ANALYSIS

In this section, the risks with regard to the electric power subsystem will be analysed. These risks together with their likelihood and impact are stated in Table 11.6, lastly the mitigation measure is given.

Table 11.6: EPS Risk Register. Likelihood: HU = highly unlikely, U = unlikely, SL = some likelihood, L = likely, HL = highly likely. Impact: M = marginal, S = some, H = high, C = catastrophic

Risk	Consequence	Likelihood	Impact	Mitigation
Solar panels do not deploy	It is not possible to supply power to the subsystems	SL	C	Add a second deployment mechanism for redundancy.
Solar panels get damaged	The solar panels do not produce the required power	SL	H	Add a safety factor to the solar panel size
Power distribution system fails	It is not possible to distribute power among subsystems	U	C	Design the power distribution system such that it is redundant

11.6. RELIABILITY, AVAILABILITY, MAINTAINABILITY, AND SAFETY CHARACTERISTICS

Because the power system is one of the vital subsystems of the spacecraft, it is very important to design a system that is reliable during operation. During operation of the spacecraft, there are three components that could potentially fail. These are the solar panels, the batteries and the power distribution system. First of all, as has already been discussed in Section 11.5 it is possible that the solar panel deployment mechanism fails or that the solar panels get damaged during manufacturing, launch or operation (micrometeorites). In order to increase the reliability of the solar panel deployment mechanism, it is possible to add a second motor to the spacecraft. This second motor ensures that in case one fails, the solar panel can still be deployed. Besides that, extensive testing of the solar panel deployment mechanism and discovering its limitations also increases the reliability. Furthermore, it is possible to increase the redundancy of the solar panels by increasing the solar panel area such that failure of cells throughout the lifetime of the spacecraft is taken into account. Because the batteries are taken off-the-shelf, it will not be necessary to take measures for possible failure of the batteries. However, it will be necessary to add a safety factor to take into account aspects that cannot be modelled. Finally, during the design of the power distribution system it is important to make the system safe to avoid excessive voltages passing through the system. It should also be designed such that there is always a backup in case a specific components fails. It can thus be concluded that the redundancy measures that are applied during the design of the power system is to add extra more material/components than is strictly required.

Regarding the availability of components, it can be deduced that the solar cells and batteries will be off-the-shelf products. However, the solar cells will have to be mounted on the solar panel structure produced by mission specific labourers. Furthermore, it will be necessary to order each of the individual power distribution system components and assemble them to a mission specific power distribution system. For this reason it will be necessary to have people with the right skills and knowledge, a workshop and tools available for the assembling of the electric power system.

11.7. REQUIREMENT COMPLIANCE

Table 11.7: EPS Requirement Compliance Matrix

Identifier	Requirement	Met?	Confirmation
EPS-GEN-02a	The EPS batteries shall have a capacity of at least 28.7 Wh for the spacecraft to L1	✓	Section 11.2.2
EPS-GEN-02b	The EPS batteries shall have a capacity of at least 398.9 Wh for the spacecraft to L5	✓	Section 11.2.2
EPS-GEN-03a	The power system shall be able to provide at least 44.5 W for the payload at L1	✓	Section 11.1.3
EPS-GEN-03b	The power system shall be able to provide at least 85 W for the payload at L5	✓	Section 11.1.3
EPS-GEN-04a	The power system shall be able to provide at least 463.6 W for the spacecraft to L1	✓	Section 11.2.3
EPS-GEN-04b	The power system shall be able to provide at least 556.2 W for the spacecraft to L5	✓	Section 11.2.3
EPS-GEN-05a	The total mass of the power system shall not exceed 11.8 kg for the spacecraft to L1	✓	Section 11.2.3
EPS-GEN-05b	The total mass of the power system shall not exceed 22.3 kg for the spacecraft to L5	✓	Section 11.2.3
EPS-GEN-06a	The total volume of the batteries shall not exceed 0.11 dm ³	✓	Section 11.2.2
EPS-GEN-06b	The total volume of the batteries shall not exceed 6.32 dm ³	✓	Section 11.2.2
EPS-GEN-07a	The total cost of the power system shall not exceed €5957000 [45]	TBD	
EPS-GEN-07b	The total cost of the power system shall not exceed €6897000 [45]	TBD	
EPS-GEN-08	The reliability of the power system shall at least be 99 % [49]	TBD	
EPS-GEN-09	The power system shall be able to operate in the space environment	TBD	
EPS-GEN-10	The solar panels shall be pointed towards the Sun at most 90 seconds after deployment	✓	Section 11.2.2
EPS-GEN-11	The deployment time of the solar panels shall not be larger than 30 seconds	✓	Section 11.2.2
EPS-SA-01a	The linkages of the solar arrays shall be able to cope with an acceleration of 0.25 g	TBD	

11.8. CONCLUSION AND RECOMMENDATIONS

In Table 11.8, the determined values for each of the designed components for the electric power system can be observed. The type of solar cells that will be used are TJ GaAs ultraflex solar cells. Furthermore, the solar panels will deploy in 30 seconds with a maximum angular velocity of 4.5° s⁻¹. To improve the current design, there are a number of recom-

Table 11.8: Electric Power System Characteristics

Parameter	OB1 Spacecraft	OB2 Spacecraft
Battery Type Launcher	Lithium–thionyl chloride	Lithium–thionyl chloride
Battery Capacity Launcher [kWh]	7.3	2.5
Battery Mass Launcher [kg]	36.6	12.6
Battery Volume Launcher [dm ³]	12.2	4.2
Solar Panel Area [m ²]	1.4	1.7
Battery Type Spacecraft	Li-Ion	Ni-H ₂
Battery Capacity Spacecraft [Wh]	28.7	379.0
Battery Mass Spacecraft [kg]	0.23	6.32
Battery Volume Spacecraft [dm ³]	0.11	6.32

mendations for the electric power system. For the analysis of the power required for each mission phase, the propulsion system power, thermal control power, EPS power and ADCS power have been taken from SMAD [45], which has provided a preliminary power estimation tool. In order to improve the power system design, a detailed analysis of each subsystem needs to be performed, as some of these power requirements show deficiencies compared to the budgeted values. Furthermore, the solar cell/battery specifics that have been used for the power calculations (efficiency, degradation etc.) have been taken from average values [12], however depending on the manufacturer, these values might show some deficiencies. For this reason, a further analysis on these parameters would result in a more detailed design. Furthermore, more research could be done on the impact of the launch, manufacturing deficiencies and micrometeorites on the performance of the solar panels. Finally, research could be done into the use of springs for solar panel deployment and the time required to perform detumbling manoeuvres.

12

ATTITUDE DETERMINATION AND CONTROL CHARACTERISTICS

Now that the requirements for most of the subsystems are defined, the detailed design process of the Attitude Determination and Control System (ADCS) can be conducted. Many payload instruments rely heavily on the ADCS for pointing accuracy, stability and control. The same is true for a multitude of subsystems, the TT&C system of the spacecraft will fail if the attitude determination system is inadequate. Realising the importance of this subsystem, the following section will elaborate on all the steps taken to construct this subsystem.

The section will commence by defining specific spacecraft control modes selecting the driving requirements for each situation. Next, the spacecraft operating environment and influential internal and external disturbances will be discussed and quantified. Once these influences are specified a control mode can be selected which will in turn lead to a selection process for attitude sensors and control actuators. Finally the system layout will be presented along with an overview of the ADCS hardware.

12.1. MISSION MODES AND CORRESPONDING REQUIREMENTS

During its lifetime the spacecraft will spend the majority of its time observing the sun and predicting its activity. As such, there are mission segments before and after the operational period that do not require the same performance indices. Even within the operational mission phase shorter mission modes of functional origin such as pointing of the spacecraft communication system are embedded. Keeping aspects as these in mind and using SMAD [45] as guidance this subsection will present the different mission modes that are of relevance for the SWAN mission.

As stated earlier, the mission mode that will occupy most of the spacecraft's life time is the **Operational Mode**. This mission segment defines the whole purpose of the mission and contains nearly all of the driving mission requirements for accuracy both for OB1 and OB2. During this phase the ADCS must continuously point the payload in its directional operating vector, monitoring slew and adjusting if necessary. For the pointing accuracy at L5 the magnetograph is the driving instrument requiring a pointing accuracy of 0.55 arcminutes or 0.0092° . The requirement for drift is dictated both at L5 and L1 by the coronagraph demanding a drift rate lower than 26.5 arcminutes in 4 seconds or $0.11^\circ \text{ s}^{-1}$. The accuracy requirement in the L1 point is driven by the coronagraph, needing a pointing accuracy of 4.3 arcminutes or 0.072° while operating. Table 12.1 summarises all of the requirements in the operational mode.

Since the spacecraft has to first get to L1 and L5 before it can engage in its operational mode, an adequate system has to be in place to guide the spacecraft from launch to orbit insertion. Attitude control during launch is the responsibility of the company providing the launcher system. After the satellite is completely decoupled, it has to perform a range of manoeuvres which lead to the introduction of a **Orbit Insertion Mode**. Both for OB1 and OB2 the requirements for this mode are deduced from the orbit insertion manoeuvres at L1 and L5. For insertion of OB2, the spacecraft will need to perform a burn for 35.9 minutes while keeping within a 2.004 arcminute margin, while for OB1 the burn will take 40.88 seconds staying within a margin of 3.44 arcminutes. Another important aspect is that the spacecraft should be properly pointed and aligned before and after the burn procedures to continue planned operations. For this reason and from Chapter 13, a turn time of 2 minutes for 180° seems reasonable to minimise stress on the structure while completing the turn within a relatively fast time interval. Apart from meeting the payload requirements for pointing and stability, continuous communication is a top level requirement that must also be met in operational mode. However, these require an accuracy of 3.5° for OB1 and 0.5° for OB2 (this is when the loss exceeds 1dB, which is taken into account in the margin Chapter 7) which will be met either way if the payload requirements are met. Table 12.1 below gives a requirement overview for this mission mode.

For the duration of the transfer from earth to L1 and L5 the ADCS will enter the **Travel Mode**. During this time the spacecraft shall be able to provide power and adequate pointing requirements to make sure that the communication and thermal control system remain functional, as the payload will be inoperative at this point. In this mode the communication system defines the accuracy, which have been defined earlier as 3.5° for OB1 and 0.5° for OB2.

Next to all these rather functional modes certain situations might require the need for safety measures. In those cases the spacecraft might somehow experiences a situation where only the bare minimum for spacecraft survivability requirements are needed. This is why a **Safe Mode** has been defined that ensures that the spacecraft can continue communi-

cation with ground control while also making sure that the power system continues running. For these two reasons the spacecraft should be able to still successfully point its solar arrays and point its antennas. The ADCS should also be able to detect how its attitude has changed or if it is caught in a tumble. Table 12.1 again presents all the relevant requirements for the Safe Mode.

In case the spacecraft does indeed end up in a tumble an additional mode has been introduced, the **De-tumble Mode**. After the spacecraft has recognised that it is in a tumble it should be able to counteract it and determine a control sequence to autonomously re-stabilise itself. According to E Aghili [45] the optimal de-tumbling time for spacecraft can be determined by the following equation:

$$t_f = \frac{\|I_c(\omega(0) - \omega_f)\|}{\tau_{max}} \quad (12.1)$$

Where ω and τ represent the angles of angular velocity, I_c is known as the inertia tensor and t_f is the de-tumbling time. The inertia tensor takes into account the spacecraft's mass moment of inertia about all 3-axes. In order to minimise the attitude change of the spacecraft the ADCS should be able to compute and initiate the de-tumbling sequence within 3 seconds after tumble detection, which seems like a reasonable amount of time to fulfill this task but has yet to be confirmed in a later design stage. Tumble detection should not take longer than a minimum number of consecutive measurements, a number that needs to be determined once more information is available on computer system of the spacecraft. In Table 12.1 the resulting requirements for this mission mode can be found.

Table 12.1: Main Attitude and Control Requirements for each mode

L5	ID	Operational Mode Requirements	Traceability
	ADCS-OPML5-01	The ADCS system shall have an accuracy of 0.55'	PL-MNG-17
	ADCS-OPML5-02	The ADCS shall not drift more than 26.5' in 4 seconds	PL-CRG-07-a
L1			
	ADCS-OPML1-01	The ADCS system shall have an accuracy of 4.3'	PL-CRG-05
	ADCS-OPML1-02	The ADCS shall not drift more than 26.5' in 4 seconds	PL-CRG-07-a
	ADCS-OPML1-03	The orientation of the Magnetometer shall be known within 33'	PL-MTM-17-a
L5	ID	Orbit Insertion Mode Requirements	Traceability
	ADCS-ORL5-01	The ADCS shall be able to determine spacecraft attitude with an accuracy of 2.004'	-
	ADCS-ORL5-02	The ADCS shall be able to keep this accuracy for 35.9 minutes	-
	ADCS-ORL5-03	The spacecraft shall be able to rotate 180 degrees from and going back to standstill within 2 minutes	-
L1			
	ADCS-ORL1-01	The ADCS shall be able to determine spacecraft attitude with an accuracy of 3.44 arcminutes	-
	ADCS-ORL1-02	The ADCS shall be able to keep this attitude for 40.88 seconds	-
	ADCS-ORL1-03	The spacecraft shall be able to rotate 180 degrees from and going back to standstill within 2 minutes	-
L5	ID	Travel Mode Requirements	Traceability
	ADCS-TML5-01	The ADCS shall be able to point the solar arrays sunward	-
	ADCS-TML5-02	The ADCS shall be able to point the communication antennas with an accuracy of 0.5°	-
L1			
	ADCS-TML1-01	The ADCS shall be able to point the solar arrays sunward	-
	ADCS-TML1-02	The ADCS shall be able to point the communication antennas with an accuracy of 3.5°	-
L1 & L5	ID	Safe Mode Requirements	Traceability
	ADCS-SM-01	The system shall provide the pointing accuracy required to communicate and point the solar arrays	-
	ADCS-SM-02	The ADCS shall be able to determine attitude and rotational velocity	-
L1 & L5	ID	De-Tumble Mode Requirements	Traceability
	ADCS-DM-01	The spacecraft shall have an on board de-tumble program that computes the optimal attitude restitution sequence within 3 seconds	-
	ADCS-DM-02	The ADCS system shall be able to perceive a tumble within <TBD> seconds	-

12.2. EXTERNAL AND INTERNAL DISTURBANCES

Now that the requirements have been defined the next step is to dive into the factors that affect the attitude of both spacecraft. These influences can be categorised in two types: external and internal disturbances. The former come from entities such as the earth, sun or other celestial bodies in the solar system. Internal disturbances originate mainly from production errors and uncertainties, such as thruster misalignment or centre of mass deviations. The subsequent sections will investigate the level of influence of a variety of these disturbances and determine which ones are the most significant. At the end of this section a brief comparison of the disturbance torques will be given.

12.2.1. AXIS SYSTEM DEFINITION

Before diving into the analysis, it has to be clear with respect to what axis system the calculations will be performed. Two axis systems are used. The most simple one for the spacecraft is a 3-axis, body fixed cartesian axis system, with the positive x-axis pointing perpendicularly out of the spacecraft face with the instruments, with its origin at the spacecraft bus centre of solar radiation pressure (c_{p_s}). The z-axis points out of the spacecraft side panel where the boom is located. Using the right hand rule the y-axis will point 'to the right'. In Figure 12.1a the axis system is presented from three different views.

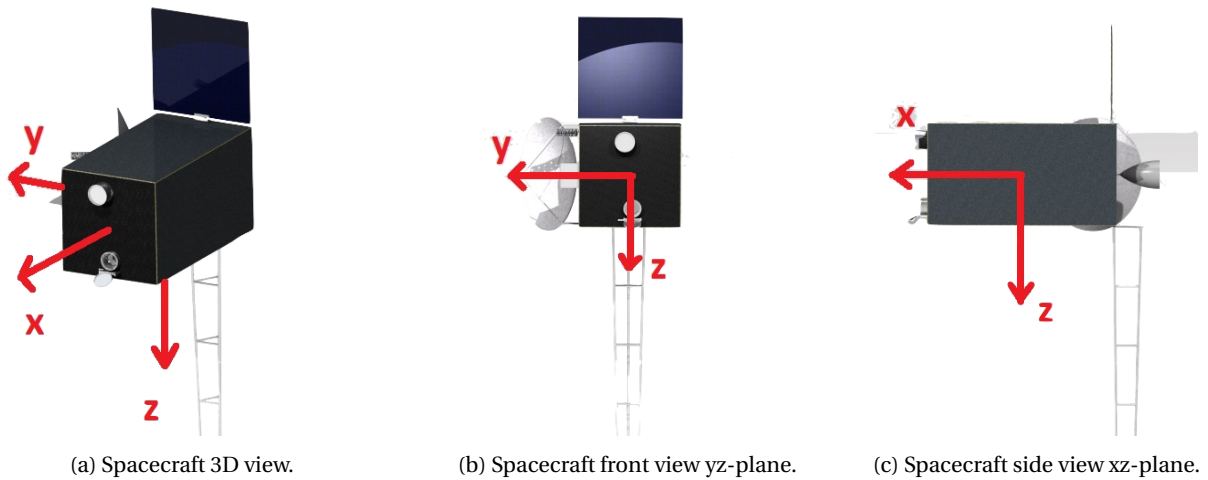


Figure 12.1: Spacecraft axis system from three different perspectives.

This is then compared to a heliocentric axis system to determine the orientation of the spacecraft.

12.2.2. EXTERNAL DISTURBANCES

The external disturbances are mainly caused by the activity and interactions between other celestial bodies. Depending on its altitude near celestial bodies such as the Earth, the magnetic field, gravity gradient and atmosphere have the strongest influence on a spacecraft's attitude in space. These disturbances induce torques on the spacecraft that can shift its attitude and point the systems off target. Without proper attitude determination and control this can quickly lead to power shortage due to wrong solar array pointing or unreliable payload data. In interplanetary space solar wind causes solar radiation pressure (SRP) and is the most dominant disturbance [45] along with occasional larger magnetic disturbances from magnetic fields embedded in Coronal Mass Ejections (CME). As such, the latter disturbances will be addressed first followed by other, near-Earth disturbances.

SOLAR RADIATION PRESSURE

In interplanetary space at relatively close proximity at the sun, the solar radiation pressure proves to be the most continuous disturbance. The constant flux of photons hitting the spacecraft in combination with a difference between centre of solar radiation pressure and centre of mass locations can cause a torque around any of the spacecraft axes. The c_{p_s} is the point where the resulting SRP force acts. According to SMAD [45] a preliminary way of sizing this torque is by using the following equation:

$$T_s = \frac{\Phi}{c} A_s (1 + q) (c_{p_s} - c_m) \cos(\phi) \quad (12.2)$$

The first part of the equation represents the force the solar flux generates on a given illuminated surface A_s . Φ is the solar flux which has a value of roughly 1362 W m^{-2} at 1 AU, while c is the speed of light as approximately $300 \cdot 10^6 \text{ m s}^{-1}$ and q being the unitless reflectance value of the illuminated surface. The second part of the equation contains the moment

arm, which is the difference between the centre of solar radiation pressure and the centre of mass multiplied by the cosine of the incidence angle ϕ taken to be 0° . Since the spacecraft will be facing the sun for almost the whole mission duration, it is assumed that only torques about the y and z-axes will be of significance.

MAGNETIC TORQUE

OB1 and OB2 will be far enough away from the Sun and Earth such that the torques induced by their magnetic fields can be neglected. From SMAD [45] the equation for magnetic torque is given by Equation (12.3).

$$T_m = D \cdot B = D \left(\frac{M}{R^3} \lambda \right) \quad (12.3)$$

Where D is the spacecraft's residual dipole moment in $A \cdot m^2$ usually taken as $1 A \cdot m^2$. B is the magnetic field strength in tesla, R is the distance between the spacecraft and Earth in meters and M represents the magnetic moment of the celestial body in $tesla \cdot m^3$. Finally, λ is the unitless function of the magnetic latitude ranging from 1 at the equator to 2 at the magnetic poles. It can be assumed that due the scaling of the distance to the sun and the earth by the negative R^3 that the magnetic field strengths of the Earth and the Sun can be neglected. However, Coronal Mass Ejections harbour stronger magnetic fields. These magnetic fields can be as strong as 204.8 nT as shown in Section 6.2.9 and should be considered for possible torque accumulation even if these magnetic field occurrences only take up a small fraction of the total time scale.

ATMOSPHERIC DRAG

One disturbance that only arises for a very brief period of the whole mission duration, but which should still be considered is the atmospheric drag. After its orbit inclination manoeuvre OB2 makes one more close earth pass after launcher detachment before escaping towards L5. This brings the spacecraft to an altitude of 200km at high velocities. Even though 200 km altitude is already considered space it would serve as a good check to investigate if this does not impose too much torque on the spacecraft. First off, eq. (12.4) gives a preliminary torque value for the atmospheric drag.

$$T_a = 0.5 \rho V^2 t A_r C_d (c_{p_a} - c_m) \quad (12.4)$$

V is the spacecraft relative velocity to earth, ρ is the local atmospheric density, A_r is the ram area and C_d is the drag coefficient usually between 2.0 and 2.5 for spacecraft. The product of these parameters represents the drag force that acts upon the spacecraft, while the difference between c_{p_a} and c_m defines the moment arm.

To investigate the effect of this close earth fly by, python using numpy has been applied to determine the accumulated drag torque. For this model density values from the MSISE-90 Model of Earth's Upper Atmosphere² are used. Since these values are given in increments of 20 km from 0 up to 900 km altitude, linear interpolation has been applied to approximate the density values between these 20km increments. Using these densities in combination with the spacecraft escape data from chapter 8 the accumulated torque can be calculated and the added fuel needed to dump this moment can be computed.

GRAVITY GRADIENT

The last major factor that can play a role in space missions is the gravity gradient of nearby celestial bodies such as the earth. Equation (12.5) shows the equation proposed by SMAD [45] for computing the gravitational torque on a spacecraft.

$$T_g = \frac{3\mu}{2R} |I_z - I_y| \sin(2\theta) \quad (12.5)$$

Where μ is the gravitational constant of the celestial body having a magnitude of $3.986 \cdot 10^{14} m^3 s^{-2}$ for Earth and $1.327 \cdot 10^{20} m^3 s^{-2}$ for the Sun. R is the distance from the celestial body to the spacecraft, while I_z and I_y represent the mass moments of inertia around the z and y axis respectively. Lastly θ is the angle between the local vertical and principal Z axis. Given the distance of OB1 and OB2 from the Earth and the Sun, this gravity gradient will not have much relevance for the mission.

12.2.3. INTERNAL DISTURBANCES

The internal disturbances originate largely from manufacturing imperfections, manufacturing uncertainties, rotating machinery and liquid sloshing. Slight misalignments of the thruster or reaction wheel friction torques are two examples of such disturbances. It is thus a high priority to minimise these production flaws to reduce the load on the ADCS system.

¹https://spacegrant.colorado.edu/COSGC_Projects/symposium_archive/2010/papers/CUSRS10_13%20Estimation%20of%20Small%20Satellite%20Magnetic%20Torquing%20and%20Momentum%20Storage%20Requirements.pdf

²<http://www.braeunig.us/space/atmos.htm>

To do this, detailed knowledge of the spacecraft layout and subsystem interactions must be known with elaborate computer modelling and precise apprehension of the actuator parameters. This level of detail goes beyond what is achievable for this design phase and available time. For these reasons this section will not go too much into the magnitudes of these internal torques, but rather explain how they could possibly be calculated.

DISTURBANCES DUE TO PRODUCTION FLAWS

Imperfect manufacturing can lead to uncertainties in terms of centre of gravity location. Firing of thrusters can lead to unintended torques being created. This can have its origin in two different flaws. One would be the actual uncertainty of the location of the centre of gravity, either due to shifts of mass within the spacecraft system or due to the models being slightly off from reality. The uncertainty in centre of gravity location can be in a range of 1-3 cm.[45]

The second possible flaw would be a mismatch of thruster output, with one thruster firing slightly longer or with a slightly higher force than the other. The mismatch in thruster output can typically be $\pm 5\%$ [45]. In case of a thruster malfunction this value could be even higher, but those cases are seen as emergency situations.

Lastly, thrusters could also be misaligned from the centre of gravity due to mounting inaccuracies. If the main thruster is misaligned from the centre of gravity by a few arcminutes, this can already cause considerable disturbances. Typical values for these offsets can be between 0.1° and 0.5° .

REACTION WHEEL FRICTION

Reaction wheels turn at high speeds serving as means of making a spacecraft's attitude torque resistant. As the wheels turn they inevitably generate friction which is translated onto the spacecraft structure. In order to size for this phenomena the friction torque can be deduced from the following equation given by V. Carrara and H.K. Kuga [108]:

$$T_\omega = J_\omega \dot{\omega} + b\omega + \text{sgn}(\omega) \left[c + d e^{\text{frac} - \omega^2 \omega_s^2} \right] \quad (12.6)$$

This is the same equation used to compute the torque of an engine, in a similar way it can be used to compute the torque needed to spin the reaction wheel at a given angular velocity. The last part of this equation accounts for the reaction wheel friction, which increases with higher wheel rotation rates. ω is the angular velocity of the wheel and ω_s is known as the Stribeck speed. c is the Coulomb torque and $d = T_s - c$, where T_s is the static torque of the wheel. The Stribeck speed, Coulomb torque and static torque are specific parameters that differ per reaction wheel and in depth analysis is needed to determine these [108].

LIQUID SLOSH

Liquid sloshing can induce torques if fluid substances are taken on board like propellants that can shift when the spacecraft is accelerating. If the tanks and propellant mass are asymmetrically distributed about the centre of mass, creating torques which should be controlled by the ADCS system. At this point not enough knowledge is available about the tanks, their propellant and the structural disposition of the spacecraft to fulfil such an analysis.

ROTATING MACHINERY AND THERMAL SHOCKS

The SWAN mission will take place in interplanetary space, where both spacecraft will continuously face the sun and not experience any cyclic thermal shocks by passing through the shadow of a celestial body. Due to this it is assumed that disturbances due to thermal shocks can be neglected in this part of the analysis. Furthermore, the only rotating machinery on board are the solar array deploying mechanism and the boom torques. Either way the process of actuating these mechanisms will take a few minutes at most and do not continuously torque the spacecraft, thus they will not play a significant role in the sizing of the ADCS system.

12.2.4. TORQUE OVERVIEW AND CONTROL METHOD SELECTION

In order to easily compare the relevance of each reaction torque, this section provides a table that shows the magnitudes of each external disturbance torque. Based on those conclusions and considering the space environment where both OB1 and OB2 are situated the type of control system will be determined.

TORQUE OVERVIEW

The data for the dimensions and centre of mass locations, as well as moment of inertia are provided by the SWAN structures department.

For OB2, the most significant torque is the solar radiation pressure (SRP), even if the atmospheric drag is 2 orders of magnitude higher, it is only experienced for about 14 seconds, producing an accumulated torque of 0.0168 Nms and can

Table 12.2: Torque Overview table

L5	Disturbance Torque	Symbol	Torque	Unit
	Solar Radiation Pressure about y	T_{sy}	$4.6 \cdot 10^{-6}$	Nm
	Solar Radiation Pressure about z	T_{sz}	$5.1 \cdot 10^{-6}$	Nm
	Averaged Atmospheric Torque for 200 km pass	T_a	$1 \cdot 10^{-2}$	Nm
	Magnetic field Torque (max CME values)	T_m	$2.1 \cdot 10^{-7}$	Nm
	Solar Gravity Gradient	T_{gSun}	0	Nm
	Earth Gravity Gradient	T_{gEarth}	0	Nm
L1	Disturbance Torque	Symbol	Magnitude	Unit
	Solar Radiation Pressure about y	T_{sy}	$2.5 \cdot 10^{-6}$	Nm
	Solar Radiation Pressure about z	T_{sz}	$1 \cdot 10^{-8}$	Nm
	Magnetic field Torque (max CME values)	T_m	$2.1 \cdot 10^{-7}$	Nm
	Solar Gravity Gradient	T_{gSun}	0	Nm
	Earth Gravity Gradient	T_{gEarth}	0	Nm

be neglected. The torque due to a CME's magnetic field is one order of magnitude smaller than the one experienced by the SRP. In combination with the relative rarity of a CME and the fact that a 0.25AU CME, only last for about a day[15] this torque becomes insignificant for ADCS sizing. Furthermore, as predicted in Section 12.2.2, the gravity gradient torque values prove that the gravity gradient will not be of significance either in terms of disturbances as they all converge to 0 Nm .

CONTROL METHOD

This selection process uses Table 19-6 on page 574 in SMAD[45] to provide an overview of possible attitude control methods. Taking into account the analysis of the previous section a few options can be scrapped straight away. Given the fact that no strong magnetic field will continuously be present and that the gravity gradient torque is virtually non-existent at L1 and L5, any control method making use of the two torques can be discarded. This leaves us with 7 different control method.

Spin stabilisation was a commonly used control method for many spacecraft. For the SWAN mission however this is not an option since the payload (Chapter 6) needs to be pointed sun wards without rotation about the viewing axis for the whole operational mission phase of the spacecraft. Separating the spacecraft into a spinning and non-spinning BUS section is also not an options for SWAN as this control method is mechanically complex and would lead to many design challenges. Taking those factors into account this method can be dismissed and it can be concluded that 3-axis stabilisation techniques are the way to go.

The latter decisions leave 5 options on the table. Now it becomes important to look at the accuracy requirements of the spacecraft. In Table 12.1 the most stringent requirement comes from the coronagraph for which an accuracy of 0.0092° is needed. This argument quickly discards 3 options and also supports the decision of not using spin stabilisation which only offers accuracies in the range of $\pm 0.1^\circ$ to $\pm 1^\circ$.

The last two available options left are Zero momentum Attitude control type using 3 wheels or a zero momentum control type using Control Moment Gyros (CMGs). According to SMAD [45] CMGs are mainly applied where agile high angular rate manoeuvres are required. Both OB1 and OB2 will not be executing any agile manoeuvres during their operational mode. As CMGs come at a high cost in terms of complex control laws, mechanical wear and careful control moment management the decision has been made to use 3-axis stabilisation using a zero momentum method with at least 3 momentum wheels that store control torque disturbances in any direction. Since these wheels store the momentum introduced by the disturbances, regular momentum dumps should be conducted to bring the wheels back to their nominal spin rate. From earlier analysis it will not be feasible to try and dump the momentum using gravity gradient torque or magnetic torque. Thus, thrusters must be applied for momentum dumping.

12.3. ATTITUDE CONTROL ACTUATOR SIZING

Having decided upon a control method and knowing the approximate magnitudes of the various disturbance torques at L1 and L5 it is now possible to size the control wheels and thrusters for both spacecraft. First the wheels will be sized, which is followed by the thruster sizing.

12.3.1. WHEEL SIZING

In this section three parameters will be quantified that size the momentum wheels: Torque from Momentum Wheel for Disturbance Rejection, Momentum storage in Reaction Wheel and Momentum Storage in Momentum Wheel [45].

The first parameter, the control torque T_C , determines how much momentum is added to the momentum wheel by the disturbance torque and is found by multiplying the maximum disturbance torque T_D by a margin factor. Table 12.2 provides these values at $5.8 \cdot 10^{-6}$ Nm for OB2 and $2.8 \cdot 10^{-6}$ for OB1 using a margin factor of 0.15.

The second parameter is the momentum stored before each momentum dump. This is used to help determine the momentum dump interval and is calculated using Equation (12.7). The torque calculated in Equation (12.7) is small and cannot be dumped immediately since it would require continuous extremely small thrust outputs. Thus the momentum is accumulated until a realistic value is reached at which available thrusters can be used for momentum dumping.

$$h = T_D \cdot P \cdot \frac{(0.707)}{4} \quad (12.7)$$

Where P is the orbital period of the spacecraft, 0.707 is the rms average of a sinusoidal function and the $\frac{1}{4}$ depends on the amount of momentum dumps per orbit. In SMAD [45] an example of an Earth orbiting satellite with $P=5926$ s and 4 momentum dumps per orbit leads to a momentum accumulation time of 1332.25s, for now this value will be used as a placeholder number until after the wheel selection. This parameter can be adjusted according to how much momentum one desires to add before initiating a momentum dump.

The third parameter is dependent on the accuracy requirement of the ADCS. The equation for momentum storage is as follows:

$$h = \frac{T P}{\theta_a 4} \quad (12.8)$$

In this equation, h is the stored momentum for the required accuracy, θ_a is the required accuracy angle in radians and P is the orbital period. Again, the fraction $\frac{1}{4}$ depends on the amount of momentum dumps one aims to perform. At a later stage these parameters might need adjustment in order to lower the fuel mass or reaction wheel rotational velocity. The discussion on this and the final values can be found in Section 12.4.

12.3.2. THRUSTER SIZING

Now that the wheels have been sized and the momentum needed for momentum dumps are known the thrusters can be sized. The force level for the thrusters is determined from three equations:

$$F = \frac{T_D}{L} \quad (12.9)$$

$$T = F \cdot L = I \cdot \alpha \iff F = \frac{I \cdot \alpha}{L} \quad (12.10)$$

$$F = \frac{h}{L t_b} \quad (12.11)$$

Equation (12.9) uses the moment arm L about the axis experiencing the highest disturbance torque T_D . The moment arm depends on the spacecraft bus configuration and where the thrusters will be positioned. For efficient momentum dumping it is beneficial to put the thrusters as far apart as possible for a maximum moment arm and reduced thruster burn times.

Equation (12.10) uses the mass moment of inertia I about the axis that a certain slew is required. The Swan mission requires the spacecraft to turn 180° in 2 minutes about its z-axis and x-axis to point the solar arrays. Of those minutes 5% of the time the spacecraft is accelerated about the desired axis then it coasts for 90% of that time and deceleration again takes % of the total turn time. α is determined by first computing the angular velocity ω in radians per second. Divided by the 5% acceleration time this gives the angular acceleration: $\alpha = \frac{\omega}{t_{turn}}$. This can then be inserted into Equation (12.10).

Finally Equation (12.11) computes the force level needed for momentum dumping. This equation depends on the accumulated moment h obtained from Equation (12.7). The thruster moment arm L depends on the axis about which the momentum is dumped and the burn time t_{burn} depends on how much time one wishes to burn per orbit. The latter is a time percentage that helps size the thrusters and can be adjusted to lower or increase the force level needed per momentum dump.

The next step in the process is to figure out how much fuel will be needed to cope with the torques and meet the requirements. To find out how much fuel is needed for momentum dumping the result of Equation (12.11) is used and inserted into the following equation:

$$m = \frac{F \cdot t_b}{I_{sp} \cdot g} \quad (12.12)$$

Where t_b is the thruster burn time, I_{sp} is the specific impulse of the thrusters and g is the gravitational acceleration of 9.8 m s^{-2} . Finally, the mass needed for performing pointing manoeuvres needs to be calculated. Equation (12.12) is also applied for this purpose, but the inputs are slightly different. F is the selected thrust force dependant on the selected thruster and $t_b = t_{b_{on}}$ which is the thruster on-time for the manoeuvre. The thruster on-time is computed in a sequence of steps. First, the momentum bias needs to be changed where we have:

$$t_{bias} = \frac{h}{F \cdot L} \quad (12.13)$$

Next, the time to burn during acceleration and deceleration of the spacecraft is determined described by Equation (12.14)

$$t_{accel} = t_{decel} = I \cdot \omega \quad (12.14)$$

Where I is the mass moment of inertia about the slew axis and ω is the angular velocity. The thruster on time is the sum $t_{b_{on}} = t_{accel} + t_{decel} + 2t_{bias}$.

12.4. WHEEL AND THRUSTER SELECTION

Now that the equations given in the previous section have been discussed, they can be put into a sheet using Excel together with all the relevant structural, dimensional and material properties of the spacecraft. From this it promptly becomes apparent that the propellant mass for both L1 and L5 is too high, 32.22kg and 23.28kg respectively. The mass budget dedicated to the ADCS is 24.2 kg for L1 and 28 kg for L5 including all the sensor and actuator instruments. Clearly measures need to be taken to reduce this propellant mass. From the torque analysis it is clear that the SRP torque is the driving factor behind the propellant quantity. To tackle this problem the two possible solutions are:

1. Reconfigure spacecraft layout to bring centre of mass and centre of solar radiation pressure closer together, essentially reducing the moment arm.
2. Use reflective vanes that deliver counter acting torques to minimise the accumulated momentum in the reaction wheels.

The first option would require a lot of effort from the structures department. Although this is not a feasible option to implement within the given time frame, it does however remain a possibility for a later design phase.

Nonetheless, there was enough time to look into the second option and see what the effects are of using vanes to mitigate the disturbance torque effect. After some preliminary iterations Table 12.3 presents the final values for this design phase, showing the disturbance torques, wheel sizing parameters and thruster sizing parameters. Two vanes were used for L5 on for control about y of 0.85 m^2 and one for control about z of 0.6 m^2 . For L1 only one vanes was necessary for control about z of 0.55 m^2 . These are relatively large area values, but it is assumed that in the next design phase these vanes can be reduced in size and/or left out completely by applying and optimising solution 1.

Table 12.3: Parameter overview

Torques			
Parameter	OB1	OB2	Unit
Solar Radiation pressure about y	$1.6 \cdot 10^{-6}$	$5.75 \cdot 10^{-6}$	Nm
Solar Radiation pressure about z	$2.24 \cdot 10^{-7}$	$1.25 \cdot 10^{-8}$	Nms
Magnetic field Torque	$2.05 \cdot 10^{-7}$	$2.05 \cdot 10^{-7}$	Nms
Wheel sizing			
Parameter	OB1	OB2	Unit
Torque from Reaction Wheel from disturbance rejection	$5.82 \cdot 10^{-6}$	$2.84 \cdot 10^{-6}$	Nm
Momentum storage in reaction wheel	0.309	0.151	Nms
Momentum storage in momentum wheel	3141.1	170.4	Nms
Thruster sizing			
Parameter	OB1	OB2	Unit
Force level to meet slew rate	0.699	0.093	N
Force level for momentum dump	0.172	0.14	N
Fuel mass per momentum dump	$6.11 \cdot 10^{-5}$	$3.47 \cdot 10^{-4}$	kg
Fuel mass per 180° turn	0.018	$7.92 \cdot 10^{-4}$	kg

After having compiled a good overview of the wheel and thruster parameters a selection of these actuators can be compiled. Looking at the momentum wheels the most important parameters are the angular velocity in rpm (revolutions per minute) and the weight of each momentum wheel. To compute the angular velocity of a wheel one has to divide it angular momentum h by its mass moment of inertia (MMOI):

$$\omega = \frac{h}{MMOI} \quad (12.15)$$

where

$$\omega = \frac{1}{2} \cdot mass \cdot R^2 \quad (12.16)$$

Equation (12.15) gives the angular rate in rad s^{-1} which should then be divided by Π and multiplied by 60 seconds to find the value in rpm. Remember Equation (12.8) where h can be sized depending on the amount of momentum dumps one wishes to conduct. This value can be adjusted to bring down the rpm of needed for spacecraft stabilisation. On the other hand the $MMOI$ is reliant on the momentum wheel radius and mass. We thus insert the mass and radius for each momentum wheel on the list and check what rpm that would give for the reaction wheel momentum that we need and then adjust the moment dumps per orbit accordingly.

Table 12.4: List of potential Momentum wheels

Name	Manufacturer	Mass [kg]	Nominal power [W]	Maximum power [W]	Dimensions [mm]	Operational speed [rpm]	Angular momentum [Nm/s]
RSI 12-75/60 ^a	Rockwell	4.85	20	90	Ø247x85	6000	12
RSI 4-75/60 ^a	Rockwell	3.7	20	90	Ø222x85	6000	4
HR 0610 ^b	Honeywell	3.6-5.0	15	80	Ø267x120	6000	4-12
HR12X [109] ^c	Honeywell	6-9.5	22	170	Ø316x159	6000	12-50
HR14X [109] ^c	Honeywell	7-10.5	22	170	Ø366x159	6000	20-75
HR16X [109] ^c	Honeywell	10.6-14	22	170	Ø418x178	6000	75-150
200 SP-M ^d	Surrey	5.2	16.3	145	Ø240x90	5000	12
200SP-O ^d	Surrey	5.2	16.3	145	Ø240x90	5000	12
10SP-M ^e	Surrey	0.96	2.8	10	Ø109x101	5000	0.42
100SP-O ^e	Surrey	2.6	10	113	Ø131x120	5000	1.5

^a <https://www.rockwellcollins.com/Products-and-Services/Defense/Platforms/Space/RSI-12-Momentum-and-Reaction-Wheels.aspx>

^b https://aerocontent.honeywell.com/aero/common/documents/myaerospacecatalog-documents/HR_0610_Reaction_Wheel.pdf

^c <http://www.ltas-vis.ulg.ac.be/cmsms/uploads/File/AddendumADCS.pdf>

^d <http://www.sst-us.com/getfile/1686dd6a-a408-481a-8a76-14ab055d365a>

^e <http://www.sst-us.com/getfile/0f0df2ba-76ed-4a46-b863-d4b7aa9887fe>

To find the optimal momentum wheel for the SWAN mission a trade-off is conducted. Four different parameters will be given scores adding up to 100. Since the ADCS is really limited on weight, it is considered the driving parameter and gets a weighting of 35/100. To ease the process any wheel above 5 kg is discarded, leaving 5 options. The mass moment of inertia will also be taken into consideration, this parameter gives a good insight into how well the wheel is designed and how mass and size balance each other. For these reasons MMOI gets a score of 30/100. Following this, the size of the reaction wheel plays a lesser role but since volume in the spacecraft is limited it gets a weight of 20/100. Finally we will consider the number of momentum dumps that need to be performed, it is of interest to keep this parameter as low as possible for operational purposes. The number of momentum dumps gets a weighting of 10/100.

Table 12.5: Reaction wheel trade-off

OB2	Mass	MMOI	Size	# of momentum dumps	Final score
RSI 12-75/60	10/35	25/30	15/20	15/15	65/100
RSI 4-75/60	25/35	20/30	17/20	12/15	74/100
HR 0610	25/35	30/30	5/20	14/15	74/100
10SP-M	35/35	5/30	20/20	0/15	60/100
100SP-O	30/35	10/30	18/20	2/15	60/100

As one can observe, two momentum wheels obtain the same score of 74/100. To decide between the two, the nominal power is considered where the HR 0610 scores the best. As a result the HR 0610 is chosen for the SWAN mission at the L5 point with 70 momentum dumps within 24 hours. 70 dumps per day is a legitimate assumption given that SMAD [45] provides an example of the FireSat II performing 4 momentum dumps in 5926 seconds. This adds up to about 58 momentum dumps a day.

The spacecraft at the L1 point is not so limited by the number of momentum dumps it has to perform. For this reason the most light weight, power efficient option is chosen: the 10SP-M needing 54 momentum dumps per day.

The next step is to select the thrusters for the ADCS. In order to determine a list of possible thrusters, a number of criteria need to be taken into account. From Table 12.3, the thruster needs to deliver at least 0.699N to fulfill both the requirement on slew rate and for momentum dumping. Furthermore, in certain situations it is useful to adjust the thrust level of the control thrusters. It gives additional flexibility when coping with internal and external disturbance torques. Taking that into consideration narrows down the thruster selection to thrusters that can be adjusted in their force output. Another decisive criteria is that the thrusters should have a maximum burn time as indicated in Table 12.3, thus 110376 seconds.

In Table 12.6 a selection of potential attitude control and station keeping monopropellant thrusters are displayed that meet the earlier criterias. Note that only thrusters for which enough data was found are presented, some other thrusters offered promising thrust levels and even 'green'propellants. Sadly only limited information for other parameters were found, hence those were not considered in the selection. From this table, the first thruster up to the MRM-103D 1N thruster work on MMH. The 10N biprop works on NTO with MMH. All of these thrusters are commercially available.

Table 12.6: Monopropellant and bipropellant Thrusters

Name	Thrust [N]	ISP [s]	Max single burn time [s]	Max accumulated burn time[s]	Mass [kg]
1N chemical monopropellant thruster [110]	0.32 - 1.1	200 - 223	43200	180000	0.29
MR-103D 1N [111]	0.22 - 1.02	209 - 224	5000	401040	0.33
MR-103G 1N [111]	0.19 - 1.13	202 - 224	1000	146160	0.33
MR-103M 1N [111]	0.28 - 0.99	206 - 221	30000	216000	0.16
MR-111C 4N [111]	1.3 - 5.3	215 - 229	5000	-	0.33
MR-106L 22N [111]	10 - 34	229 - 235	4000	-	0.59
MRM-103D 1N [111]	0.22 - 1.02	209 - 224	2880	636840	1.27
10N biprop ^a	6 - 12.5	292	28800	248400	0.35 - 0.65

^a <http://www.space-propulsion.com/spacecraft-propulsion/bipropellant-thrusters/10-bipropellant-thrusters.html>

Table 12.6 includes a variety of possibilities, the option that seems the most feasible though is the MR-111C 4N. This thruster works within a thrust range of 1.3-5.3N, starting at 1.3N it accomplishes the 0.699N requirement but being slightly higher than that it reduces burn time minimising the effect on normal operations. The upper bound of the range is 5.3N this gives the spacecraft a nice range to work in, allowing it to adjust thrust to a lower level for more precise thrust vectoring while also allowing it to quickly dump a lot of momentum if needed. On top that the thruster is relatively light weight and has a good specific impulse range of 215-229 seconds. Thus both OB1 and OB2 will be using MR-111C 4N thrusters for momentum dumping.

To round off the actuator selection, the only thing left to do is to select a tank for the propellant. Taking into account that solar vanes will be used on the mission a fuel mass of 9.06kg will be needed for L5 and 7.34kg for L1. Using MMH as propellant with a density of 880 kg m⁻³ this leads to a volume of 10.3 litres for L5 and 8.3 litres for L1. Thus, the lightest, smallest tank will be chosen from Table 9.4. The Northrop Grumman 80184-1 propellant tank will be the thruster of choice for the SWAN mission having a volume of 13.6 litres and a mass of 1.3 kg.

12.5. ATTITUDE DETERMINATION SENSOR SELECTION

The final step in selecting the ADCS hardware is to select the sensors needed to meet the accuracy requirements. The actuation processes to keep the desired attitude are in place, yet the spacecraft is still in need of a system that actually measures its orientation, velocity and acceleration. SMAD [45] Table 19-13 on page 583 gives an overview of available sensor equipment that will be considered for OB1 and OB2.

Given the distance from Earth many attitude determination instrument options can quickly be dismissed. In the absence of a strong magnetic or gravitation field attitude sensors making use of those two factors cannot be applied as supported by Table 12.2. Earth sensing equipment in absence of a celestial body can also be discarded. According to SMAD [45] this leaves only one option to meet the directional accuracy requirements of 0.55 arcminutes: star sensors. Besides from the fact that not many other sensor options lie on the table, star sensors are the only sensors that can provide the type of accuracy that project SWAN needs. However, even though they provide high accuracy they do need another set of sensors in order to operate properly. As the sun is our object of interest in this mission and pretty much no other sensor types are applicable it is apparent that sun sensors are the best possible option. Sun sensors have a relatively high accuracy, mostly around 0.1°, are cheap and can thus easily be used to determine the location of the sun in a 2-axis system. This preliminary attitude determination can then in turn be used by the star sensors to accurately measure the spacecraft orientation in 3D and to such an extent that all accuracy requirements are met.

In order to find the best possible option available a trade-off for both systems has been conducted. the trade-off looks at mass, power, accuracy and size giving all of them an equal weight of 25/100. Out of the four options, the best option gets 25/25 the second best options 20/25, the third best option 15/25 and the worst option 10/25. All the star sensors are radiation tolerant and can thus readily be used for manoeuvres in Earth proximity, even when passing through the Van Allen belts.

Table 12.7: Sun sensor trade-off

Sun sensor	Mass	Power	Accuracy	Size	Score
Adcole digital sun sensor +/- 32 deg ^a	10/25	10/25	20/25	10/25	50/100
Bradford fine sun sensor ^b	20/25	20/25	10/25	20/25	70/100
S3 (Smart Sun Sensor) ^c	25/25	15/25	25/25	25/25	90/100
Jena Optronik Fine Sun Sensor ^d	15/25	25/25	15/20	15/25	70/100

^a <https://www.adcolemai.com/digital-sun-sensors>

^b <http://bradford-space.com/products-aocs-fine-sun-sensors.php#>

^c <http://www.leonardocompany.com/en/-/s3-smart-sun-sensor>

^d <http://www.jena-optronik.de/en/aocs/fss.html>

The S3 Smart Sun Sensor turn out to be the most feasible option. These sun sensors can detect 2 axes of orientation with the star sensors providing the last axis and required accuracy along the axes. An additional advantage of this sun sensor is that it can also be used on rotating spacecraft, meaning that even if the spacecraft is in a tumble this equipment can determine sun direction and tumble sequence which is required for the de-tumble and safe mode.

The same process is applied to a selection of star sensors that all meet the accuracy requirement. Again, all of the selected star sensors are radiation hardened and should be able to cope with high levels of radiation.

Table 12.8: Star sensor trade-off

Star sensor	Mass	Power	Accuracy	Size	Score
Jena Optronik Autonomous Star Sensor ASTRO 15 ^a	10/25	10/25	15/25	15/25	50/100
Ball CT-2020 ^b	20/25	15/25	25/25	10/25	70/100
SODERN HYDRA-M ^c	25/25	20/25	10/25	20/25	75/100
TERMA T2 star tracker ^d	15/25	25/25	20/25	25/25	85/100

^a <http://www.jena-optronik.de/en/aocs/astro15.html>

^b http://www.ball.com/aerospace/Aerospace/media/Aerospace/Downloads/D3408_CT2020_0118.pdf?ext=.pdf

^c http://www.sodern.com/website/docs_wsw/RUB_316/tile_689/HYDRA_M_Datasheet.pdf

^d https://www.terma.com/media/437079/t1_t2_star_tracker_rev2.pdf

It thus follows that the TERMA T2 star tracker will be the star tracker of choice. This tracker provides a 3.5 arcsec accuracy in Cross-boresight and 21 arcsec accuracy in Roll-boresight³. The Cross-boresight being accuracy in pitch and yaw, while the Roll-boresight is the accuracy in roll along its main viewing axis. For star trackers that lack Roll-boresight accuracy usually a second star tracker is applied to meet the accuracy requirement in all three axes. Since the Terma T2 also meets the accuracy requirement of 0.55 arcmin about its Roll-boresight, 1 should suffice for full 3-axis coverage.

Finally, the ADCS needs to be able to determine acceleration and velocity about all its axes and in all directions. To meet the slew requirement of 26.5 arcminutes in 4 seconds, the system should be able to measure that value as a minimum. For this purpose gyroscopes are commonly used to measure rotational rate. There are 3 main types of gyroscopes: the Ring Laser Gyro (RLG), the Mechanical Gyro and the Fibre Optic Gyro (FOG). SMAD [45] states that due to its gimbaled design and complex mechanical interfaces, mechanical gyroscopes are relatively unreliable and need a high level of redundancy. Following this advice, two options are left. F Napolitano [112] lists multiple advantages of FOG over RLG. One reason is that because the telecom industry already uses many of the components needed to design a FOG, they have high reliability and proven performance. Another listed advantage is that RLGs use moving parts while FOGs are solid state designs. Adding to that all companies producing gyroscopes that are on the list provided by SMAD produce FOG and only rarely have a RLG available suggesting that FOG is indeed a more feasible, technically viable option.

To complete the whole unit a method for measuring directional velocity and acceleration needs to be implemented to the ADCS. Researching different options for this system quickly provided a definitive winner that clearly stood out from the rest in terms of weight and size, the Northrop Grumman LN-200S. This inertial measurement unit (IMU) combines a FOG with an accelerometer, being more light weight as a unit than any stand alone FOG found during the research.

³<https://www.terma.com/space/space-segment/star-trackers/>

12.6. SENSITIVITY ANALYSIS

The sensitivity of the ADCS depends mainly on the accuracy requirements and the spacecraft structure. The disturbance torques and their relative magnitude will not change since the space environment of the satellite will not differ. The spacecraft structure and material selection however, can change the disturbance torque, since the latter is linked to the illuminated spacecraft area A_s , the spacecraft reflectivity q , centre of mass c_m and centre of SRP c_{p_s} . Furthermore the accuracy requirements also play an important roll for the ADCS system and will be analysed too. This mainly concerns the pointing accuracy and the requirements on slew rate.

If the pointing accuracy is increased in terms of sensors, not much changes since star sensors are still the most accurate sensing equipment available. Nevertheless, it does increase the momentum stored in the momentum wheels to meet the accuracy requirement. The momentum in Equation (12.8) increases when θ_a decreases, leading to increments in rpm, size, weight and/or number of momentum dumps. The latter can result in a different momentum wheel being selected, which consequently can lead to a different power consumption and ADCS mass. On the other hand, if the pointing accuracy requirement decreases, star sensors might become irrelevant. This would cause a decrease in power consumption and mass both in terms of sensors and momentum wheels. The slew rate requirement mainly has an effect on the gyroscope selection. If this parameter increases, more accurate gyroscopes might be needed which in turn will also influence the mass and power consumption.

Knowing that SRP is the defining torque for the ADCS design Equation (12.2) shows that an increases in A_s , q and difference between c_m and c_{p_s} will raise the torque to a higher value. In turn both the stored momentum that needs to be dumped and the momentum needed to stabilise the spacecraft with momentum wheels increases. Equation (12.11) sizes depending on how much momentum must be dumped by the thrusters. The higher this thrust level, the higher the propellant mass becomes according to Equation (12.12). The additional momentum due to a δc_m increase, necessitates either bigger reaction wheels, more frequent momentum dumps or higher rpm. The increase in mass also leads to slightly different MMOI, but since sensor equipment and control actuators have a relatively low mass in general and are often distributed quite evenly over the spacecraft this effect will not be of high consequence.

12.7. SYSTEM OVERVIEW

Figure 12.2 shows how the ADCS is connected. it shows how commands are distributed and how information is collected and gathered.

12.8. VERIFICATION AND VALIDATION

Verification and Validation was a continuous process along the design of the ADCS. As SMAD [45] was the primary guideline throughout the ADCS design process, the examples provided in the book were compared to the obtained values. SMAD uses the FireSat II and SCS missions as example missions to determine the preliminary values.

DISTURBANCE, WHEEL AND THRUSTER SIZING CALCULATION VERIFICATION

The values obtained for T_a by applying Equation (12.2) both for SMAD and the values in the Excel sheet from Table 12.2 fall within the 10^{-6} to 10^{-5} magnitude range. Entering the same inputs as SMAD into the Excel sheet gives the same values as produced by the calculations in SMAD, which verifies that this computation for the disturbance torque is reliable. The same type of comparison is conducted for other relevant parameters.

In the Wheel and thruster sizing sections the same procedure is applied. Both values from SMAD and Table 12.2 fall within comparable orders of magnitude for control torque, with the values from SMAD at 10^{-5} and the value from Table 12.2 at 10^{-6} . The difference in order of magnitude can be traced back to different maximum continuous torques for the SWAN mission compared to the FireSat II mission. Comparing input values and entering the values provided by SMAD is a sound way of verifying whether the output values make sense. This process is applied for all subsequent parameters and is also applied to the thruster selection. In the end the parameters such as thrust level, momentum wheel rpm and weight all appear to produce reliable values, which is confirmed by the fact that they fall within the ranges of commercially manufactured products.

VALIDATION

For validation of the resulting hardware reference missions are considered and the ADCS hardware is compared in type and number of units. The STEREO missions had a comparable mission scope to project SWAN and is therefore used as a reference mission of choice. The mission spacecraft are 3-axis stabilised, use 2 IMUs provided by Honeywell and apply 1 star tracker in combination with 5 sun sensors for accuracy purposes [113]. This is very much in line with the selected hardware for the SWAN mission. Their actuation hardware is also very similar, using Hydrazine as fuel with 12 thrusters

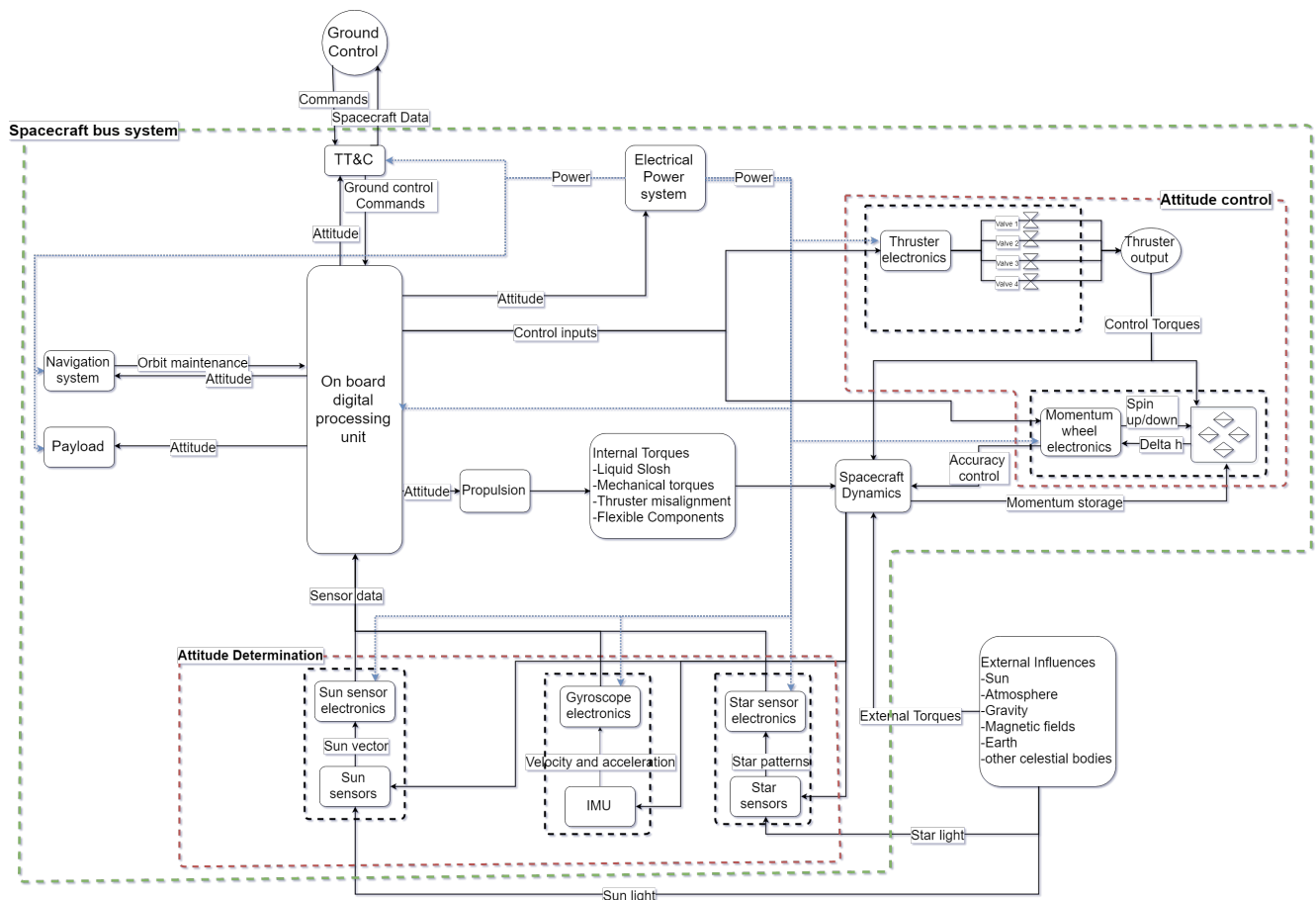


Figure 12.2: ADCS system layout

and 4 Reaction Wheels for momentum storage.

12.9. RISK ANALYSIS

Table 12.9: ADCS Risks. Likelihood: HU = highly unlikely, U = unlikely, SL = some likelihood, L = likely, HL = highly likely. Impact: M = marginal, S = some, H = high, C = catastrophic

Risk	Consequence	Likelihood	Impact	Mitigation
Momentum Wheel Failure	Consequence	HL	C	Component redundancy
Star Sensor Failure	Star sensors fail and tumbling cannot be monitored	L	C	Component redundancy
Sun Sensor Failure	Magnetograph fails	SL	H	Component redundancy
IMU Failure	Spacecraft cannot perform orbit insertions accurately	U	C	Component redundancy
Thruster Failure	No momentum dumps leading to momentum wheel failure	M	C	Component redundancy and testing before launch
Propellant tank leakage	Decrease in ADCS lifetime	U	H	Careful inspection and testing before launch

12.10. RELIABILITY, AVAILABILITY, MAINTAINABILITY, AND SAFETY CHARACTERISTICS

To increase reliability of the system component redundancy is a key aspect in ADCS design particularly in space since maintenance is not an option once the satellite is on space. Let's start off with the sun sensors. Sun sensors are cheap, light weight and low in power consumption and serve as good means to measure tumble and initial spacecraft-sun vector. For this purpose 6 sun sensors are used pointing along the positive and negative of each axis for L5. As the sun sensor effectiveness in determining the sun angle decreases if the angle of incidence is lower, additional sun sensors on the

sun facing side of the spacecraft is added in case one should fail. For the L1 orbiter no star sensors will be necessary since they meet the 4.3 arcminute requirement.

The star sensors are directly dependent on the sun sensors for initial orientation. To make them a redundant system at least 2 star sensors for 3-axis redundancy are required for L5 where the accuracy depends on this system. At L1 the accuracies provided by the sun sensors should suffice, yet full 3-axis would not be possible with sun sensors alone. One could argue that a third axis can be determined through help of the payload which can measure the rotational direction of the sun and thus spacecraft orientation. Nevertheless, this remains an option that needs to be investigated in more detail at a later design stage. For now, let's add one star tracker to OB1 to guarantee full 3-axis coverage at L1.

The Northrop Grumman LN-200S provides 3-axis stabilisation but no redundancy as only 3 gyros are used in the system. For this reason a second unit is installed to make the system redundant. All of the sensor equipment is commercially available and no extraordinary materials are needed for their design. The FOGs especially are produced from widely used materials and technologies already at hand from the telecomm industry making this a readily available and reliable product. Only the star tracker possibly requires titanium for radiation hardening.

For the actuator system, a minimum of 3 momentum wheels and 12 thruster are necessary [45] to have full 3-axis control. For redundancy 1 momentum wheel is added and 4 thrusters. All these actuator mechanisms are commercially available and do not require any dangerous materials for production. The propellant itself though is extremely hazardous and measures should be taken that none of it is leaked potentially harming workers and the environment. This is why careful checks of the propellant tanks and propellant containing systems should be conducted to guarantee safety.

12.11. REQUIREMENT COMPLIANCE

Table 12.10: ADCS requirement compliance matrix.

Identifier	Requirement	Met?	Confirmation
ADCS-OPML5-01	The ADCS system shall have an accuracy of 0.55'	✓	Section 12.5
ADCS-OPML5-02	The ADCS shall not drift more than 26.5' in 4 seconds	✓	Section 12.4
ADCS-OPML1-01	The ADCS system shall have an accuracy of 4.3'	✓	Section 12.5
ADCS-OPML1-02	The ADCS shall not drift more than 26.5' in 4 seconds	✓	Section 12.4
ADCS-OPML1-03	The orientation of the Magnetometer shall be known within 33'	✓	Chapter 13
ADCS-ORL5-01	The ADCS shall be able to determine spacecraft attitude with an accuracy of 2.004'	✓	Section 12.5
ADCS-ORL5-02	The ADCS shall be able to keep this accuracy for 35.9 minutes	✓	Section 12.4
ADCS-ORL5-03	The spacecraft shall be able to rotate 180 degrees from and going back to standstill within 2 minutes	✓	Section 12.4
ADCS-ORL1-01	The ADCS shall be able to determine spacecraft attitude with an accuracy of 3.44 arcminutes	✓	Section 12.5
ADCS-ORL1-02	The ADCS shall be able to keep this attitude for 40.88 seconds	✓	Section 12.4
ADCS-ORL1-03	The spacecraft shall be able to rotate 180 degrees from and going back to standstill within 2 minutes	✓	Section 12.4
ADCS-TML5-01	The ADCS shall be able to point the solar arrays sunward	✓	Section 12.4
ADCS-TML5-02	The ADCS shall be able to point the communication antennas with an accuracy of 0.5°	✓	Section 12.5
ADCS-TML1-01	The ADCS shall be able to point the solar arrays sunward	✓	Section 12.4
ADCS-TML1-02	The ADCS shall be able to point the communication antennas with an accuracy of 3.5°	✓	Section 12.5
ADCS-SM-01	The system shall provide a pointing accuracy of 0.5° to communicate and point the solar array	✓	Section 12.5
ADCS-SM-02	The ADCS shall be able to determine attitude and rotational velocity	✓	Section 12.5
ADCS-DM-01	The spacecraft shall have an on board de-tumble program that computes the optimal attitude restitution sequence within 3 seconds	<TBD>	-
ADCS-DM-02	The ADCS system shall be able to perceive a tumble within <td> seconds	<TBD>	-
ADCS-GENL5-01	The total mass of the ADCS system shall not exceed 28 kg	✓	Section 12.12
ADCS-GENL5-02	The total power used by the ADCS system shall not exceed 88.3 W	X	Section 12.12
ADCS-GENL5-03	The total cost of the ADCS system shall not exceed 14354 K euro	<TBD>	-
ADCS-GENL5-04	The reliability of the ADCS system shall be at least 99.5%	<TBD>	[49]
ADCS-GENL5-05	The ADCS shall be redundant	✓	Section 12.10
ADCS-GENL5-06	The ADCS shall provide enough accuracy to point the solar arrays	✓	Section 12.5

ADCS-GENL5-07	The spacecraft shall be able to rotate 180 degrees from and going back to standstill within 2 minutes	✓	Section 12.4
ADCS-GENL5-08	The ADCS system shall have a sampling frequency twice as high as the structural natural frequency	<TBD>	-
ADCS-GENL1-01	The total mass of the ADCS system shall not exceed 24.2 kg	✓	Section 12.12
ADCS-GENL1-02	The total power used by the ADCS system shall not exceed 80.2 W	✓	Section 12.12
ADCS-GENL1-03	The total cost of the ADCS system shall not exceed 12693 K EUR	<TBD>	-
ADCS-GENL1-04	The reliability of the ADCS system shall be at least 99.5 %	<TBD>	[49]
ADCS-GENL1-05	The ADCS shall be redundant	✓	Section 12.10
ADCS-GENL1-06	The ADCS shall provide enough accuracy to point the solar arrays	✓	Section 12.5
ADCS-GENL1-07	The spacecraft shall be able to rotate 180 degrees from and going back to standstill within 2 minutes	✓	Section 12.4
ADCS-GENL1-08	The ADCS system shall have a sampling frequency twice as high as the structural natural frequency	<TBD>	-

12.12. CONCLUSION AND RECOMMENDATIONS

The final hardware selected for the SWAN mission is represented in Table 12.11 with only the vanes not included.

Table 12.11: ADCS hardware.

L5	Hardware	Mass [kg]	Power [W]	Size[mm]	Number
	Honeywell HR 0610 Momentum Wheel	3.6	15	267x120	4
	MR-111C 4N Thruster	0.33	0	-	16
	S3 (Smart Sun Sensor)	0.33	0.7	112x112x43	7
	TERMA T2 star tracker	0.76	2	Ø155x213	2
	LN-200S Northrop Grumman Inertial Measurement Unit	0.784	12	Ø88.9x85.1	2
L1	Hardware	Mass [kg]	Power [W]	Size	Number
	Surrey 10SP-M Momentum Wheel	0.96	2.8	109x101	4
	MR-111C 4N Thruster	0.33	0	-	16
	S3 (Smart Sun Sensor)	0.33	0.7	112x112x43	7
	TERMA T2 star tracker	0.76	2	Ø155x213	1
	LN-200S Northrop Grumman Inertial Measurement Unit	0.784	12	Ø88.9x85.1	2

To further refine the ADCS system and select better thrusters with more suitable momentum wheels it is recommended that in the next steps of the spacecraft design further attention is paid to bringing the c_m and c_{p_s} closer together without the use of SRP vanes. The vanes are still an option but add weight and complexity to the system that could be avoided if the rest of the spacecraft is smartly designed. On the other hand, vanes should not be discarded wholly since they can serve as good alternatives for controlling torque if combined with an adjustable actuation mechanism that controls the incidence angle.

Another recommendation is to look deeper into the internal torques once a more refined understanding of the spacecraft structure and subsystems is at hand. Furthermore it is useful to take into account a variety of potential emergency situations such as a micro meteorite hit or a thruster malfunction. These types of disturbance torques can be catastrophic and it should be checked whether the ADCS can cope with these factors.

Furthermore for the second star tracker for OB2 one should look into the possibility of using the heliospheric imager as an additional star tracker. If this turns out to be possible, only one star tracker might be needed for L5 saving on weight and more importantly cost. Another possible simplification of the ADCS system would be to look into using the Doppler effect as means of measuring directional velocity and acceleration of the spacecraft. To find out if this type of measurement is indeed more feasible more research should be conducted to determine the pros and cons.

Finally an elaborate cost analysis for this section should follow in the subsequent design phas. Due to competition between companies, prices are not shown online for such sensitive equipment and a formal request to each company would be needed to get a good grab on the exact costs. For now, the estimate made in the technical budget sheet in Chapter 15 will be kept.

13

STRUCTURAL CHARACTERISTICS

The structure forms the backbone of both satellites. Not only does it provide the main shape, strength, and stiffness for the spacecraft, but it also functions as the primary mechanical interface to attach all subsystems to. First of all, this chapter introduction shall elaborate on a number of initial design decisions that were made for the structural design. In Section 13.1 the different loads that act on the satellite will be discussed. This is followed by the material selection for all structure types within the spacecraft in Section 13.2. Once the material selection has been decided upon, the primary, secondary, and tertiary structure are discussed in Section 13.3, Section 13.4, and Section 13.5, respectively. Section 13.6 presents the centre of gravity and mass moments of inertia of the spacecraft design. Next, the verification and validation procedures for the structural design are discussed in Section 13.7, followed by a RAMS analysis in Section 13.8. All structural requirements are checked to see if they are met in Section 13.9, and finally Section 13.10 summarises all results and states recommendations for future research.

One of the first decisions for the satellite structure, is to choose a specific type of structure. The most straight-forward type is a skin-frame structure: the primary structure consists of a network of axial and lateral frames, to which a secondary structure of panels and skins is mounted. In such a configuration, the primary structure supports the axial, bending, and torsional forces. The skin panels mainly support the shear forces induced on the structure. All exterior components, such as the solar arrays, will be mounted to the primary structure, since the panels are not meant to take high loads. [114]

13.1. LOADS

The structure has to hold all the elements of the spacecraft together during all phases of the mission. Therefore, it needs to resist all the loads that will act on the spacecraft throughout its lifetime, as such these loads have to be defined.

Several types of loads act on the spacecraft throughout its lifetime: static loads, dynamic loads (Section 13.1.1), and vibrational loads (Section 13.1.2).

13.1.1. STATIC AND DYNAMIC LOADS

During construction, assembly, transport, launch of the satellites, and their operation a range of dynamic, and sometimes also static, loads will act on them. The loads in Figure 13.1a and Table 13.1 include the static and dynamic loads. Clearly the launch loads provided in Figure 13.1a are more critical than the transport loads in Table 13.1. Moreover, a longitudinal accelerations up to 2.2 ms^{-2} can act on the spacecraft during the burns in space. The axial or longitudinal axis is the X-axis as defined in Figure 13.1b. The lateral axis in Figure 13.1a refers to an axis in the YZ-plane. In Table 13.1 the Y- and Z-axes are the lateral and vertical axes, respectively.

Table 13.1: Quasi-static load factors for transportation.[57]

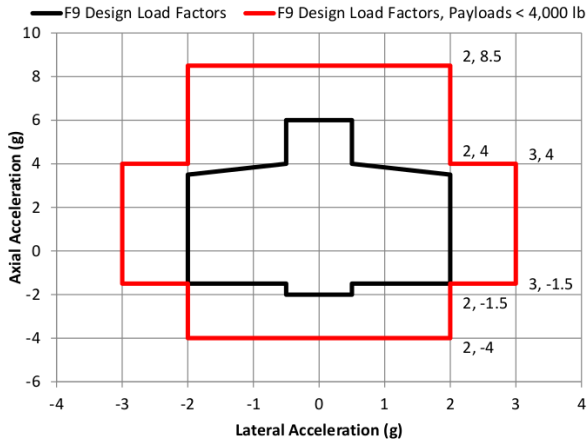
Transportation Method	Longitudinal Load [g]	Lateral Load [g]	Vertical Load [g]
Slow-moving dolly	± 1.0	± 0.75	± 2.0

The loads at the launch vehicle interface are defined in Equation (13.1), with the load factors (n_i) given in Figure 13.1a and Table 13.1. Here N_{axial} is a force along the X-axis, V_{shear} a force along the selected lateral acceleration axis, and M_{bend} the bending moment due to the latter acceleration. The mass of the spacecraft is m_{SC} , and L_{CG} is the distance between the launch vehicle interface and the location of the spacecraft centre of gravity.

$$N_{axial} = m_{SC} \cdot a_{axial} \quad V_{shear} = m_{SC} \cdot a_{lateral} \quad M_{bend} = m_{SC} \cdot a_{lateral} \cdot L_{CG} \quad a_i = n_i \cdot g_0 \quad (13.1)$$

13.1.2. VIBRATIONAL LOADS

During launch the spacecrafts are subjected to vibrations, both in axial and lateral axes, for the low frequencies this is the sinusoidal vibration environment as shown in Figure 13.2a. At somewhat higher frequencies lie vibrations due to acoustic excitation, as provided in Figure 13.2b. Finally, Table 13.2 provides the shock loads, which are often high frequencies. However, these shock loads only occur during separation of the spacecraft. Moreover, the time over which this shock



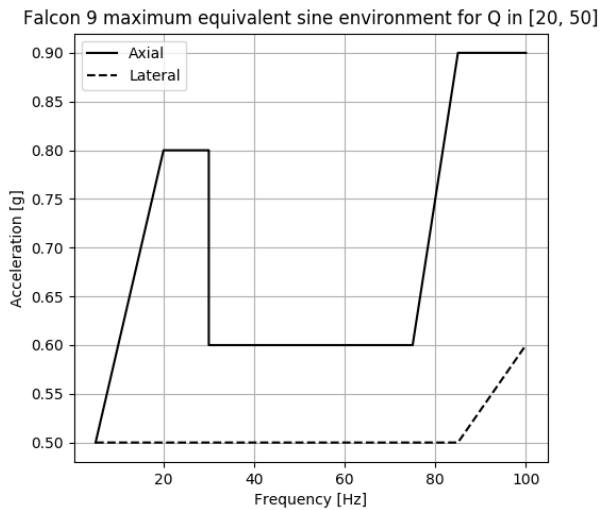
(a) Falcon 9 payload design load factors, Light mass (under 4,000 lb).[57]



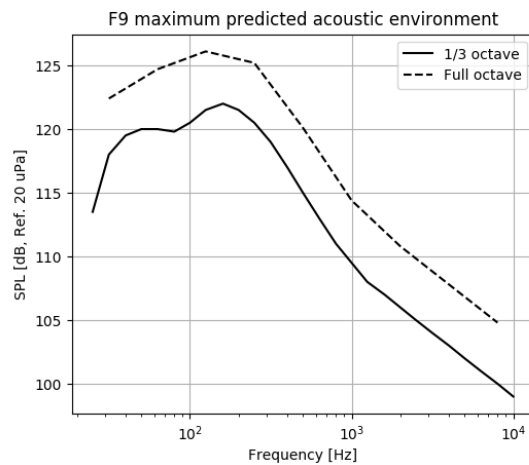
(b) Falcon vehicle coordinate frame.[57]

Figure 13.1: Launch loads.

occurs is extremely small, as such the energy it imparts upon the spacecraft is limited.



(a) Sine vibrations during launch.[57]



(b) Acoustic limit levels.[57]

Figure 13.2: Falcon vibrational loads.

Table 13.2: Payload adapter-induced shock at the spacecraft separation plan. SRS:shock response spectrum.[57]

Frequency [Hz]	100	1,000	10,000
SRS [g]	30	1,000	1,000

13.2. MATERIAL CHARACTERISTICS

The selection of the right materials for the SWAN satellites is a crucial part of the structural design process. As mentioned in the introduction of this chapter, the satellite will incorporate a skin-frame structure. For this reason, it must be stressed that different structural elements have different structural functions within the spacecraft, and thus may have different materials which are best suited for the function. Hence, this section makes a distinction between the material selection for the primary truss-structure in Section 13.2.1, and the secondary structure of skin panels in Section 13.2.2.

13.2.1. PRIMARY STRUCTURE MATERIAL SELECTION

The primary structure of the satellite consists of a network of trusses and beams. As mentioned before, this network will mainly take the bending, torsional, and axial loads on the satellite. To carry all these different loads, an isotropic material is preferable. Materials such as metals, ceramics, and polymers have the same material properties regardless

of the direction of the load path. To choose between these families, one must naturally consider the performance of the materials, such as strength, stiffness, density, and thermal properties. However, also cost and ease of manufacturing play an important roll in the selection process. The three material families mentioned before will briefly be discussed here.

- **Metals.** This material family is extremely versatile in its application possibilities. Metals suitable for space applications have a high specific strength and stiffness, while also being very tough. This last property gives them a good resistance to fracture and crack propagation. Additionally, a lot of metal alloys are relatively cheap, and can be easily formed, milled, and joined. The draw-back of metals, is that most alloys have a poor thermal expansion coefficient (TEC); relatively low changes in temperature can cause a fairly large expansion of a structural member.
- **Ceramics.** Technical ceramics have some of the best specific strength and stiffness performance of any material family, sometimes even higher than high-end composites. Compared to metals, this material family also has better thermal expansion properties. However, their main draw-back is their brittleness, along with the fact that complex ceramic structures are very hard to produce. These factors are the main reason that technical ceramics are hardly ever used as primary structure for space applications.
- **Polymers.** These materials are very easy and cheap to produce; almost any structure can be either formed, milled, or cast. This comes at the cost of less favourable performance properties that metals or ceramics. Another draw-back of polymers is their susceptibility to high temperatures.

From this top-level comparison, it has been decided that a metal alloy will be optimal for the primary structure. The good performance properties of metal alloys, combined with their cost and their ease of production and attachment, make this material family the overall best option.

Now that the material family has been decided upon, the next step is to choose a specific metal alloy for the primary structure. This requires a more in-depth comparison of different options. In Table 13.3, a number of alloys which are commonly used in space applications are presented: two aluminium alloys, a titanium alloy, and a grade of stainless steel. The material properties shown are the performance characteristics that are deemed most important for the material selection.

Table 13.3: Primary Structure Material Options

	ρ [kg m ⁻³]	E [GPa]	σ_y [MPa]	α_t [$\mu\text{m}^\circ\text{C}^{-1}\text{m}^{-1}$]	C_{sp} [USD m ⁻³] ^a
Al-7075^b	2810	71.7	503	25.2	5994
Ti-6Al-4V^c	4430	113.8	880	9.2	75600
Stainless Steel 304^d	8000	195	215	17.8	34621
AL-6061^e	2700	68.9	276	25.2	5994

^a http://www.roymech.co.uk/Useful_Tables/Matter/Costs.html

^b <http://asm.matweb.com/search/SpecificMaterial.asp?bassnum=MA7075T6>

^c <http://asm.matweb.com/search/SpecificMaterial.asp?bassnum=mtp641>

^d <http://asm.matweb.com/search/SpecificMaterial.asp?bassnum=mq304a>

^e <http://asm.matweb.com/search/SpecificMaterial.asp?bassnum=ma6061t6>

For a good comparison of the specific properties, Ashby's *Materials Selection in Mechanical Design*[115] presents an elegant way to quantify this. It incorporates the use of so-called material indexes to compare the specific material properties for different geometries under different types of loading. An example of how such a material index is determined, will now be discussed for stiffness, strength, and thermal performance.

STIFFNESS

A simply supported beam is considered, with an arbitrary cross-section, which is loaded under bending as shown in Figure 13.3. The goal is to minimise the mass of this beam (in order to achieve a light-weight design), while maximising the stiffness. The mass of the beam is simply given by Equation (13.2).

$$m = \rho \cdot A \cdot L \quad (13.2)$$

First of all, the bending stiffness is given by Equation (13.3). This very general expression takes all possible clamping conditions of the beam into account by introducing the variable C_{clamp} .

$$S = \frac{F}{\delta} = \frac{C_{clamp}EI}{L^3} \quad (13.3)$$

Next, the area and area moment of inertia are expressed in terms of the beam width, as can be seen in Equation (13.4). The coefficients α and β are correction factors for the cross-section. For any cross-section that is not square, these coefficients will have a value of < 1 .

$$A = \alpha b^2 \quad I = \beta \frac{b^4}{12} \quad (13.4)$$

The next step is to substitute I into Equation (13.3), and then rewrite this relation for the beam width b . These two relations can be found in Equation (13.5). The last expression can then be substituted in the equation for the area, which can finally be substituted in the mass equation in Equation (13.2). The final expression for the mass of the beam can be seen in Equation (13.6)

$$S = \frac{C_{clamp} E \beta b^4}{L^3} \frac{1}{12} \implies b = \left(\frac{12SL^3}{C_{clamp} E \beta} \right)^{\frac{1}{4}} \quad (13.5)$$

$$m = \rho L \alpha \left(\frac{12SL^3}{C_{clamp} E \beta} \right)^{\frac{1}{2}} \quad (13.6)$$

There are a lot of variables in this equation. However, only the Young's Modulus (E) and the density (ρ) are material properties. To minimise the beam mass, it can be seen that the ratio $E^{\frac{1}{2}}/\rho$ needs to be maximised. This is thus the material index related to a light, stiff beam under bending.

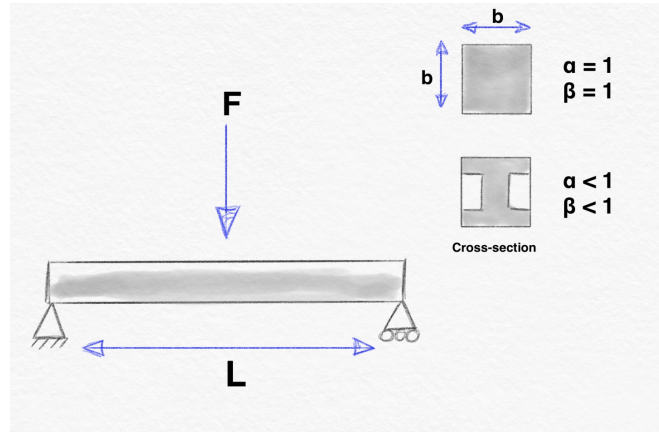


Figure 13.3: Simply Supported Beam under Bending

STRENGTH

To find the material index for a light, strong beam, the process is fairly similar. Again, the basis of this derivation is the mass equation in Equation (13.2). The stress in a simply supported beam under bending, is given in Equation (13.7).

$$\sigma = \frac{F L b}{I 4 2} \quad (13.7)$$

Also now, the expressions for A and I are given by Equation (13.4). The expression for I is substituted in Equation (13.7), and again rewritten for b . This is shown in Equation (13.8). The final equation for the mass is obtained in Equation (13.9), similarly to the stiffness derivation.

$$\sigma = \frac{3FL}{2\beta b^3} \implies b = \left(\frac{3FL}{2\beta\sigma} \right)^{\frac{1}{3}} \quad (13.8)$$

$$m = \left(\frac{3F}{2} \right)^{\frac{2}{3}} \frac{\alpha}{\beta} L^{\frac{5}{3}} \left(\frac{\rho}{\sigma^{\frac{2}{3}}} \right) \quad (13.9)$$

In this mass equation, the only variables related to the material properties are the yield strength (σ) and the density (ρ). To minimise the beam mass, the ratio $\sigma^{\frac{2}{3}}/\rho$ needs to be maximised. This is thus the material index for a light, strong beam under bending. Note how this material index maximises the strength, whereas the previous material index minimised the deflection.

THERMAL PERFORMANCE

The final important class of material index, is related to the thermal properties of each material. For this derivation, a constrained beam is considered, which is initially in a stress-free condition. When a positive temperature change of ΔT is introduced, the beam expands and experiences a thermal stress, which is given by Equation (13.10).

$$\sigma_t = E\epsilon_t = E\alpha_t\Delta T \quad (13.10)$$

$$\frac{\sigma_t}{\Delta T} = E\alpha_t \quad (13.11)$$

Rewriting this in the form of Equation (13.11), it is apparent that the product of the Young's Modulus (E) and the thermal expansion coefficient (α_t) must be minimised, in order to minimise the the specific thermal stress. Hence, $E^{-1}\alpha_t^{-1}$ is the material index related to the thermal performance of each material, which must be maximised.

The final type of material index included in the selection process, is related to the cost of the material. This is found by maximising the amount of material one can get for a unit price. It should be noted, that this only includes the raw material costs, so differences in production costs are not considered in this material index.

An overview of all calculated material indexes can be seen in Table 13.4. Conveniently, the strength and stiffness indexes for beam tension and torsion are the same. In the first column, the stiffness indexes for this type of loading fall within a few percent margin for all options. Hence, this material index will not be taken into consideration. In the second column, the strength index for beam bending is shown. The titanium alloy is the winner here, but the Al-7075 alloy comes in a fairly close second place. The third and fourth column look at the beam bending material indexes. The third column shows that both the aluminium alloys score highest on the stiffness index, whereas Al-7075 greatly out-performs Al-6061 on the strength index in the fourth column. The thermal material index is determined in the fifth column, and clearly shows that the titanium alloy is the best. However, when looking at the cost index for each option, the titanium alloy is roughly 8 times more expensive than Al-7075, which is the best option.

Table 13.4: Primary Structure Material Indexes

	Beam tension/Torsion		Beam Bending		Thermal	Cost
	E/ρ	σ/ρ	$E^{\frac{1}{2}}/\rho$	$\sigma^{\frac{2}{3}}/\rho$	$1/(E\alpha)$	ρ/C_{sp}
Al-7075	0.02552	0.1790	0.003013	0.02251	0.0005535	0.4688
Ti-6Al-4V	0.02569	0.1986	0.002408	0.02073	0.0009551	0.05791
Stainless Steel 304	0.02438	0.02688	0.001746	0.004486	0.0002881	0.2311
Al-6061	0.02552	0.1022	0.003074	0.01570	0.0005759	0.4505

All in all, it is apparent that the main selection will take place between Ti-6Al-4V, and Al-7075; stainless steel is an overall low scorer on most indexes, and Al-6061 either scores comparable to Al-7075, or lower. The biggest merit of the titanium alloy, is the low thermally induced stress in the material, when it is exposed to a temperature change. Furthermore, Ti-6Al-4V has very good specific stiffness and strength properties. However, it is a very expensive material compared to the others. Al-7075 is far cheaper, and also shows good strength and stiffness properties. Its major drawback is the lower thermal material index, which may prove to be a a major problem in the challenging thermal environment of the SWAN satellites. The higher cost of titanium must also be compared relative to the overall mission costs. Since the satellites will contain instruments in the order of millions of USD, the relative cost of the spacecraft structure will be far less significant. Hence, it can be justified to choose a more expensive material for the structure, without causing a large impact on the total cost budget. For the aforementioned reasons, **Ti-6Al-4V** was chosen for the primary structure of the spacecraft.

13.2.2. SECONDARY STRUCTURE MATERIAL SELECTION

The secondary structure of the spacecraft will consist of skin panels, filling up the faces of the primary truss structure. These panels will mainly support the shear loads on the structure. Due to the directional nature of these shear forces, it is also possible to consider an anisotropic material, such as composites, for the secondary structure. Below, the main material families are briefly discussed.

- **Metals.** Also for the secondary structure, it is possible to use a metal alloy, in the form of a sheet. Metal sheets are very cheap and easy to bond to a structure. However, they have a low stiffness, which leads to poor vibrational properties. Additionally, metals have a high thermal conductivity, making them poor insulators.

- **Composites** A very common option for skin panels, is the use of composite sandwich structures. These structures consist of two skins, with a light-weight core material in between, which gives the main stiffness to the panel. These composites are thus characterised by a high specific stiffness. Furthermore, sandwich panels generally have a low thermal conductivity, since the core usually has a lot of empty space to minimise mass. However, this also introduces the threat high internal stresses, when exposing such an air-filled structure to a vacuum. To avoid these stresses in the SWAN satellites, the core of a sandwich panel must be able to vent any trapped air fast enough. Such core materials are called slotted cores.

From this top-level comparison, it has been decided to use composite sandwich panels for the secondary structure. The good stiffness characteristics, combined with the low weight and thermal conductivity make sandwich panels the best choice for the skin panels.

Now that it has been decided to use sandwich panels for the secondary structure, the specific core and skin materials can be investigated. A number of common aerospace composites are shown in Table 13.5, along with their relevant properties. For the skin sheets, the shear strength and stiffness are more important for the selection process, since the skins take almost all of the shear loads. A standard carbon fibre with 45° fibre orientation, a glass fibre with 45° fibre orientation, and a kevlar fabric will be compared. The core material still mainly requires good in-plane strength and stiffness to resist any bending deflections due to vibrations. The selection will be made between an aramid honeycomb core, an aluminium honeycomb core, and a PVC foam core.

Table 13.5: Secondary Structure Material Options

		ρ [kg m ⁻³]	τ_y [MPa]	G [GPa]	k [W m ⁻¹ K ⁻¹]	C_{sp} [USD m ⁻²] ^a
Sheet Material	Std CF +- 45°^b	1600	260	33	10	40.0
	E Glass Fabric +-45°^b	1900	100	11	1.0	9.44
	Kevlar Fabric^b	1400	50	5	0.30	40.0
		ρ [kg m ⁻³]	σ_y [MPa]	E [MPa]	k [W m ⁻¹ K ⁻¹]	C_{sp} [USD m ⁻²]
Core Material	A1-48-5 Aramid Honeycomb^c	48	0.138	2.40	0.100	48.70
	PVC Foam^d	80	0.063	2.00	0.0330	22.23
	ECM 4.8-77 Aluminium Honeycomb^e	77	0.265	3.94	2.37	38.01

^a <https://polyestershoppen.nl/>

^b http://www.performance-composites.com/carbonfibre/mechanicalproperties_2.asp

^c http://www.hexcel.com/user_area/content_media/raw/A1A10_eu.pdf

^d <http://www.ecfibreglasssupplies.co.uk/images/pdfs/flexyfoamtds.pdf>

^e <https://www.amtcomposites.co.za/sites/default/files/media/data-sheets/Data%20Sheet%20ECM.pdf>

Also for the secondary structure, material indexes can be determined clearly compare all options. The procedures to set up these indexes are similar to those shown for the primary structure, but the individual indexes are not all the same. For instance, for the skin material, the material indexes will mainly focus on the shear properties of the material, whereas the core material will compare the bending indexes. Since the secondary structure covers almost all of the outer surface area of the spacecraft, the thermal conductivity of the material greatly influences the thermal environment in the spacecraft. Ideally, the spacecraft would be perfectly insulated, thus the thermal conductivity (k) of the secondary structure should be minimised. This leads to the material index of maximising k^{-1} . All relevant material indexes are summarised in Table 13.6.

Table 13.6: Secondary Structure Material Indexes

		Sheet Shear		Thermal	Cost
		$\gamma^{\frac{1}{2}}/\rho$	$G^{\frac{1}{3}}/\rho$	1/k	ρ/C_{sp}
Sheet Material	Std CF +- 45°	0.01008	0.002005	0.1	40.0
	E Glass Fabric +-45°	0.005263	0.001171	1.0	202.1
	Kevlar Fabric	0.005051	0.001221	3.3	35.0
		Sheet Bending		Thermal	Cost
		$E^{\frac{1}{3}}/\rho$	$\sigma^{\frac{1}{2}}/\rho$	1/k	ρ/C_{sp}
Core Material	A1-48-5 Nomex Honeycomb	0.01077	0.03228	10.0	0.9856
	PVC Foam	0.004974	0.01768	30.30	3.599
	ECM 4,8-77 Aluminium Honeycomb	0.008342	0.02578	0.4219	2.026

When comparing the material indexes for the face materials, it is apparent that carbon fibre has by far the best mechanical properties. On the other hand, it has the least optimal thermal characteristics of all options, combined with the fact that it is relatively expensive. Again however, the relative cost of the structure is far less than other more expensive subsystems, hence it can be justified to choose a more expensive structural material. Regarding the thermal conductivity, all options would require additional thermal control to meet the thermal requirements imposed on the spacecraft. Since it is feasible to achieve these requirements for all options, also this material index weighs less than the mechanical properties. For the core material, the same general reasoning is applied; although the Nomex honeycomb does not necessarily have the best cost and thermal performance, its good mechanical characteristics are deemed more important. To summarise, the secondary structure will consist of composite sandwich panels with faces made of **standard +- 45° carbon fibre sheets** with a core material of **Al-48-5 Nomex honeycomb**, which is slotted to allow for decompression during launch.

13.3. PRIMARY STRUCTURE DESIGN

As discussed in the introduction the structure has three elements. In this section the focus will be the design of a primary structure, which forms the backbone of the satellite and the main load path between the components of the satellite and the launch vehicle adaptor.

Firstly, the shape and configuration of the satellite will have to be finalised. Afterwards, the stresses in the structure can be analysed using a finite elements method. Using the same structural model the eigenfrequencies of the structure will be determined to check if they meet the 10 Hz limit on the natural frequency, as imposed by the launcher. For the stress and vibration analysis CATIA™ V5R21 is used.

13.3.1. SHAPE AND CONFIGURATION

As mentioned in the introduction, the choice for a skin-frame structure was made early on. Compared to a monocoque cylinder design or a cylindrical skin-stringer design the flat panels that form the skin allow for easy mounting of the elements within or on the outside of the satellite. The same holds true for a truss structure, however the skin allows for a large surface through which heat can be dissipated.

The launch vehicle adaptor provides a circular support to the satellite, as such the most efficient way to transfer the loads from the payload to the launcher would be to keep the cross-section as constant as possible. For this reason a central stiffening structure is chosen, which would transfer the loads from the frame structure to the launcher. The structure would be clamped to an adaptor on the launcher using a system provided by SpaceX[57], to allow this the cylinder ends in a small lip. Several other elements can be housed within this cylinder. Preferably the thruster and tanks would be positioned as closely as possible to the centre of mass to limit the torque during burns. Therefore, all tanks and the thruster were positioned within the cylinder. However, placing these tanks behind each other results in an extremely long and slender satellite. Structurally, it is advantageous to keep the distance between the object and the launch vehicle interface small to limit the moment arm and therefore the stresses. OB2 has a large oxidiser and a large propellant tank, therefore these were placed next to each other. The empty space next to these tanks can be filled up by the instruments, allowing the length of their load paths to be minimised. The largest tank in OB1 is the pressurant tank, however placing the coronagraph outside the cylinder would actually require a larger cross section than if the cylinder would be enlarged to fit this instrument. Therefore, the coronagraph is placed next to the pressurant tank, leaving room next to it for an oxidiser tank and the other instruments. The end results can be seen in Figure 13.4.

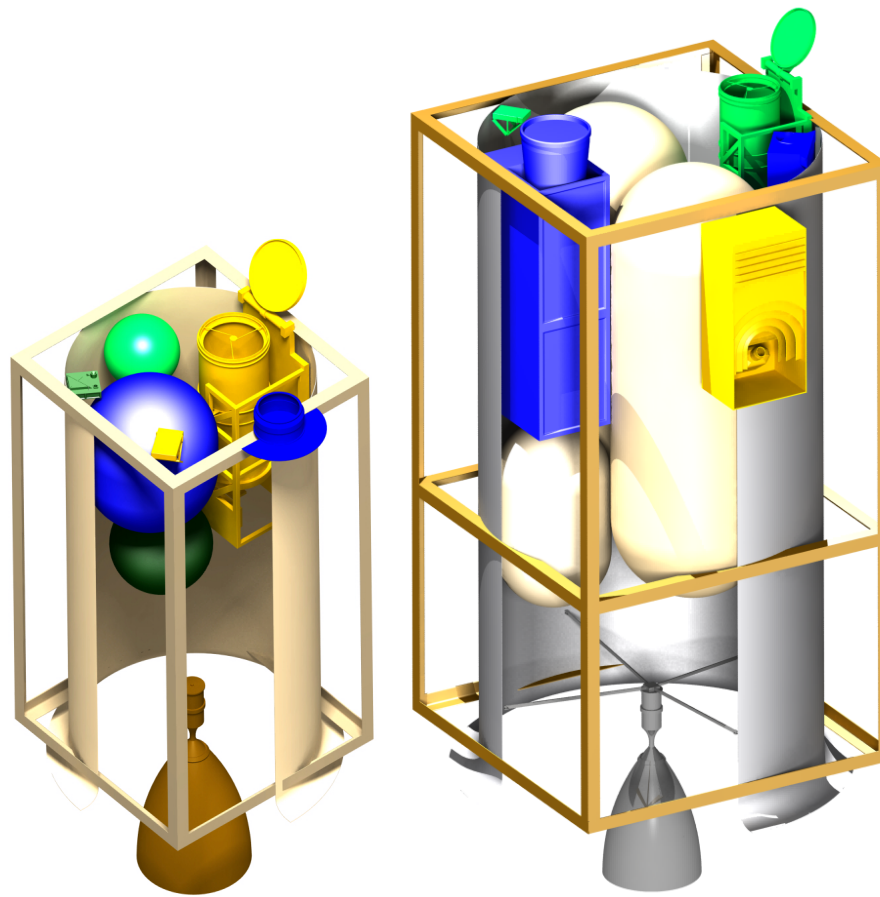
The length of the two large tanks in OB2 means that the two pressurant tanks can be placed underneath the coronagraph and magnetograph, next to the larger tanks. Finally, about 50 cm of room is left between the lowest point of the tanks and the thruster to allow for the feed system. A similar configuration is used for OB1, except that only a propellant tank remains which is positioned underneath the pressurant tank.

Several other subsystems still have to be housed in the spacecraft, and while some electronics or small elements can also be housed inside the cylinder, most will be housed outside the cylinder. Housing these elements outside of the cylinder enables easy access to them, as only the sheet has to be removed. By placing the frame against the cylinder the loads can more easily be transferred and the frontal size of the satellite is minimised. Enough room remains in the corners of the frame to store all other subsystems.

13.3.2. STRESS ANALYSIS

With the shape of the structure chosen its parameters have to be determined. The stresses in the structure play a large roll in the sizing of the structure, too high and the structure fails, too low and a lot of potential is wasted with a heavy structure. Titanium 6AL-4V will be used for the primary structure due to its excellent thermal properties, as discussed in Section 13.2.1.

A first iteration of the satellite used a central cylinder thickness of 5 mm and a frame element thickness of 7.95mm. This



(a) OB1 Configuration and Shape.

(b) OB2 Configuration and Shape.

Figure 13.4: OB1 and OB2 configuration and shape.

yielded a heavily over-designed structure weighing several hundreds of kilograms. Finally, setting the central cylinder thickness to 1 mm and the frame element thickness to 3 mm results in a very light design. As such, the structure can easily carry the stresses as visible in Figure 13.5 and Figure 13.6, while being rigid enough to not allow for too large deformations that could damage its internals. In these figures several forces are placed on studs to simulate the attachment of the elements on the structure, as seen in Figure 13.5 and Figure 13.6. These forces are proportional to the inertial forces caused by an acceleration of 8.5 g in the x direction, and 2 g in the z direction for OB2. While the accelerations on OB1 are -8.5 g in the z direction, and 2 g in the y direction, this is simply due to a different axis system in the models. The lip at the end of the cylinder is clamped.

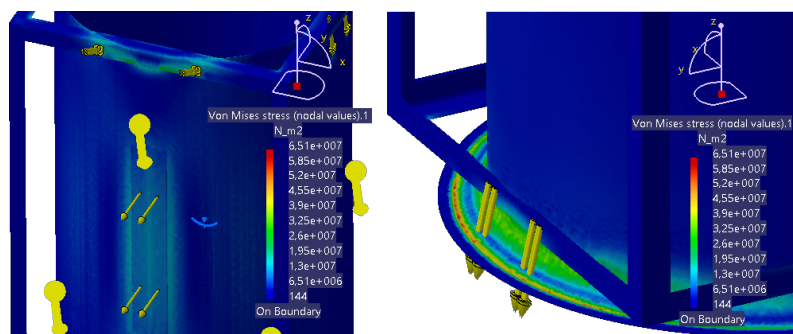


Figure 13.5: OB1 Von Mises stress. | Left: OB1 Von Mises stress on negative y face. Stress concentrations near coronagraph and connection cylinder and frame. Right: OB1 Von Mises stress on positive y face. Stress concentration near launch vehicle interface. | Element size : 5 mm, absolute sag : 10 mm.

Several stress concentrations exist where the frame transfers its loads to the central cylinder, as in Figure 13.5. In reality this transfer might occur more gradually since the frame and cylinder are seen as a single element here and their connection results in an abrupt change of geometry forming local stress concentrations. In Figure 13.5 and Figure 13.6, another region of high stresses is visible near the launch vehicle interface, as all loads pass through it and the moment arm is the largest here. These concentrations can be seen on OB1 in Figure 13.5. However, even the peak stress values with a

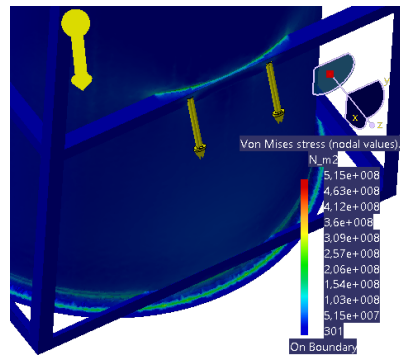


Figure 13.6: OB2 Von Mises stress. Element size : 10 mm, absolute sag : 10 mm.

safety margin of 1.25[57] lie within the yield strength of the chosen titanium (Table 13.3). One might think this structure to be over-designed, however a thinner structure results in extremely large deformations, especially for OB1 near the coronagraph as in Figure 13.5.

13.3.3. VIBRATIONAL ANALYSIS

The model used from stress analysis is used to estimate the eigenfrequencies. The results for OB1 and OB2 are given in Table 13.7.

Table 13.7: Satellite eigenfrequencies.

Mode [-]	Frequency [Hz]		Mode [-]	Frequency [Hz]		Mode [-]	Frequency [Hz]	
	OB1	OB2		OB1	OB2		OB1	OB2
1	0	0	8	71.0	88.3	15	108.3	129.3
2	0	0	9	72.8	90.1	16	116.2	129.6
3	0	0	10	72.9	90.2	17	118.9	133.6
4	2.9E-4	4.7E-4	11	85.2	110.1	18	124.1	142.0
5	4.1E-4	8.8E-4	12	90.1	118.4	19	146.4	143.1
6	6.2E-4	10.0E-4	13	105.2	122.6	20	147.2	156.9
7	67.7	82.1	14	108.2	126.7			

The first couple of modes have a negligible amplitude, as shown in A. and C. from Figure 13.7. The first eigenfrequency with visible deformations is the seventh mode, see B. and D. in Figure 13.7, and is above the 10 Hz lower bound imposed by the Falcon 9[57]. The other eigenfrequencies also have measurable deformations. Clearly, as both the vibration and stress performance of the primary structure can withstand the most critical situation during launch without deforming too much, a central cylinder and frame element thickness of 1 mm is chosen.

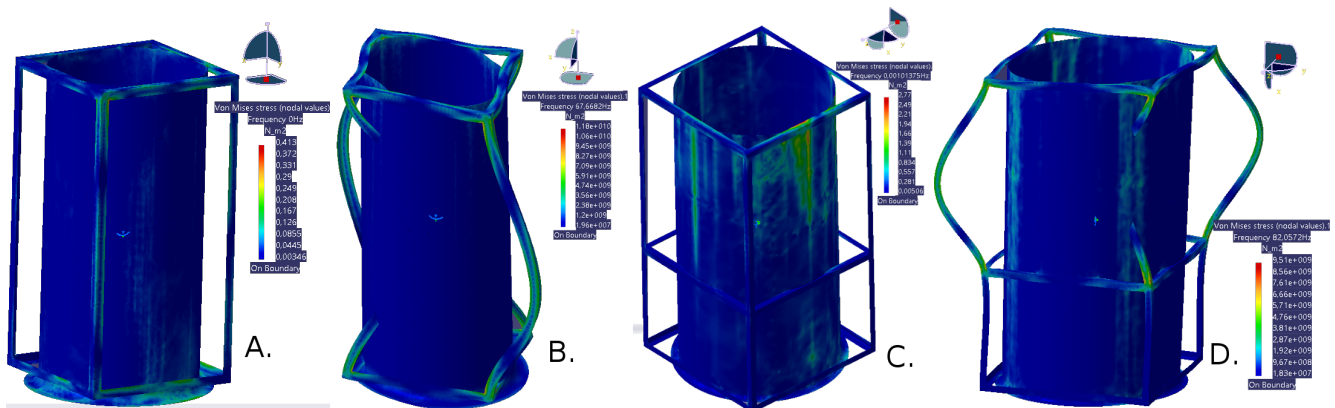


Figure 13.7: OB1 and OB2 eigenmode examples. Number of modes = 20, Maximum number of iterations per mode = 100. | A. OB1 first mode, $f = 0$ Hz. | B. OB1 seventh mode, $f = 67.7$ Hz. | C. OB2 sixth mode, $f = 10.0E-4$. | D. OB2 seventh mode, $f = 82.1$ Hz.

13.3.4. PRIMARY STRUCTURE CONCLUSION

The final dimensions and mass of the primary structures of both spacecraft is given in Table 13.8.

Table 13.8: OB1 and OB2 parameters. Both satellites have a square cross-section, see Figure 13.4.

Parameter	OB1	OB2
Outer radius cylinder [mm]	397.0	637.7
Thickness cylinder [mm]	1.0	1.0
Width frame [mm]	821.2	1296.6
Mid-frame height from bottom plate [mm]	-	872.5
Total height frame [mm]	1560.2	2397.9
Thickness flanges frame [mm]	3.0	3.0
Total mass [kg]	51.2	74.6

13.4. SECONDARY STRUCTURE DESIGN

13.4.1. SKIN PANELS

Skin panels are placed against all sides of the frame of the primary structure. These panels are meant to carry the majority of the shear acting on the satellite. They will also provide an easy method of attachment for many subsystems. A sandwich structure will be used for these panels, as described in Section 13.2.2. Most of the instruments will be attached to the front skin panel, therefore it will endure the highest loads of all panels during operation.

For these panels it is clear that a single ± 45 degrees carbon fibre sheet (ca. 0.3 mm) at each side of a 10 mm core is sufficient core to carry all the loads. A thinner core would lower the weight but would not provide a very stiff platform to mount elements onto, as such the 10 mm core offers a good balance between weight and stiffness.

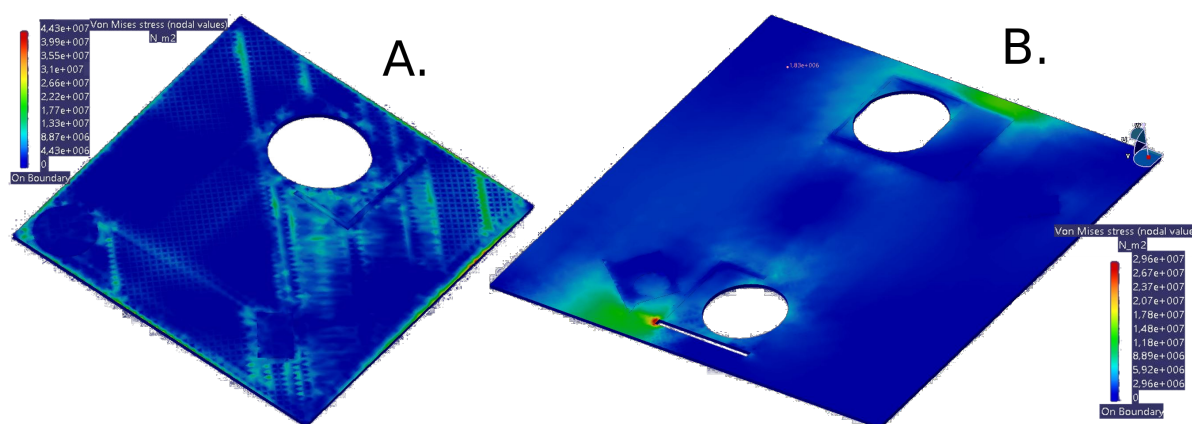


Figure 13.8: Front Panel Von Mises stresses. | A. OB1 front panel. | B. OB2 front panel. | Element size : 5 mm, absolute sag : 10 mm.

From Figure 13.8 it can be seen that near the edges of the panels the bulk of the shear stress is concentrated, this is due to it being attached to the rest of the structure at these locations. For OB2 additional stress concentrations exist near the slot through which the lens cap of the coronagraph extends. This concentration is very apparent due to it amplifying the already large stress field in this region. The large stress is caused by the magnetograph and coronagraph being accelerated in the direction of the slot and downwards, resulting in large moments near the those clamped edges. However, even then the highest stress is only 29.6 MPa, which can easily be carried by the skin of the sandwich.

Comparatively to the front panel, all other other panels have to carry much lower loads. However, they do limit deformation and vibration of the primary structure considerably. A closer inspection of the impact of the panels on deformation and vibrations should be carried out in the detailed design of this project. But they should easily be able to carry all stresses that might present themselves during operation.

13.4.2. SOLAR ARRAY STRUCTURE

The solar cells are mounted to panels, which are part of the secondary structure of the spacecraft. When designing these panels, the strength, stiffness, and vibrational requirements for both the panels and the connecting hinges are important. This section will discuss the process and calculations behind the sizing of the solar array structure.

STRENGTH

First of all, it is most important that the panels and hinges are strong enough to carry all loads imposed on the arrays. The most critical load condition is the launch, in which the solar array is retracted against the spacecraft. The worst-case

loads that the satellite may experience have been discussed in Section 13.1, and will form the base for the sizing of the solar array structure. During this phase, the panel itself will experience normal stresses in the form of compression, due to the longitudinal acceleration, and bending, due to the lateral acceleration. The maximum normal stresses in the panel can be calculated by superimposing the individual bending and compression stresses, as shown in Equation (13.12).

$$\sigma_{panel} = \frac{F}{A} + \frac{My_{max}}{I} \quad (13.12)$$

Similarly, the hinge experiences bending stress, due to the lateral acceleration, and shear stress due to the longitudinal acceleration. The individual shear and bending stress must first be calculated, which can be seen in Equation (13.13).

$$\sigma_{hinge} = \frac{My_{max}}{I} \quad \tau_{hinge} = \frac{VQ}{Ib} \quad (13.13)$$

To calculate the total maximum stress due to these two stresses, a Mohr's circle can be set up. The centre of the circle is $\sigma_{hinge}/2$, with a radius given by Equation (13.14). The maximum stress in the hinge can then be found by adding the radius to the value for the centre of the circle.

$$R = \sqrt{\left(\sigma_{hinge} - \frac{\sigma_{hinge}}{2}\right)^2 + \tau_{hinge}^2} \quad (13.14)$$

VIBRATION

Finally, the solar array must be able to withstand the vibrations imposed on their structure during the launch. From the Falcon9 launch manual [57], it can be found that the payload must be able to endure a steady vibration of 10Hz. This means that also the solar array should have a natural frequency higher than 10Hz. If this requirement is not met, the solar arrays could resonate with the launcher's frequency, causing violent and potentially destructive oscillations. To calculate the natural frequency, the solar array is modelled as a beam, which has a uniform weight and is rigidly clamped at the base. An approximation for the natural frequency is given in Equation (13.15).

$$f_n = 0.560 \sqrt{\frac{EI}{m_b L^3}} = 0.560 \sqrt{\frac{(E_c I_c + 2E_f I_f)}{m_b L^3}} \quad [12] \quad (13.15)$$

DEFLECTION

The next important part of the sizing, is to calculate the maximum deflection of the solar array. This deflection must be calculated to ensure the retracted solar panel will not bang against the spacecraft or fairing. For simplicity, the solar panel is modelled as a beam, which is rigidly clamped at its base. The lateral forces during the launch are modelled to be located at the centre of gravity, at the array's centre. The maximum deflection of the beam tip is then given by Equation (13.16).

$$\delta_{max} = \frac{5PL^3}{48EI} \quad (13.16)$$

The maximum allowed tip deflection is not a specified value for the spacecraft, but is a parameter that does need to be taken into account when sizing the solar array hinges. These hinges must provide an offset that is large enough to allow for the solar array's maximum deflection.

STRUCTURAL SIZING

For the precise dimensions of the subsystem, the first design decision is to either mount one single solar array, or multiple smaller arrays. In order to balance out the mass and moment of inertia of the magnetometer boom, it was chosen to mount a single solar array on the opposite side of the spacecraft. From Equation (13.15), it can be seen that a smaller length will give the solar array a higher natural frequency. The next design choice is thus to make the solar array as wide as the spacecraft it is attached to. The length is then derived from the required area, which has been determined in Chapter 11. An extra margin of 2% is added to this length to take into account that not the entire area of the structure is covered with solar panels (due to clamping, side margins, etc.). The dimensions for both spacecraft can be found in Table 13.9.

The next step in the sizing of the structures is to determine the thickness and lay-up of the composite sandwich panels of the structure. For the panel, the sizing process is performed by iterating different combinations of face sheet and core thickness, in order to achieve the requirements for the strength and vibrational properties of the solar array structure. Additionally, the launch manual for the Falcon 9 [57] recommends a safety factor of at least 1.25, which is conventional

for unmanned missions. Hence, this safety factor will also apply for the sizing of the solar array structure. The resulting optimal lay-up can be seen in Table 13.9, along with the natural frequency and maximum stress in the panel. From the process, it is clear that the vibrational requirements imposed on the solar panel are driving for the design, since its strength requirements are more easily met. From the designed structure, the maximum tip deflection of the solar array can also be computed. As mentioned before, this deflection forms a requirement for the sizing of the solar array hinges. In Table 13.9, the deflection for both spacecraft is shown to be in the order of millimetres, which is assumed to be a reasonable value to size the hinges for.

Once the structural parameters of the panels are known, the solar array hinges can be designed. In this preliminary design phase, the hinge is assumed to be a rigid attachment, hence only a stress analysis will be performed for this component. Similar to the primary structure, the hinges will be manufactured out of Ti-6Al-4V. Also for the hinges, the minimum safety factor of 1.25 is required. By expressing the total stress in the hinge as function of the hinge radius, the exact optimal radius can be found. For manufacturing purposes, this radius is rounded up to a dimension feasible for production. The final value can be found in Table 13.9. Additionally, a preliminary layout for the solar array structure and hinge can be seen in Figure 13.9.

Table 13.9: Solar Array Structure

Parameter	OB1	OB2	Unit
Array Length	1.70	1.33	m
Array Width	0.821	1.28	m
Array Thickness	31.2	21.2	mm
Lay-Up	2 sheets CF 30mm Honeycomb 2 sheets CF	2 sheets CF 20mm Honeycomb 2 sheets CF	-
Structural Mass	4.61	5.60	kg
Natural Frequency	14.9	16.4	Hz
Safety Factor	1.49	1.64	-
Maximum Panel Stress	4.29	7.16	MPa
Safety Factor	45.1	28.0	-
Maximum Tip Deflection	3.18	2.61	mm
Hinge Radius	10.0	10.0	mm
Hinge Total Stress	202.5	244.6	MPa
Safety Factor	1.64	1.35	-

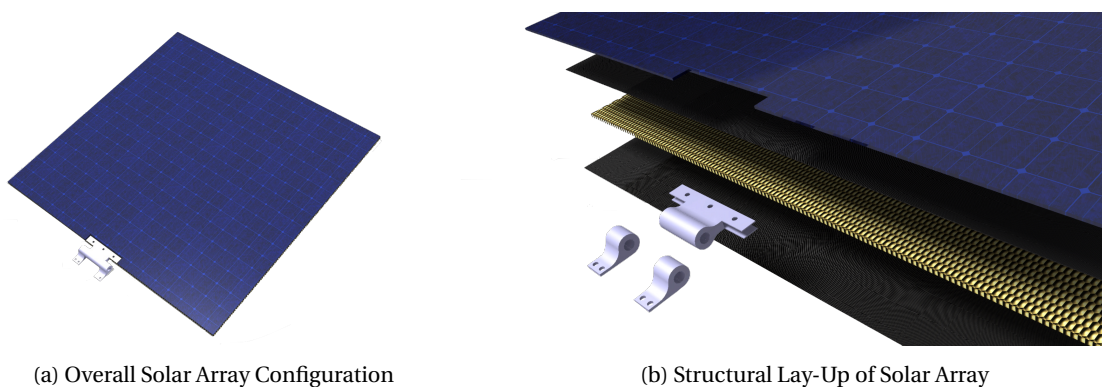


Figure 13.9: Solar Array Model

SENSITIVITY ANALYSIS

To analyse the design robustness of the solar array structure, a sensitivity analysis will be performed. This is done by changing various design parameters, in order to see to which extent it affects the structural characteristics. For both the structural panels and the hinge a such an analysis is performed.

First of all, the solar array panels are investigated. This is done by calculating the natural frequency of the panels for a slightly different lay-up in face and core materials: either one layer of carbon fibre more or less, or one more or less layer of Nomex honeycomb. The honeycomb core can be purchased in layers of 10mm each, hence this will form the step size for the sensitivity analysis. The resulting changes in natural frequency can be seen in Table 13.10. It is found that even the smallest changes possible for the panel manufacturer lead to changes of up to 50% in the natural frequency of the panels.

In particular, it should be noted that any attempt to reduce the number of layers (and thus also the mass) will result in a natural frequency that does not fall within the safety margins of the mission. This validates the combination of face and core material chosen for both SWAN satellites.

Table 13.10: Solar Array Natural Frequency Sensitivity

	OB1			OB2		
	f_{nat} [Hz]	Safety Margin [-]	Change [%]	f_{nat} [Hz]	Safety Margin[-]	Change [%]
Design Value	14,89	1.49	-	16,45	1.65	-
1 Extra Layer of CF	16,98	1.70	14,04	20,13	2.01	22,38
1 Less Layer of CF	11,47	1.15	-22,97	11,66	1.17	-29,10
Design Value	14,89	1.49	-	16,45	1.65	-
10mm Extra Honeycomb	19,14	1.91	28,61	24,71	2.47	50,20
10mm Less Honeycomb	10,32	1.03	-30,67	8,22	0.822	-50,05

A similar process can be executed for the solar array hinge. Here, the hinge radius will be changed to observe its effect on the maximum stress within the hinge. For the analysis, a change of 1mm is taken. The results are shown in Table 13.11. This table shows that a 10% decrease in hinge radius can cause a 37.17% increase in stress. This leads to the conclusion that the hinge design is fairly sensitive to the radius of the hinge. For off-the-shelf type hinges, a hinge radius of 10mm is readily available. It may be possible to opt for a more specialised hinge radius, however this would most likely require custom made hinges for the solar array.

Table 13.11: Solar Array Hinge Stress Sensitivity

	OB1			OB2		
	σ_{max}	Safety Margin [-]	Change[%]	σ_{max}	Safety Margin [-]	Change[%]
Design Value	202,48	1,63	-	244,64	1,35	-
1mm Smaller Radius	277,75	1,19	37,17	335,58	0,99	37,17
1mm Larger Radius	152,13	2,18	-24,87	183,81	1,80	-24,87

13.4.3. BOOM STRUCTURE

As discussed in Section 6.2.9, a 6.13 m long boom is required to keep the magnetometers away from the stray magnetic field of the satellite. Two magnetometers will be mounted on this boom, one at its end, and one midway. The boom will be present on both OB1 and OB2. The extended boom also contributes to the overall mass, and the overall moment of inertia of the spacecraft. Moreover, the boom can cause torques due to solar pressure. Therefore, a preliminary design of such a structure is needed to design the structure that will carry this boom, as well as other subsystems. A more detailed design of this structure will focus on the design of the deployment of the boom, which will likely require a different structural design of the boom. However, the contribution of the current preliminary design to the weight and moment of inertia of the boom to the satellite are representative of a boom structure. The following discussion includes the stresses, buckling, natural frequencies, and deflections of this secondary structure. A more detailed design will require the same analysis to be performed.

CONCEPT

The mass of the magnetometer is assumed to be 2.5 kg, which is common for fluxgate magnetometers used on similar missions and is documented in the Midterm-report[3]. As can be seen in Figure 13.10, a simple triangular structure is chosen. This choice is made for the structural efficiency that this simple design brings, and its widespread use for spacecraft booms. A root dimension of 40 cm is used, as this offers a wide platform, minimising the stresses through the stringers, while not being too wide to fit on the spacecraft.

STRENGTH

The boom is modelled as three cantilevered stringers that only carry loads in their lengthwise direction. Two three-dimensional forces are placed at the locations of the magnetometers, equal to the inertial force due to the accelerations during launch as given in Figure 13.1a times a contingency factor of 1.1. Here longitudinal loads act in the negative x direction and lateral loads in the yz-plane, as the boom is assumed to be stowed during launch.

The stringers are enumerated in an anti-clockwise manner starting from the upper stringer, as seen in the left plot of Figure 13.10. This results in system in Equation (13.17).

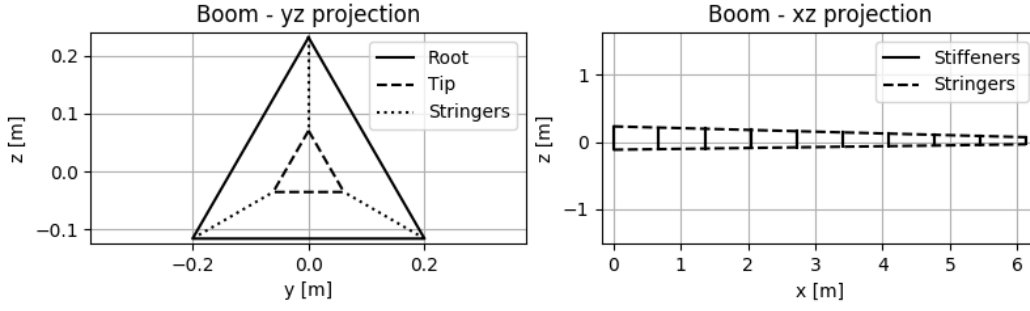


Figure 13.10: Geometry of boom

$$\begin{bmatrix}
 -\cos \alpha & -\cos \alpha & -\cos \alpha \\
 0 & -\cos \frac{\pi}{6} \sin \alpha & \cos \frac{\pi}{6} \sin \alpha \\
 \sin \alpha & -\sin \frac{\pi}{6} \sin \alpha & -\sin \frac{\pi}{6} \sin \alpha \\
 0 & \cos \frac{\pi}{6} \sin \alpha \cdot z_2 - \sin \frac{\pi}{6} \sin \alpha \cdot y_2 & -\cos \frac{\pi}{6} \sin \alpha \cdot z_3 - \sin \frac{\pi}{6} \sin \alpha \cdot y_3 \\
 -\cos \alpha \cdot z_1 & -\cos \alpha \cdot z_2 & -\cos \alpha \cdot z_3 \\
 0 & \cos \alpha \cdot y_2 & \cos \alpha \cdot y_3
 \end{bmatrix} \cdot \begin{bmatrix} F_1 \\ F_2 \\ F_3 \end{bmatrix} = \begin{bmatrix} F_{a,x} \\ F_{a,y} \\ F_{a,z} \\ F_{b,x} \\ F_{b,y} \\ F_{b,z} \end{bmatrix} \quad (13.17)$$

$$\begin{bmatrix}
 [-1] & 0 & 0 & -1 & 0 & 0 \\
 0 & [-1] & 0 & 0 & -1 & 0 \\
 0 & 0 & [-1] & 0 & 0 & -1 \\
 0 & 0 & 0 & 0 & 0 & 0 \\
 0 & 0 & [L/2 - x] & 0 & 0 & L - x \\
 0 & [x - L/2] & 0 & 0 & x - L & 0
 \end{bmatrix} \cdot \begin{bmatrix} F_{a,x} \\ F_{a,y} \\ F_{a,z} \\ F_{b,x} \\ F_{b,y} \\ F_{b,z} \end{bmatrix}$$

In Equation (13.17) α is the angle of the stringers to the x-axis, where the stringers are angled inwards, crossing the x-axis in $y=0$ and $z=0$. For these computations, an α of 1.5 degrees is used. The distances of the stringer i in the considered cross-section is defined as y_i and z_i . The normal force through each stringer is F_i , and is the values for which this system is solved. The two inertial forces of the magnetometers are denoted $F_{a,i}$ for the mid-ways magnetometer, and $F_{b,i}$ for the outermost magnetometer. Finally, for sections with $x \in [L/2, L]$ metres the values in brackets are zero, otherwise they are the denoted values, with x the longitudinal position of the considered section, and L the length of the boom.

This system is solved for multiple sections along the boom, and the forces are then divided by the cross-sectional area of the boom. For the stringers, a 10 mm outer radius, and 9.5 mm inner radius was chosen. While the stiffeners have a 5 mm outer radius, and a 4 mm inner radius. The angle of the lateral acceleration to the y-axis can be changed, and is denoted θ . The results of the computations are provided in Table 13.12.

Table 13.12: Stress extrema in boom through several loading angles for $(a_{axial}, a_{lateral}) = (3g, 4g)$

θ [deg]	-30	0	30
σ_{min} [MPa]	-96.4	-83.7	-49.1
σ_{max} [MPa]	45.6	80.2	92.9

Using the Tresca criterion, and a safety factor of 1.25, as recommended by SpaceX[57], every material from Table 13.3 has an adequate yield stress. Throughout this section, Al-6061 is chosen for the boom for its low cost and high stiffness to weight, as demonstrated in Table 13.4.

BUCKLING

Another requirement is that the boom can not buckle under load. The stiffeners are used to provide support against buckling for the stringers, their spacing is computed using Euler's equation for column buckling with two pinned ends, as shown in Equation (13.18).

$$P_{cr} = \frac{\pi^2 EI}{(KL)^2} \quad L_{cr} = \sqrt{\frac{\pi^2 EI}{K^2 F}} \quad K = 1.0 \text{ for pinned ends} \quad (13.18)$$

The critical loading situation occurs when the lateral acceleration is 3g, and the axial acceleration is 4g with θ -30 degrees. This is due to the fact that this case involves the highest compressive stresses. A critical buckling length of 0.59 metres results from this equation, requiring eleven stiffening triangles between the root and tip of the boom, which are evenly spaced lengthwise, as shown in Figure 13.10.

VIBRATION

As mentioned in the vibrational analysis of the solar array, the satellite and its elements must have a natural frequency above 10 Hz. To model the eigenfrequencies of the boom a simple spring-mass system was made, as shown in Equation (13.20). In this system, the boom is split after each stiffener. A concentrated mass is placed at the stiffener location equal to the stiffener mass and that section of the stringers. Each boom section has a stiffness in lateral and axial direction computed using Equation (13.19).

$$k_{axial} = \frac{AE}{L_i} \quad k_{lateral} = \frac{3EI_i}{L_i^3} \quad (13.19)$$

$$M = \begin{bmatrix} \ddots & & 0 \\ & m_i & \\ 0 & & \ddots \end{bmatrix} \quad K = \begin{bmatrix} \ddots & & & & 0 \\ & \ddots & & & \\ & & -k_{i-1} & & \\ & & & k_{i-1} + k_i & -k_i \\ 0 & & & & \ddots & \ddots \end{bmatrix} \quad \tilde{K} = M^{-1/2} K M^{-1/2} \quad (13.20)$$

$$\omega_n = \text{eigenvalues of } \tilde{K} \quad f_n = \frac{\omega_n}{2\pi}$$

The lowest frequencies of the boom are 79.0 Hz in the axial direction and 43.0 Hz in the lateral direction, which are both above the required 10 Hz.

DEFLECTION

Another critical element is the deflection of the boom, this to ensure that it does not collide with the satellite or the fairing during launch. The deflections in all directions are computed using Equation (13.21).

$$\delta_x = \frac{F_{b,x}x}{3AE} + \begin{cases} \frac{F_{b,x}x}{3AE} & \text{for } x \leq L/2 \\ 0 & \text{for } x > L/2 \end{cases} \quad (13.21)$$

$$\delta_i = \frac{F_{b,i}x^2}{6EI_j}(3L-x) + \begin{cases} \frac{F_{a,i}x^2}{6EI_j}(3/2L-x) & \text{for } x \leq L/2 \\ \frac{F_{a,i}(L/2)^2}{6EI_j}(3x-L/2) & \text{for } x > L/2 \end{cases} \quad \text{with } i = y \text{ or } z, \text{ and } j = z \text{ or } y$$

The same case is used as for the buckling, resulting in maximum deflections of: -0.08 mm in the x direction, 565.64 mm in the y direction, and -326.57 mm in the z direction. These deflections are considerable, but they are only valid for a fully extended boom, which is not the case. Retracting the beam telescopically, or by folding it with a hinge will reduce the moment arms of the forces, lowering the overall deformations.

DEPLOYMENT

The easiest way to stow the boom would be to fold it in the middle and at the root to move it parallel with the spacecraft body. The deflections at the mid point of the fully extended boom are only: -0.08 mm in the x direction, 41.56 mm in the y direction, and -24.00 mm in the z direction. The hinges would lower the stiffness of the boom locally, resulting in higher overall deflections, but this would be offset by the smaller moment arms.

Other common methods of deploying the boom would be telescopically, either by simply making the stringers telescopic or by twisting the boom as demonstrated by Orbital ATK. Another design promising great length-to-mass characteristics would be the reel-stored boom, however the straightness of such a solution might be difficult to design for with its periodic distance to the Sun. This would cause unequal solar pressure torques due to the solar array remaining the same size, and the torques of this pressure being more or less balanced for a fully extended boom[116].

SENSITIVITY ANALYSIS

The design of the boom has to be tested for its robustness with a sensitivity analysis. The design parameters that will be tested are: the stringer cross-section (Table 13.13), the slope of the stringers with respect to the x-axis (α , Table 13.14), and the root dimensions (Table 13.15).

In Table 13.13 the thickness of the stringer is kept constant to put the focus on the material being moved further from the stringer centroid, without adding too much mass, which would heavily disadvantage higher radii for the cross-section. Clearly, a smaller cross-section has a negative effect on the stresses and deflections. However, even at the large differences in dimensions the changes are not very large. A small defect in the cross-sectional dimension of the stringers would not affect the performance of the boom too much.

⁰<https://www.goes-r.gov/spacesegment/mag.html>

Table 13.13: Boom stinger cross-sectional dimension sensitivity

$r_{outer} r_{inner}$ [mm]	$\sigma_{min} \sigma_{max}$ [MPa]	f_n (x y/z) [Hz]	δ (x y z) [mm]
5 4.5	-197.87 93.51	70.00 107.77	-0.15 1177.94 -680.09
10 9.5	-96.40 45.56	79.05 43.03	-0.08 565.64 -326.57
15 14.5	-63.72 30.11	100.48 25.73	-0.05 365.05 -210.76

Table 13.14: Boom stinger slope sensitivity

α [deg]	$\sigma_{min} \sigma_{max}$ [MPa]	f_n (x y/z) [Hz]	δ (x y z) [mm]
1	-96.29 45.50	78.35 61.24	-0.08 184.96 -106.79
1.5	-96.40 45.56	79.05 43.03	-0.08 565.64 -326.57
2	-96.25 45.48	79.76 15.01	-0.08 7.52E3 -4.34E3

Compared to the cross-sectional dimensions of the stringers, the slope of the stringers are more critical, as shown in Table 13.14. Even half a degree of change for the angle results in large changes in natural frequency, but more importantly in deflections. It is very important to get this angle correct in manufacturing. But the stiffeners, limit the error one can make in this respect as they hold the boom in the correct shape if correctly manufactured.

Table 13.15: Boom root dimension sensitivity

Root width [m]	$\sigma_{min} \sigma_{max}$ [MPa]	f_n (x y/z) [Hz]	δ (x y z) [mm]
0.28	-136.57 65.64	105.83 9.30	-0.08 29.65E3 -17.12E3
0.4	-96.40 45.56	79.05 43.03	-0.08 565.64 -326.57
0.6	-64.79 29.75	102.33 69.19	-0.08 82.31 -47.63

The results in Table 13.15 show that errors in the root width dimensions, and with that all other stiffener dimensions, can also have a large effect on the boom performance. The considered change in the three designs is much larger than for α , however if left unchecked, it too can heavily impact the structural integrity of the boom. However, clearly the small angle assumption that the equations for deformation are build upon no longer hold for most of the results in this table.

13.5. TERTIARY STRUCTURE DESIGN

The final structure type that will be discussed, is the tertiary structure. Among other things, the tertiary structure of the SWAN satellites consists of mounting brackets for the tanks and payload, cable-supports, bolts, and the engine mounting. During the later design phases of both spacecraft, a more detailed sizing of the tertiary structure can be performed. During this preliminary phase, only the concepts for a number of tertiary structures will be discussed, along with a initial size estimate for each.

13.5.1. TANK ATTACHMENT

The propellant and pressurant tanks take up a large part of the spacecraft volume. This section describes possible solutions to mount these heavy subsystems in the SWAN satellites. The most common way to attach the fuel tanks of a satellite to the primary load carrying structure, is by use of mounting brackets. This form of attachment is rigidly wrapped around the fuel tank, with two or more connection points. A key aspect of the design philosophy for the mounting brackets, is to take thermal strain into consideration. To allow for thermal expansion, the mounting brackets will be designed with curved attachment points, as can be seen in Figure 13.11. This way, the brackets can expand with the structure, and internal stresses are avoided.

Table 13.16: Dimensions of Tank Mounting Brackets

OB1	Nr. of Clamps	$t_{bracket}$ [mm]	$w_{bracket}$ [mm]	r_{bolt} [mm]
Fuel Tank	1	2.0	2.05	2.90
Oxidiser Tank	1	1.0	4.32	2.98
Pressurant Tank	1	0.01	3.01	2.48
OB2				
Fuel Tank	2	2.0	30.2	11.1
Oxidiser Tank	2	2.0	30.2	11.1
Pressurant Tank	2	1.0	2.46	2.25

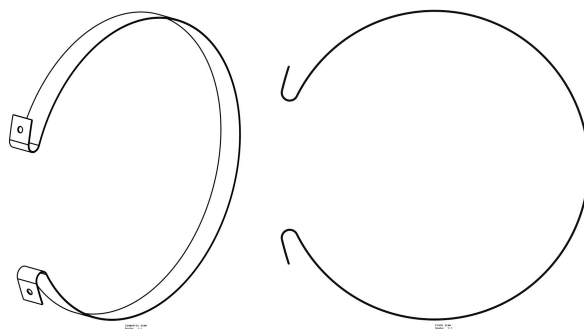


Figure 13.11: Tank Mounting Bracket Concept

For this preliminary sizing, the mounting brackets are considered to be loaded in pure shear. In reality, the brackets will be loaded under a combination of shear, bending, and torque. However, the shear force is expected to induce the largest stresses on the brackets. When sizing the brackets, the dimensions of the brackets themselves are determined, as well as the minimum radius of the bolts that attach the brackets to the main structure. The shear stress in both the bolt and the bracket can be calculated using Equation (13.22).

$$\tau = \frac{QV}{Ib} \quad (13.22)$$

Using the loads on the spacecraft during launch, combined with the mass of each tank, the shear force on each bracket and bolt can be calculated. For the initial material choice, the mounting brackets will be manufactured out of Al-7075, whereas the most commonly available option for bolts is stainless steel. Applying the recommended safety factor of 1.25 for unmanned space missions, the exact dimensions for the mounting brackets and bolt can be computed. These dimensions are given for each tank in Table 13.16.

13.5.2. PAYLOAD ATTACHMENT

Most of the payload on board of OB1 and OB2 consists of delicate instruments, which may not experience excessive loads or stresses. A good attachment is vital, since the mission can not be conducted to its full potential (if at all), if any of the instruments fail.

Most instruments will either be attached to the front panel of the spacecraft, to the main cylinder, or to both. Ideally, an instrument is constrained in all 3 axis at two or more points. This way, the loads on the instrument are distributed over multiple connections. However, the thermal environment of the satellites may pose another challenge for the instrument mounting. If different materials are used for the instrument housing and the main structure, a change in temperature will also cause a different thermal strain. This will induce thermal stresses in the instrument, which may cause inaccuracies in measurements taken. To avoid this problem, a sliding support surface is conceptualised. This support will allow for thermal expansion in the lengthwise direction of the instrument, while constraining it in the other two directions. Only the front side of each instrument shall be rigidly clamped to the satellite structure, thus fully constraining the payload. A conceptual sketch of the sliding support system is shown in Figure 13.12. For the material choice, it is necessary for the inner bracket to be made of the same material as the payload housing. The sliding rails must be made of Ti-6Al-4V, which is the same material as the primary structure. This way, no thermal stresses will be generated between the bracket and the elements it is attached to. Enough margin will be left between the two parts of the support to minimise the thermal stresses caused by the different thermal expansion of both parts.

13.5.3. THRUSTER LOAD CARRYING STRUCTURE

To attach the thruster to the satellite, a load carrying structure (LCS) is required. The main function of the LCS is to transfer the thrust loads introduced by the engine in to the main structure. This structure is also used for securing and attaching the valves, thrust vector control actuators, cable harness and other feed system components. This section describes the design steps of the LCS.

CONCEPT

There are two common strategies in attaching liquid engines to the main structure. These are:

- A cone structure
- A truss structure

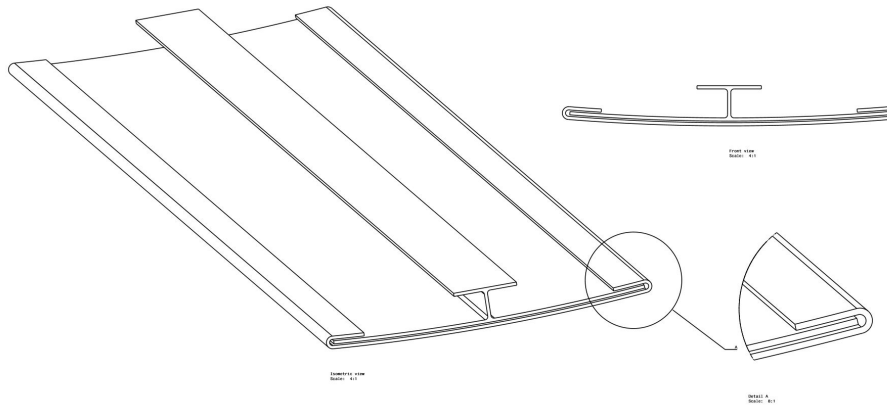


Figure 13.12: Sliding Payload Support

The solid cone structure is the strongest. However, it is almost never used in reality due to its high weight and limited accessibility of the system. Most commonly used is the truss structure, of which two examples are shown in Figure 13.13. This option allows for the lowest weight to volume ratio of the system and provides the engineers with a good level of accessibility to the systems inside the truss structure.



(a) Aerojet Rocketdyne RS-68 engine clearly showing a longitudinal load carrying structure consisting of four trusses¹



(b) Radial Load carrying structure by Ariane Group.[62]

Figure 13.13: Examples of load carrying structures

The most critical failure mode of the LCS is either buckling or shear of the main struts depending on whether these struts are positioned longitudinally as shown in Figure 13.13a or radially such as shown in Figure 13.13b. If this happens, severe loads could act on the rigid feed system lines, which they are not meant to carry. Moreover, thrust vector control actuators connected to the structure could, when buckling has occurred, fail to manoeuvre the main thruster into the correct position, leading to major mistakes in the burn direction.

When looking at possible truss structures it can be noted that most structures used in the industry have three or four attachment points on the rocket structure. From the German V2² to SpaceX's Merlin 1D engine³, most of the engines throughout history have used this structure. Having a single (or double) connection with the rocket structure results in a much heavier system, since all loads have to be carried by this one connection. Moreover, this is less space efficient, but it does provide a lot of torsional resistance around the longitudinal axis. If the three connections and four connections are considered and the application of thrust vectoring is taken into account, it is seen that a LCS having four connections is more suitable as it is symmetric.

The LCS should in theory not hold any torsion and only compression, shear and bending. Due to imperfections, some torsion could occur. However, with four single connections, the assembly can be considered constrained, given the connections are rigid. Thus, with the assumption that the connections will be rigid, a LCS design with four single connections is chosen.

Since the thrust of the main engine of the satellite is very low in comparison to the thrust of for instance to RS-68 engine (623 N vs 3.4 MN), the more space-efficient radial load carrying structure is more applicable in this case, as the loads on

¹<http://www.rocket.com/rs-68-engine>

²<http://www.v2rocket.com/start/makeup/motor.html>

³http://www.360doc.com/content/16/0705/10/16755731_573211945.shtml

the force-carrying members will not be very significant.

STRUCTURAL SIZING

To make the analysis relatively easy, it is assumed that the engine provided a point load to the end of each of the load carrying members and that these members can be modelled as cantilever beams. Moreover, it is assumed that the normal forces in the members are negligible due to small angles of thrust misalignment and small deflections during thrust vector control. This means that only shear and moment stresses will act on the members. Modelling the members as a cantilever beam with a point force acting at the end, these stresses can be determined by

$$\tau_{max} = \frac{F_T Q}{4It} \quad (13.23)$$

$$\sigma_{max} = \frac{TLh}{8I} = \frac{3TL}{2bh^2} \quad (13.24)$$

where F_T is the thrust produced by the engine, Q is the first moment of area, I is the second moment of area and t is the thickness of the member. L is the length of one member which is equal to the radius of the central cylinder. h is the height of the cross section of the member and b is the width. Assuming that the member is made out of Ti-6Al-4V just like all main structural components in the spacecraft, the yield stress becomes 880 MPa and the maximum allowable shear stress becomes 550 MPa⁴. The maximum load during launch comes from the weight of the engine. The force applied by this is equal to the mass of the engine multiplied by the maximum longitudinal acceleration. From Figure 13.1a it can be found that the maximum acceleration is 8.5 ms^{-2} . This results in a maximum launcher load of 450 N, which is lower than the engine thrust. Thus, this is not the critical load case. The bending stress is much more critical than the shear stress. Assuming a beam width b of 5 mm, the required beam height becomes 12 mm when taking into account a design safety factor of 1.1[117]. The total mass of four members of 5x12x620 then becomes 0.66 kg.

13.6. CENTRE OF GRAVITY AND MOMENT OF INERTIA

Using the same axis system as in Figure 12.1, the centre of gravity and mass moment of inertia of the complete spacecraft is given in Table 13.17.

Table 13.17: Centre of gravity (CG) location and moment of inertia in axis system as defined in Figure 12.1.

	x_{CG} [mm]	y_{CG} [mm]	z_{CG} [mm]	I_{xx} [kgm ²]	I_{yy} [kgm ²]	I_{zz} [kgm ²]	I_{xy} [kgm ²]	I_{xz} [kgm ²]	I_{yz} [kgm ²]
OB1	-762.42	0.45	-19.94	57.82	83.09	39.95	0.01	-5.28	-0.002
OB2	-1039.40	184.22	57.67	513.09	743.81	422.22	51.99	63.93	0.98

13.7. VERIFICATION AND VALIDATION

It is important to see if the results that stem from models actually provide the correct result, by providing the correct solution to the model and by correctly modelling that which one seeks to model. The first part of this problem is discussed in verification, while the latter part is touched upon in validation. Each structural element designed in this chapter will go through these two steps.

PRIMARY STRUCTURE

The primary structure was analysed using a finite element method from CATIA™ V5R21 with the parameters as specified in that section. However, one can see if the solution converges to the same one under different mesh sizes and absolute sag values. The convergence can be checked by refining the mesh and seeing if it converges to the same solution. An advantage of using the build-in FEM from CATIA is that the exact functions that were used to shape the structure can be used to define the boundaries in the analysis software. This lowers the error linked to the boundary geometry considerably, which is important when abrupt changes in geometry can lead to peaks in stress that would not be present in reality. As such, the model boundaries closely follow reality, minimising errors that could emanate from this.

The vibration results were checked by increasing the number of allowed iterations, but this did not change the results considerably. However, as can be seen from Table 13.7, some eigenfrequencies are clearly erroneous, i.e. those linked to the first six modes. These can be caused by errors in the model, however this would also appear in the stress model as it is the same, or by discretisation errors in splitting the model up into point masses.

⁴<http://asm.matweb.com/search/SpecificMaterial.asp?bassnum=mtp641>

As an additional verification method, other finite element modelling software can be used to compare the individual results for each satellite. Especially software types that use different discretisation methods than CATIA™ are interesting for comparison.

SECONDARY STRUCTURE

The front skin panel was analysed using CATIA™ V5R21, as such the same considerations hold as for the primary structure that used the same software. The solar array and the thruster load carrying structure was sized using several equations implemented in Microsoft® Excel. These formula's were checked by multiple individuals and compared to hand calculations to check if any error was present.

For the boom structure some parameters as deflections were computed using analytical formulas that were verified in a similar manner to those for the solar array, however the natural frequency and stresses were computed using a model. For both of these the error was estimated using Richardson extrapolation, as described in Computational Modelling from S.J. Hulshoff[118]. Using a mesh spacing ratio of 10, the observed order of accuracy and the estimation of discretisation errors was computed. However, this method could not be used for the stresses as there was no difference in result observed between the different step sizes. This is due to the fact that this method uses analytical equations in matrix form and solves exactly for each section, any error would be due to inverting matrices iteratively and other reasons. However, this error could not be observed, and therefore this error could not be analysed. The observed order of accuracy for the longitudinal natural frequency was 0.465, and 0.046 for the lateral natural frequency. The estimated discretisation error of both resulted in $-1.523E-3$ and 1.55 for the axial and lateral natural frequency, respectively. The large error could be due to the low number of point masses considered in the model, i.e. 13 sections.

TERTIARY STRUCTURE

Initial size estimated were computed for the tertiary structure, this was done with analytical equations. Possible errors could be present due to not taking the different thermal expansion of itself and the two elements that it connects, however these designs are focused on minimising the thermal stresses transferred to the other elements. Therefore, enough margin will be left in the hinge to allow the hinge to expand and retract without too much constraint, which would induce thermal stresses. As such the computed stresses inside these tertiary structures closely approximate those that would occur under operating conditions.

TESTING

An important part of structural validation is testing elements of the structure or simply materials under a given load. Each tertiary structure should be produced, and should be able to sustain the limit loads. Each element should also not break until ultimate load is reached. The same holds true for structural sub-assemblies, e.g. secondary structures and primary structures. These types of tests can be quite expensive, especially on primary and secondary structures, however they are essential in the validation of the structure.

13.8. RELIABILITY, AVAILABILITY, MAINTAINABILITY, AND SAFETY CHARACTERISTICS

Also for the structure of the SWAN satellites a reliability, availability, maintainability, and safety analysis will be performed. First of all, the reliability of the SWAN satellites is fairly good. The skin-frame option for the structure is a tried and proven concept within engineering, for which reliable models and analysis methods are available. Since both the main frame and the central cylinder provide stiffness, the structure is also redundant.

Next is the availability of the structure. The frame of the primary structure is made of standard, off-the-shelf profiles, and the stiffening cylinder can easily be manufactured from sheet metal. Furthermore, all materials that form the layers in the secondary sandwich panels are commercially available. Standard curing ovens or autoclaves can finish the sandwich panels for all required sizes, adding to the availability of the secondary structure. Only the tertiary structure contains more specialised components. For instance, all bolted interfaces will require specific nuts that do not loosen under high vibrational loads. Such components need to be ordered at specialised companies. In addition to the bolts, also the sliding rails for the payload must be custom made for each instrument.

Although maintenance is near impossible when a spacecraft is in its final orbit, maintainability is still an important aspect to consider during production. Accessibility during the manufacturing phase is a key design consideration for the SWAN satellites, since there is a large chance that various subsystems are continuously mounted and dismounted. Since all interfaces between the skin panels and the main frame are removable bolts, almost the entire spacecraft is easily accessible. Only the fuel tanks, which are housed in the middle of the central cylinder, are harder to reach once they are installed. Similar to the secondary panels, the payload is also mounted to the main structure with non-permanent attachments. Especially the payload is expected to need continuous tuning and readjusting, hence their accessibility may be the most important of the satellite.

Finally, the safety of the structure is analysed. The titanium primary structure poses no direct health risks, since it is a non-toxic metal, and causes no health hazards when machined or formed. However, when working with carbon fibre composites, a number of safety issues must be addressed. First of all, handling carbon fibre sheets can cause rashes or other irritation to the skin and eyes. It is thus advisable to always wear protective eye-wear and clothing. More importantly, machining carbon fibre composites introduces fine particulate matter into the air, which may cause long-term health issues to the lungs. Protective masks and good air ventilation or filtration of the work place are mandatory.

13.9. REQUIREMENT COMPLIANCE

This section shows the requirement compliance matrix for the structural requirements. It can be seen that all structural requirements are met.

Table 13.18: Structures Requirement Compliance Matrix

Identifier	Requirement	Met?	Confirmation
STR-PRM-01	The eigenfrequency of the primary structure shall be higher than 12.5 Hz	✓	Section 13.3.3
STR-PRM-02	The primary structure of OB1 shall be able to cope with forces proportional to the inertial forces caused by an acceleration of -8.5 g in the z-direction	✓	Section 13.3.2
STR-PRM-03	The primary structure of OB1 shall be able to cope with forces proportional to the inertial forces caused by an acceleration of 2 g in the xy-plane	✓	Section 13.3.2
STR-PRM-04	The primary structure of OB2 shall be able to cope with forces proportional to the inertial forces caused by an acceleration of 8.5 g in the x-direction	✓	Section 13.3.2
STR-PRM-05	The primary structure of OB2 shall be able to cope with forces proportional to the inertial forces caused by an acceleration of 2 g in the yz-plane	✓	Section 13.3.2
STR-SCD-01	The skin panels shall be able to cope with a stress of 208 MPa	✓	Section 13.4.1
STR-SOP-01	The solar panels shall have a strength of at least 208 MPa	✓	Section 13.4.2
STR-SOP-02	The natural frequency of the solar panels shall be higher than 12.5 Hz	✓	Section 13.4.2
STR-BOM-01	The boom shall be able to cope with a maximum stress of 220.8 MPa	✓	Section 13.4.3

13.10. CONCLUSION AND RECOMMENDATIONS

The main goal of this chapter, was to describe the design of the structure of the SWAN satellites. This included an identification of the loads on the spacecraft, followed by a material selection for each structural type, and an initial sizing of both the primary and the secondary structure. The main parameters are summarised in Table 13.19. Additionally, preliminary estimates have been made for a number of tertiary structures, such as the load carrying structure of the engine and the tank mounting brackets.

For the detailed design of the spacecraft structure, a number of recommendations are stated below. These additional points are expected to improve the depth and quality of the structural design.

- The current primary structure design has a higher safety margin than is required. This means the structure can be optimised further, which would lead to weight reduction.
- In this phase, the possible presence of thermal loads has been taking into consideration for designing all elements of the structure. For future design phases, it is recommended to determine the precise values for all stresses and strains induced by the thermal environment during the mission, in order to achieve a better design.
- During the material selection for the primary and secondary structure, the cost index only considers the raw material costs. For a more accurate comparison, manufacturing costs should also be included in this criterion.
- For a more detailed stress analysis, the internal stresses of all subsystems can be modelled, and their interaction with the main spacecraft structure. Especially large subsystems such as the fuel tanks may add extra stiffness to the structure, instead of only introducing loads to the frame.
- In this preliminary design, all connections are modelled as rigid interfaces. However, all these hinges and joints are not infinitely stiff. Hence, for the detailed design of the SWAN satellites, the vibrational properties of all connections must be modelled too.

Table 13.19: Structural Parameters of OB1 and OB2

		Unit	OB1	OB2
Primary Structure	Width	m	0.82	1.30
	Height	m	1.56	2.40
	Mass	kg	51.2	74.6
	Material	-	Ti-6Al-4V	Ti-6Al-4V
Secondary Structure	<i>Skin Panels</i>			
	Thickness	mm	10.6	10.6
	Mass Per Panel	kg	8.72	21.0
	Material	-	CF - Nomex HC Sandwich	CF - Nomex HC Sandwich
	<i>Solar Array</i>			
	Length	m	1.70	1.33
	Width	m	0.82	1.28
	Thickness	mm	31.2	21.2
	Mass	kg	4.61	5.60
	Material	-	CF - Nomex HC Sandwich	CF - Nomex HC Sandwich
	<i>Boom</i>			
	Length	m	6.13	6.13
	Root Width	m	0.40	0.40
Tip Width	m	0.12	0.12	
Mass	kg	2.39	2.39	
Material	-	Al-6061	Al-6061	
Tertiary Structure	<i>Thruster LCS</i>			
	Beam Width	mm	5.00	5.00
	Beam Height	mm	12.0	12.0
	Mass	kg	0.42	0.66
	Material	-	Ti-6Al-4V	Ti-6Al-4V

- The next step in the design phase must also include a detailed sizing of the tertiary structure, based on the preliminary concepts and calculations performed in this chapter.

14

INTERFACES

A spacecraft is a complex system that consists of many subsystems. During the mission, all of these subsystems have to work together to achieve a common goal. For this reason, it is important to analyse the interfaces between the different subsystems. This analysis will be performed in this section and consists first of all of an N2-chart. After that the N2-chart is visualised in a hardware block diagram. Finally, the information flow among the subsystems and the each segment of the mission is shown in the software block diagram and the communication flow diagram. After analysing these interface diagrams, one can clearly visualise the dependency of each instrument and how they are related to each other.

14.1. N2-CHART

The N2-chart, shown in Table 14.1, gives all the interfaces between different subsystems of the spacecraft. This is not necessarily how all information flows through the system, but rather how each subsystem interacts with other subsystems and the effects each has on the other. This is useful to identify all links in the system such that nothing is overlooked.

There are a lot of obvious connections. However, some of the less expected interfaces are for instance the interface between the thermal control system and the ADCS. Due to the reflectivity of the materials, torques on the spacecraft could be induced. These need to be taken into account when designing the ADCS system. Moreover, the interfaces of all subsystems with the TT&C system apart from the payload could also be forgotten. This needs to be taken into account as the sensors on all of these subsystems will generate a certain data rate as well, which will need to be sent down to Earth.

14.2. HARDWARE BLOCK DIAGRAM

The hardware block diagram is illustrated in Figure 14.1. In essence, the hardware block diagram is a visual representation of the N2-chart. The chart distinguishes between the main subsystems of the spacecraft: EPS, payload (includes all instrumentation), ADCS, command and data handling, Thermal, propulsion and TT&C. The arrows indicate inputs and outputs of each subsystem as to clearly indicate how the subsystems interface with one another. It should be noted that these input and outputs are not consistent and can indicate power flow, data flow and even fuel flow.

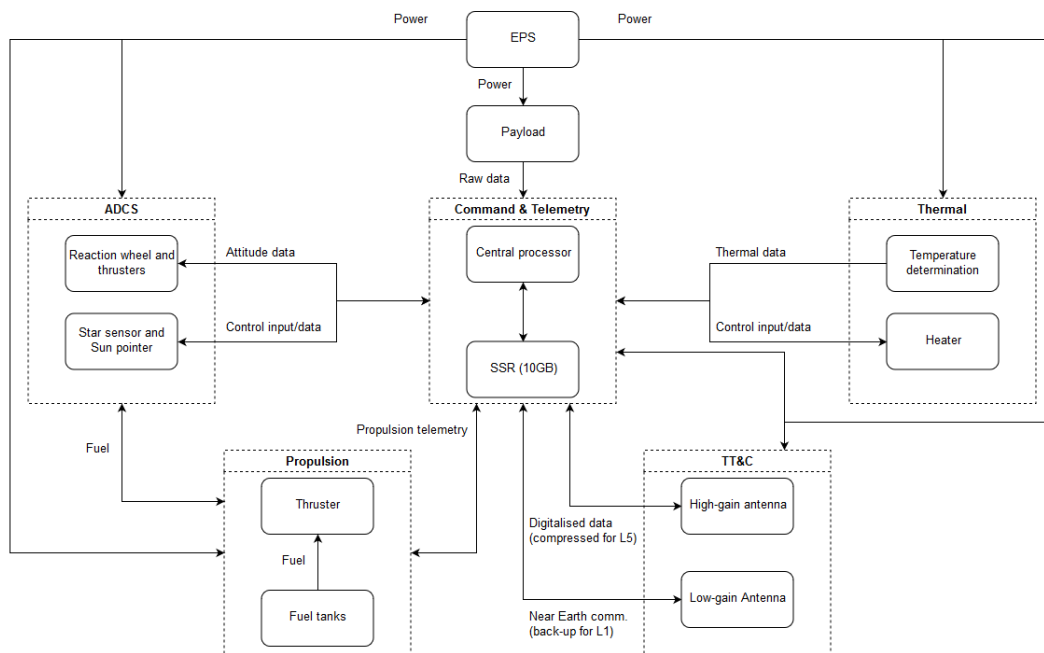


Figure 14.1: The hardware block diagram showing the interfaces between all the subsystems

Table 14.1: N2 Chart

Output ->								
← Input	Attitude Determination	Current Attitude	Current Attitude	Required Power	Current Attitude	Current Attitude	Current Attitude	
	Updated Attitude	Attitude Control	Control System Performance	Required Power		Heat Generation		
		Attitude Commands	Telemetry, Tracking and Command	Power distribution	On / off commands	Thermal control commands	Orbit correction commands	All telemetry and compressed scientific data
	Power	Power	Power	Electrical Power System	Power	Power	Power	
		Effect of Inertia	Performance Measurements		Line of Sight Interference	Heat Generation Requirements		
		Stability and precision Limits attitude	All Raw Scientific Data	Required Power	Payload	Thermal Limits		
		Reflectivity of coatings/foils	Temperature Measurements	Required Power	Switching on/off if thermal limit exceeded	Thermal Control	Switching Propulsion system on/off when possible	
		Additional Torques	Performance Measurements	Required Power		Heat Generation, status, and requirements	Propulsion	
		Orbit Distance						
		All Commands					Ground station	

14.3. SOFTWARE BLOCK DIAGRAM

The software block diagram, shown in Figure 14.2 shows how information is shared among the subsystems. The system is centralised, and data from all subsystems flows through the data handling system (processor). The processor controls every part of the spacecraft, which either compresses the data from the instruments and relays it to the TT&C subsystem to be sent down to Earth, or handles all telemetry and commands between the subsystems to monitor and maintain control of the spacecraft. Since the processor is critical, there are 2 backup processors to ensure the survival of the spacecraft. This also increases reliability as opposed to having a processor for each subsystem.

14.4. COMMUNICATION FLOW DIAGRAM

The communication flow diagram in Figure 14.3 gives a top level overview of how all information flows through all segments of the mission, all the way from gathering information from the environment to providing prediction of space weather to the stakeholders. Again, the spacecraft itself is centralised around the data handling system, which communicates commands coming from the ground to the rest of the spacecraft and all information to be send down with the communications subsystem. Here, ground stations pick up the signal, where all spacecraft status and performance data is transferred to control, while the scientific data is usually sent to servers to be accessed by stakeholders to be analysed.

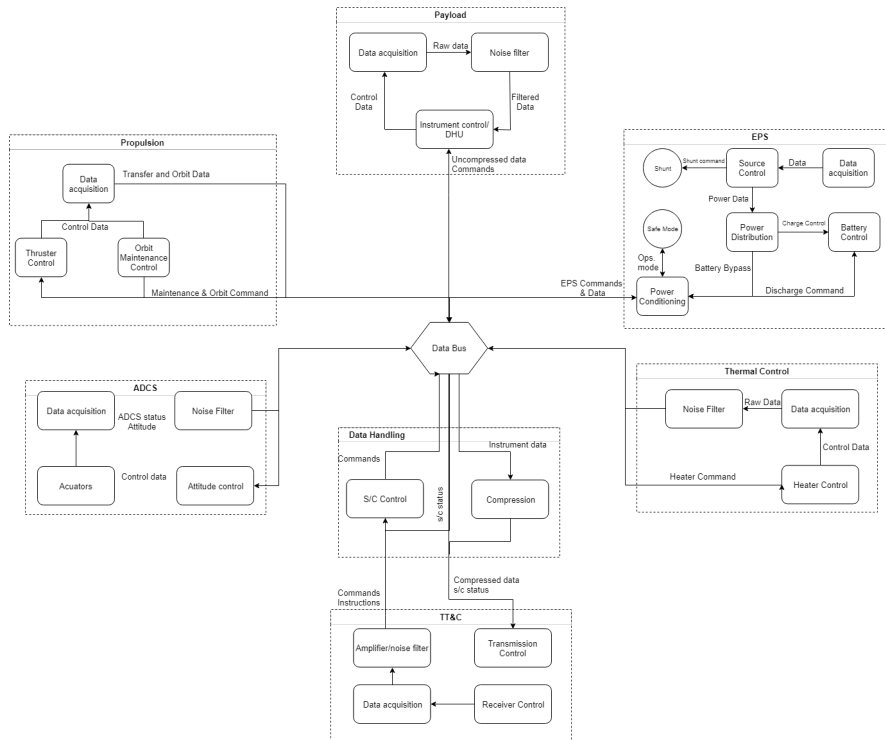


Figure 14.2: The software block diagram showing the information flow between the subsystems

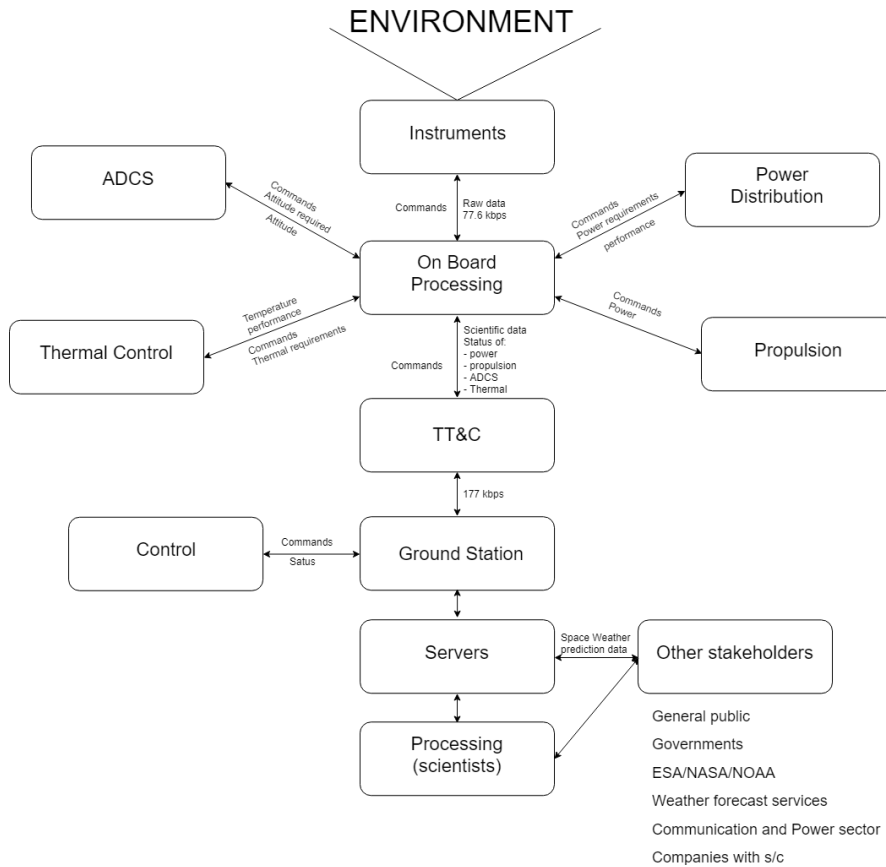


Figure 14.3: Communication flow diagram

15

MASS AND COST BUDGET

In this chapter the final mass and cost budgets of the SWAN mission are presented. The power budget can be found in Section 11.1. The velocity increment budget can be found in Section 8.9. The link budget can be found in Section 7.2. In Table 15.1 the cost budget is shown. Table 15.2 shows the mass budget.

Table 15.1: Cost Budget of the SWAN Spacecraft^[45]

	Component	Cost [k€]		
		OB1	OB2	
Payload	Coronagraph	15,000	15,000	
	Magnetometer	2,000	2,000	
	Magnetograph	-	15,000	
	Heliospheric Imager	-	1,000	
	Faraday Cup	5,000	-	
	EUV Imager	-	15,000	
	X-ray sensor	7,000	7,000	
	SEP Monitor	10,000	-	+
	<i>Total Payload</i>	39,000	55,000	
Structures & Thermal	Non-recurring	13,757	15,207	
	Recurring	2,006	2,323	+
	<i>Total</i>	15,763	17,529	
Propulsion	Non-recurring	2,566	12,584	
	Recurring	164	202	+
	<i>Total</i>	2,729	12,786	
EPS	Non-recurring	3,940	4,562	
	Recurring	2,017	2,335	+
	<i>Total</i>	5,957	6,897	
TT&C	Non-recurring	26,079	26,079	
	Recurring	3,923	4,215	+
	<i>Total</i>	30,002	30,294	
ADCS	Non-recurring	7,597	8,796	
	Recurring	5,096	5,559	+
	<i>Total</i>	12,693	14,354	
Integration	Non-recurring	17,559	23,093	
	Recurring	1,587	5,082	+
	<i>Total</i>	19,146	24,851	+
Total Technical		125,290	161,711	
Programme	Non-recurring	44,323	58,291	
	Recurring	4,586	5,082	+
	<i>Total</i>	48,910	63,374	
Non-Technical	Ground Equipment	85,071	111,879	
	Launch	26,350	26,350	
	Launch Operations	5,850	5,850	+
Total Spacecraft Cost		291,470	369,163	
<i>Budget</i>			800,000	-
<i>Margin</i>			17.4%	

Table 15.2: Mass Budget of the SWAN Spacecraft

	Component	Mass [kg]		Mass Including 18% Contingency [kg]	
		OBI	OB2	OBI	OB2
Payload	Coronagraph	10.5	10.5	12.4	12.4
	Magnetometer	5	5	5.9	5.9
	Magnetograph	-	26	-	30.7
	Heliospheric Imager	-	17	-	20.1
	Faraday Cup	5	-	5.9	-
	EUV Imager	-	10	-	11.8
	X-ray sensor	2	2	2.4	2.4
	SEP Monitor	1.4	-	1.7	-
	<i>Total Payload</i>	23.9	70.5	28.2	83.2
Structures	Central Cylinder	36.9	42.2	43.5	49.8
	Primary Trusses	14.6	59.8	17.2	70.6
	Skin Panels	8.8	21.0	10.4	24.8
	Fuel Tank	2.7	17.0	3.2	20.1
	Oxidiser Tank	1.3	14.5	1.5	17.1
	Pressurant Tank	9.5	27.2	11.2	32.1
	ADCS Fuel Tank	1.3	1.3	1.5	1.5
	Boom	2.1	2.1	2.5	2.5
	Solar Array Support Structure	4.6	5.8	5.4	6.8
	Thrust Frame	0.7	0.8	0.8	0.9
	Other	1.7	4.1	2.0	4.8
	<i>Total Structure</i>	84.2	195.8	99.4	231.0
Propulsion	Main Thruster	5.4	5.4	6.4	6.4
	Oxidiser Feed System	5.6	5.6	6.6	6.6
	Fuel Feed System	5.6	5.6	6.6	6.6
	Pressurant Feed System	12.6	14.6	14.9	17.2
	ADCS Feed System	19.2	19.2	22.7	22.7
	<i>Total Propulsion System</i>	48.4	50.4	57.1	59.5
TCS	<i>Total TCS</i>	4.0	5.0	4.7	5.9
C&DH	Processor	0.5	0.5	0.6	0.6
EPS	Solar Cells	4.0	4.8	4.7	5.7
	Secondary Batteries	0.2	6.3	0.24	7.4
	Power Management System	2.9	5.5	3.4	6.5
	<i>Total EPS</i>	7.0	10.4	8.3	12.3
TT&C	High-Gain Antenna	0.8	10	0.9	11.8
	Low-Gain Antenna	0.4	0.4	0.5	0.5
	<i>Total TT&C</i>	1.2	10.4	1.4	12.3
ADCS	Sun Sensors	2.3	2.3	2.7	2.7
	Star Sensors	0.8	2.0	2.4	-
	Fibre optic gyro	1.6	1.6	1.9	1.9
	Momentum Wheels	3.8	14.4	4.5	17.0
	ACS thrusters	5.3	5.3	6.3	6.3
	ACS Propellant	7.5	9.1	8.9	10.7
	<i>Total ADCS</i>	21.0	38.5	24.8	45.4
Total Dry Mass		190.8	381.5	225.1	450.2
Propellant	Oxidiser	14.4	381.5	17.0	450.2
	Fuel	12.0	319.0	14.2	376.4
	<i>Total Propellant</i>	26.4	700.5	31.2	826.6
Total Spacecraft Mass		217.2	1082	256.3	1276.8

16

POST-DSE ACTIVITIES

This section will describe all procedures and actions that will take place within SWAN's mission after the DSE project all the way up until end of life. The various stages are described in Section 16.1, where the testing and qualification procedures are described in more detail in Section 16.2, followed by all other operations and activities that follow in the utilisation and disposal phases in Section 16.3. Finally the project Gantt chart in section 16.4 will give a final overview of all the activities.

16.1. PROJECT DESIGN AND DEVELOPMENT LOGIC

A project can be divided into seven phases according to ECCSS-M-30A[119], of which the first three phases are included in the DSE followed by a detailed design, production and qualification of the spacecraft and lastly the utilisation and disposal phase. This can be seen in Figure 16.1:

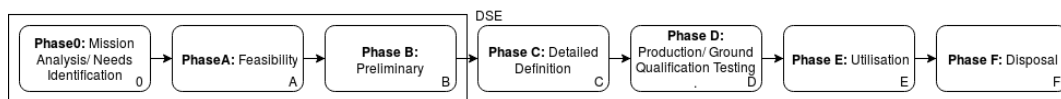


Figure 16.1: Top level production design & development logic

16.1.1. PHASE C: DETAILED DEFINITION

At the end of phase B, the requirements and architectural specifications are defined. These specifications serve as input for the detailed definition phase, in which each element of the mission is designed thoroughly as to comply with the specifications. At the end of phase C (see Figure 16.2) detailed specifications for each component should exit, and a thorough description of their interfaces and the functions they provide should be given.

First, the complete payload and ground segment are fully defined (C2.1-X). From the final payload specifications that result from the complete design (C2.1.2-X), a final bus design can be made (e.g. C2.1). During this process previously defined and new interfaces are defined in the configuration baseline (C2.5.1) and they are closely monitored with the configuration control (C2.5.2). Finally, the actual orbits can be updated to see if these follow the requirements (C3.1 and C3.2). During this process, the Production Master File (C3.5.1) can be updated and several important elements of the design can be produced to test and qualify these. With the Master File complete, the entire production can be laid out (C3.5.2), providing the last information needed to update the Cost Breakdown (C3.5.3). While some elements are already being qualified at this point (C3.3.2), these methods must be defined, and other processes, like production, need to be verified (C3.7). A more detailed overview of these production, testing and qualification procedures is given in Section 16.2.

16.1.2. PHASE D: PRODUCTION/ GROUND QUALIFICATION TESTING

During phase D (see Figure 16.3) the qualification of the methods, procedures, and the production and verification means should be finalised (D1). With this, a qualified definition of the system and all its elements can be made (D2), completing the ground qualification process (D3). The qualified definition of the system should enable the different production phases (D4-1.X) to be completed, during which the required software can also be developed (D4-2.1). Both of these elements must be qualified during the Design qualification, which verifies the technical conformity of these elements against their requirements (D4-3). Finally, one can check if these elements can fulfil their purpose operationally (D5). With the production finalised and fully qualified, the margins can be checked (D6). Then, the integrated logistic support documentation can be set up (D7). This defines the material and support strategy. Finally, the customer must officially acknowledge that the system complies with the predetermined definition of the system (D8).

16.1.3. PHASE E & F: UTILISATION AND DISPOSAL

During the utilisation period the satellites must initially be launched (E2). This involves several activities (E1) such as transportation to the launch site, storage of the spacecraft, implementation of the spacecraft into the launcher and the

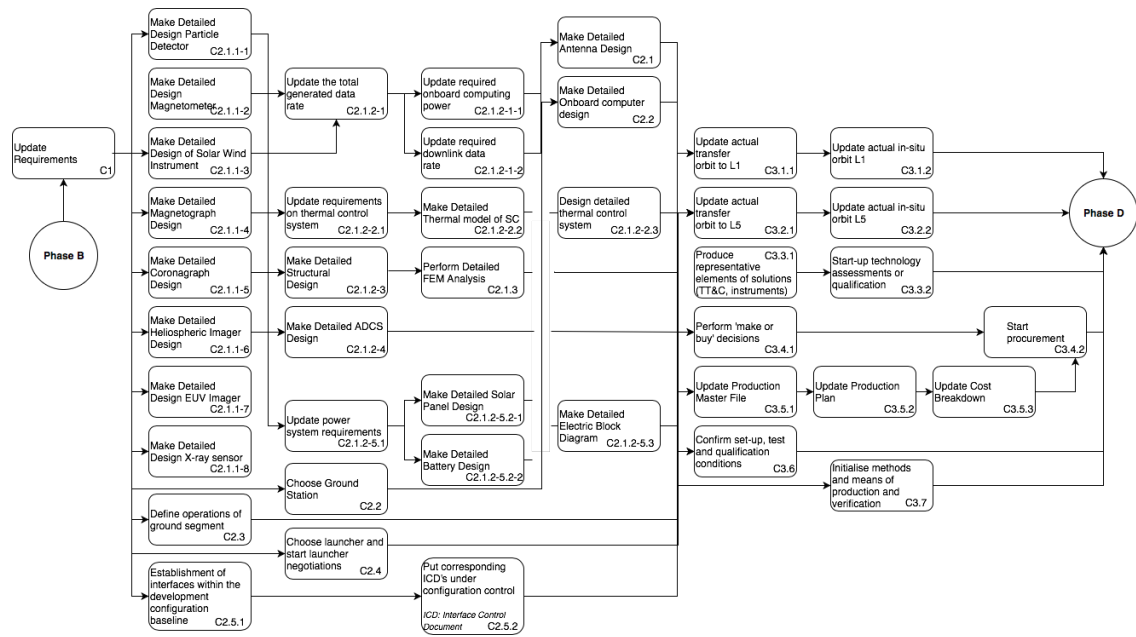


Figure 16.2: Phase C production design & development logic

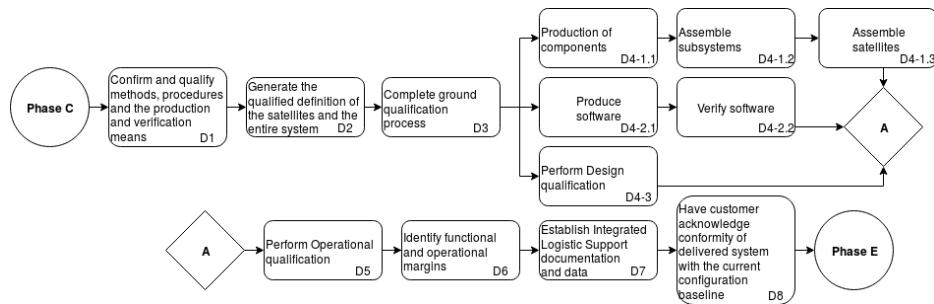


Figure 16.3: Phase D production design & development logic

final checks just before launch. The last qualification activities can be performed when the satellite is in flight (E3). As has been explained in Chapter 8, after 5 years, the spacecrafts will reach their end of life, at which point they will enter a heliocentric orbit to make room for a new generation of spacecraft. At this point they will most likely not be able to perform their initial tasks anymore.

During the operation of the system feedback will be obtained, both on the satellite (E4-1.1-2) as well as on the operational aspect of the mission. This feedback will be used to improve the service by updating the ground segment periodically (E4-1.3-1) and by updating the design of the satellites for the next generation (E4-1.3-2). However, the main purpose of this system remains the reporting of the space weather data. Due to the fact that the SWAN mission is a collaboration between different governmental organisations, the raw data will be provided to citizens (E4-2). The processed data will be distributed among the relevant parties such as governments (E4-3). Finally, the data can be used to improve existing space weather models as well (E4-4). [119]

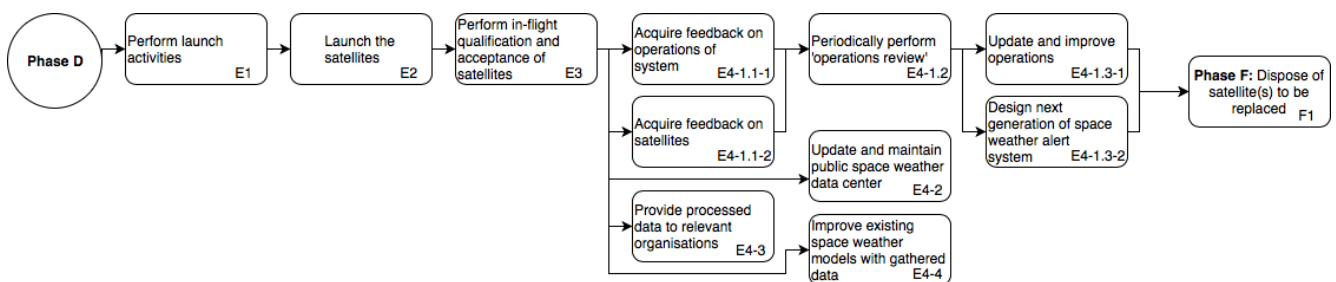


Figure 16.4: Phase E and F production design & development logic

16.2. MANUFACTURING, ASSEMBLY AND INTEGRATION PLAN

The final stages before the both spacecraft are prepared for launch include: manufacturing, assembly and testing. These stages are described in the production plan. Adhering to the production plan is of utmost importance determines whether both spacecraft are space-qualified and are capable of enduring the harsh space environments. This production plan applies to the production and testing of each subsystem and the subsequent integration into a main assembly. The phases of the production plan and its elements are presented in Figure 16.5.

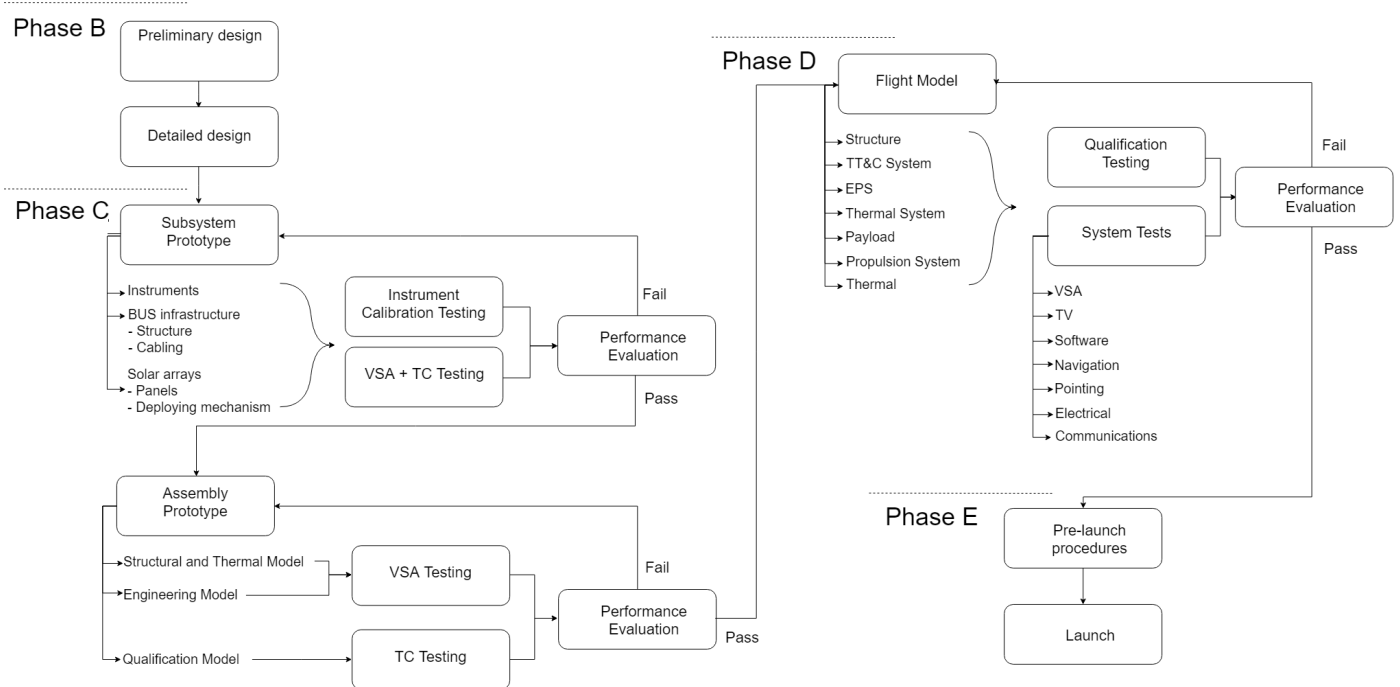


Figure 16.5: Production Flow diagram

16.2.1. DETAILED DEFINITION

The initial phase of the production plan involves producing early models of the subsystems. Scale models are made that are subjected to various tests. From ESA¹, it can be found that in that a structural and thermal model (STM) and an engineering model (EM). These models are then subjected to test that replicate the conditions the spacecraft will experience during launch and during operation. After these models a qualification model (QM) will also be built, this model is then tested to verify system performance. The following test are conducted on the models: vibration, shock and acoustic (VSA) tests and thermal vacuum (TV) tests.

- **Vibration, Shock and Acoustic (VSA) Tests:** These tests are aimed at simulating the conditions the spacecraft will experience during the launch. This is accomplished by rigging the spacecraft to a vibrating table. The vibrations produces are typically 25% greater than what is to be expected during the actual launch.
- **Thermal Vacuum Test:** This test sees the spacecraft placed in a vacuum chamber whilst a Sun simulator replicates the temperature environment experienced at L1 and L5. This test is used to verify that the spacecraft is capable of withstanding the extreme temperature variations experienced in space.

The aforementioned tests also apply to the subsystem assemblies that need to be manufactured. Many of the subsystems are can be purchased "off-the-shelf", whereas other are purpose-built and thus need to be produced to spec. These assemblies include: all instruments, boom structure, spacecraft structure (BUS) and solar arrays. These subsystem assemblies will also be verified by means of VSA and TV tests. Furthermore, subsystems such as the deployment mechanism for the solar arrays will undergo testing of the actuators to ensure that the system will function properly.

INSTRUMENTATION

Parallel to testing the STM and EM, the payload will undergo testing and calibration. For the SWAN mission the instruments are highly specialised and complex and thus require additional tests to ascertain the reliability and decay/drift of

¹http://www.esa.int/Our_Activities/Space_Science/Building_and_testing_spacecraft

these instruments. In particular the magnetometer will undergo static noise calibrations, as described in Section 6.2.9, in addition to zero level drift tests to determine its properties over time. In short, in this phase of the production, tests will be conducted to validate the requirements and specifications of each instrument (see Table 6.13).

16.2.2. SUBSYSTEM MANUFACTURING

All the subsystems that are integrated into the spacecraft need to be manufactured. Many can be purchased off-the-shelf, whereas some need to be developed separately. Typically subsystem manufacturing is conducted in a cleaning room as to comply with planetary protection regulations stated by COSPAR [120]. From these regulations it can be found that the SWAN spacecraft do not require cleaning in regard to planetary protection, since the target of the mission is not interesting for the research of life. However, due to the sensitive optical instruments that are included manufacturing is to be conducted in a clean room. During the entire manufacturing process the philosophy of "lean manufacturing" will be applied, this aims to keep the production of waste at a minimum and improve the sustainability of the mission.

16.2.3. INTEGRATION

Likewise, the assembly of all the subsystems into the spacecraft will also be conducted in a clean room. This too is done to prevent contamination of sensitive instruments. The process of assembly will see numerous sub-assembly operate in parallel, this will reduce the time required for the assembly. Assembly of the STM, EM and QM will occur during prototyping, after which the flight model will be assembled before final testing and qualification.

16.2.4. FINAL TESTING AND CERTIFICATION

Once the critical design review has been approved and the flight model has been assembled, final testing can commence. In this situation, the entire flight model is put through TV and VSA tests. Furthermore, the operation of the instruments and electronics will also be tested. Deployment of the solar array and boom will also be tested. The software is checked including that which is necessary for successful navigation of the spacecraft. Once all these checks are successfully completed the spacecraft is fully-certified.

16.3. OPERATIONS AND LOGISTICS CONCEPT DESCRIPTION

To maintain a good overview of all tasks and costs related to the operations and logistics of the SWAN mission, it is necessary to perform a preliminary investigation into these aspects for all post-DSE phases. A division is made between all pre-launch operations in Section 16.3.1, and all post-launch operations in (Section 16.3.2). In this preliminary analysis, the (expected) necessary resources for all stages are listed, in order to have a good overview for a potential detailed design cost and resource investigation.

16.3.1. PRE-LAUNCH OPERATIONS

Figure 16.6 shows the pre-launch operations flow diagram. The previous section described the production, qualification and certification phases. For the remaining phases, this section will discuss the content of each step.

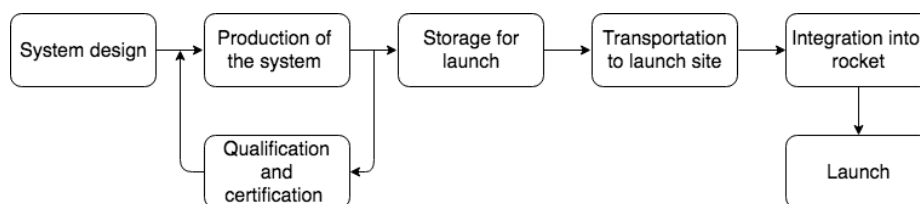


Figure 16.6: Pre-Launch Operations Flow Diagram

Storage for launch; upon finishing the spacecraft, it will not directly be transported to the launch site and launched into space. In order to store the spacecraft, facilities are required that are able to store the spacecraft in a safe and clean environment. In the design of the spacecraft the dimensions of the spacecraft should be made such that safe storage is assured.

Transportation to launch site; depending on the assembly location of the spacecraft, different transportation methods can be used to transport the spacecraft from the assembly location to the launch site. This may result in additional requirements that have to be added to the design of the spacecraft. For instance, the spacecraft should fit on a train, or inside an aircraft, this limits thus the dimensions of the spacecraft. Furthermore qualified personnel is needed to transport the satellite via aircraft or trains. Besides that, the risk exists that during transportation the spacecraft will be damaged, therefore the assembly should be designed to ensure relative easy detachment and repair of the spacecraft.

Integration into launcher; as has been discussed in Chapter 8, the two spacecraft will be implemented into one launcher with an inner fairing between the two spacecraft. This results in the fact that the spacecraft have to be designed such that they both fit inside the payload bay of the launcher. Also batteries will be stored in the launcher, to give power to the spacecraft during the launch phase. Therefore extra care should be taken during detachment of the launcher that the batteries will not hit the spacecraft. Overall personnel is needed who can mount the two satellites on the launcher and make sure everything is attached safely to the launcher.

Launch; in order to launch the satellite into the desired orbit, it is necessary to make a selection of launch facilities that suit the mission. All staff and operations during launch are provided by the launch facilities and are thus included in the launch costs.

16.3.2. POST-LAUNCH OPERATIONS

In Figure 16.7 the post-launch operations are visualised in a flow diagram. This overview focuses on all logistics and operations related to keeping the system functional, while also forming the link between the SWAN mission and the external stakeholders. A number of different links in the operations chain can be identified.

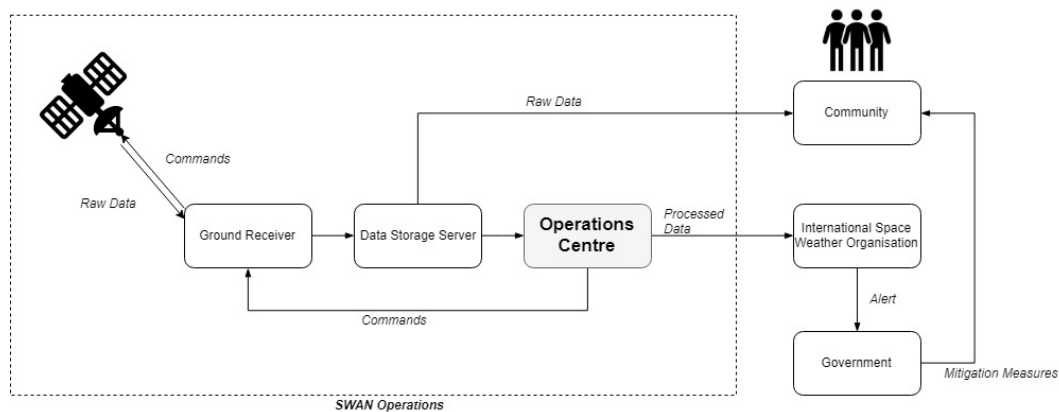


Figure 16.7: Post-Launch Operations Flow Diagram

Ground Receiver; this station forms the link between the satellite and the operations centre of the mission. As discussed in Chapter 7, to save money on developing new facilities for the ground receivers, it is considered to use existing communication infrastructure from other missions to do this. This may, however, lead to costs for 'renting' these facilities and hiring personnel for these facilities.

Data Storage Server; to store all space weather information, separate servers are necessary to keep an archive of the raw data. The most efficient option is to integrate this server in the main operations centre. The server should be an open source for the community to view the collected data, as its accessibility is an important value to the mission and its stakeholders. Furthermore the reliability of the server should be guaranteed, when this server fails, it is namely not possible to acquire the data for research.

Operations Centre; the heart of all operations related to the SWAN mission, is located here. As a minimum, a separate facility is necessary, along with sufficient staff. Data handlers will analyse and process the measurements from the spacecraft, while system administrators will maintain the servers and external interfaces for all stakeholders. The operations centre sends commands back to the spacecraft, while also sending the processed data to the international space weather organisations.

16.3.3. SYSTEM MAINTENANCE

Maintenance is an important part of operating a system. However, for a complicated space mission such as SWAN, it is near impossible to perform reparations or tune-ups on the spacecraft once they are in their orbit. Hence, maintenance on the spacecraft is not a relevant aspect of the mission. Once the spacecraft have reached their EOL, it is the intent of the mission to keep all of its ground operations and to send new satellites to take over the tasks of their predecessors. Contrary to the spacecraft themselves, this means that all ground operation facilities and equipment do need regular maintenance and check-ups. This can easily be done in the form of technicians, website administrators, and cleaners to keep everything running smoothly.

17

CONCLUSION

The objective of this report was to design a Space Weather Alert Network at the L1 and L5 Sun-Earth Lagrangian points. This report consisted of the design of the payload used during the mission and the design of each of the subsystems of the spacecraft. After performing a market analysis, it can be concluded that the mission is financially viable. The investors are able to gain a return on their investment due to the reduction in damage caused by Coronal Mass Ejections (CMEs). On top of this, an additional revenue of \$ 4 to \$ 5 mln can come from investing in industry specific predictions. During the design of both spacecraft, emphasis was put on a sustainability strategy for both spacecraft. This strategy has taken into account during design trade-offs, such as when choosing for a single launch over a double launch and during the material selection of the spacecraft.

Due to budget constraints, it was not possible to incorporate all payload on both spacecraft. For this reason, it was decided to divide the payload, such that Observation Beacon 1 (OB1) mainly consists of in-situ instruments and Observation Beacon 2 (OB2) mainly consists of remote-sensing instruments. Using this configuration, it is possible to detect a CME approximately 21 hours before it possibly reaches the Earth. However, the definite warning can only be issued 12 minutes before a CME strikes the Earth. The data that is generated by the payload will be uncompressed for OB1 and compressed for OB2 using JPEG 2000 compression, resulting in a data rate of 69 kbps and 177 kbps for OB1 and OB2 respectively. The transmission of data is performed by a 0.2 m diameter horn antenna on OB1 and a 1.44 m diameter parabolic dish antenna on OB2.

In order to get to the L1 and L5 points, it was necessary to perform an astrodynamical analysis. This analysis led to the conclusion that it is feasible to use a single launcher for both spacecraft. The Falcon 9 Block 5 full thrust launcher carrying both spacecraft will lift-off on 29 July 2023 at 15:03:52 UTC. After 122.9 and 406.8 days respectively, OB1 and OB2 will arrive at their destination. For this transfer, each spacecraft is equipped with a propulsion system using Nitrogen Tetroxide and Methylhydrazine as propellants.

During the transfer, OB1 will be able to keep its temperature between the required 15° and 30°. However, the temperature of OB2 drops to -5°. This problem does not seem to be particularly significant as the temperature critical instruments are non-operational during this period. Meanwhile, a subsystem that is continuously operational during the mission is the power subsystem. During the launcher phase, primary batteries will be attached to the launcher and will supply power before separation from the launcher. After separation, GaAs TJ ultraflex solar panels will be used as a primary power source. During insertion or correction burns, secondary batteries will be used to provide the required power.

Since most of the payload instruments and TT&C system have stringent pointing requirements, the driving accuracy being 4.3 arcminutes for OB1 from the coronagraph and 0.55 arcminutes for OB2 from the magnetograph, the spacecraft will include 4 momentum wheels, 16 thrusters, 7 sun sensors, 2 star trackers and 2 inertial measurement units to be able to determine and control the attitude of the spacecraft. This zero momentum attitude control method will allow the spacecraft to achieve the required orientation as well as cope with perturbations such as solar radiation pressure, magnetic torque, atmospheric drag and gravity gradients. Routine momentum dumps are required to dissipate the accumulated 3,141 Nms and 170 Nms for OB1 and OB2 respectively. All the components are redundant, ensuring that if one component fails, the spacecraft will still be able to function properly.

The structure of the spacecraft consist of a central cylinder providing the spacecraft's main stiffness. Furthermore, the frame provides the main strength for axial bending and torsional forces. Finally, skin panels of the spacecraft are made of a composite sandwich structure with an aramid honeycomb core and carbon fibre face sheets.

RECOMMENDATIONS

First of all, after attending a meeting with the company Science [&] Technology Corporation it was suggested to perform research in the field of CubeSats. For the SWAN mission, 800 million euros have been reserved in order to design an accurate space weather alert network. However, it might be interesting to assess the plausibility of a mission that has similar capabilities as the SWAN mission, whilst minimising the cost. CubeSats could offer an opportunity to do so.

Furthermore, it is assumed that the SWAN mission is executed in a "perfect world" without any political issues between different parties such as NASA, ESA and NOAA. However, in reality, this is not the case. In reality, there is much bureaucracy involved in the design of the SWAN mission. This would not only influence the design choices of the mission

(such as launcher choice) but also might result in mission delay and increased mission costs. For this reason, it would be valuable to perform an elaborated research on the effect of the SWAN mission taking place in the real world.

Another recommendation is the reexamination of the thermal model. In the analysis presented in Chapter 10 the heat dissipation assumed was assumed to be 30 W, actual values shall be in the order of 500 W. This heat dissipation is close to the total power that is generated by the spacecraft. With this new value, it is expected that the spacecraft will require a degree of active thermal control aimed at cooling the spacecraft.

It is also recommended to take a further and more detailed look into the possibility for multiple burns per orbit for station keeping. This approach might decrease the sensitivity of the orbit around L1, and decrease the fuel required for both L1 and L5 during the operational phase and insertion, respectively.

Finally, more assessment is required for the boom of both spacecraft. Particularly, it is recommended to look into a deployment mechanism for the boom such that it can fit into the fairing of the launch vehicle.

BIBLIOGRAPHY

- [1] S. van Diepen, N. Griffioen, F. van Kan, *et al.*, *Space Weather Observation System at Two Lagrangian Points: AE3200 Design Synthesis Exercise Project Plan*, Unpublished (2018).
- [2] S. van Diepen, N. Griffioen, F. van Kan, *et al.*, *Space Weather Observation System at Two Lagrangian Points: AE3200 Design Synthesis Exercise Baseline Report*, Unpublished (2018).
- [3] S. van Diepen, N. Griffioen, F. van Kan, *et al.*, *Space Weather Observation System at Two Lagrangian Points: AE3200 Design Synthesis Exercise Midterm Report*, Unpublished (2018).
- [4] P. Riley, *On the probability of occurrence of extreme space weather events*, *Space Weather* (2012).
- [5] A. Shaw, *ESA space weather study*, ESYS plc (2001).
- [6] B. Cugny, N. Karafolas, and Z. Sodnik, eds., *Remote sensing optical instrumentation for enhanced space weather monitoring from the L1 and L5 Lagrange points*, International Conference on Space Optics, Vol. 10562, 105620F-1 (SPIE. Digital Library, Biarritz, France, 2016).
- [7] R. B. Horne, *Rationale and Requirements for a European Space Weather Programme*, British Antarctic Survey (2001).
- [8] E. A. Taylor, *ESA space weather study - final presentation market analysis*, Astrium (2001).
- [9] NOAA, *NOAA Satellite and Information Service Deep Space Climate Observatory (DSCOVR)*, NOAA (N.A.).
- [10] J. Heiligers, B. Diedrich, B. Derbes, and C. McInnes, *Sunjammer: Preliminary end-to-end mission design*, *AIAA/AAS Astrodynamics Specialist Conference 2014* (2014).
- [11] L. Johnson, *Multiple NEO Rendezvous Using Solar Sails*, MSFC Advanced Concepts Office (N.A.).
- [12] B. Zandbergen, *Aerospace Design & System Engineering Elements I - Part: Spacecraft (bus) Design and Sizing* (Delft University of Technology, 2015).
- [13] A. D. Basiago, *Economic, social, and environmental sustainability in development theory and urban planning practice*, *Environmentalist* **19**, 145 (1998).
- [14] F. Khan, R. Sadiq, and B. Veitch, *Life cycle iNdeX (LInX): a new indexing procedure for process and product design and decision-making*, *Journal of Cleaner Production* **12**, 59 (2004).
- [15] M. Moldwin, *An Introduction to Space Weather* (Cambridge University Press, 2008).
- [16] D. Reames, *Solar Energetic Particles: A Modern Primer on Understanding Sources, Acceleration and Propagation*, Lecture Notes in Physics (Springer International Publishing, 2017).
- [17] Russell C. T., *Solar Wind and Interplanetary Magnetic Field: A Tutorial*, in *Space Weather* (American Geophysical Union (AGU), 2013) pp. 73–89, <https://agupubs.onlinelibrary.wiley.com/doi/pdf/10.1029/GM125p0073>.
- [18] K. H. Schatten and J. M. Wilcox, *Response of the Geomagnetic Activity Index to the Interplanetary Magnetic Field*, *Journal of Geophysical Research* (1967).
- [19] I. G. Richardson, E. W. Cliver, and H. V. Cane, *Long-term trends in interplanetary magnetic field strength and solar wind structure during the twentieth century*, *Journal of Geophysical Research* (2002).
- [20] M. Hapgood, *Space Weather*, Vol. 8 (IOP Publishing, 2017).
- [21] D. Cabrera Solana, L. R. Bellot Rubio, and J. C. del Toro Iniesta, *Sensitivity of spectral lines to temperature, velocity, and magnetic field*, *A&A* **439**, 687 (2005).
- [22] T. J. Spirock, *Next generation digital vector magnetograph; high cadence, precision and resolution*, (2005).
- [23] A. Landé, *Über den anomalen Zeemaneffekt (Teil I)*, *Zeitschrift für Physik* **5**, 231 (1921).
- [24] M. Collados, V. Martinez Pillet, B. Ruiz Cobo, J. C. del Toro Iniesta, and M. Vazquez, *Observed differences between large and small sunspots*, *AAP* **291**, 622 (1994).
- [25] F. T. Watson, M. J. Penn, and W. Livingston, *A Multi-instrument Analysis of Sunspot Umbrae*, *The Astrophysical Journal* **787**, 22 (2014).
- [26] J. Delaboudiniere, G. Artzner, J. Brunaud, *et al.*, *EIT: Extreme-Ultraviolet imaging telescope for the SOHO mission*, *Solar Physics* (1995).
- [27] A. Vourlidas, *Mission to the Sun-Earth L5 Lagrangian Point: An Optimal Platform for Space Weather Research*, AGU publications (2015).
- [28] J. R. Lemen, A. M. Title, D. J. Akin, *et al.*, *The Atmospheric Imaging Assembly (AIA) on the Solar Dynamics Observatory (SDO)*, *Solar Physics* (2010).
- [29] A. Katsiyannis, D. Berghmans, B. Nicula, *et al.*, *SWAP: An EUV imager for solar monitoring on board of PROBA2*, American Institute of Physics (2006).
- [30] K. F. Middleton, A. Bourdelle, J. A. Davies, *et al.*, *Coronal and Heliospheric imagers for solar wind phenomena*, SPIE Optical Engineering (2015).
- [31] M. J. Lewis and B. J. Kellett, *Determining the correlation between the GOES XRS and the ESA SMART-1 instrument XSM in the 1 – 8 Å spectral region*, Science Direct (2006).
- [32] G. Simnett and R. Harrison, *The Onset Of Coronal Mass Ejections*, University of Birmingham (1985).
- [33] A.-Q. Chen and W.-G. Zong, *Relationship between CME velocities and X-ray fluxes of associated flares*, *Astronomy*

- and *Astrophysics Journal* (2009).
- [34] J. Laukkanen, V. Lamsa, A. Salminen, *et al.*, *Radiation hardness studies for the X-ray Solar Monitor (XSM) onboard the ESA SMART-1 mission*, *Nuclear Instruments and Methods in Physics Research* (2004).
- [35] A. J. Lazarus, J. C. Kasper, and K. W. Ogilvie, *A Faraday-Cup Solar Wind Experiment for Solar Orbiter*, in *Second Solar Orbiter Workshop*, ESA Special Publication, Vol. 641 (2007) p. 92.
- [36] K. W. Ogilvie, D. J. Chornay, *et al.*, *SWE, a comprehensive plasma instrument for the WIND spacecraft*, *Space Science Reviews* **71**, 55 (1995).
- [37] L. Desorgher, W. Hajdas, *et al.*, *The Next Generation Radiation Monitor- NGRM*, in *2013 IEEE Nuclear Science Symposium and Medical Imaging Conference (2013 NSS/MIC)* (2013) pp. 1–6.
- [38] M. H. Acuña, *Space-based magnetometers*, *Review of Scientific Instruments* **73**, 3717 (2002).
- [39] D. Carter, D. Freesland, *et al.*, *Correcting GOES-R magnetometer data for stray fields*, in *2016 ESA Workshop on Aerospace EMC (Aerospace EMC)* (2016) pp. 1–6.
- [40] D. Baker, R. Belian, *et al.*, *Deep dielectric charging effects due to high-energy electrons in earth's outer magnetosphere*, *Journal of Electrostatics* **20**, 3 (1987).
- [41] S. Lai, K. Cahoy, *et al.*, *Deep Dielectric Charging and Spacecraft Anomalies* (Elsevier, 2018) pp. 419–432.
- [42] O. D. Giersch, J. Kennewell, and M. Lynch, *Solar Radio Burst Statistics and Implications for Space Weather Effects*, *Space Weather* **15**, 1511 (2017).
- [43] G. Yu, T. Vladimirova, and M. N. Sweeting, *Image compression systems on board satellites*, *Acta Astronautica* (2009).
- [44] A. Kwok, *201, Rev. B Frequency and Channel Assignments*, *DSN Telecommunications Link Design Handbook* (2009).
- [45] J. R. Wertz, D. F. Everett, J. J. Puschell, *et al.*, *Space Mission Engineering: The New SMAD* (Microcosm Press, 2011).
- [46] A. Cervone, *AE2111-II Aerospace Design and Systems Engineering Elements II*, TU Delft (2017).
- [47] T. Teshirogi and T. Yoneyama, *Modern millimeter-wave technologies*, IOS Press (2001).
- [48] A. R. Jablon and R. K. Stillwell, *Spacecraft Reflector Antenna Development: Challenges and Novel Solutions*, Johns Hopkins APL Technical Digest (1994).
- [49] J.-F. Castet and J. Saleh, *Satellite and satellite subsystems reliability: Statistical data analysis and modeling*, *Reliability Engineering & System Safety* (2009).
- [50] S. Hughes, R. Qureshi, D. Cooley, *et al.*, *Verification and Validation of the General Mission Analysis Tool (GMAT)*, NASA (2013).
- [51] N. Capitaine, P. Wallace, and J. Chapront, *Expressions for IAU 2000 precession quantities*, *Astronomy & Astrophysics* (2003).
- [52] A. Berger, M. Loutre, and J. Laskar, *Stability of the Astronomical Frequencies Over the Earth's History for Paleoclimate Studies*, *Science* (1992).
- [53] F. Zazzera, F. Topputo, and M. Massari, *Assessment of Mission Design Including Utilization of Libration Points and Weak Stability Boundaries* (Dipartimento di Ingegneria Aerospaziale Politecnico di Milano, 2004).
- [54] M. W. Lo, P. J. Llanos, and G. R. Hintz, *An L5 Mission to Observe the Sun and Space Weather, Part 1*, AAS/AIAA Spaceflight Mechanics Meeting (2010).
- [55] K. Wakker, *Fundamentals of Astrodynamics* (Delft University of Technology, 2015).
- [56] Unknown, *Fiche technique (Falcon 9)*, *Espace et exploration* (2017).
- [57] Space Exploration Technologies Corporation, *Falcon 9 Launch Vehicle Payload User's Guide*, Boulevard de l'Europe, BP 177 91006 Evry-Courcouronnes Cedex, France, 2nd ed. (2015).
- [58] The GMAT Development Team, *GMAT User Guide R2018a*, NASA (2018).
- [59] P. Llanos, J. Miller, and G. Hintz, *Navigation Analysis for an L5 Mission in the Sun-Earth System*, Conference Paper (2011).
- [60] MOOG, *MOOG Upper Stage Engines*, N.A. (2013).
- [61] Northrop Grumman Space Technology, *TR-308 Dual Mode Liquid Apogee Engine*, Northrop Grumman Propulsion Systems (N.A.).
- [62] Ariane Group, *Chemical Bi-propellant Thruster Family*, Bipropellant Thruster Brochures (2018).
- [63] Aerojet Rocketdyne, *Bipropellant Rocket Engines*, N.A. (2009).
- [64] G. Sutton and O. Biblarz, *Rocket Propulsion Elements - 9th Edition* (John Wiley & Sons, Inc., Hoboken, New Jersey, 2010).
- [65] I. Martinez, *Properties of Liquids*, N.A. (2018).
- [66] M. W. Leeds, R. N. Eberhardt, and R. L. Berry, *Development of the Cassini spacecraft propulsion subsystem* (AIAA, 1996).
- [67] D. Huzel and D. Huang, *Modern Engineering for Design of Liquid-Propellant Rocket Engines*, *Ingenieria de transportes y aeronautica* (American Institute of Aeronautics & Astronautics, 1992).
- [68] NASA, *Apollo 15 Mission Report*, National Aeronautics and Space Administration (1971).
- [69] NASA, *Potential Failure of Dual Simultaneously Initiated Pyrotechnic Operated Valves*, NASA Engineering and Safety Center Technical Bulletin (2010).
- [70] IndiaMart, *L&T,AUDCO,KSB & BDK Swing Check Valve*, Product Catalogue (2018).
- [71] A. G. Crosby, *Pressure Relief Valve Engineering Handbook*, Technical Seminar Manual (2018).
- [72] J. F. Ball, *Specification of Rupture Disk Burst Pressure*, *Powder Metallurgy and Metal Ceramics* (2011).

- [73] V. Sychuk, O. V. Zabolotnyi, and A. J. Mcmillan, *Developing New Design and Investigating Porous Nozzles for Abrasive Jet Machine*, Powder Metallurgy and Metal Ceramics (2015).
- [74] Omnidea-RTG, *Space Propulsion Components Product Catalogue*, Product Catalogue (2016).
- [75] R. Myers and S. Oleson, *Small Satellite Propulsion Options*, 30th Joint Propulsion Conference (1994).
- [76] VACCO, *Low Pressure Fill & Drain Valves*, Product Catalogue (2014).
- [77] ArianeGroup, *Orbital Propulsion Fluidic Equipment*, Product Catalogue (2018).
- [78] VACCO, *Check Valves*, Product Catalogue (2014).
- [79] VACCO, *Low pressure relief valve*, Product Specifications (2018).
- [80] Technetics, *SAFE-SHEAR® Burst Disc Technology*, Product Specs (2018).
- [81] Emerson, *Paine Miniature-Satellite Series Pressure Transmitter*, Product Specifications (2018).
- [82] B. Zandbergen, *Thermal Rocket Propulsion v.2.05* (Delft University of Technology, Delft, Netherlands, 2016).
- [83] MT Aerospace, *PVG Family 40 - 75 L High Pressure Tank (HPV) – Helium/Nitrogen - COTS*, Product Specifications (2018).
- [84] D. Eakman, R. Lambeck, M. Mackowski, and L. Slifer, *Small Spacecraft Power and Thermal Subsystems*, National Aeronautics and Space Administration (1994).
- [85] R. Karam, *Satellite Thermal Control for Systems Engineers*, Vol. 181 (American Institute of Aerodynamics and Astrophysics, 1998).
- [86] V. L. Pisacane, *Fundamentals of Space Systems*, Vol. 2 (Oxford University Press, 2005).
- [87] P. Poinas and J. Candé, *SOHO spacecraft thermal control aspects*, Space Environmental Control Systems (1977).
- [88] D. F. da Silva, I. Muraoka, and E. Castejon Garcia, *Thermal Control Design Conception of the Amazonia-1 Satellite*, Instituto Nacional de Pesquisas Espaciais (2014).
- [89] R. Durbeck, *Output Hardcopy Devices*, International Business Machines Corporation (2012).
- [90] J. F. Clawson, G. T. Tsuyuki, B. J. Anderson, et al., *Spacecraft Thermal Environments*, N.A. (N.A.).
- [91] J. Meseguer, I. Pérez-Grande, and A. Sanz-Andrés, *2 - Space environment*, in *Spacecraft Thermal Control* (Woodhead Publishing, 2012) pp. 15 – 38.
- [92] R. Wordsworth, *Spacecraft thermal control II*, (2016).
- [93] K. S. W. Champion, A. E. Cole, and A. J. Kantor, *Chapter 14 Standard and Reference Atmospheres*, (N.A.).
- [94] J. H. Henninger, *Solar Absorptance and Thermal Emittance of Some Common Spacecraft Thermal Control Coatings*, Scientific and Technical Information Branch (1984).
- [95] A. Anvari, F. Farhani, and K. Niaki, *Comparative Study on Space Qualified Paints Used for Thermal Control of a Small Satellite*, Iranian Journal of Chemical Engineering (2009).
- [96] D. A. Jaworske and S. E. Kline, *Review of End-of-Life Thermal Control Coating Performance*, N.A. (2008).
- [97] I. Martinez, *Properties of Solids*, N.A. (2018).
- [98] A. C. Wright, *USAF Propellant Handbook Nitric Acid/Nitrogen Tetroxide Oxidizers*, Vol. 2 (Martin Marietta, 1977).
- [99] R. J. Page, W. A. Stoner, and L. Barker, *A Design Study of Hydrazine and Biowaste Resistojets*, NASA (1986).
- [100] ANSYS, *ANSYS Mechanical Users Guide 18*, ANSYS (2018).
- [101] ANSYS, *ANSYS Meshing Users Guide 18*, ANSYS (2015).
- [102] R. Peyrou-Lauga, *Using real Earth Albedo and Earth IR Flux for Spacecraft Thermal Analysis*, European Space Agency (2017).
- [103] H. Hecht and M. Hecht, *Reliability Prediction for Spacecraft*, Rome Air Development Center (1985).
- [104] D. W. Miller and J. Keesee, *Spacecraft Power Systems*, MIT (Unknown).
- [105] A.J.Ball et al., *Planetary Landers and Entry Probes* (Cambridge University Press, 2007).
- [106] Unknown, *Tadiram Lithium Batteries*, Tadiram Batteries (Unknown).
- [107] Unknown, *D.C. Geared Motors Datasheet*, Crouzet (Unknown).
- [108] V. Carrara and K. Kuga, *Estimating Friction Parameters in Reaction Wheels for Attitude Control*, Mathematical Problems in Engineering **2013**, 1 (2013).
- [109] T. Marshall and M. Fletcher, *Meeting High-quality RWA Commercial Demand through Innovative Design*, Honeywell Inc., *Satellite Systems Operation* (1999), <http://esmats.eu/esmatspapers/pastpapers/pdfs/1999/marshall.pdf>.
- [110] ArianeGroup, *1N, 20N, 400N and Heritage Thruster*, N.A. (N.A.).
- [111] Aerojet, *Monopropellant Thruster Datasheet*, N.A. (2006).
- [112] F. Napolitano, *Fibre Optic Gyroscopes Key technological Advantages*, IXSEA - AN IXBLUE COMPANY, 1 (2010).
- [113] C. Russell, *The STEREO Mission* (Springer, Los Angeles, CA 3845, USA, 2008).
- [114] G. F. Abdelal, N. Abuefoutouh, and A. H. Gad, *Finite Element Analysis for Satellite Structures*, Vol. 1 (Springer, 2003).
- [115] M. F. Ashby, *Materials Selection in Mechanical Design*, Vol. 3 (Elsevier, 2005).
- [116] G. G. Herzl et al., *Tubular Spacecraft Booms (Extendible, reel stored)*, *NASA Space Vehicle Design Criteria (Guidance and Control)* (1971).
- [117] P. Gaudenzi, *Design criteria and procedures of space structure*, The ESA SME Initiative Training Courses (N.A.).
- [118] S. Hulshoff, *Course AE2220-II: Computational Modelling*, Vol. 1 (Delft University of Technology, 2016).
- [119] ECSS Secretariat, *Space Project Management: Project Phasing and Planning* (ESA Publications Division, ESTEC, P.O. Box 299, 2200AG Noordwijk, The Netherlands, 1996).
- [120] G. Kminek, C. Conley, et al., *COSPAR's Planetary Protection Policy*, COSPAR (2017).

A

WORK DIVISION

In Table A.1 the work division of Group 6 can be seen. R means that the member has performed research into the task, W means that the member has written the task, and P means the member has proofread the part in the report.

Table A.1: Task Division. R = Researched, W = Written, P = Proofread

Task	Simon D	Nathan	Ferran	Krijn	Christopher	Olivier	Simon O	Nikhil	Tim	Nick
Nomenclature	W									
Executive Summary	W		P					P	R,W	
Introduction							W		P	
Functional Flow Diagram	P			R,W				R		
Functional Break-down Structure	P			R,W				R		
Budget Allocation				R,W						
Sustainable Development Strategy			R,W,P						R,W,P	
Aerodynamic Characteristics	R,W							P		
Payload			R,W,P	P				R,W,P		
TT&C			R,P					R,W		
Main Propulsion System			P	R,W			R		R	
ADCS		R,W,P					R	P	R	
Thermal Power			P						R,W,P	R,W,P
Structural Characteristics				P	R,W,P	R,W,P				
Interfaces	W		R,W	R,W				R,W,P		
Configuration Layout					R,W,P	R,W				
Market Analysis			P	R,W					R,W,P	R,W,P
Post-DSE Activities			R,W		R,W,P	R,W	R,W	R,W,P	R,W	
Conclusion		P	R,W				W		R,W	
Bibliography	W									
Work Division	W									
Trade-off Revision	P		P	R,W			R,W			